

REMANENT CREEP LIFE PREDICTION
IN LOW-ALLOY FERRITIC STEEL
POWER PLANT COMPONENTS

By
Peter Wilson
Pembroke College
Cambridge

A dissertation submitted for the degree of
Doctor of Philosophy
at the University of Cambridge
November 1990

PREFACE

This dissertation is submitted for the Degree of Doctor of Philosophy in the University of Cambridge. The investigation described herein was carried out under the supervision of Dr H.K.D.H. Bhadeshia in the Department of Materials Science and Metallurgy, University of Cambridge, between October 1986 and September 1990.

Except where acknowledgement and reference is specifically made to the contrary, this work is, to the best of my knowledge, original and has been carried out without collaboration. Neither this, nor any substantially similar dissertation has been, or is being, submitted for any degree, diploma or other qualification at any other university.

This dissertation does not exceed 60 000 words in length.

A handwritten signature in black ink, appearing to read 'Peter Wilson', with a long horizontal flourish extending to the right.

Peter Wilson

Pembroke College

November 1990

ACKNOWLEDGEMENTS

I am indebted to Dr H.K.D.H. Bhadeshia for his invaluable advice and support during the course of this research, and to Professor D. Hull for the provision of laboratory facilities in the Department of Materials Science and Metallurgy at the University of Cambridge.

I must also express my gratitude to friends and colleagues in the Department, and especially in the Phase Transformations Group, in particular to Dr Jer-Ren Yang and Dr Serdar Atamert for their advice on practical techniques during the earlier stages of my research.

Thanks are also extended to the technical staff of the department, particularly Mr John Leader for technical guidance with dilatometry, Mr Dave Nichol for his help and advice on electron microscopy and carbon replica preparation, Mr Brian Barber for his photographic services, and Messrs David Duke, Graham Morgan, Paul Stokes and the workshop staff who provided much valuable technical assistance.

This work was supported by the Central Electricity Generating Board, and my thanks are extended to them. Particular gratitude is expressed to Dr David Gooch of the National Power Technology and Environment Centre (NPTEC) for the interest he has shown in the project, and to Martin Askins and Jackie Maguire for guidance and help during visits to NPTEC.

CONTENTS

Preface	i
Acknowledgements	ii
Table of Contents	iii
Abstract	v
Abbreviations	vii
List of symbols	ix
Chapter 1: Introduction to Remanent Life Prediction	1
1.1 Problems With High-Temperature Plant Operation	1
1.2 The Need for Accurate Life Prediction	2
1.3 Plant Life Extension: British Experience	3
1.4 Plant Life Extension: Critical Areas	4
1.5 Materials and Conditions	9
1.6 Current Remanent Life Assessment Procedures	12
1.7 Methods Based on Operational Data Monitoring	15
1.8 Methods Using Post-Service Material	24
Chapter 2: Microstructure of Creep Resistant Low-alloy Ferritic Steels	34
2.1 The Austenite–Ferrite Transformation	34
2.2 The Bainite Transformation	41
2.3 Carbide Precipitation in Allotriomorphic Ferrite	50
2.4 Changes in Alloy Carbides Within Ferrite During Ageing	55
2.5 Cavitation During Creep	59
2.6 Ageing Behaviour of Bainitic Cementite	61
Chapter 3: Characterization of Pre-Service Microstructure	70
3.1 Introduction	70
3.2 Optical Metallography	70
3.3 Quantitative Metallography	75
3.4 Hardness Measurements	77
3.5 Energy Dispersive X-ray Analysis	81
3.6 Summary	85
Chapter 4: Modelling the Austenite–Ferrite Transformation	87
4.1 Introduction	87
4.2 Theoretical Calculation of TTT Diagrams	88
4.3 Calculation of Phase Diagrams	93
4.4 Heat Treatments on Steam Header Section	94
4.5 Results of Dilatometric Experiments	98
4.6 Metallographic Examination of Heat Treated Specimens	117
4.7 Summary	119

Chapter 5: Ageing of Bainitic Microstructures:	
Experimental procedure	126
5.1 Introduction	126
5.2 Programme of Heat Treatments	126
5.3 Procedure for Microanalysis	129
5.4 Interpretation of Microanalytical Data	134
Chapter 6: Ageing of Bainitic Microstructures:	
Fe-Cr-Mo Steel	144
6.1 EDX Compositional Data	144
6.2 Variation of Composition Change with Particle Size	146
6.3 Variation of c^θ with Time: Analytical Approach	184
6.4 Theoretical Modelling of the Ageing Process	195
6.5 A Finite Element Analysis of the Ageing Process	202
6.6 Variation of c^θ with Time: Finite Difference Approach	209
6.7 Alloy Carbide Precipitates	217
6.8 Summary	218
Chapter 7: Ageing of Bainitic Microstructures:	
Fe-Cr Model Alloy	220
7.1 EDX Compositional Data	221
7.2 Variation of Composition Change with Particle Size	222
7.3 Variation of c^θ with Time	228
7.4 Alloy Carbide Precipitates	234
7.5 Summary	236
Chapter 8: Summary	241
8.1 Composition Changes During Ageing of Bainitic Cementite	241
8.2 Remanent Life Prediction	243
References	245
Appendix 1: Steels Used in the Programme	251
Appendix 2: Program to Simulate Stochastic Scatter in EDX Composition Analysis	254
Appendix 3: Finite Difference Program to Analyse Ageing of Bainitic Cementite	257

ABSTRACT

It is believed that the safe creep life of low-alloy steel components used in the boiler systems of power stations has in the past been underestimated. The underestimation arises in part from inaccuracies associated with current predictive techniques, and in part due to variations in service conditions which are difficult to monitor (and may, at times, exceed the design specifications). A large incentive for producing more accurate creep life estimates is provided by the imminent closure of large quantities of power plant (due to life exhaustion on the basis of current estimates). The work in the current project had its origin in this engineering problem, and in particular in addressing the problem of accurate determination of the temperature regime experienced by these materials in service, when operating temperatures are known to be subject to fluctuation.

It has been suggested by a number of authorities that measurements of compositional changes which occur in carbides within the material during ageing could, if coupled with a rigorous theory predicting enrichment rates, produce a more representative indication of the true thermal history of the component than has been possible to date. This would provide a particularly powerful technique in relation to extending the service life of existing plant, as it is essentially non-destructive. The major aim of the current work has been to characterize those precipitates which are found in these alloy systems and, by carrying out EDX compositional analysis of aged specimens, to test and develop a model for the enrichment process which is more fundamentally-based and representative than the largely-empirical models commonly used in industrial practice.

In chapter one of this dissertation an analysis is made of the problem of remanent life prediction in engineering terms, with particular emphasis on the sources of approximation in current estimates. Chapter two considers the available theory to explain the development of creep-resistant microstructures in low-alloy steels during component fabrication, and the subsequent microstructural changes which occur in these steels during ageing under service conditions. Particular emphasis is given to the question of cementite enrichment with sub-

stitutional alloying elements, and it is noted that recent work based on diffusion theory predicts enrichment which varies as $(\text{time})^{1/2}$, a result which contrasts with relations of a $(\text{time})^{1/3}$ form which have hitherto been applied industrially.

In chapter three, the microstructure of a typical example of a $1\text{Cr}\frac{1}{2}\text{Mo}$ power plant steel in the as-fabricated condition is examined and discussed. Chapter four involves the study of the austenite–ferrite transformation in this steel, both on the basis of current phase transformation theory and by dilatometric experiment.

The procedure used for determining composition changes which occur during ageing is outlined in chapter five, and the results discussed and analysed in chapters six and seven. Chapter six compares enrichment of cementite by substitutionals in the $1\text{Cr}\frac{1}{2}\text{Mo}$ steel with theoretical predictions based on both an analytical model which considers the rate of enrichment to be controlled by diffusion within a semi-infinite ferrite matrix to the α/θ interface, and a finite difference method which takes account of the finite inter-cementite spacing, and hence of soft impingement effects. A good correlation is found between experiment and theory: in particular, enrichment occurs in accordance to a $(\text{time})^{1/2}$ relationship, and the level of enrichment at a given time is found to vary as the reciprocal of the particle size. Chapter seven analyses enrichment in a higher-chromium alloy in which precipitation of another alloy carbide species (M_7C_3) at the expense of cementite takes place during ageing; thus, the effect of this on cementite enrichment can be examined.

In chapter eight, some general conclusions are drawn, a consideration given to the possible applicability of measurements of this type to the remanent life question, and suggestions for future work are made.

ABBREVIATIONS

bcc	body-centred cubic
BF	bright field
CAF	cavity area fraction
CCT	continuous cooling transformation
CEGB	Central Electricity Generating Board (of England & Wales)
CERL	Central Electricity Research Laboratories (of the CEGB)
CVN	Charpy V-notch
DF	dark field
EDX	energy dispersive X-ray analysis
fcc	face-centred cubic
GB	grain boundary
HAZ	heat affected zone
hcp	hexagonal close-packed
IPS	invariant plane strain
K-S	Kurdjumov-Sachs relationship
MDHS	mean diameter hoop stress
MTDATA	Metallurgical and Thermodynamic Data Service
NAG	Numerical Algorithms Group
NDT	non-destructive testing
NPLE	negligible-partitioning local equilibrium
OA	optic axis
ParaE	paraequilibrium
PS	proof stress
RCL	remanent creep life
RF	radio frequency
SADP	selected area diffraction pattern
SEI	secondary electron image/imaging
SEM	scanning electron microscopy
TEM	transmission electron microscopy
TTT	time-temperature-transformation

VHN	Vickers hardness number
YS	yield strength

LIST OF SYMBOLS

a	lattice parameter of cubic crystal
Ae_3	the temperature of the equilibrium $\alpha + \gamma/\gamma$ phase boundary
Ae'_3	the temperature of the para-equilibrium $\alpha + \gamma/\gamma$ phase boundary
B_s	bainite start temperature
C	non-dimension variable in finite element analysis associated with concentration
$C_{i,j}$	normalized composition of finite element i, j
c_x	concentration of element X
c^z	concentration in phase Z
\bar{c}	mean alloy composition
$c^{\alpha\theta}$	composition of ferrite in equilibrium with cementite
$c^{\theta\alpha}$	composition of cementite in equilibrium with ferrite
d	diameter
d_b	bore (inner) diameter of pipe
d_o	outer diameter
e	engineering strain or conventional strain
e_α	coefficient of linear thermal expansion of ferrite
e_γ	coefficient of linear thermal expansion of austenite
I	intensity
I'	observed intensity of EDX signal when reduced by absorption
k	partition coefficient
L	liquid
\bar{L}	mean linear intercept
l	length
l_0	initial length
M_s	martensite start temperature
P	steam pressure
T	temperature
t	time, pipe wall thickness

T'	non-dimension variable in finite element analysis associated with time
T_{amb}	ambient temperature
T_{aus}	austenitising temperature
t_{aus}	austenitising time
t_c	ageing time required to reach a given composition
t_f	time to failure
T_{hom}	homogenising temperature
T_{iso}	isothermal transformation temperature
T_s	service temperature
t_s	time at service conditions
$t_{s,f}$	time to failure at service conditions
T_t	test temperature
t_t	time at test conditions
$t_{t,f}$	time to failure at test conditions
$t_{t,f_{\text{ex}}}$	rupture time for service exposed material under test conditions
$t_{t,f_{\text{unex}}}$	rupture time for unexposed material under test conditions
T_0	original temperature, temperature at which α and γ of the same composition have the same free energy
T'_0	T_0 temperature adjusted to allow for 400 Jmol^{-1} strain energy
V	volume
V_{α_b}	Volume fraction of bainite
$V_{\alpha'}$	Volume fraction of martensite
$V_{\gamma_{\text{ret}}}$	Volume fraction of retained austenite
V_{α}	Volume fraction of allotriomorphic ferrite
W_s	Widmanstätten ferrite start temperature
wt %	proportion of element as percentage by weight
X	non-dimension variable in finite element analysis associated with distance
x_{θ}	thickness of cementite plate
α	ferrite, allotriomorphic ferrite

α	tilt angle in EDX technique
α_a	acicular ferrite
α_b	bainite
α_{lb}	lower bainite
α_{ub}	upper bainite
α_w	Widmanstätten ferrite
α'	martensite
β	elevation of EDX detector
γ	austenite
γ_{ret}	retained austenite
δ	delta-ferrite
Δ	difference
Δl	length change
Δl_{rel}	relative length change ($\Delta l / l_0$)
ΔT	temperature difference, undercooling
Δ_m^v	maximum volume free energy change for nucleation
ε	strain
$\dot{\varepsilon}$	strain rate
$\dot{\varepsilon}_m$	minimum creep strain rate
θ	cementite
θ	angle between detector and tilt axes in EDX technique
σ	stress
σ_{mdhs}	mean diameter hoop stress
σ_{ref}	reference stress
σ_s	service stress
σ_t	test stress
σ_1	maximum principal stress
$\sigma_{\theta\alpha}$	surface energy of cementite particle in ferrite
τ	transformation incubation time
ψ	EDX take-off angle
ω	creep damage parameter

Chapter 1

INTRODUCTION TO REMANENT LIFE PREDICTION

1.1 Problems With High-Temperature Plant Operation

Creep life assessment is essential for the determination of a safe operating life for high-temperature power plant. Furthermore, the accuracy of such assessments has a strong bearing on the economical operation of power stations; accurate life prediction allows the maximum safe use to be achieved with each component, whereas the lack of an accurate predictive model necessitates the use of expensively-large safety factors.

High-temperature component design codes are customarily based principally on uniaxial creep rupture data. Additionally, depending on operating conditions, cyclic creep, creep fatigue, environmental attack etc. may also be of significance. The base material is usually assumed to be chemically homogeneous, which is a further potential source of inaccuracies, and design codes must always be conservatively determined for safety reasons (Cane & Williams, 1987).

Evidence obtained from examinations of components removed from service, however, has shown that the safe creep design life of creep resistant low-alloy steels may have been underestimated significantly leading to the expense of unnecessary replacements. This problem is thought to arise in part as a result of inaccuracies in present predictive techniques (Cane & Townsend, 1984; Cane & Williams, 1987); in particular, the complexity of the systems and the harshness of the operating environment make the modelling procedure more complex.

Cane (1986) has found that a particularly significant inaccuracy arises from the use of standard creep data derived from small test samples whose behaviour in a given environmental condition would be expected to differ from that of the bulk component. An example of this is provided by the relative effect of oxidation on creep data for different thickness test pieces, which shows a specimen thickness dependence; oxidation effects are negligible for thick specimens, but of

increasing importance as the surface:volume ratio increases. A general discussion of the problems associated with the use of standard data and extrapolation to on-plant conditions is given in section 1.7.2.

It is also known that service conditions can be highly variable and, at times, exceed those allowed for in the design specifications, especially in localized areas. Cane and Townsend (1984) found variations of 30–40°C in exceptional circumstances, equivalent to an order of magnitude change in the creep lifetime of the material and thus a serious limiting factor on any remanent life¹ assessment.

A further source of imprecision in component lifetime prediction can be attributed to welds and weldments, where the complex microstructure and chemical inhomogeneity can lead to a non-uniform stress distribution and sites of stress concentration where cavitation in the initial stage of creep can occur. Nevertheless, although such regions are critical for creep damage, they are not necessarily so in terms of life exhaustion; in many cases, non-destructive damage monitoring and repair are relatively easy for weldments. In consequence, most efforts directed at predicting remanent life are concentrated on the parent material. Accurate assessment of the problems in high-risk areas is of particular importance, so that critical components can be identified and carefully monitored (Price & Williams, 1982; Parker & Sidey, 1986); thus the locating of those areas where the creep environment is especially harsh must constitute a significant part of any remanent life prediction procedure.

1.2 The Need for Accurate Life Prediction

- (i) To satisfy the various safety standards demanded by legislating and licensing bodies, insurers *etc.*
- (ii) To avoid the large expense and risk of plant damage and serious injury to personnel associated with sudden high-temperature failures.

¹ Remanent creep life is the time remaining before creep induced failure occurs in a partially-creep-damaged artefact, such as a high-temperature component which has been exposed to service conditions for a fraction of the time in service which would result in creep rupture.

- (iii) To predict in advance when the need for component replacement is likely to arise in order to allow time for the manufacture of a replacement before it is needed in service. British experience suggests that for steam headers² advanced warning should ideally be three to four years, although for less specialised components this can be much reduced (Cane & Townsend, 1984).
- (iv) To allow safe extension of service life, and maximize plant usage.
- (v) To avoid complete replacement of existing plant and adopt instead where possible a repair/replace single components philosophy.

1.3 Plant Life Extension: British Experience

Realistic lifetime assessment is of particular interest to the large generating companies in the United Kingdom, because of their large capital investment in low-alloy ferritic steel plant. There have been very few catastrophic high-temperature failures recorded which have resulted in major steam leakage and serious plant damage or injury, but this is primarily due to the high degree of caution which must be employed in the field of creep life prediction specifically to avoid such failures. In many cases, this policy is found to lead to the premature decommissioning of plant and consequent loss of capital which makes representative remanent life prediction of substantive value in relation to extension of plant life (Gooch & Townsend, 1986).

The electricity generating industry in England and Wales has 54 000 MW of generating capacity, which includes twelve large stations comprised of 41 high-merit 500 MW coal fired units. These units are noted for their good thermal efficiency and low operating cost. Designed in the 1960s and 70s for 150 000 hour (25 year) operation, they have reached 90 000–120 000 hours of service each. A programme to increase plant life to 250 000 hours or more is thought to be feasible and two procedures to achieve this are proposed, by Townsend (1986), to form the basis of a plant life prolongation programme initiated by the Central Electricity Generating Board of England and Wales (CEGB):

² Steam headers are those parts of the boiler system of a power station which act as junctions between the simple boiler tubing. They can be very large and of complex design, hence the long replacement times noted above.

- (i) Replacement of all critical components at 150 000 hours;
- (ii) Predictive assessment coupled with a replacement of only those components shown to have a total potential lifetime of less than 250 000 hours.

In principle, the second solution is the more satisfactory as all components work through an entire useful life: in practical situations considerations including the engineering feasibility of life extension and the relative costs of the two options must also be factors in the question of replacement versus extension. It is likely that for cheap components which are easily replaced (*e.g.*, boiler tubes) the strategy outlined in option (i) will be favoured, whereas for more expensive and complex components (*e.g.*, steam headers) development of improved anticipatory techniques to allow life extension should be of economical benefit (Townsend, 1986).

In the case of the 12 large stations mentioned above, a strategy based on extending life could be practicable, as the original design remains relatively advanced in engineering terms with few technical improvements probable in the foreseeable future. This negates the principal value of new plant construction: improved efficiency achieved by incorporating improved design. A prolongation of working life to 40 years or more would produce considerable financial advantage: retaining current plant in service would be achieved at around one third of the cost of building new plant; and the many problems associated with siting new power stations (environmental concerns, lengthy public enquiries and so on) could also be avoided if the service life of existing power plant were lengthened significantly. Improvement of current predictive techniques is thus of great interest and potential value to the large scale electricity generation industry.

1.4 Plant Life Extension: Critical Areas

1.4.1 Power plant arrangement

The majority of the generating capacity in England and Wales produces electricity with a steam turbine arrangement, with various initial fuel sources (coal, oil, the nuclear pile *etc.*) being used to heat the steam. The basic furnace and

boiler arrangement of steam turbine generating plant is the same regardless of the fuel source used.

Water is supplied to the steam drum by feed pumps, usually passing through an economizer. This device is heated by hot gases from the furnace (as are the superheaters and reheaters (see below), thus enabling pre-heating of the feedwater). The water is drawn from the steam drum into tubes on the furnace walls, and returns to the drum as a mixture of water and steam. The water and steam are separated in the drum, and the water recycled to the furnace wall, with the steam passing on through the superheaters to the high-pressure cylinder where it is directed at the turbines, producing rotation. Exhaust steam from the high-pressure cylinder is passed through reheaters to get it back up to temperature, thence to the intermediate- and low-pressure cylinders to drive further turbines. A diagram of the general boiler and steam plant arrangement is given in figure 1.1.

1.4.2 Applicability of life extension to steam headers

Several components have been identified as being particularly susceptible to high-temperature failure, and these are listed in table 1.1 and figure 1.2. Accurate remanent creep life prediction would be conducive to improvement in overall operating lifetime assessment if concentrated in these areas.

On the basis of the criteria considered in Section 1.3, it is evident that boiler components, both for their complexity and cost, and for the harshness of the operating regime, are especially suited to a life extension programme. Moreover, the steam header is operated under a particularly severe service regime, especially in relation to localized heating to as much as 40–50°C over design temperature (which is 568°C); this arises mainly due to the complexity of the shape, which causes a highly irregular heat flow during operation. Localized heating above design specifications effects a more rapid exhaustion of creep life at those localized sites.

A recent CEGB survey indicated that nearly all steam header replacements are made as a result of exhaustion of design creep life. In only 25% of these

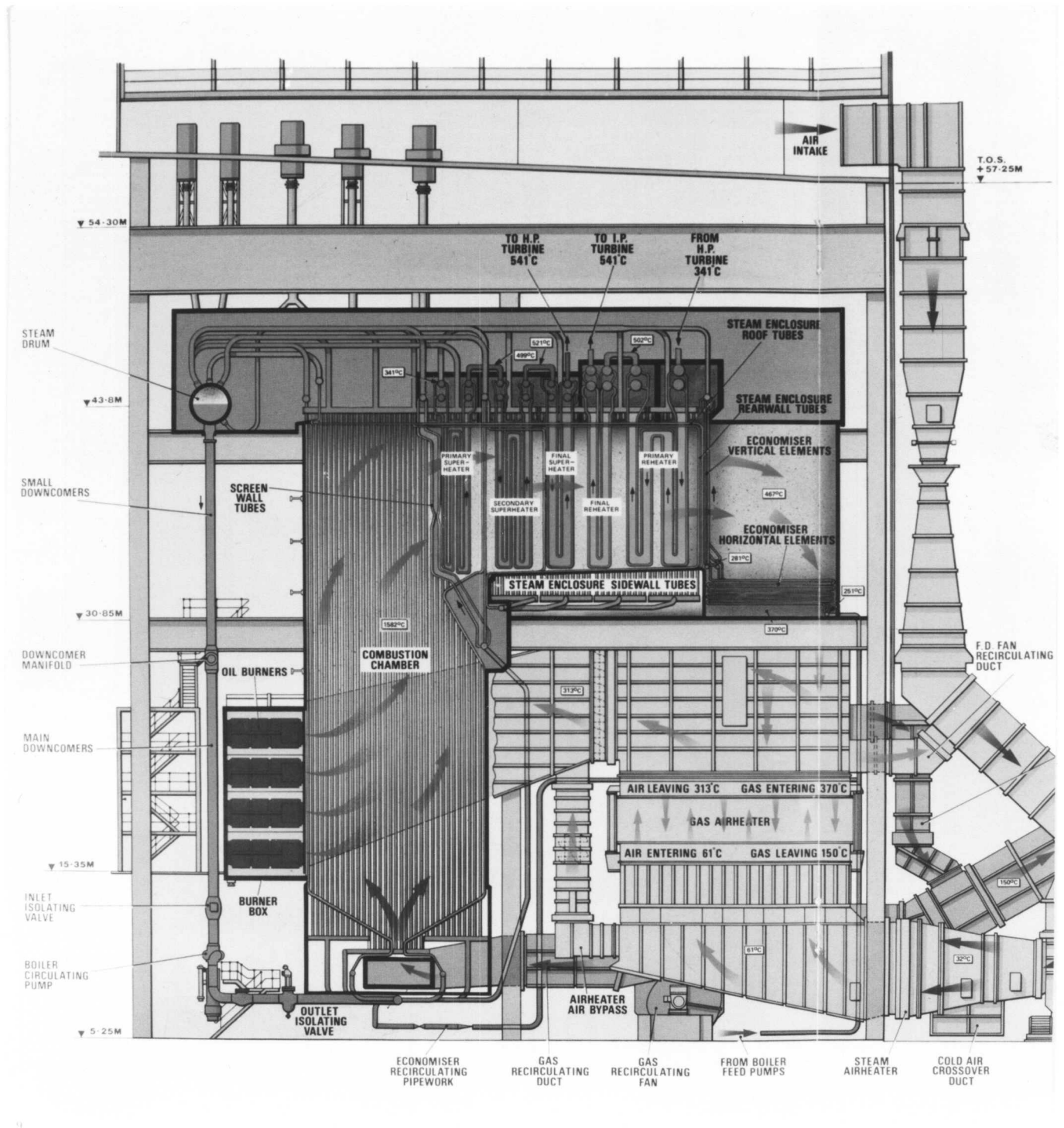


Figure 1.1: A power station boiler and associated steam plant (Littlebrook Power Station Guide, National Power Technical Publications)

Area		Materials	Life-limiting factor
<i>Boilers</i>	Drums	Carbon steels	Creep and thermal fatigue
	Headers	Carbon & Cr-Mo steels, austenitic stainless steels	Creep and thermal fatigue
	Furnace wall, superheater, reheater tubing	Carbon & Cr-Mo steels, austenitic stainless steels	Fireside and waterside corrosion
<i>Pipework</i>	Main and reheater pipes	Cr-Mo, Cr-Mo-V steels, austenitic stainless steels	Creep and thermal fatigue, weld and HAZ cracking
<i>Turbines</i>	All rotors	Cr-Mo-V (-Nb-W) steels	Creep and thermal fatigue
	Low pressure rotors and turbine blades	Ni-Cr-Mo-V steels	Fretting fatigue, corrosion fatigue, stress corrosion & pitting <i>etc.</i> , temper embrittlement
	Steam chests and casings	Cr-Mo, Cr-Mo-V steels	Creep & thermal fatigue
	Elevated temperature boltings	Cr-Mo-V (-B) steels, nickel based alloys	Creep and thermal fatigue stress corrosion

Table 1.1: Critical areas for high-temperature failure

cases was evidence of creep damage exhibited in the form of inlet stub tube weld cracking or swelling of the steam header body: many of the remainder were found to have significant potential service life left.

Cane and Townsend (1984) outline the specific problem that the Industry faces as a result of creep life exhaustion. Included in British generating plant are more than 300 headers which, on the basis of present creep life theories, will

typical areas of attention for plant life extension on coal

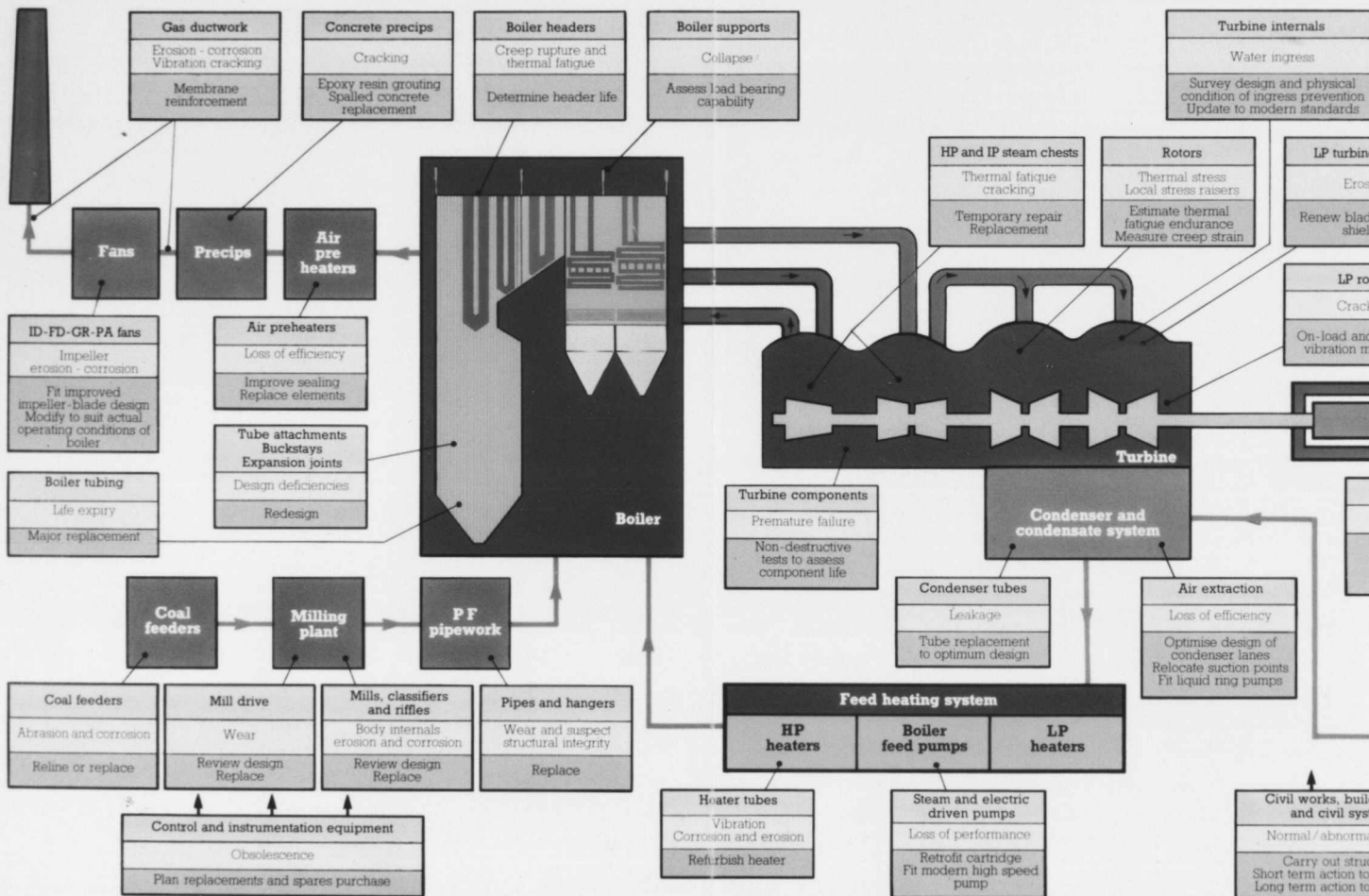


Fig 1.2

require replacement at some time during the next 25 years at a cost, in engineering terms alone, of some £170–£200 millions; thus, the financial incentive for extending safe creep life in this area is very large indeed. Furthermore, the absence of cost-effective and practicable alternative monitoring procedures that are applicable to steam headers, a problem not associated with most of the other critical areas listed in the table, provides further incentive for the development of predictive models; the header body is difficult to observe, expensive to replace, and, due to the complexities of its manufacture, must be ordered 2 years or more in advance of the need for replacement arising. Accurate anticipation of failure can avoid potentially disastrous long periods of plant repair, whilst at the same time reducing the financial and material wastage arising from unnecessary replacement. In contrast, other critical boiler components such as welded joints or boiler tubes are easier to inspect and repair; hence, in those cases, investment in remanent life research does not produce such high levels of return.

1.5 Materials and Conditions

1.5.1 *Materials used in current steam headers*

Of the more than 300 steam headers mentioned above as requiring replacement within 25 years, three are mild steel and the remainder are low-alloy ferritic steels. Chromium and molybdenum are the primary alloying elements in all of these steam headers, with vanadium also used in some more recent designs. The carbon content in all three of the alloys used is in the range 0.10–0.12 wt %. A breakdown of the currently-predicted replacement dates for the steels is given in figure 1.3. The figure applies to the larger headers (> 2 m length) which are a particular problem.

A breakdown of figure 1.3 reveals that ninety-five 1Cr– $\frac{1}{2}$ Mo class steel steam headers are due for replacement over the period, all within the next 15 years, and the bulk of the 126 $2\frac{1}{4}$ Cr–1Mo class steel headers of the $2\frac{1}{4}$ Cr–1Mo class steel which are due to be replaced by 2010 will also reach the end of their anticipated service life over the same 15 year period. The more recently designed steam headers, made from $\frac{1}{2}$ Cr– $\frac{1}{2}$ Mo– $\frac{1}{4}$ V class steel, make up the rest. On the basis

of current estimates 79 of these are due to be replaced before 2010 (Cane & Townsend, 1984). It can be seen from the pie chart and the accompanying figures that low-alloy ferritic steel steam headers are predominant in this list of problem steam headers, and as a consequence it is on these steels that the work in this project will focus, specific study being made of 1Cr- $\frac{1}{2}$ Mo type material.

1.5.2 Microstructure

It is known that in low-alloy ferritic steels the cementite is initially present either as relatively coarse lamellae in pearlite or as finer precipitates in tempered martensites and bainites, the latter case usually applying to steam boiler system materials (Wilson, 1986). The microstructure of header materials is commonly a mixture of allotriomorphic ferrite and bainite, formed by continuous cooling from austenite. The bainitic region is partially annealed during the fabrication process.

Bainitic carbides in these steels will be subject to coarsening during the high-temperature operation of the plant. The rate of such coarsening has long been known to increase greatly during creep (Jenkins & Mellor, 1942), and it is suggested that carbide coarsening could be used both to determine remanent life on a microstructural level and to develop a mechanistic creep damage model to improve remanent life assessment in the future (Wilson, 1986). The monitoring of microstructural development during service to develop a mechanistic model is a major aim of the work and is discussed fully in chapter four.

1.5.3 Operating conditions

The design operating temperature for fossil fuel boilers in UK power stations is typically about 568°C for 600MW plant, and about 540°C for 500MW plant, figures that are arrived at as a compromise between the increased efficiency and reduced service life associated with higher superheated steam temperatures. It has already been noted, however, that at certain times in problem areas (such as at the inlet tubes) this can be exceeded by some 40°C to 50°C. Operating temperatures at variance to design temperatures are found in two forms: irregular fluctuations during operation (figure 1.4), and spatial variations and the

development of problem ‘hot spots’ within a component (figure 1.4 and figure 1.5).

The operating temperatures for boiler systems with other fuel sources (*e.g.*, oil and gas fired power stations) are generally lower so that creep life exhaustion in the boiler system does not present such a problem (Cane & Townsend, 1984). Similar operating design temperatures are found in some nuclear installations outside the UK, but otherwise non-UK experience is similar (Wilson, 1986). Typical operating conditions in a 500MW fossil fuel power station are presented in table 1.2. The steam header regions in the boiler system of fossil fuel power stations, and in particular the critical areas noted, can therefore be expected to experience significant levels of creep during service.

Parameter	Typical value
Evaporation	$1.58 \times 10^6 \text{kg h}^{-1}$
Drum temperature	680°C
Drum pressure	18.3MPa
Superheater outlet temperature	541°C
Superheater outlet pressure	16.6MPa
Reheater inlet temperature	348°C
Reheater inlet pressure	4.3MPa
Reheater outlet temperature	541°C
Reheater outlet pressure	4.1MPa
Inlet feedwater inlet temperature	254°C

Table 1.2: Typical plant operating conditions

1.6 Current Remanent Life Assessment Procedures

The various procedures available to facilitate remanent life assessment can be considered to comprise two broad approaches.

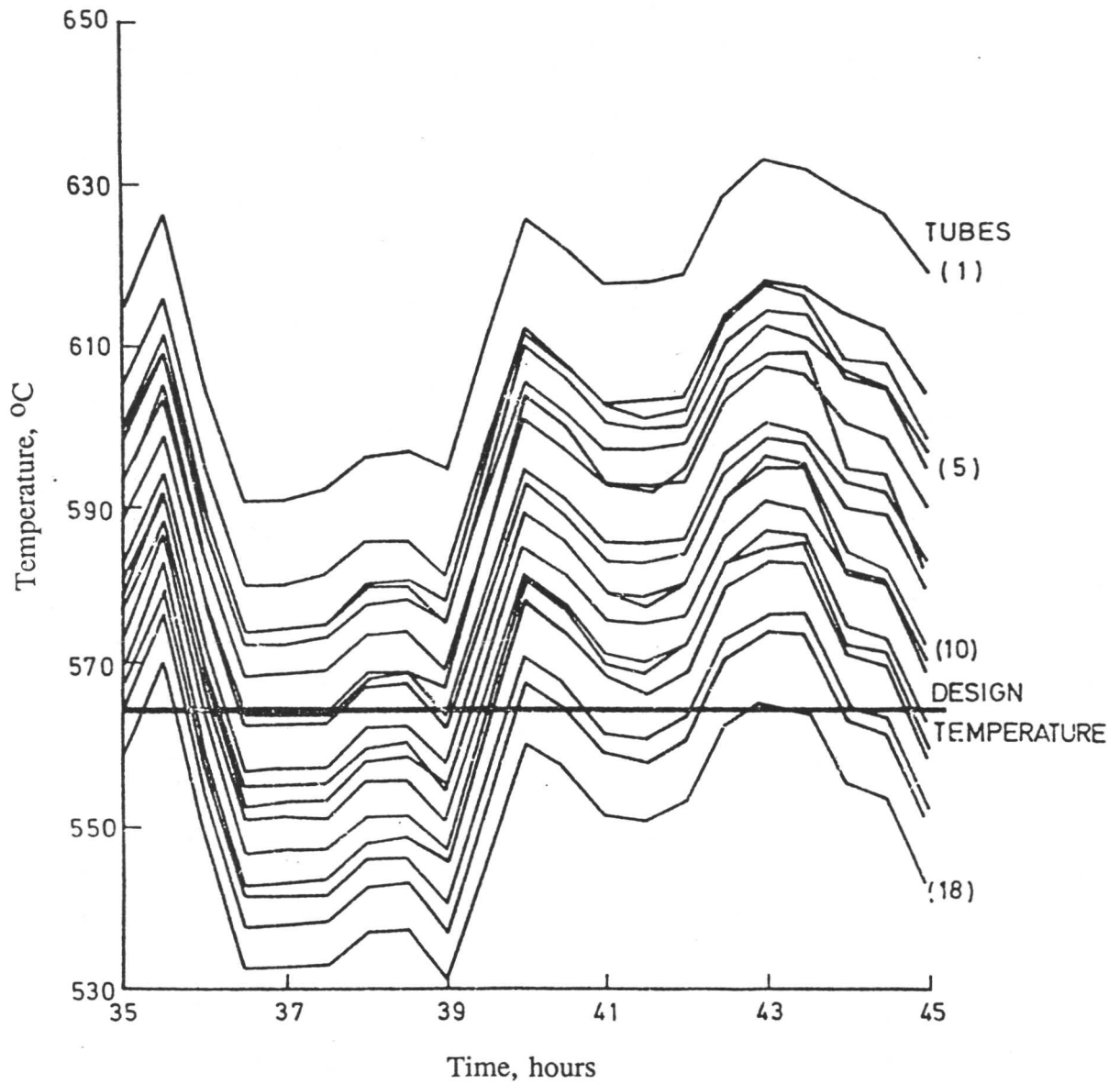


Figure 1.4: Inlet stub tube temperature variation around an eighteen tube element on a 500 MW reheater drum (from Cane & Townsend, 1984)

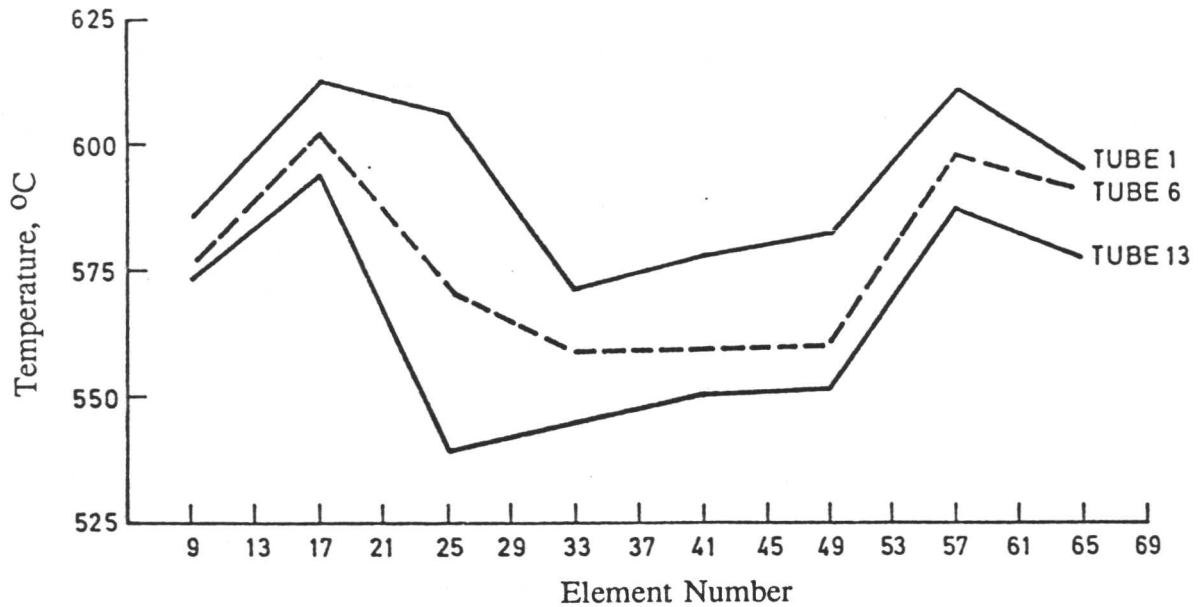


Figure 1.5: Reheater drum inlet stub tube temperature distribution in a 500 MW boiler (from Cane & Townsend, 1984)

- (a) Involves the monitoring of operational parameters (temperature, pressure, steam data *etc.*) and the use of the data collected in conjunction with standard materials data and the life fraction rule (below) in order to produce an estimate of available life for a component.
- (b) Examination of material which has seen service, in the form of external inspection of problem areas during service, and NDT and more detailed scrutiny during periods of plant outage. Crack detection, on plant strain measurement, and 'non-destructive' removal of small test specimens can all be carried out during periods of downtime. The test specimens can be used for post-service observations which could be microstructural, bulk physical (*e.g.*, crack examination) or mechanical (*e.g.*, accelerated creep rupture tests).

A practical life prediction programme will commonly include procedures of both types.

The approach that was adopted by the CEGB is given in a general operation memorandum “Creep Life Prediction of Headers” (CEGB, 1982), which divides the proposed procedure into three stages:

Stage I Based on measurements of steam temperature data, operational lifetime, minimum stress rupture data, design data and the life fraction rule.

Stage II An extension of Stage I but using dimensional checks rather than design dimensions, and measurement of actual metal temperatures.

Stage III Based on the use of test samples from service components and methods developed by the Remanent Life Task Force (to which this project is contributing).

Stages I and II follow an approach of category (a). They use established techniques that are known to give highly conservative estimates arising from the use of minimum stress rupture data and peak temperatures without allowing for stress redistribution; the inherent conservatism in design stress calculations compounds the error. These techniques are useful in identifying problem headers, however, where failure may be expected during the lifetime of the boiler system.

Stage III uses techniques developed by an approach of category (b) and it is hoped that models will be developed to overcome the inaccuracies of current procedures, thus allowing less conservative use of the headers.

1.7 Methods Based on Operational Data Monitoring

Data measurements are taken on the plant at regular intervals, in particular pressure and temperature (whence the creep strain on plant can be determined). These data are then processed using the ‘Life Fraction Rule’, the basis of which was originally proposed by Robinson (1952), namely:

$$\Sigma(t_i/t_{if}) = 1 \tag{1.1}$$

where t_i is the time spent at the stress, σ_i , and the temperature, T_i ; t_{if} is the failure time at σ_i , T_i . The rule assumes that linear summation of life fractions is possible, and recent work (see below) shows that this is not a satisfactory approximation in all situations.

1.7.1 Life fraction rule

The life fraction rule still forms the basis for beginning a remaining life analysis utilizing operational parameter measurements. However, investigations in the last decade have revealed limitations and the need for modification to the life fraction rule to fit particular circumstances.

Hart (1976) investigated the life fraction rule approach for both accelerated stress and accelerated temperature test procedures. This was done by subjecting pre-crept steel to accelerated rupture tests by both increasing temperature at original pressure and increasing pressure at original temperature. Hart discovered that summation of rupture life fractions arising from variations in temperature is more accurate than similar summation for variations in stress in the case of low-alloy ferritic steels; this is illustrated in figure 1.6 for 1Cr- $\frac{1}{2}$ Mo³ steel, comparing the observed residual lifetime after testing with a life fraction rule approach.

Work done by Hart (1977a) exposed a further problem with the life fraction rule approach. It was found that small test specimens which had been removed from a failed artefact (*i.e.*, life fraction consumed for the artefact = 1) retained a finite remanent life (*i.e.*, life fraction consumed < 1). It became clear that a greater understanding of the failure mechanisms would be necessary if these observed non-uniform damage distributions were to be accounted for.

Cane and Williams (1979) extended Hart's work, performing increased stress and increased temperature post-exposure simulations on Cr-Mo-V steels. They found that accelerated testing by increased temperature produced a re-

³ Exact compositions are frequently not given in the literature but will be quoted in footnotes where available. It should be borne in mind that when a composition is given as above Cr, Mo and V weight percentages are only approximate, C is in the approximate range 0.10-0.15 wt%, and other alloying elements (*i.e.*, Ni, Mn) are frequently present in these types of steel.

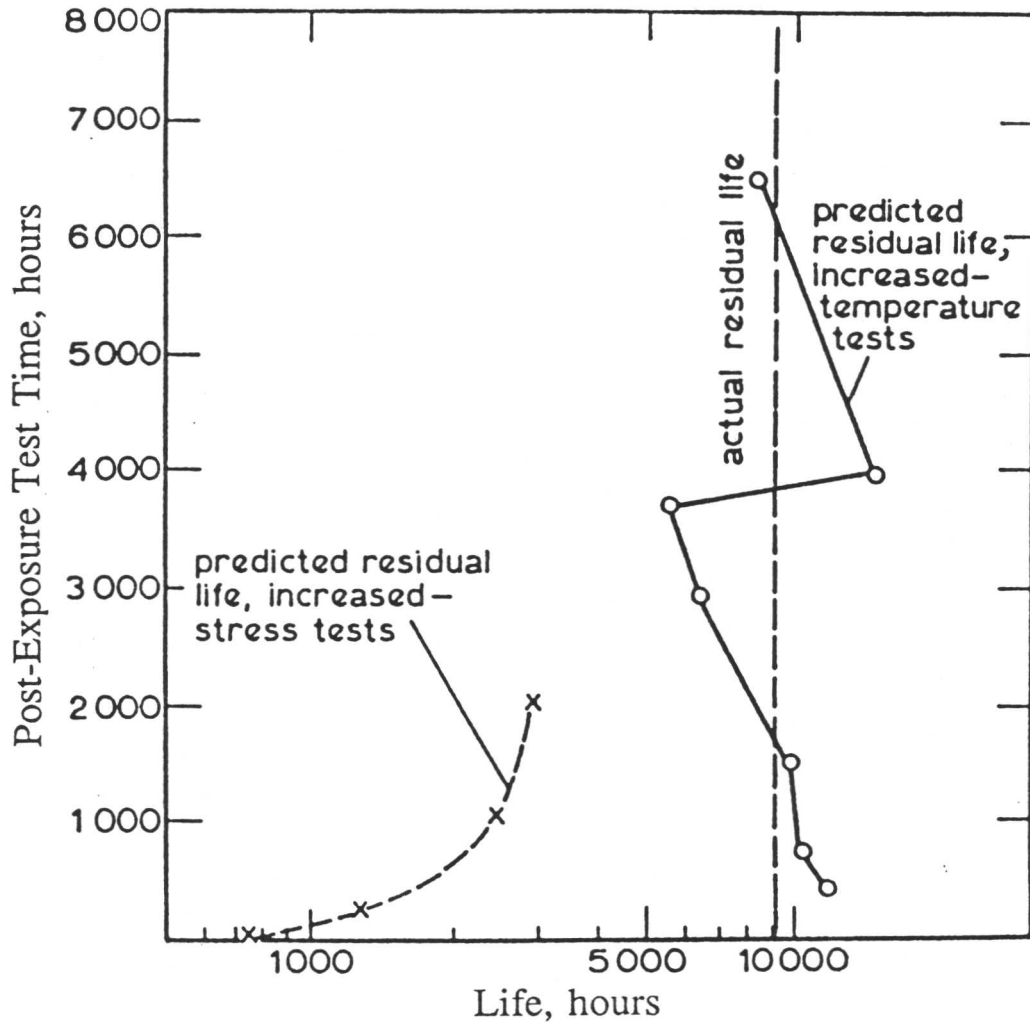


Figure 1.6: Life fraction rule life estimates for accelerated testing (from Hart, 1976)

maintaining life that was relatively insensitive to test duration, but that this was not the case for accelerated test procedures involving increased stress. This appeared to confirm the conclusion that for low alloy ferritic steel components a life fraction rule approach is a reasonable approximation where temperature varies markedly but not in cases where stress varies. It is proposed that these anomalies arise as a result of a recovery creep mechanism based on the creep damage processes proposed by Cane (1978). The general condition for validity

of the life fraction rule at all stresses, σ , and temperatures, T , is:

$$\frac{t_{tf_{\text{ex}}}(\sigma, T)}{t_{tf_{\text{unex}}}(\sigma, T)} = \text{constant} \quad (1.2)$$

where $t_{tf_{\text{ex}}}$ and $t_{tf_{\text{unex}}}$ are the failure times in tests on service-exposed and unexposed material respectively. Particle coarsening during service increases particle spacing within the microstructure compared with the pre-service material. Cane proposes that at high stresses a refinement or coarsening of the dislocation structure can occur much more freely, according to the recovery creep model, than is possible in the finer structure of the unexposed material; hence, accelerated testing by increased stress is sensitive to exposure time. At low stresses the mechanism is inhibited in both cases, and strain accumulation is governed by the resulting particle coarsening, so that test results do not show a sensitivity to exposure time.

The service conditions for steam headers will generally exhibit a much more severe variation in temperature than in steam pressure. As a result it can be concluded that for low alloy ferritic headers the limitations in the life fraction rule itself are unlikely to be of large import with respect to limitations in the accuracy of operational data measurements.

1.7.2 Errors arising during data processing

1.7.2.1 Variability in stress data

Limitations on determination of creep life from stress data are imposed by the difficulty in obtaining accurate measurements from in-service components; by variations between conditions and properties in different parts of the same cast; and by the complexity of the stress systems in components. The effect of scatter in stress data of up to 20% is shown in table 1.3 below, based on the stress to give failure in 100 000 hours in the case of $2\frac{1}{4}\text{Cr}-1\text{Mo}$ type steel for mean rupture data at 560°C (Cane & Townsend, 1984). Note that in table 1.3, zero stress represents the mean stress and -20% and $+20\%$ correspond to lower and upper bound limits respectively; the lower bound (-20%) data thus correspond

% Change in stress	-20%	-10%	-5%	0	5%	10%	20%
Failure time, hours	38 000	62 000	78 000	100 000	110 000	130 000	200 000

Table 1.3: Effect of stress variation on creep life

to an increase in the stress experienced by the test piece, and a reduction in the time to rupture.

A normal level for bounding accuracy limits in this sort of data analysis is 10% or 20% (Price & Williams, 1982) and for safety reasons the lower bound for rupture life must be used. As most measured data presently available cover only the first half of the planned operational lifetime the necessary conservatism is compounded further, so that underestimation in rupture life using such a lower bound approach could be as great as five times the actual life (Cane & Townsend, 1984).

In addition, there is an absence of significant quantities of data from fundamental investigations into the physical metallurgy of these steels; in particular, the exact chemical and microstructural composition of an individual batch of steam headers is unlikely to be known. This forces the researcher to repeat the fabrication heat treatments on service material in order to reproduce the initial microstructure before work can proceed. The reproducibility of results from such a procedure can not be guaranteed in all cases; for example, Stevens and Flewitt (1984), working with creep resistant steel Durehete 1250, found it impossible to create the initial condition by simulating the fabrication processes. This type of case is unusual, and in the absence of archive material a regenerated material procedure is normally satisfactory, but the work by Stevens and Flewitt illustrates the care which must be employed.

1.7.2.2 Errors in data extrapolation procedure

The procedures involved in extrapolating and applying standard material data

from small test specimens to $1-2 \times 10^5$ hours and thick-section material are complex. In particular, the effect of oxidation on the lifetime obtained from test specimens has been found to be significant by several workers; a comparison of creep curves for air and vacuum is shown in figure 1.7. It is clearly illustrated that an appreciable reduction in the lifetime of a test specimen when tested in air is exhibited, compared with similar testing in a vacuum; and hence, full consideration of comparative environmental factors is essential if test results are to be extrapolated to real systems.

The effect of environmental conditions on test piece lifetimes gives rise to a further complication: the creep lifetime of small test pieces can be expected to show a strong dependence on the section thickness of the test piece, as has been shown experimentally (figure 1.8). This effect is attributable to several causes: the reduction in actual metal cross-section, which occurs during creep testing as a result of oxidation, produces a non-load-bearing surface oxide layer, a process known as oxide weakening (Shahinian & Achter, 1963); surface properties may be altered by decarburization (Borgreen & Huntley, 1984); and, in some cases, a compact, partially-load-bearing film can form on the surface, leading to an increase in creep life, a process referred to as oxide strengthening (which is effectively the opposite to oxide weakening) (Shahinian and Achter, 1965). Both oxidation and decarburization effects can be exaggerated by grain boundary penetration near the surface. All the above are surface effects, so can be expected to exert a greater influence on a specimen with a higher surface:volume ratio (*i.e.*, for a smaller diameter test piece); therefore, standard data from small specimens tested in air may significantly underestimate the rupture life of thick-section material if extrapolated directly. If reasonably representative results are to be produced by post-service testing, it will frequently prove necessary that they be carried out in an inert environment, as discussed later. Nevertheless, the above factors render any attempt to extrapolate standard small cross-section test piece data to thick-section material in a moderately corrosive environment (in the sense that the component is at elevated temperature and exposed to the weather) difficult to carry out with confidence; hence the necessity of large

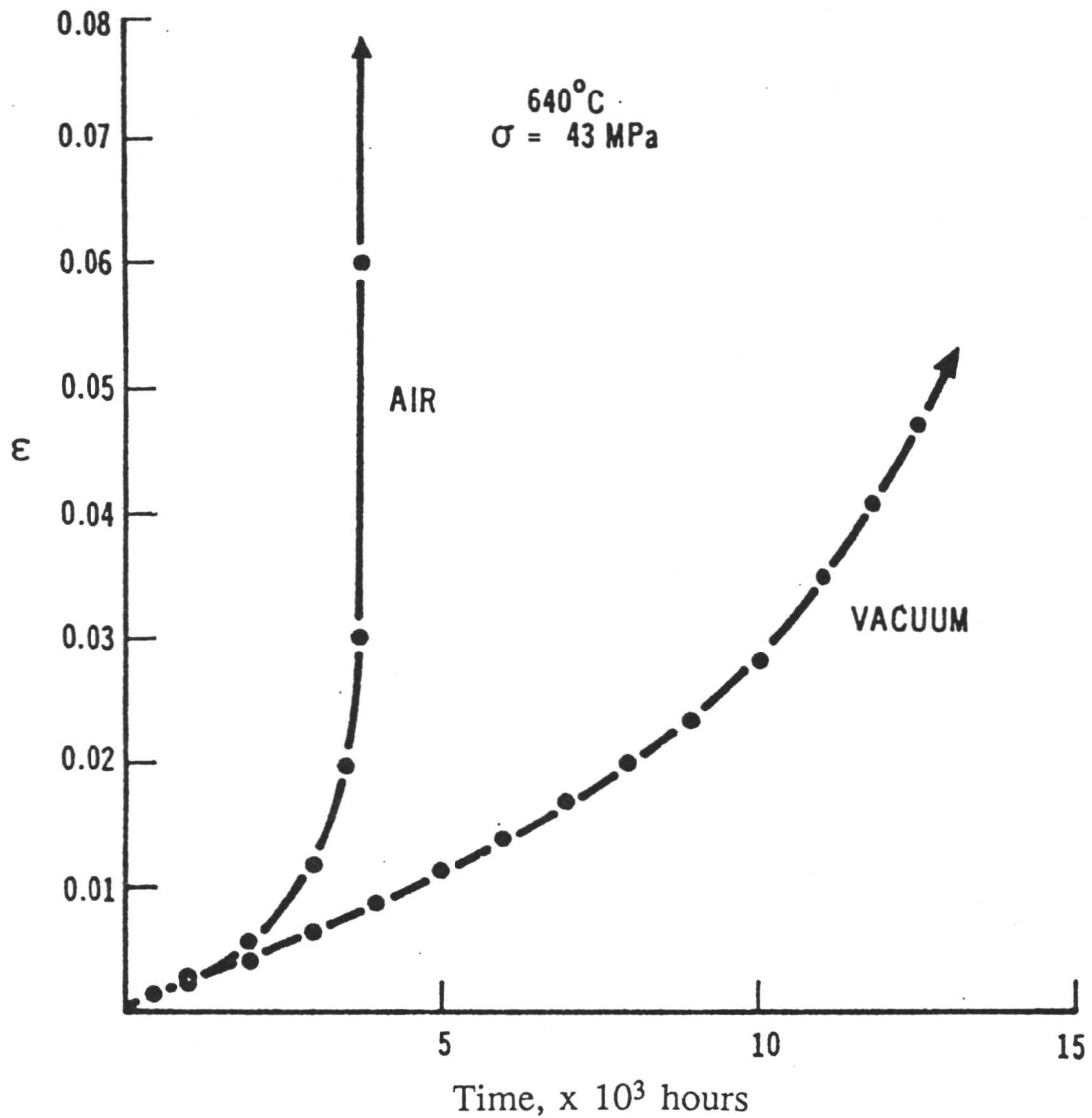


Figure 1.7: Creep curves for Cr-Mo-V steels in air and vacuum (from Cane & Townsend, 1984)

safety factors to accommodate this inevitable uncertainty, which could lead to a design life being substantively less than the true creep life of the component.

1.7.2.3 Choice of representative stress

Standard data are generated under uniaxial conditions, whereas components in service are subject to highly-complex stress systems associated with the multi-

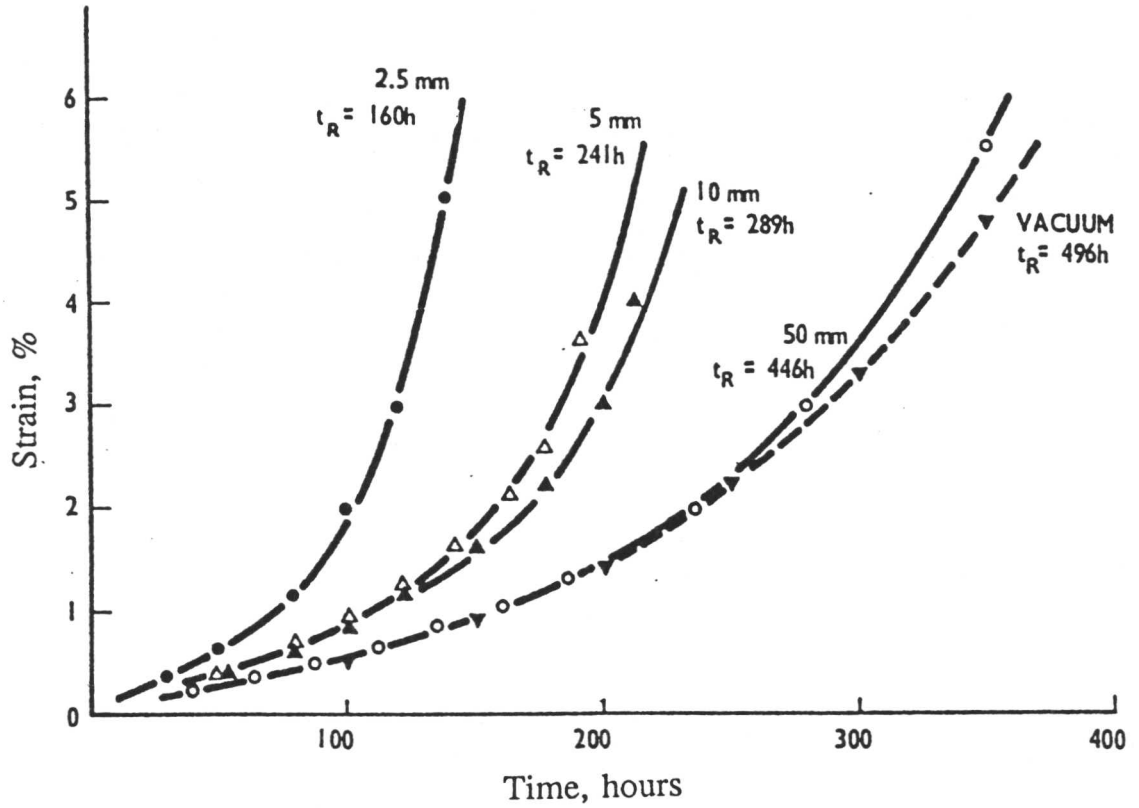


Figure 1.8: Creep curves for various test piece diameters tested in air

axial loading conditions. It becomes necessary to use a representative stress, a semi-empirical approximation to the real stress system, which is usually referred to as either σ_{ref} or σ_r , to characterize the complex system to a simple case for which standard test data exists. A simple but widely-used example of a practical representative stress is the mean diameter hoop stress (MDHS):

$$\sigma_{\text{ref}} = \frac{P(d_0 - t)}{2t} \quad (1.3)$$

where d_0 is the outer diameter, t is the wall thickness, and P is the pressure. This is referred to as an example only: various other representative stresses have also been proposed as applicable for different situations, but a detailed discussion of this method is outside the scope of this work. It should be noted, however, that any representative stress is intrinsically an empirical approximation, necessitated by the impracticability of modelling the true stress system, and work by

Cane and Brown (1982) found the true reference stress to be significantly lower than the MDHS. When the problem of accurately determining exact dimensions during the deformation process is considered (dimensions are generally taken from the design specifications to a first approximation, but will, in reality, vary by some finite amount as creep strain is accumulated during service). It has been suggested that the use of MDHS as a reference stress may overestimate the actual stress by as much as 20%; this has been shown to correspond to a lifetime underestimate by a factor of two (Cane & Townsend, 1984).

1.7.2.4 Temperature

Errors can arise from spatial variations of steam temperature within the header, irregular fluctuations of operating temperature, and instrumental imprecision. The effect of variation in temperature on rupture life is shown in table 1.4, based on a mean stress to failure in $2\frac{1}{4}\text{Cr}-1\text{Mo}$ steel at 560°C in 100 000 hours; a variation of just 10°C being found to corresponds to a factor of two difference in the resulting rupture life estimate (Cane & Townsend, 1984).

Temperature, $^\circ\text{C}$	540	550	560	570	580
Failure time, hours	250 000	170 000	100 000	56 000	32 000

Table 1.4: Effect of temperature variations on creep life

1.7.3 Summary

The problems associated with a remanent life prediction procedure based on standard data and the life fraction rule are well documented. As a result, the CEGB programme outlined in GOM101A (CEGB, 1982), and continued by National Power PLC, concentrates on post-service testing as the most probable way in which the accuracy of the assessment procedure can be improved. Operation data methods are envisaged to play an increasingly secondary role, that of iden-

tification of problem areas that should be subjected to a fuller analysis of the stage III type.

1.8 Methods Using Post-Service Material

Sampling of materials from components that have been in service can be utilized either for testing of mechanical properties or for direct assessment of the remaining life from the microstructural state. In both cases it is necessary to develop models of the processes involved in creep damage in order to determine the remaining life from the metallographic feature or bulk property under observation (Cane, 1983).

1.8.1 Creep damage models

There are two basic approaches to creep damage modelling: mechanistic and parametric modelling. Mechanistic modelling is to be preferred as service conditions can be related to microstructural changes and thus to creep damage directly. Parametric models are largely empirical models which have been found in the past to give reasonable creep life predictions from operational data in certain situations, but which are not fundamentally related to any considerations of creep damage processes. The combination of the limited theoretical basis of parametric models, and the difficulties in collecting and interpreting operational data outlined above, limits the accuracy of life prediction on the basis of parametric creep damage models. At present, however, development of good mechanistic models is far from complete so in practical situations parametric modelling is used.

1.8.1.1 Damage processes

For low-alloy steels four processes are of relevance:

- (i) Creep strain accumulation without significant decrease in creep strength. This occurs in cavitation resistant microstructurally-stable materials, the onset of failure being governed by reduction in section and corresponding increase in net section stress with increased strain rate (Cane & Williams, 1987).

- (ii) Microstructural degradation (*e.g.*, precipitate coarsening, modification of the dislocation mesh structure by the increase in interparticle spacing) leading to a continuous reduction in creep strength during service.
- (iii) Creep cavitation, which is usually observed at grain boundaries.
- (iv) Environmental attack (external scaling, internal oxidation or decarburization *etc.*).

The four processes occur simultaneously, but depending on materials and conditions one or other will predominate. Processes (ii) and (iii) are creep damage processes which will enhance the rate of increase of the strain rate until tertiary creep and failure can take place; these are of particular significance for the high-temperature failure of low-alloy ferritic steel plant. In general, coarsely-microstructured materials such as weldments are susceptible to cavitation damage, whereas in the more refined microstructure of the bulk boiler steel ductile damage processes are favoured (Cane & Townsend, 1984). Thus for steam header bodies, where, as noted earlier, improvements in current predictive techniques could be of greatest value, mechanism (ii) is of most relevance.

1.8.1.2 Mechanistic creep damage model for headers

Initially, the role of cavitation can be ignored as its contribution to header failure is small. If the dominant ductile mode of failure is then considered we can model low alloy ferritic steels as particle dispersion hardened material with a creep rate primarily dependent on particle spacing (Cane & Williams, 1987). In developing such a model it is necessary to consider:

- (a) An exact relationship between creep rate and particle spacing, which will require an understanding of the mechanism by which dislocations overcome particles to move through the matrix (Cane & Townsend, 1984).
- (b) An accurate description of the variations in particle dispersion in different regions of the material.
- (c) An understanding of the effect of time spent at elevated temperature and pressure on particle dispersion and size.

(d) Solid solution strengthening.

It is on this basis that attempts can be made to determine the creep rate from the operating conditions and thus estimate creep life. Ultimately, models of this basic design show great potential for improving the accuracy of remanent life estimates, but at present they are very much in the development stage.

1.8.1.3 Parametric creep damage model for steam headers

These models have been available for some time, developing from a continuum approach to the analysis of tertiary creep by Kachanov (1958) and others. The concept of a damage parameter, ω (a scalar quantity which is zero at the start of exposure and one at the point of failure), is introduced to give a quantified level to the creep damage and thus to the remanent life. Damage and strain are assumed in Kachanov's approach to increase as functions of stress and temperature.

Using such an approach leads to a relationship such as the one below, proposed by Rabotnov in 1969, to relate the strain rate, $\dot{\epsilon}$, and the rate of creep damage accumulation (*i.e.*, the rate of change of the creep damage parameter with respect to time), $\dot{\omega}$, to the stress state. It is presented as an example of a parametric model: a full discussion of models in current use in the Industry is beyond the scope of this summary.

$$\dot{\epsilon} = \frac{A \sigma^n}{(1 - \omega)^n} \quad (1.4)$$

$$\dot{\omega} = \frac{B \omega^\nu}{(1 - \omega)^\eta} \quad (1.5)$$

The relationship is essentially empirical, with A, B, n , η , ν , and σ being constants characteristic of the material; thus it follows that such a model requires quantities of archive test data if it is to be established, and the problems associated with determining accurate test data and operational parameters are well documented above. As a result, although a parametric model provides a reasonable basis from which to make an assessment of remaining life, a mechanistic model would be preferable.

1.8.2 Mechanical testing

1.8.2.1 Accelerated creep and rupture tests

Testing is carried out under accelerated conditions (of increased stress, temperature or both) on material taken from service, which has partially exhausted its theoretical creep life. Rupture testing involves simply the determination of time to rupture for varying simulation conditions, whereas creep testing assesses the strain response of the material as the simulation proceeds. Generally, only small pieces of material are taken for testing, but in extreme cases whole components are used (Day, Rowley & Williams, 1979).

1.8.2.2 Rupture testing

For thick walled components, such as steam headers, rupture testing is typically carried out using samples under uniaxial stress with a specimen axis parallel to the maximum principle stress direction of the component (Cane & Williams, 1979). One or other of the approaches below can then be used to determine residual life from time to test piece rupture.

(a) Parametric extrapolation

There are two general experimental techniques which allow creep life assessment to be made within reasonable periods of time, involving accelerating creep rate by changing the conditions. These accelerated tests have the disadvantage that the results have to be extrapolated to the slower strain rates associated with service conditions. The first of these, stress extrapolation, employs isothermal rupture tests performed over a range of temperatures at stresses above the nominal service stress. The extrapolation of increased stress conditions to the lower service stress is based on largely-empirical relationships which do not take account of mechanistic considerations, such as the recovery mechanism proposed by Cane (1978, see Section 1.7.1); however, it has been observed experimentally that remanent life predictions based on stress extrapolation tend to be optimistic (Cane & Townsend, 1984), so the technique has limited engineering value.

Testing in accelerated conditions achieved by raising the temperature at the nominal service stress are also carried out (temperature extrapolation). Hart (1976), Cane and Williams (1979) and others have all proposed that this is a more satisfactory method than stress extrapolation for low-alloy ferritic steels: work carried out by Hart (1980) for Cr–Mo–V samples removed after 100 000 hours service gave an extrapolated service life of 150 000 hours at 571°C, compared with the figure in excess of 200 000 obtained from stress extrapolation experiments; and experience gained from components in service suggests that the former is almost certainly a more reliable estimate.

An understanding of this observation can be achieved by considering the mechanistic applicability of accelerated testing methods. It has been observed that microstructural damage (carbide coarsening *etc.*) rather than void formation is the predominant damage mode found in practice in steam headers. At low stresses, precipitate coarsening controls the development of the dislocation structure and the distribution and movement of dislocations within the microstructure; precipitate coarsening (and the concomitant increase in interparticle spacing) will thus govern the deformation rate. At higher stresses, the dislocation mesh size will decrease until it becomes less than the interparticle spacing; dislocation movement will then cease to be governed by the precipitate dispersion, and the dislocation structure can modify allowing some recovery to take place. Consequently, the rupture life becomes highly stress sensitive, and extrapolation wildly inaccurate, as is illustrated schematically in figure 1.9.

Temperature extrapolation can then be expected to be a superior procedure provided no fundamental changes in the nature of the precipitates occur: any change in the properties of the carbides could be expected to affect the creep behaviour and introduce a temperature sensitivity. It should be noted that observations by Felix and Geiger (1961) suggested that for Cr–Mo–V steel such a change did occur, (from VC to Mo₂C at 600°C), showing that this difficulty is encountered in engineering systems, so care must be taken to monitor carbide structure if temperature extrapolation is to be carried out.

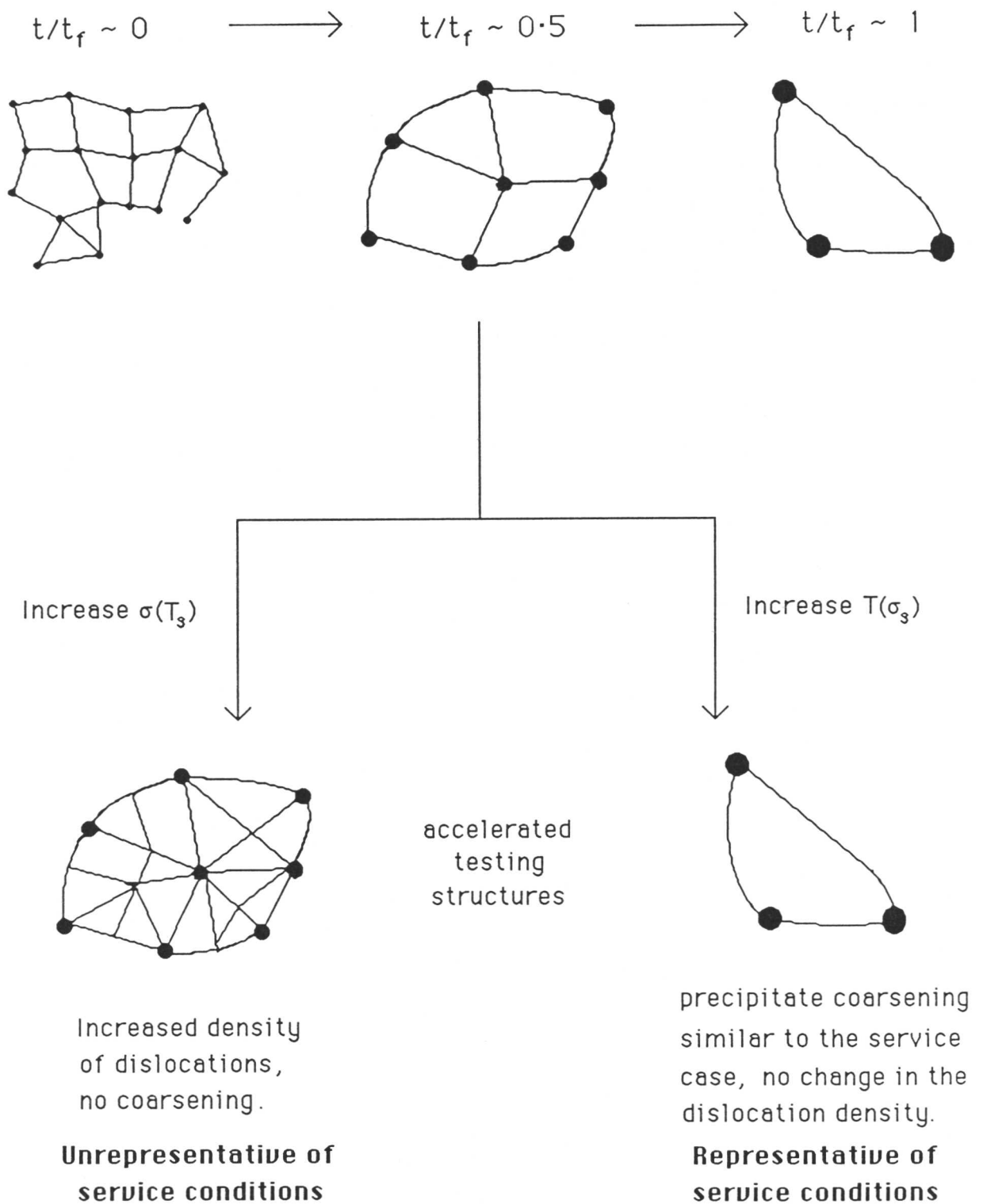


Figure 1.9: Structural aspects of accelerated rupture test methods (Cane & Townsend, 1984)

(b) Life fraction rule

The life fraction rule (equation (1.1)) can be simplified for accelerated testing, to:

$$\frac{t_s}{t_{sf}} + \frac{t_t}{t_{tf}} = 1 \quad (1.6)$$

where t_s is the time at service conditions, t_{sf} is failure time at those conditions, and t_t and t_{tf} represent the corresponding times for test conditions.

The application of the life fraction rule was discussed in Section 1.7.1, and it was noted that it is generally more applicable to accelerated temperature tests for low-alloy ferritic steel (see, for example, Hart, 1977a,b): stress acceleration is only acceptable where the creep strength has not been affected by unstressed thermal exposure (Hart, 1980). The disadvantage with a life fraction rule method is the general shortage of virgin material data (to provide t_{tf}). Thus t_{tf} must frequently be based on estimates from lower bound stress test data or from tests on regenerated material with the inherent inaccuracies that introduces (Cane & Williams, 1985).

1.8.2.3 Creep testing

(a) Constant strain rate

Material is tested under laboratory conditions at a constant, but considerably higher than service, secondary creep strain rate. This involves the extrapolation of data obtained at the high laboratory strain rates to the lower rates experienced in service, hence the same problems are encountered as those noted for high-stress rupture testing (above) (Cane & Townsend, 1984).

(b) Constant load

Testing is carried out at the service stress and the creep strain rate is increased by increasing the temperature to considerably above the service temperature. Minimum creep rate ($\dot{\epsilon}_m$) in post-exposure tests over a range of temperatures is extrapolated on a $T - \dot{\epsilon}_m$ plot to obtain the creep strain rate expected at the

service conditions. Cane (1982) and others have found that this approach, which depends on creep rupture and creep deformation having similar mechanisms, gives reasonable accuracy for low-alloy ferritic steels.

1.8.2.4 Other mechanical tests

Techniques can also be developed to relate a measured bulk physical property to the creep life; such a property must of necessity show a known correspondence to the relevant creep mechanism. Those methods which have been found useful are listed in table 1.5 (Cane & Townsend, 1984).

Test Method	Comments
Tensile	Limited applicability
Charpy V notch	Limited applicability
Hardness	Useful as a non-destructive method to isolate problem areas
Low cycle fatigue	Insensitive to structural damage, not generally applicable
Hot tensile	Sensitive to structural damage but not directly relatable to remanent life
Internal friction	Research tool only. No advantage over accelerated creep testing (see above)
Density, resistivity, magnetic permeability, small angle neutron scattering	May be useful for cavitation assessment in microstructurally-stable material

Table 1.5: Applicability of mechanical testing to the determination of remanent creep life

1.8.3 Metallographic examination

Metallographic studies, based on the models developed for creep damage (Cane, 1978), can potentially be used to estimate remanent creep life from small samples

of material taken from the exposed component. The technique has the advantage of being essentially non-destructive: samples can be taken by removing small slices, cylinders or cones of material from the critical region (which can then be repaired), or by acetate surface replica methods (Townsend, 1986), without damaging the bulk material.

Properties that can be studied include carbide size, spacing, composition and type, and local void distribution (Cane, 1984). Any carbide assessment will be via SEM or TEM procedures on post-service material, but the use of surface replication is efficacious in studying distributions of voids and microcracks (Cane & Williams, 1987). If this approach is to be practicable, it is imperative that a correspondence between remanent life and a given level of microstructural damage be established. Of the properties listed in the table, the level of cavitation, or fraction of cavitating boundaries, have been proposed as the most suitable expressions to appertain to remanent life (Cane & Needham, 1983), as is illustrated for the heat affected zone of a $2\frac{1}{4}\text{Cr}-1\text{Mo}$ type steel in simulated laboratory conditions in figure 1.10. It must be noted, however, that a given degree of cavitation could represent very different consumed life fractions for different stress states: Ludwigsen (1985) observed 0.1% cavity area as corresponding to 30%–70% damage, so that only qualitative lifetime judgements could realistically be made on such observations of the extent of cavitation. It will be necessary for genuinely representative mechanistic models to be developed before metallographic techniques can reach a high level of sensitivity.

At present, only surface replica techniques are used frequently, as they have the advantage of giving a warning of serious creep damage at critical areas cheaply and quickly and without requiring a knowledge of the thermal history of the component (Vierros, 1985). Nevertheless, metallography is of value both at present, as a preliminary NDT technique to isolate critical areas for creep life exhaustion, and as an experimental route to the development of mechanistic models.

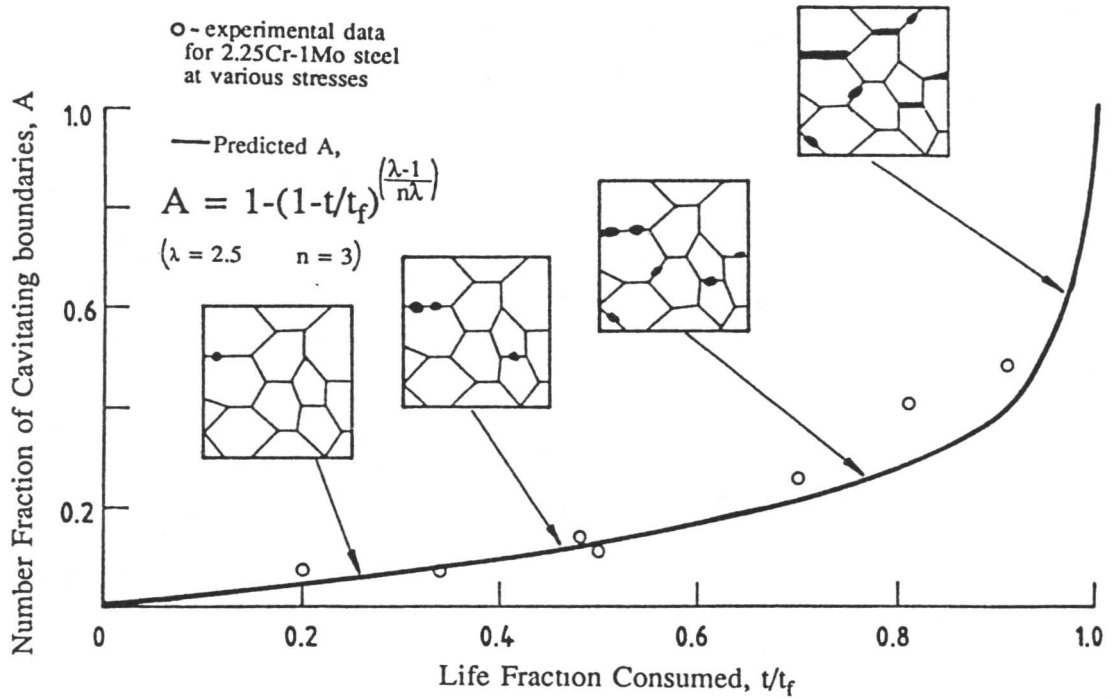


Figure 1.10: Relationship between fraction of grain boundaries showing signs of cavitation and life fraction consumed (Cane & Townsend, 1984)

Chapter 2

MICROSTRUCTURE OF CREEP RESISTANT LOW-ALLOY FERRITIC STEELS

The principal influence on development of steam header material is provided by the heat treatments that are performed to transform from austenite to ferrite, and to modify the ferritic microstructure to produce the desired properties in the final product. Nevertheless, the solidification processes effecting the production of the initial cast are of importance, as solidification induced segregation within it could have a significant effect on the development of ferrite from austenite during steam header fabrication. In this context the effect of alloying element segregation on the austenite–ferrite transformation must also be considered.

2.1 The Austenite–Ferrite Transformation

The decomposition during cooling of the higher temperature face-centred-cubic γ -iron structure to the less dense body-centred-cubic allotrope (α) gives rise to a variety of different morphologies and microstructures, depending on the cooling rate, presence of alloying elements, conditions and availability of lower-energy nucleation sites for heterogeneous nucleation.

2.1.1 *Effect of cooling rate*

Increases in undercooling and rate of cooling from the austenite region limit the ability of alloying elements in iron, and the iron atoms themselves, to diffuse during the transformation to form the equilibrium structure, hence leading to an increased tendency for the formation of metastable structures.

The alloying elements in steel can be categorized in two classes. Substitutional elements (*e.g.*, Cr, Mo) occupy lattice sites within the iron lattice and require vacant lattice sites to facilitate diffusion. Hence these species are slow diffusers, which can only maintain equilibrium at the higher transformation temperatures; the same applies to the iron atoms. Interstitial elements (*e.g.*, C) are

fast diffusers, occupying and moving between interstices within the iron lattice. Diffusion of these species is suppressed only at much higher undercoolings. Whether the reaction process and rate is under the control of one or other type of diffusing species, or is diffusionless, is determined by the free energy for the transformation (which increases with undercooling) and by the diffusion rates (decreased with temperature); hence, cooling rate is critical in determining the transformation process, and consequently the final microstructural development.

2.1.2 Summary of transformation products

2.1.2.1 Allotriomorphic ferrite (α)

At low undercoolings, given sufficient substitutional atom mobility, the fcc lattice can undergo a reconstructive transformation to the bcc form via diffusional motion of the atoms. This is possible even without the maintenance of equilibrium concentrations of alloying elements throughout the structure; indeed, in the low-alloy ferritic steels typically used in power plant construction, at all but the slowest growth rates, reconstructive transformation is generally found to occur as a carbon-diffusion-controlled growth process with no bulk partitioning of substitutional alloying elements, via a para-equilibrium mechanism suggested by Hillert (1952).

Diffusional ferrite in steels is generally found to nucleate heterogeneously and is observed to grow into two forms, allotriomorphic and idiomorphic. Allotriomorphic ferrite is the term applied to ferrite regions where the crystal structure and symmetry is not directly reflected in the shape of the bulk region, whereas in the case of idiomorphic ferrite the ferrite region has a shape which corresponds to the crystal structure (Bhadeshia, 1985). The difference arises from varying growth processes for different nucleation sites.

Allotriomorphic ferrite nucleates at prior-austenite grain boundaries, and its morphology arises from the fact that the grain boundary provides a favourable growth path, so that the ferrite grows at a preferential rate along the boundary compared with other directions. In general, it has been shown that the growth of ferrite allotriomorphs is a diffusion-controlled process (Atkinson *et al.*, 1973).

A reproducible orientation relationship is often shown between the ferrite and one of the adjacent austenite grains, and in consequence it has been proposed that transformation proceeds by a route which involves ferrite nuclei forming a partially-coherent interface with one austenite grain, and an incoherent one with the other (Smith, 1953). The former (lower energy) interface then moves via a ledge displacement mechanism, with the latter (high-energy) interface being displaced by a continuous motion of the whole. However, it has been demonstrated that a ferrite nucleus can by chance exhibit such an orientation relationship with both the austenite grains at whose interface it forms (Hillert, 1962). The ledge-type growth mechanism is believed to play a significant rôle in the precipitation mechanism for certain of the alloy carbide structures that were noted earlier to be implicated in creep strength processes in low-alloy ferritic steels (Edmonds & Honeycombe, 1978).

In alloy steels, a variety of mechanisms of allotriomorphic ferrite formation are shown at different levels of undercooling below the $\alpha / \alpha + \gamma$ phase boundaries, which are governed by the partitioning behaviour of the substitutionals. Only at slow growth rates, at undercoolings marginally below Ae_3 , will the extent of partitioning of alloying elements between the phases be that predicted by an equilibrium tie line construction through the mean alloy composition: at higher undercoolings, the transformation proceeds via a partitioning local equilibrium (PLE), negligible partitioning local equilibrium (NPLE), or paraequilibrium (ParaE) mechanism.

These mechanisms where full long range equilibrium is not maintained can be explained by the large difference in diffusivity between substitutional and interstitial alloying elements, coupled with the need to maintain a mass balance for both species across the moving interface. It can be considered that, for diffusion-controlled growth, the alloying element compositions at the growth interface should approximate to equilibrium, even at growth rates where long range equilibrium cannot be maintained (Darken & Gurry, 1953). At low undercoolings, where the driving force for growth is relatively small, reasonable levels of diffusion are possible within the austenite at the interface. The diffusion fields

at the interface are such as to allow a large degree of partitioning of alloying elements at the growth front, hence the mechanism is termed partitioning local equilibrium (PLE).

At higher undercoolings and supersaturations the driving force for interface motion is increased, reducing the extent to which long range diffusion of substitutional alloying elements can occur during growth. The composition profile of substitutionals at the interface becomes narrowed to an increasingly pronounced spike, and the extent of partitioning at the interface becomes extremely small, leading to the process being labelled negligible partitioning local equilibrium (NPLE).

It should be noted that for both local equilibrium mechanisms motion of the interface is controlled by alloying element diffusion, even where partitioning of that element is negligible. This need not be true at higher undercoolings, where the driving force for motion of the interface can be sufficiently high to cause local equilibrium to break down, with insufficient time even for the small amount of longer range diffusion which is essential to a local equilibrium mechanism. Under these conditions the alloying element is configurationally frozen, and growth of the interface is controlled solely by diffusion of carbon, which reaches equality of chemical potential subject to the constraint that the Fe:X ratio is constant everywhere. This mechanism is referred to as paraequilibrium (ParaE). It may be remarked that a ParaE growth mechanism results in identical concentrations of alloying elements in α and γ_{ret} in a partially-transformed specimen, a feature which has been employed producing some of the microstructures used in this piece of work, where accurate knowledge of starting compositions was required.

2.1.2.2 Idiomorphic ferrite

Nucleation of idiomorphic ferrite takes place intragranularly at point sites (*e.g.*, inclusions), so that no preferential growth direction exists; in consequence, the crystal symmetry of the ferrite is reflected in the morphology of the bulk structure. In steels, idiomorphic ferrite generally takes the form of equiaxed grains (see, for example, Bhadeshia, 1985).

2.1.2.3 Widmanstätten ferrite (α_w)

At slightly higher undercoolings not far below Ae_3 temperature the increased free energy driving force for the reaction and decreased atomic mobility leads to the formation of Widmanstätten ferrite. The transformed region of this reaction product is found to be plate-shaped, with a thin wedge section, and an associated shape change (Watson & McDougall, 1973). A single Widmanstätten ferrite wedge is found to exhibit a shape change consisting of two adjacent and opposite invariant plane strains with a large (~ 0.4) shear component (Bhadeshia, 1981a). This lends support to the hypothesis that atomic correspondence for substitutional atoms and iron is maintained during the formation of α_w from austenite.

The strain energy that is associated with such a shape change has been determined from strain and elasticity data and measurements of aspect ratios (Bhadeshia, 1981a), and is found to be much larger than could be sustained by the available driving force. If a plate is to form this strain energy must be dissipated during the transformation. Widmanstätten ferrite formation becomes possible because the strain energy is largely accommodated by a growth process involving cooperative development of two mutually-accommodating plates into a characteristically wedge-shaped region of α_w , as shown on figure 2.1. Both of the plates are found to exhibit a KS-NW type orientation relationship with the initial austenite (Bhadeshia, 1981a).

As Widmanstätten ferrite forms at relatively low undercoolings, diffusion of carbon occurs during growth; in fact, the growth rate has been shown to be determined by carbon diffusion rates at the (glissile) α_w/γ reaction interface (Bhadeshia, 1981a).

2.1.2.4 Bainite (α_b)

At higher undercoolings bainite forms in sheaves originating from austenite grain boundaries. The transformed region exhibits an IPS with associated shear component of 0.22. In the absence of the cooperative growth process the associated strain energy is considerably higher than was the case for α_w . This is coun-

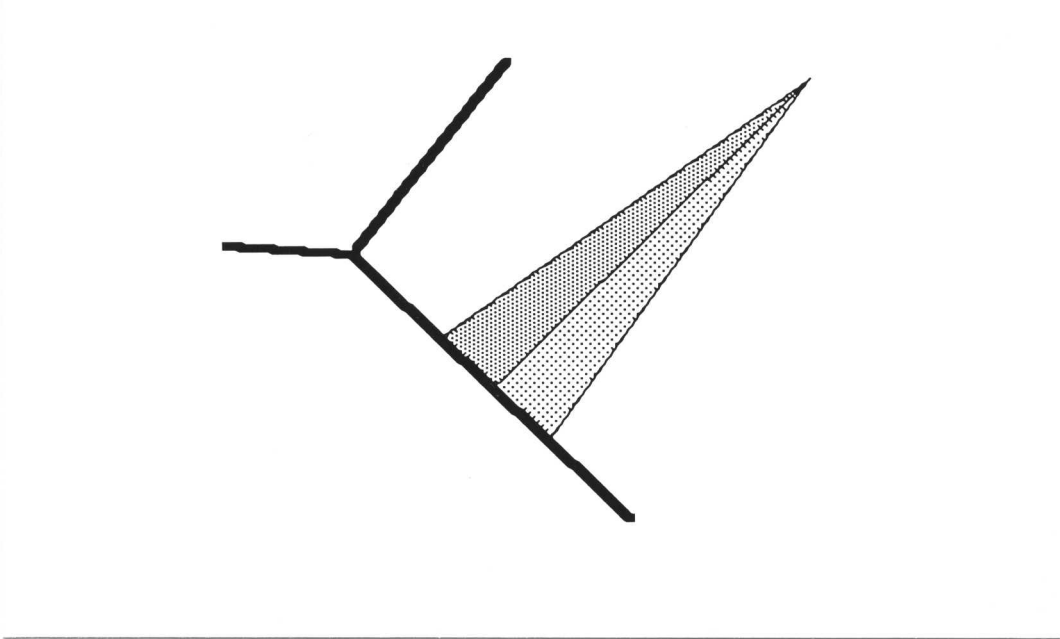


Figure 2.1: the back-to-back arrangement of plates of Widmanstätten ferrite growing from prior-austenite grain boundaries, illustrating the characteristic wedge shape of a Widmanstätten ferrite region

terbalanced by the increased free energy driving force which exists at the lower transformation temperature (Bhadeshia & Edmonds, 1980). This transformation product has been of great significance in the work outlined in this dissertation, and consequently the bainite transformation is considered in detail in a later section.

2.1.2.5 Martensite (α')

At highest undercoolings and low temperatures, where the free energy change for transformation is very large, martensite forms. The product arises as a result of a diffusionless transformation with direct atomic correspondence between parent and product lattices. There is macroscopically an IPS shape change in the transformed region giving rise to very large stored strain energy within the product phase; consequently, it is only able to form at high undercoolings where the chemical free energy change is large enough to offset this (Bhadeshia, 1985).

2.1.3 The time-temperature-transformation diagram

The concept of a time-temperature-transformation (TTT) diagram can be introduced to represent schematically the nature of transformation products and rates of reaction for different isothermal transformation temperatures in a given steel (*e.g.*, figure 2.2). Development of an accurate diagram of this sort for a particular alloy composition enables heat treatments to be designed to produce a desired transformation product.

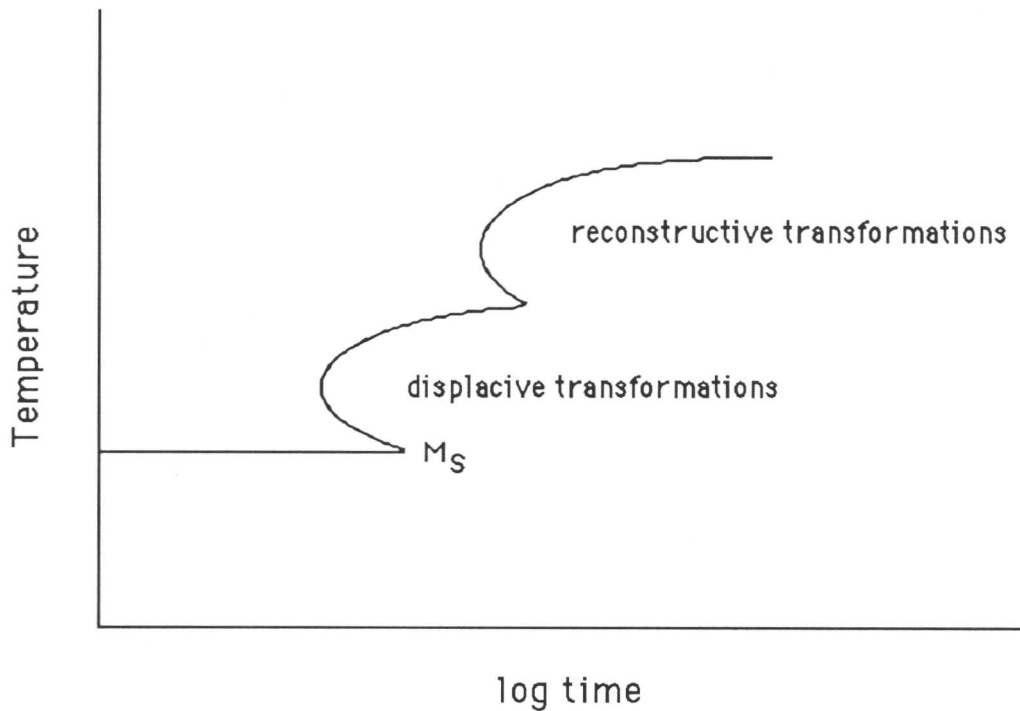


Figure 2.2: Typical TTT diagram for a low-alloy steel

2.1.4 The case of power station creep resistant steels

As we have noted for power station boiler systems the sequence of heat treatments is designed to produce a microstructure of allotriomorphic ferrite and bainite (α_b being in the range of 0.2–0.8 by volume fraction, usually around

0.2 for 1Cr- $\frac{1}{2}$ Mo type steels) (Cane & Townsend, 1986). Studies in this project have concentrated on determining remanent life from the appearance and ageing behaviour of the bainitic regions and alloy carbides found within the allotriomorphic ferrite, so a deeper consideration of these microstructural features is given below.

2.2 The Bainite Transformation

Bainite forms from austenite in steels in the temperature range below temperatures at which pearlite forms, and above the martensite start temperature. It consists of a non-lamellar aggregate of roughly lath or plate shaped ferrite grains, with carbide precipitation between and also sometimes within the ferrite. The bainite transformation has presented difficulties in interpretation, and remains the subject of some controversy.

2.2.1 Microstructural features of the transformation

Bainitic ferrite platelets or laths are observed to accumulate into sheaves possessing a roughly wedge-shaped morphology, and apparently originating from prior-austenite grain boundaries (Bhadeshia, 1988). The growth of these bainite sheaves is found to be limited by hard impingement with austenite grain or twin boundaries. The apparent relationship between the sheaf arrangement of the product phase and the grains of the parent phase is not a usual feature of a reconstructive, diffusional transformation. The sheaf arrangement of the sub-units is illustrated in figure 2.3.

The macroscopic shapes of the α_b regions are found to differ from the austenite regions from which they formed, the shape change in the transformed region corresponding to an invariant-plane strain (IPS). The IPS has a significant shear component which could be expected to produce a substantial stored strain energy in the transformed region (Hehemann, 1970).

The invariant plane of the shape change corresponds to the habit plane of the ferrite plates; in this respect the transformation product shows a similarity to martensite (Christian & Edmonds, 1984). The origin of the IPS shape change is

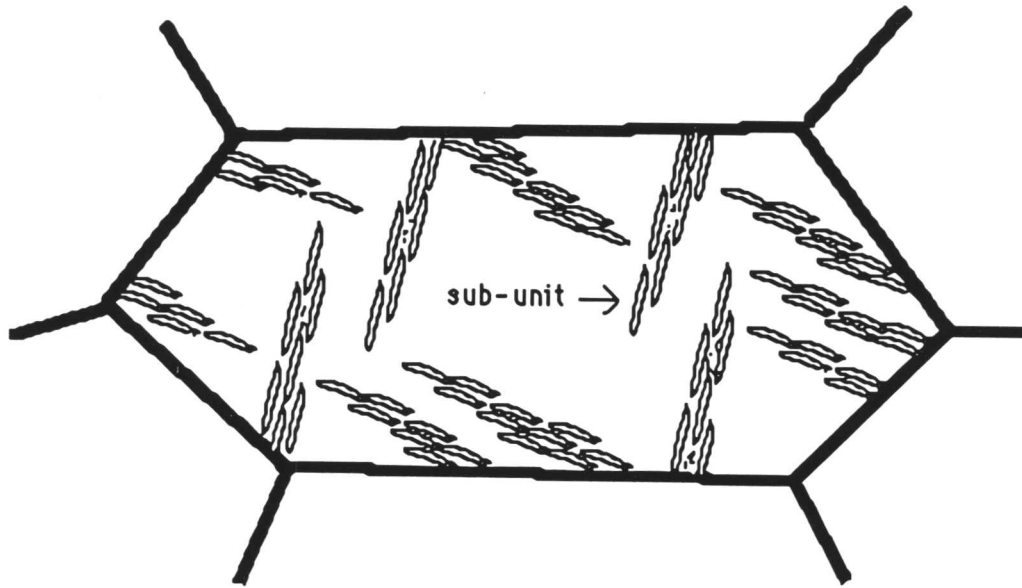


Figure 2.3: Arrangement of bainitic sub-units into sheaves within a prior-austenite grain

one of the major areas of dispute between contemporary hypotheses for a bainite reaction mechanism.

It has been suggested by Kinsman, Eichen and Aaronson (1975) that the observed IPS shape change arises during the growth of bainitic ferrite as a sessile α_b/γ semi-coherent interface is displaced by a step growth mechanism. They propose that a substantial barrier to growth of α_b develops at one orientation of the interphase boundary where ferrite and austenite lattices are sufficiently well-matched to form a partly-coherent misfit-dislocation interface. The matching is supposed to arise as a result of alignment of the close packed planes and directions in the two structures.

This boundary is then immobilized in a direction normal to itself and growth of the ferrite is then effected by the formation of ledges across the boundary.

The rate of growth of the bainitic ferrite under this mechanism is then governed by long term diffusion. In this way, it is claimed, the characteristic plate shape of ferrite develops, and the ledge migration produces ‘geometrical surface relief’ which is identified as a martensitic-type IPS on a macroscopic scale. As such, any similarity with the martensitic IPS would not necessarily demand an identical mechanism; the bainitic IPS would be consistent with a (carbon) diffusion-controlled growth process, along the lines of a bainite transformation mechanism of this type first proposed by Ko and Cottrell (1952).

It is similarly argued (Aaronson, Laird & Kinsman, 1970) that any surface relief effects associated with the IPS are not necessarily indicative of shear mechanism operation. Evidence in support of this supposition is cited from the formation of hexagonal close-packed γ -phase plates in the face-centred cubic α -phase in the Al-Ag system. In this case surface relief effects indicate an IPS (Liu & Aaronson, 1970), but Laird and Aaronson (1969) insist that the transformation mechanism involves diffusional jumps of silver atoms toward and aluminium atoms away from the edges of ledges formed on the faces of γ plates.

However, Bhadeshia and Edmonds (1979), argue that the IPS shape change necessarily implies an atomic correspondence between parent and product phase which is wholly inconsistent with a disordered diffusional transformation. It is suggested that the continuity of structure for such a coordinated movement of atoms requires a degree of atomic correspondence across all the interfaces of a product particle, and hence across a ledge structure. Thus the idea of a disordered ledge as proposed above is inconsistent with a coordinated movement of atoms.

It is concluded that the observed IPS arises due to a martensitic-type displacive transformation. The shape change will then give rise to a stored energy in the sheaves in the region of 400 Jmol^{-1} (Bhadeshia, 1981). The high dislocation density induced by attempts to relieve some of this strain energy by plastic deformation is then responsible for limiting the advance of the transformation interface and thus limiting the size of the bainitic sheaves (Bhadeshia & Edmonds, 1979). In this way, the observed limit on the growth of the bainitic regions in

the absence of any hard impingement or similar factor can be explained, as can the characteristic shape of the bainitic ferrite platelets.

Bhadeshia (1988) summarizes the bainite transformation as a displacive transformation with no diffusion of substitutional (or Fe) atoms across the transformation interface, referring to recent evidence from atom probe studies which demonstrates such an absence of diffusion across the transformation front (Stark, Smith & Bhadeshia, 1987).

2.2.2 Kinetic features of the transformation

In those alloy steels where a pronounced bay in the TTT curves is observed the bainite reaction (which corresponds to the lower C curve) can be studied carefully without interference from other, higher temperature transformations (Christian & Edmonds, 1984).

The bainite reaction exhibits all of the classical features of a nucleation and growth transformation except one: the reaction ceases before the carbon concentration in the retained austenite reaches that of the equilibrium or para-equilibrium phase boundary. The extent of reaction is a function of temperature, increasing as the transformation temperature is reduced. Extrapolation of this back to 0% bainite defines the kinetic bainite start temperature (B_s) above which bainite is not observed to form (Hehemann, 1970). The B_s is found to correspond approximately to the bay region in the TTT curve (Hehemann, 1970). These features of the bainite reaction (temperature dependence of fraction transformed, and existence of the B_s) are referred to as the *incomplete reaction phenomenon*.

Two contrary hypotheses have been advanced to explain the bay region in the TTT curve and the incomplete reaction phenomenon.

Kinsman and Aaronson (1967) postulate that the slowing down of reaction kinetics at the bay region arises due to a solute drag process caused by segregation of substitutional alloying elements across the austenite/ferrite transformation interface. It is propounded that the transformation is in reality continuous through the kinetic B_s , but that the effect of the solute drag process is to produce an apparent slowing in reaction kinetics at the bay, and the variant mor-

phologies observed above B_s (Hehemann, Kinsman & Aaronson, 1972); similar structures to bainite which form above the B_s temperature are cited as evidence for this proposal. This leads to the proposition that the observed transformation products are related by a continuum of transformation states. Purdy and Hillert (1984) extend this continuum through to lath martensite, which is seen as a kinetically-unstable extreme of the bainite reaction that is accompanied by effectively complete solute entrapment.

Contrary evidence from Bhadeshia and Waugh (1982) seems to suggest that segregation of substitutional alloying elements does not take place at the transformation interface. Significant supporting evidence for their results has been provided recently by further work on this problem involving a detailed atom probe study of the behaviour of substitutional atoms at the transformation interface (Stark, Smith & Bhadeshia, 1987). This leads to an alternative explanation for the features of the bainite reaction, which argues that a clear distinction between structures formed above B_s (*e.g.*, pro-eutectoid α_w) and bainite must be drawn. Different reaction mechanisms are operating (Christian & Edmonds, 1984), with products below B_s being produced by a transformation of a displacive character; it follows that the bay region can be explained as the point of overlap between two distinct C curves (for diffusional and displacive transformations), rather than a kinetic feature of a single transformation mechanism (Bhadeshia, 1988).

It has been noted that bainitic sheaves appear to originate at prior-austenite grain boundaries, and to be limited in their extent by hard impingement at those boundaries. As a consequence it is postulated that the austenite grain size, and hence the nature of the austenitizing treatment and in particular the temperature, can influence the kinetics of the transformation (Umemoto, Furuhashi & Tumura, 1986); in practice the effect of grain size on rate of transformation is found to be small (Umemoto, Horiuchi & Tumura, 1982).

2.2.3 Carbon content of bainitic ferrite

The carbon content of bainitic ferrite is of considerable significance in any attempt to develop a mechanism to explain the incomplete reaction phenomenon.

As an occupier of interstitial sites in the iron lattice, carbon has the ability to diffuse rapidly at temperatures low enough to reduce the rate of diffusion of substitutionals at the growth interface to negligible levels. It can be reasonably assumed that the reaction is brought to a halt by an increase in the carbon content of the retained austenite above some critical level. This must correspond to either a two phase equilibrium being achieved between ferrite and austenite, or a carbon enrichment of austenite to a point at which diffusionless growth is impossible (Bhadeshia & Edmonds, 1980).

Bhadeshia and Edmonds (1980) submitted that the carbon content is found in all cases to be considerably less than that expected for a diffusional growth process to be operating. They proposed that the undercooling in the bainite region is of a sufficient level as to give a $\gamma \rightarrow \alpha$ driving force high enough to cause α_b to be formed with a full supersaturation of carbon, which subsequently redistributes to the remaining austenite. Calculations predicting the time-scale of such redistribution at the order of only a few milliseconds (Kinsman & Aaronson, 1967), and thus entirely inconsistent with observed bainitic ferrite growth rates, have recently been corrected and modified (Bhadeshia, 1988); the resultant predicted redistribution times, of the order of a few seconds, are now in agreement with observed growth rates.

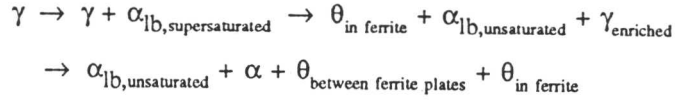
Thus, it may be suggested that bainite forms with supersaturation with respect to carbon by way of a martensitic-type nucleation process and growth of lath-like sub units. This is followed by a redistribution of carbon to the surrounding regions of remaining austenite, but after, rather than during, the formation of the bainite plate, as shown on figure 2.4 (Bhadeshia, 1981). Enrichment of the retained austenite progressively reduces the free energy driving force for bainite formation; the enriched austenite carbon concentration approaches the T'_0 curve, at which point the free energy available for transformation becomes insufficient to drive the displacive mechanism, no further bainite formation is possible, and the reaction then ceases. Thus, a model is provided by which it is possible to explain the incomplete reaction phenomenon, as is summarized in figure 2.5. It has been observed that carbon enrichment can dictate that

(a) Upper Bainite



(b) Lower Bainite

High dislocation density



Low dislocation density

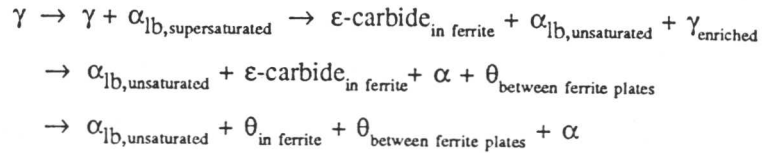


Figure 2.5: The bainite transformation (from Bhadeshia, 1988)

2.2.4.1 Upper bainite

This consists of aggregates of lath-, plate- or needle-like ferrite with carbides precipitated in the inter-lath regions. As the temperature is lowered, or the carbon content of the alloy increased, the laths become thinner and show an increased tendency to group together into sheaves, a process which has been entitled sympathetic nucleation (Aaronson, 1962), and the inter-lath carbides become near complete cementite films (Christian & Edmonds, 1984). The sub-units in such sheaves are observed to have the same habit plane with respect to the austenite from which they form, and a roughly parallel orientation in space (Ohmori, 1971). The width of these laths is observed to decrease as the transformation temperature is decreased, but the length remains fairly constant and is believed to be governed by prior-austenite grain size constraints (Pickering, 1967). Neither the sheaves, nor their constituent sub-units, are found to extend across prior-austenite grain boundaries, which is consistent with a displacive mechanism for their formation.

On the basis of several observed rational orientation relationships between

the inter-lath carbides and the original austenite it is assumed that these carbides are formed directly from the austenite rather than from the bainitic ferrite; hence, interlath carbide precipitation may be absent in some steels containing alloying elements that suppress cementite formation by raising the activity of carbon within austenite (especially silicon), which will generally result in carbon-rich austenite films being retained between the bainite laths after transformation.

2.2.4.2 Lower bainite

The lower temperature morphology is similar to upper bainite, but cementite or ϵ -carbide is found also within the α_b laths; these microstructural differences provide the foundation for the definition of the two categories of bainitic morphology, first suggested by Mehl (1939). In most steels the transition to lower bainite occurs at around 350°C (a temperature which shows little composition dependence according to Christian and Edmonds (1984)), although higher temperatures have been noted for some steels (*e.g.*, Pickering (1967) recorded a transition as high as ~550°C for 0.5 wt% Mo steels at around 0.5 wt% C). There is usually a short transition range over which both morphologies are exhibited.

It is suggested that the different morphologies are attributable to differing mechanisms by which decarburization of the supersaturated bainitic ferrite proceeds. The decarburization process is controlled by the diffusivity of carbon. At higher temperatures the carbon is able to diffuse sufficiently quickly to be expelled into the interlath austenite. As the temperature reduces, the carbon diffusion rate becomes insufficient to allow complete unsaturation of the bainitic ferrite by carbon diffusion into austenite; hence decarburization of bainite is then effected, at least in part, by cementite precipitation. It is found that very-low-carbon steel will not form lower bainite, since the free energy driving force for cementite precipitation will never be high enough to make it preferable to carbon diffusion into retained austenite as a mechanism of decarburization of supersaturated ferrite.

The intra-bainitic carbides are typically orientated at about 60° to the long axis of the α_b laths. Bhadeshia (1980) has asserted that the absence of a reproducible orientation relationship between austenite and intrabainitic cementite

indicates that these carbides are generated from supersaturated bainitic ferrite, rather than at the growth interface between α_b/γ during growth of the bainite sheaves as had previously been suggested by some authorities. The nature of the carbides within the ferrite is then determined by the dislocation density generated in the bainite before precipitation of carbides takes place: at high dislocation density, carbon associated with the dislocations allows direct precipitation of cementite at these sites, so that ϵ -carbide formation is disfavoured. According to this hypothesis ϵ -carbide should not be present in steels of C < 0.55 wt% (Bhadeshia, 1980), which is in good agreement with practical observations.

2.2.5 Conclusions

The considerable controversy attached to various aspects of this transformation as set out above are unlikely to be wholly resolved for some time. Whilst it is impossible fully to discount a carbon-diffusion-controlled growth mechanism for bainite, the balance of recent evidence is in favour of Hehemann's mechanism of nucleation and martensitic-type growth of lath-like sub-units. Thus, bainite forms through a displacive transformation, and as such by way of a mechanism distinct from that which generates pro-eutectoid ferrite and pearlite, and the bay in TTT curves for alloy steels is attributable to this (the curves are, in fact, separate curves representing diffusional and displacive products) rather than to a solute drag process at the transformation interface.

2.3 Carbide Precipitation in Allotriomorphic Ferrite

It is a fundamental feature of the iron-carbon system that carbon solubility is much greater in austenite than it is in ferrite under the same conditions; thus, precipitation of carbides during the austenite-ferrite transformation is likely to play a significant part in the transformation for all but the lowest carbon steels. In plain carbon steels carbide precipitation is in the form of discrete cementite particles or pearlitic nodules after substantial ferrite growth. Addition of alloying elements can lead to precipitation of alloy carbides instead of iron carbides, and such carbide structures play a significant rôle in contributing to the creep strength of low-alloy ferritic creep resistant steels. In addition, if

the alloying elements are strong carbide formers, then ferrite growth may be restricted by the need for alloying elements to partition by diffusion, and the carbide may then be observed to grow simultaneously with ferrite (Honeycombe & Pickering, 1972). The most important forms of alloy carbide precipitate found in steels are summarized below, categorized according to precipitation site.

2.3.1 Interphase precipitation

This is the term given to arrays of fine, evenly spaced precipitates, which have been noted as being desirable to enhance creep properties. Interphase carbide precipitates frequently occur in banded structures within the ferrite grain, but irregular dispersions are also observed. These precipitates are believed to form during the transformation to ferrite, being nucleated at the α/γ interface as the ferrite region grows (Davenport, Berry & Honeycombe, 1968). The process is of particular importance in microalloyed steels containing niobium, vanadium and titanium, but in higher alloy steels coarser precipitates related to Fe_3C are also observed (Honeycombe, 1984). Honeycombe classifies interphase precipitation into two forms, depending on the nature of the interface between the growing ferrite and retained austenite.

2.3.1.1 Planar interphase precipitation

Planar arrays of precipitates are found to be associated with low-energy, semi-coherent, planar (faceted) α/γ growth interfaces. Edmonds and Honeycombe (1978) found that such boundary structures are very common at all transformation temperatures on a local scale, and planar interphase precipitation is not confined to those transformation products (*e.g.*, Widmanstätten ferrite) where the presence of such boundaries on a larger scale is well known; indeed interphase precipitation is much more common in fully equiaxed ferrite than in Widmanstätten ferrite.

These semi-coherent interfaces are associated with step migration during ferrite development (see figure 2.6). Regularly-spaced steps give rise to evenly-spaced precipitate arrays (marked a on figure 2.6) and irregular steps produce irregularly-spaced arrays (b). Note that precipitation does not usually occur at

the high-energy, high-angle interfaces at the transformation front (*i.e.*, the step faces); growth rates are too high to allow sufficient diffusion to the precipitate site. On the occasions when there is precipitation the step movement is impeded or stopped, leading to a discontinuity in the array. Instead, precipitation takes place on the low-energy, less mobile interfaces. There is typically an orientation relationship across the transformation interface of the Kurdjumov-Sachs (K-S) form (Honeycombe, 1984), viz:

$$\langle 111 \rangle_{\gamma} \parallel \langle 110 \rangle_{\alpha} \quad \{ \bar{1}\bar{1}0 \}_{\gamma} \parallel \{ \bar{1}\bar{1}1 \}_{\alpha}$$

The interphase plane for such precipitation is normally $(111)_{\gamma} \parallel (110)_{\alpha}$ and this will be reflected in the crystallography of the precipitates (Honeycombe, 1984).

Precipitates found in association with planar austenite/ferrite interfaces include VC, NbC, TiC, TaC, Cr₂₃C₆, Cr₇C₃, M₆C, W₂C, Mo₂C, ϵ -Cu and Au (the last two are not carbide structures but are observed to precipitate and behave in the same way). The crystallography of these precipitates is listed in table 2.1 (from Honeycombe, 1984).

Phase	Structure	Habit	Orientation relationship with α matrix
VC, NbC, TiC, TaC	fcc	plates	$(100)_p \parallel (100)_{\alpha} : [010]_p \parallel [110]_{\alpha}$ (Baker-Nutting)
Cr ₂₃ C ₆	complex cubic	rods or laths	$(111)_{Cr_{23}C_6} \parallel (101)_{\alpha} : [\bar{1}10]_{Cr_{23}C_6} \parallel [\bar{1}11]_{\alpha}$ (Kurdjumov-Sachs)
Mo ₂ C	c-p hex.	rods, $[100]_{\alpha}$ growth dir.	$(0001)_{Mo_2C} \parallel (011)_{\alpha} : [2\bar{1}\bar{1}0]_{Mo_2C} \parallel [100]_{\alpha}$
ϵ -Cu, Au	fcc	spheres, rods	$(111)_{\epsilon-Cu} \parallel (101)_{\alpha} : [\bar{1}10]_{\epsilon-Cu} \parallel [\bar{1}11]_{\alpha}$ (Kurdjumov-Sachs)

Table 2.1: Crystal structures of common interphase precipitates in ferrite (Honeycombe, 1984)

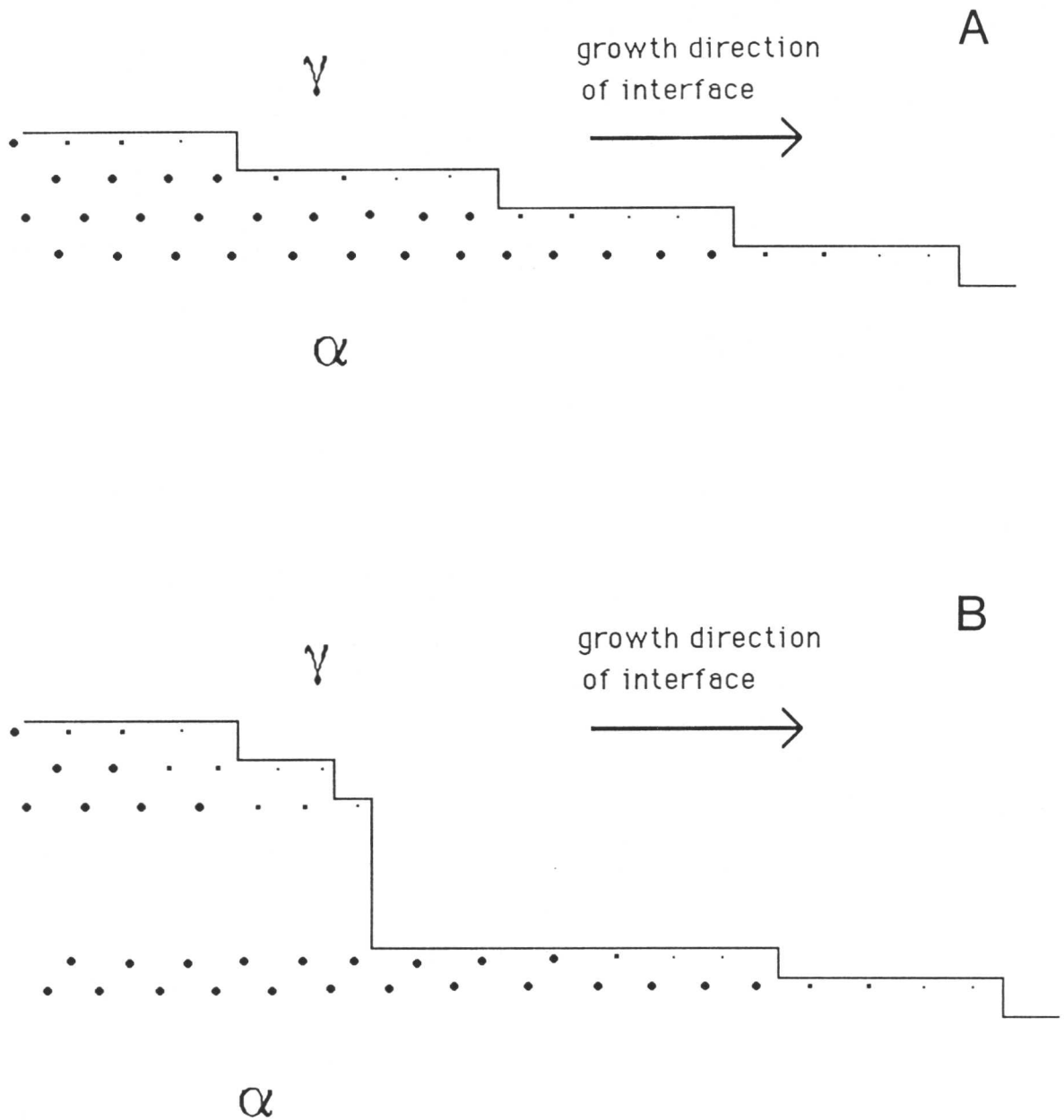


Figure 2.6: Planar interphase precipitation (from Honeycombe, 1984)

2.3.1.2 Non-planar interphase precipitation

In these cases the precipitates are believed to be associated with high-energy, incoherent α/γ interfaces, forming into irregularly organized periodic arrays. Campbell and Honeycombe (1974) conjecture that the arrangement of such particles is determined by the pinning action of the precipitate on the α/γ growth front. As a result of such pinning, the interface is forced to bow around in a way analogous to Orowan bowing of dislocations if the transformation is to advance, which gives rise to an irregularly orientated array of still regularly-spaced

precipitates.

Non-planar precipitate arrays are especially prevalent for coarser Cr_7C_3 and Cr_{23}C_6 types, and for other alloy systems where the precipitates are generally coarser and more widely spaced (Honeycombe, 1984).

2.3.2 Fibrous carbide precipitation

Fibrous carbide structures are found to precipitate in many of the steels that exhibit interphase precipitation, often under the same conditions and at the same time; for example, Mo_2C , VC, TiC, NbC, Cr_{23}C_6 , Cr_7C_3 , $\epsilon\text{-Cu}$ and Au are all observed in this morphology. The fibrous structures are typically 100–300Å in diameter, 200–500Å apart, and with a length of the order of several μm (Honeycombe, 1984). In some cases, *e.g.*, with chromium steels transformed at higher temperatures, the structures have been found to be directly analogous to cementite (Campbell & Honeycombe, 1974), but as a general rule important differences are found in the alloy carbide morphologies, such as an almost total absence of branching.

As was the case for interphase precipitation, fibrous carbides are found to be associated with the austenite/ferrite interface, nucleating at incoherent boundaries, and growing in a direction approximately normal to the transformation front (Davenport, Berry & Honeycombe, 1968); both forms of precipitation have been noted in the same steel in many cases. The exact nature of the α/γ interface is thus very important in determining the relative proportions of fibrous and interphase precipitation in cases where both are found to occur, and this is in turn dependent on the transformation conditions. Investigations have shown that fibrous precipitation predominates for longer reaction times, whether this arises as a result of alloying (Batte & Honeycombe, 1973), or reduction of the temperature (Berry & Honeycombe, 1970).

2.3.3 Precipitation on dislocations

At higher undercoolings the ferrite can, to some extent, remain supersaturated throughout the transformation such that the precipitation processes documented above, associated with the austenite/ferrite transformation front, do not take

place. Subsequent precipitation can then occur on sites such as dislocations within the ferrite and at α/α grain boundaries, which provide lower energy locations for heterogeneous nucleation of intragranular precipitates. Dislocations are generated in the transformed region as a result of the volume change from γ to α ; higher dislocation densities are found in Widmanstätten ferrite than in equiaxed ferrite, probably reflecting shear processes in α_w formation (Smith & Honeycombe, 1982). Such precipitation has been noted by Ballinger and Honeycombe (1980) for VC in low-carbon vanadium steels, and by Ricks, Howell and Honeycombe (1980) for ϵ -copper in Fe–Cu–Ni alloys.

2.3.4 Precipitation at austenite grain boundaries

Precipitation has been found to take place in some cases at the prior austenite grain boundaries, even preceding the initiation of ferrite formation (Honeycombe, 1984). Grain-boundary precipitation is also observed at heterogeneous sites on newly-formed ferrite grain boundaries during transformation. Carbides generated in this way are generally found to be much coarser than interphase precipitates, and as such regarded detrimental to creep strength in creep resisting steels of the class under investigation in this project; grain boundary precipitation is therefore to be avoided in low-alloy ferritic creep resisting steels.

2.3.5 Summary

In general, creep resisting properties are optimized by the generation of a fine dispersion of regularly-spaced alloy carbide particles, rather than coarser or fibrous structures (Cane & Townsend, 1984). A consideration of the above alloy carbide precipitation routes is therefore of substantive importance in determining heat treatments to maximize creep life. The carbide structures actually produced in creep resistant boiler system steels are considered, along with their behaviour under service conditions, in a later section.

2.4 Changes in Alloy Carbides Within the Ferrite During Ageing

The microstructure of the low-alloy ferritic steel found in power station headers is relatively fine-grained. The material can be considered to achieve creep re-

sistance from particle dispersion, and to accumulate damage by degradation of the precipitate structure, which can occur in two ways.

- (i) Particle coarsening due to diffusion at the elevated service temperature (with a concomitant increase in particle spacing), leading to a particle dispersion which is no longer optimal for creep properties.
- (ii) Ageing during service where the carbide in the initial structure is not the equilibrium phase at the ageing temperature may result in precipitation of other (more stable) carbides with properties detrimental to creep behaviour. This will frequently be compounded by loss of the beneficial carbide structures as they go back into solution.

It has been postulated by several workers that monitoring of carbide structure may supply the means to assess creep damage accumulation levels in those materials where degradation of the precipitate structure is the dominant damage mode. In addition, such work could provide a basis for mechanistic creep damage models to be developed for the creep processes in these materials.

Some of the earliest quantitative analysis of carbide compositions during creep was performed by Murphy and Branch (1969). Working with turbine casing steels of both 1Cr-Mo-V and $2\frac{1}{4}$ Cr-Mo-V type,¹ they observed that during ageing at 575°C there was a tendency for coarse M_3C carbides to form. These will denude the surrounding region of chromium, molybdenum and vanadium, and hence reduce the quantity of the fine alloy carbides (in these cases they were observed to be primarily vanadium carbides) that provide the creep strength, which will therefore be reduced during ageing. The effect of dissimilarities in composition between different casts (see the footnote) on creep properties was also highlighted; although in this case molybdenum and chromium carbides were

¹ a number of different steels of either general class were used, with actual compositions (in wt %) within the following ranges:

1Cr type: 0.11–0.13C, 0.49–0.58Mn, 0.68–0.98Cr, 0.09–0.28Ni, 0.77–1.06Mo, 0.14–0.24Cu 0.23–0.32V, 0.27–0.47Si wt%;

0.25Cr type: 0.11–0.17C, 0.51–0.60Mn, 0.28–0.32Cr, 0.05Ni, 0.48–0.50Mo, 0.05Cu, 0.25–0.26V, 0.25–0.27Si wt%.

not believed to be directly critical for creep strength, Murphy and Branch noted that the amount of coarse M_3C formed was closely related to chromium and molybdenum concentrations. As a result the contribution of M_3C to the creep strength was similarly related to concentrations of the alloying elements other than vanadium. It was concluded that segregation effects involving alloying elements that do not form the precipitate dispersion which gives the creep strength can also, indirectly, have a significant local effect on that creep strength.

A study by Collins (1978) on $\frac{1}{2}Cr-\frac{1}{2}Mo-\frac{1}{4}V$ (approximate compositions) steam pipe material removed from service revealed Mo_2C as the predominant carbide within the ferrite. However, when accelerated creep testing was performed by raising the temperature, VC was observed to be more abundant. Closer examination showed that the carbides were in the form of a capital-H-shaped structure, with Mo_2C forming the uprights and VC the crossbar. The Mo_2C appeared to go back into solution if the material was heated to $690^\circ C$ after exposure at the service temperature leaving only narrow rods of VC. Collins questions the wisdom of accelerated creep testing by raising the temperature in such materials, where the carbide structure changes fundamentally between service and test temperatures.

The 'H' carbide structures have been found to be associated with dislocations, although VC precipitation is also observed at points within the bulk material where high dislocation densities are not found (Williams, 1981). Williams suggested that VC was precipitated as a metastable carbide form during fabrication, but that Mo was able to diffuse along the easy diffusion paths provided by dislocation pile ups associated with some of the VC precipitates. This provided a mechanism by which Mo_2C , the more stable form at service temperatures and below, could form at these points. Ultimately during service VC is replaced entirely by the more stable carbide form, which is also coarser, less evenly distributed, and hence detrimental to creep properties. Note that this is completely the reverse of what happens during accelerated creep testing above $690^\circ C$ (Collins, 1978, above) where Mo_2C appears the less stable form and is replaced by VC in time; great doubt must be cast on the representativity of

accelerated temperature testing in these materials.

For non vanadium containing steels of the $2\frac{1}{4}\text{Cr}-1\text{Mo}$ class Williams (1981) found Mo_2C to be the precipitate of most relevance to creep strength. This was observed to coarsen during service, in particular where associated with dislocations. As a result the precipitate structure became much more irregular, as well as coarser, to the detriment of the creep strength.

More detailed work on changes in carbide composition in a $\frac{1}{2}\text{Cr}-\frac{1}{2}\text{Mo}-\frac{1}{4}\text{V}$ type steel² (Carruthers & Collins, 1983) confirmed VC as the primary carbide, but initially containing up to 30 wt% molybdenum (typical levels were around 10 wt%) with a little chromium, manganese and iron in place of some of the vanadium. After exposure at 575°C , the proportion of molybdenum in the alloy carbides had increased; compositions in the range 5–100 wt% vanadium and 0–85 wt% molybdenum were recorded. It is submitted that the variations illustrate local differences in ease of diffusion of Mo to the VC, the process that effects the replacement of V by Mo to form the more stable carbide structure.

Carruthers and Collins also noted the substitution, to some extent, of chromium for iron in Fe_3C , a process which was found to show a significant temperature dependence (chromium content in the cementite had risen to 10 wt% in 125 hours at 625°C but 8000 hours at 575°C was needed for a similar effect). It has been suggested that there is a potential use for chromium concentration in cementite as a method of determining a representative thermal history of the component

To summarize the above we can say the following.

- (i) MC carbides in Cr–Mo–V class steels are replaced by M_2C over a period of exposure at temperatures lower than 600°C .
- (ii) At a greater temperature MC remains the more thermodynamically stable form and is not replaced. Hence experimental results obtained in this temperature regime cannot be reliably extrapolated to service conditions, and

² actual compositions (in wt %) were in the ranges: 0.11–0.13C, 0.26–0.28Si, 0.42–0.52Mn, 0.010–0.011P, 0.55–0.56Mo, 0.35–0.36Cr, 0.03–0.17Ni, 0.12–0.19Ni, 0.010–0.011Sn, 0.25–0.32V.

results obtained which rely on such an extrapolation must be treated with great caution.

- (iii) In Cr–Mo type steels M_2C is the more thermodynamically stable form at both the service and at elevated temperatures so extrapolation of results from higher temperatures to the service temperature is not invalidated in the same way as for the Cr–Mo–V steels.
- (iv) Particle size measurements do not appear to provide an accurate or reliable method of remanent life determination.
- (v) Chemical analysis of both the primary alloy carbides and the cementite may enable improved determination of remanent life, even in the absence of a direct mechanistic relationship to creep damage, by providing a representation of the effective temperatures experienced during service by a particular component (Carruthers & Collins, 1983, for example).

2.5 Cavitation During Creep

It was noted that for low-alloy ferritic steels creep damage accumulation occurs via microstructural degradation (particle coarsening leading to a loss of the optimum precipitate distribution) or void accumulation. For the sake of completion the latter process is considered briefly in this section.

In general, cavitation is the predominant damage mode in low-alloy ferritic steels where the microstructure is coarser grained. A greater susceptibility to this mode of damage accumulation is also exhibited in higher alloy steels and at higher creep strain rates (Dyson, 1976). Thus, in the majority of situations relating to low-alloy ferritic steel steam header bulk material, cavitation can be expected to be of reduced significance (but in isolated positions local variations in material properties and conditions could increase the tendency for cavitation). Formation of cavities is of most relevance in relation to creep damage accumulation in the coarser grained heat affected zone region of welds and weldments within the power station boiler system (Cane & Townsend, 1984).

2.5.1 Initiation of cavities

Cavities may nucleate homogeneously either at the grain boundaries or in the bulk grain due to shear deformation caused by the applied stress. However, it has been proposed (Cane, 1976) that typical low-alloy ferritic steels, where cavitation is the predominant damage mode, will nucleate cavities in a heterogeneous manner on non-wetting grain boundary precipitates. Dislocation pile up at the precipitate caused by localized deformation makes such a precipitate a highly-favoured cavity nucleation site.

Cane (1979), performed work on $2\frac{1}{4}\text{Cr}-1\text{Mo}$ steel³ with a coarse bainitic microstructure achieved by austenitizing at 1300°C for 1 hour and air cooling, followed by 4 hours at 700°C . Cane observed the cavities and found them to be distributed heterogeneously throughout the prior-austenite grain boundaries. They were associated in particular with M_{23}C_6 particles, and found to nucleate in the very early stages of exposure. The quantities present showed relatively little sensitivity to effective mean stress levels for a given strain, but instead appeared to be dependent on the magnitude of the maximum principal stress.

Similar observations of heterogeneous cavity nucleation at grain boundary precipitates (especially alloy carbides) during secondary creep have been made for other steels (*e.g.*, Needham & Gladman, 1980; Dyson, 1976).

2.5.2 Cavity accumulation and growth

Various models have been proposed for the growth of cavities during ageing of these materials. The majority of early analyses used as a basis the diffusional growth concept proposed by Balluffi and Seigle (1957), which involves diffusion of atoms from the cavity surface to other parts of the grain boundary region more favourably orientated to the maximum principal stress. More recent work has exposed limitations in such a model.

Dyson (1976) conjectured that in some circumstances growth by a diffusion mechanism would be constrained by the creep deformation process in polycrystals. He suggested that vacancy diffusion could provide only an upper bound

³ specifically, $\text{Fe}-2.25\text{Cr}-1.0\text{Mo}-0.48\text{Mn}-0.48\text{Si}-0.18\text{Ni}-0.06\text{As}-0.02\text{P}-0.02\text{S}-0.02\text{Sn}-0.11\text{C}$ wt%.

growth rate, with the lower bound being determined by the mean applied shear stress rather than the maximum principal stress. Any constraint is likely to be most marked in higher alloy materials (with high cavitation densities of non-uniform distribution) and at higher strain rates, so is of limited significance in the case of low-alloy ferritic steel steam headers.

In Cane's study (1979, see above) the growth rate was monitored for various maximum principal stresses (σ_1) at constant mean effective stress ($\bar{\sigma}$), and for various σ_1 at constant $\bar{\sigma}$. Cavities were found to grow initially in a spherical manner, but as they became larger ($> 1\mu\text{m}$) growth proceeded by spreading across the grain boundary area and by accumulation of several voids into one larger cavity.

The growth rate appeared to depend more on $\bar{\sigma}$ than σ_1 when circular notch tests were carried out. At low ($< 150\text{ MPa}$) stress the growth rate appeared to be proportional to the creep rate in a uniaxial system. Cane therefore suggests that the diffusional growth model requires considerable modification in order to take account of the tendency for voids to grow along the favourable grain boundary regions, and to cope with the real engineering situation of complex, multiaxial stress systems.

2.6 Ageing Behaviour of Bainitic Cementite

2.6.1 Composition change as an indicator of thermal history

Carruthers and Collins (1983) commented on the possibility of using changes in composition of cementite during service as a route to a more accurate determination of the thermal history of the component in question. Creep resistant steels typically contain bainitic regions (see above, where the typical mixed allotriomorphic ferrite/bainite microstructures in low-alloy ferritic creep resistant steels was discussed). Cementite is also found in a pearlitic region in some of these materials.

Even in those creep resistant steels where pearlitic cementite is observed, it does not seem feasible to extrapolate thermal history from cementite composition for a number of reasons, namely: initial composition lies between

equilibrium and paraequilibrium (figure 2.7), and no sound theory exists to calculate the starting composition exactly; pearlitic cementite composition is frequently found to vary as a function of distance from the austenite/ferrite interface (Chance & Ridley, 1981, *et al.*); and the mean starting composition may show a size dependence. Without a knowledge of the starting composition, no fundamental model could be constructed to chart the approach of the cementite composition to equilibrium during ageing.

Bhadeshia proposes that the lower transformation temperature and higher driving force for cementite formation from carbon-enriched austenite during the bainite transformation, and the consequent negligible redistribution of substitutional alloying elements during the transformation, means that such difficulties as are encountered in pearlite are considerably reduced; therefore, the use of carbide compositional changes to determine thermal histories is a practical option. Although similar problems are encountered for both pearlite and bainitic cementite, in that no rigorous model for predicting θ composition immediately after the transformation exists, the composition change in bainitic cementite during ageing could still be modelled provided the original redistribution of substitutional alloying elements during transformation was sufficiently small to be negligible relative to the composition changes owing to diffusion (as the cementite moves towards an equilibrium composition of substitutionals) occurring over longer time scales.

Experimental evidence that this condition holds for the bainite reaction is provided by Hultgren (1947), who observed that bainitic cementite had a substitutional alloy content only just above that of the material as a whole, and very much less than would be expected for pearlite where appreciable redistribution of substitutional alloying elements does take place. More recent work by Chance and Ridley (1981) confirmed that k_{Cr} (the partition coefficient, wt % Cr in θ / wt % Cr in α_b) was very close to unity (figure 2.7). All the experimental data indicate that there is very much less partitioning during the growth of bainitic cementite than there is during the growth of pearlitic cementite.

During tempering in service the equilibrium composition can be expected

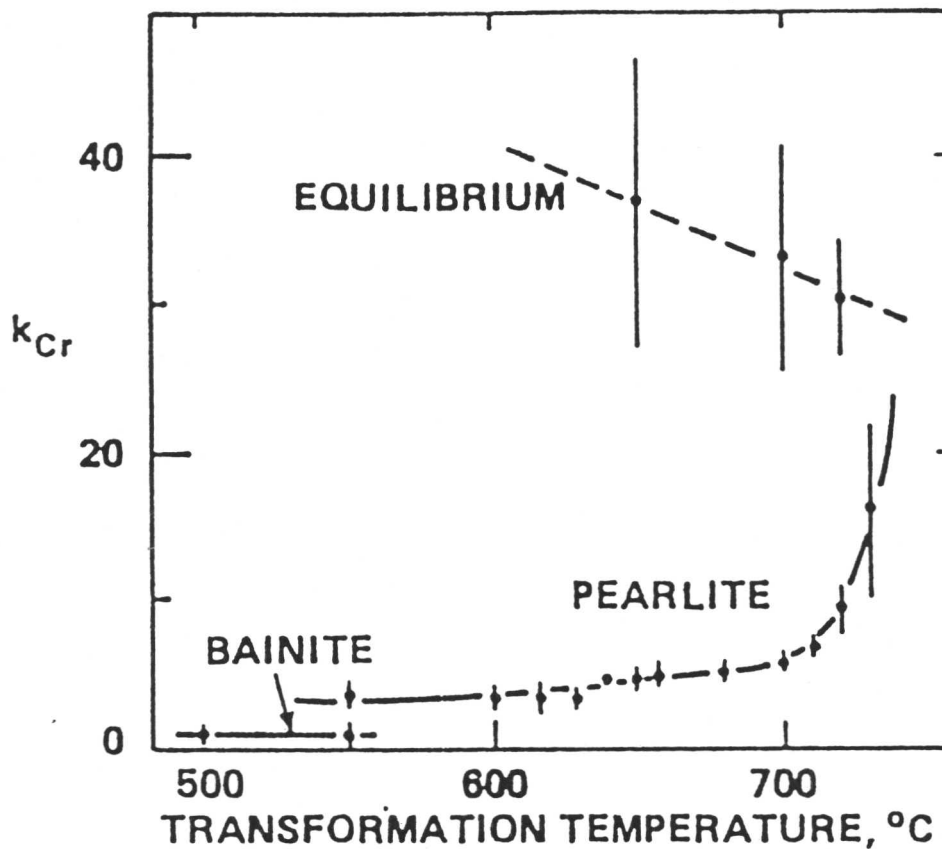
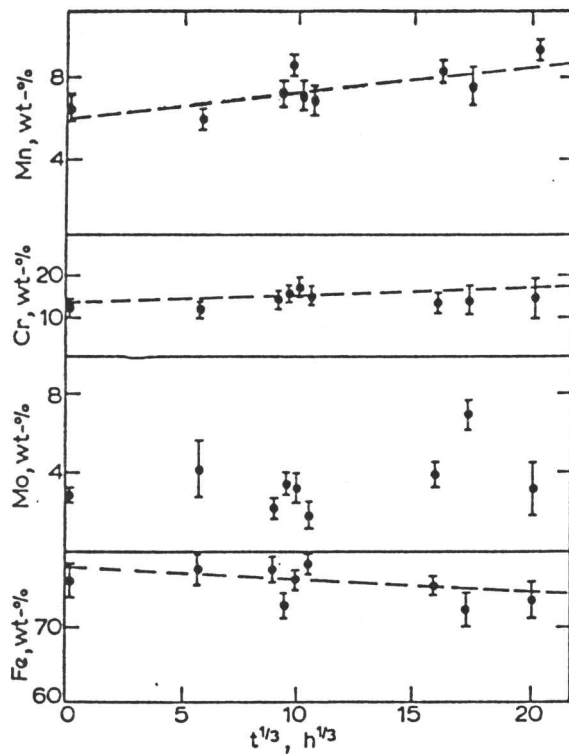


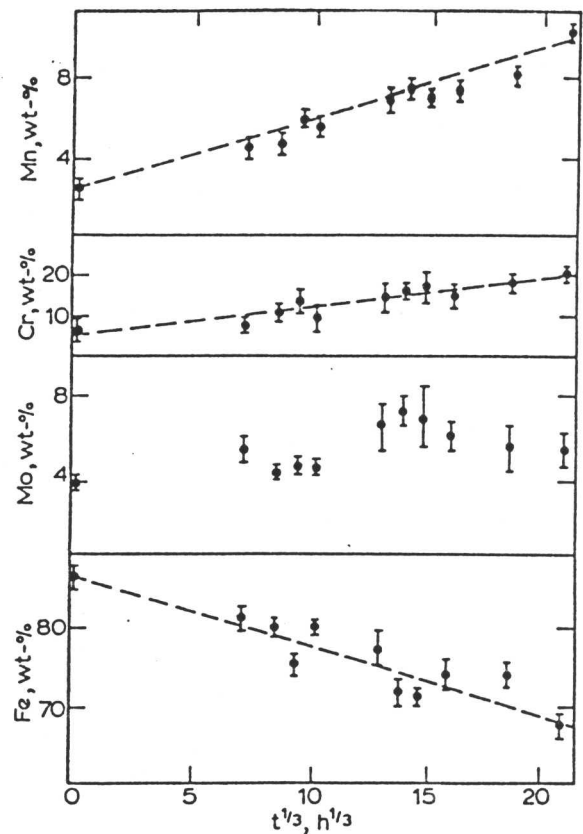
Figure 2.7: Variation of cementite composition with transformation temperature following isothermal transformation (Chance & Ridley, 1981)

to be approached in a manner dependent on initial composition, microstructure and conditions. This approach was applied by Carruthers and Collins (1981) to determine a relationship between cementite composition and ageing time. They found that the chromium and manganese concentrations in pearlitic cementite increased according to an approximately $(\text{time})^{1/3}$ relationship, a relation which tries to model enrichment based upon particle coarsening theory, rather than on diffusion of substitutionals within the ferrite; this condition has not been justified theoretically.

Composition change measurements which appear to be in accordance with a relationship of the $(\text{time})^{1/3}$ type have subsequently been observed for bainitic



partially service exposed



regenerated material

Figure 2.8: Change in substitutional alloying element concentrations in cementite during ageing (Afrouz, Collins & Pilkington, 1983)

cementite using service exposed 1Cr- $\frac{1}{2}$ Mo material⁴ (for 70000 hrs at 565°C) (Afrouz, Collins & Pilkington, 1983). Chromium and manganese concentrations in bainitic M_3C were found to increase in a similar manner to that noted for pearlite, an approximately $t^{1/3}$ relationship (figure 2.8).

It is apparent that the time^{1/3} relationship cannot continue indefinitely, and the composition versus time^{1/3} graph will flatten out as the limiting situation of equilibrium composition is approached. The equilibrium concentrations (in wt %) in ferrite and cementite have been calculated for both the service and the test temperatures for the material used by Afrouz, Collins and Pilkington

⁴ specifically, Fe-0.84Cr-0.48Mo-0.48Mn-0.24Si-0.07Ni-0.04P-0.035S-0.02V-0.11C wt %

(Bhadeshia, 1989), and were found to be:⁵

Element	$\alpha(976\text{K})$	$\theta(976\text{K})$	$\alpha(823\text{K})$	$\theta(823\text{K})$
Cr	0.52	21.3	0.30	36.0
Mo	0.40	5.8	0.34	9.3
Mn	0.38	6.7	0.29	13.2

To summarize, determination of a rigorous model based on the diffusion processes involved during the ageing of these materials could enable cementite compositions to be monitored in order to provide information on thermal history in the manner suggested by Carruthers and Collins, thence generating improved remanent life estimates. A condition of such a procedure, however, is that the time taken for equilibrium concentrations to be approached must be of the same order as component life time (*i.e.*, the composition must be changing throughout the service life of the material).

2.6.2 A theoretical analysis of the composition change

As was noted above, the classical approach has been to relate composition change with the coarsening of cementite during ageing, leading to a predicted variation of composition with time^{1/3}. This relationship has met with limited experimental success in some cases. Nevertheless, it is imperative that an approach based on a consideration of the enrichment of cementite by way of diffusion of substitutional alloying element atoms within the bainitic ferrite be used, if a model of real physical significance is to be developed.

A simple analytical approach, which is limited to the case where no soft impingement occurs in the ferrite, can be obtained by considering a cementite slab in an infinite ferrite matrix (Bhadeshia, 1988). The cementite slab is assumed to have a composition, c^θ , which does not vary with distance from the interface, and the composition of the ferrite, c^α , is assumed to be $c^{\alpha\theta}$ at the

⁵ Note that these are specific to this particular alloy (although it has a composition sufficiently close to that of the material used in this programme that these figures can be taken as an approximate guide to that material also.)

interface and \bar{c} at infinity. If the cementite portion has a thickness x_θ , and t_c is taken to be the time required for that slab to reach a concentration c^θ , then a standard mass balance procedure requires that:

$$0.5x_\theta(c^\theta - \bar{c}) = \int_0^\infty \bar{c} - c^\alpha(x, t_c) dx \quad (2.1)$$

where

$$c^\alpha(x, t_c) = \bar{c} - (\bar{c} - c^{\alpha\theta}) \operatorname{erfc} \left\{ \frac{x}{2\sqrt{D_\alpha t_c}} \right\} \quad (2.2)$$

hence

$$0.5x_\theta(c^\theta - \bar{c}) = (\bar{c} - c^{\alpha\theta}) \int_0^\infty 1 - \operatorname{erf} \left\{ \frac{x}{2\sqrt{D_\alpha t_c}} \right\} dx \quad (2.3)$$

where t_c is the time to reach cementite of concentration c^θ ,

\bar{c} is the mean alloy composition,

x_θ is the cementite particle size,

$c^{\alpha\theta}$ is the composition of α in equilibrium with θ ,

and D_α is the diffusivity in ferrite.

A substitute variable, y , is defined such that

$$y = \frac{x}{2\sqrt{D_\alpha t_c}} \quad dy = \frac{dx}{2\sqrt{D_\alpha t_c}} \quad (2.4)$$

and substituting y in equation (2.3), and redefining the upper limit of the integral in equation (2.3) to be a finite variable, y' , yields equation (2.5)

$$0.5x_\theta(c^\theta - \bar{c}) = 2\sqrt{D_\alpha t_c}(\bar{c} - c^{\alpha\theta}) \int_0^{y'} 1 - \operatorname{erf}\{y\} dy \quad (2.5)$$

But

$$\int_0^{y'} \operatorname{erf}\{y\} dy = \left[y \operatorname{erf}\{y\} - \frac{(1 - e^{-y^2})}{\sqrt{\pi}} \right]_0^{y'} \quad (2.6)$$

hence equation (2.5) becomes

$$0.5x_{\theta}(c^{\theta} - \bar{c}) = 2\sqrt{D_{\alpha}t_c}(\bar{c} - c^{\alpha\theta}) \left[y - y\text{erf}\{y\} + \frac{(1 - e^{-y^2})}{\sqrt{\pi}} \right]_0^{y'} \quad (2.7)$$

Let $y' \rightarrow \infty$; then $\text{erf}\{y'\} \rightarrow 1$, $e^{-y'^2} \rightarrow 0$, and $y' - y'\text{erf}\{y'\} \rightarrow 0$; and equation (2.7) can be simplified to

$$0.5x_{\theta}(c^{\theta} - \bar{c}) = \frac{2\sqrt{D_{\alpha}t_c}(\bar{c} - c^{\alpha\theta})}{\sqrt{\pi}} \quad (2.8)$$

It follows that

$$t_c = \frac{\pi[x_{\theta}(c^{\theta} - \bar{c})]^2}{16D_{\alpha}(\bar{c} - c^{\alpha\theta})^2} \quad (2.9)$$

This gives a working relationship between ageing time and composition for plate-like cementite particles which will remain valid until the onset of soft impingement in ferrite (typically about 8000 hours of service life in power plant materials); that is, the equation will be applicable to the early stages of the ageing process in these materials, especially in respect of the properties of the equation noted below.

- (i) The time taken for the cementite to reach a given concentration varies with the square of particle thickness; or conversely, composition varies with the reciprocal of the square of the particle thickness for different particles aged over a given time.
- (ii) The composition of cementite of a given x_{θ} should vary with $(\text{time})^{1/2}$ rather than the $(\text{time})^{1/3}$ relationship proposed by Afrouz *et al.* (1983). It is noted that the data used by Afrouz *et al.* in fact fits the $(\text{time})^{1/2}$ relationship as well as (if not better than) the $(\text{time})^{1/3}$ relationship (see figure 2.9).
- (iii) The temperature dependence of the process can be attributed mostly to D_{α} , given that $c^{\alpha\theta}$ is a relatively weak function of temperature (and \bar{c} is

constant and x_θ is assumed to be so). Consequently, for experiments carried out over a range of temperatures in a regime where this equation holds (*i.e.*, no soft impingement), a plot of $\ln(t_c)$ vs. $(1/T)$ should give a positive slope of a value corresponding to the activation energy for diffusion divided by the universal gas constant.

- (iv) It has been noted earlier that the amount of bainite in a power plant material can vary considerably, even within a given batch of material. Moreover, it is well established that in general x_θ will increase, and the interparticle separation will decrease as the carbon concentration increases. Thus the difference in cementite distribution and structure in a mostly-bainitic microstructure will be very different to that of a mostly-allotriomorphic ferrite microstructure from the same material. The ferrite forms first, enriching with carbon the retained austenite whence the bainite subsequently forms. As a result the effective carbon concentration in the bainite can vary by an order of magnitude, with a dramatic effect on the microstructure of the bainitic region and hence on its ageing behaviour.

Note that the analysis used to produce equation (2.9) is applicable to a plate-like slab of cementite. Bhadeshia (1989) produces a similar analytical approach for spherical cementite, whence, for a particle of radius a , the solute distribution at a given distance ahead of the particle, s , is given by

$$c^\alpha(s, t_c) = \frac{a(\bar{c} - c^{\alpha\theta})}{(a + s)} \operatorname{erfc}\{s/2(D_\alpha t_c)^{0.5}\} \quad (2.10)$$

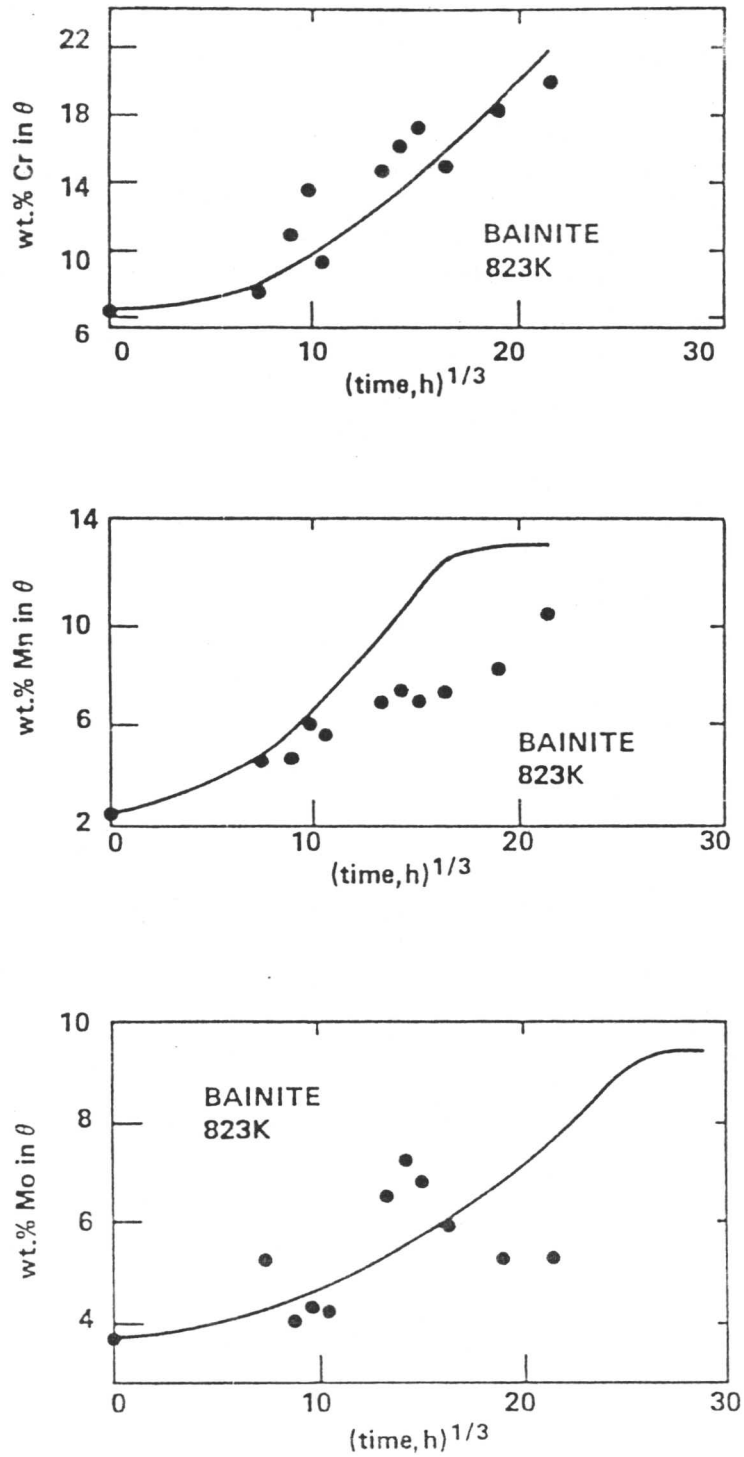


Figure 2.9: A comparison between calculated curves (Bhadeshia, 1989) and experimental data (Afrouz *et al.*, 1983) for the ageing of bainitic cementite in a $1\text{Cr}-\frac{1}{2}\text{Mo}$ type power plant steel

Chapter 3

CHARACTERIZATION OF PRE-SERVICE MICROSTRUCTURE

3.1 Introduction

The objective of this work was to gain a reasonably accurate knowledge of the microstructure of a typical steam header before it had been subjected to service conditions; such a characterization should show the way to a reproduction of such a microstructure by reaustenitizing and transforming back to a mixture of allotriomorphic ferrite and lower bainite. Thence the transformations associated with the production of steam header microstructures could be monitored closely, so as to provide a basis to study the influence of initial transformation conditions and variations in steel composition on the microstructure produced (and hence on the creep properties of the finished artefact). In order to do this it was necessary to characterize the microstructure of the unexposed steam header section as supplied in the as-received condition, and in particular to determine the proportions of the two phases present. Details of the composition of the as-received material, and of the heat treatments used in production of the finished header, can be found in the appendices.

3.2 Optical Metallography

3.2.1 Procedure

Specimens representing both transverse and longitudinal sections of material from the unexposed steam header were prepared. The specimens were mounted in acrylic under hot compression; ground down to 1200 grade emery paper in the first instance; given a final polishing with diamond paste to a minimum of $0.25\mu\text{m}$; and then etched in 2% nital, to bring out the microstructural features. Photography was carried out on an Olympus reflected light microscope using, in most cases, Ilford FP4 (100 ASA) film in the camera and Ilford multigrade paper to produce the positive image (for some of the work at highest magnification a

slower film and high-contrast photographic paper were used in order to improve resolution).

3.2.2 Observed microstructure

Typical micrographs from the transverse section are shown in figures 3.1–3.2, for samples taken from the bore and outer regions of the pipe respectively. Two main microstructural features are apparent: a region of allotriomorphic ferrite, and a region of tempered bainite, containing carbides and ferrite. This is what would have been expected given the heat treatments (appendix).

The ferritic region of these micrographs shows virtually no microscopic detail. This is in accordance with the fact that the intragranular alloy carbide precipitation that accompanies its growth, and which is of such importance to the creep strength and service behaviour of 1Cr– $\frac{1}{2}$ Mo type low-alloy ferritic steel components, is on a very small scale which cannot be resolved optically. The stress relief treatment has not introduced a large degree of coarsening. Some detail in the ferrite was observed occasionally, but it seems quite probable that it was an etching artefact; Rostoker and Dvorak (1977), for example, suggest similar results to the above are attributable to preferential etching in overetched specimens showing segregation of alloying elements to concentrations of dislocations.

One relatively long range feature becomes immediately apparent from an examination of the transverse section micrographs: in the regions nearest to the bore (*i.e.*, the inside surface) of the pipe the microstructure is very strongly banded, that is, the bainitic regions are aligned in rows around the pipe following the circumference. This banding effect is gradually reduced towards the outside of the pipe, becoming indistinguishable at around 15 mm from the bore (distance measured radially), by which point the microstructure ceases to show any degree of alignment with direction. An illustration of the gradual reduction in banding which takes place as the outside of the steam header section is approached is given by figure 3.3.

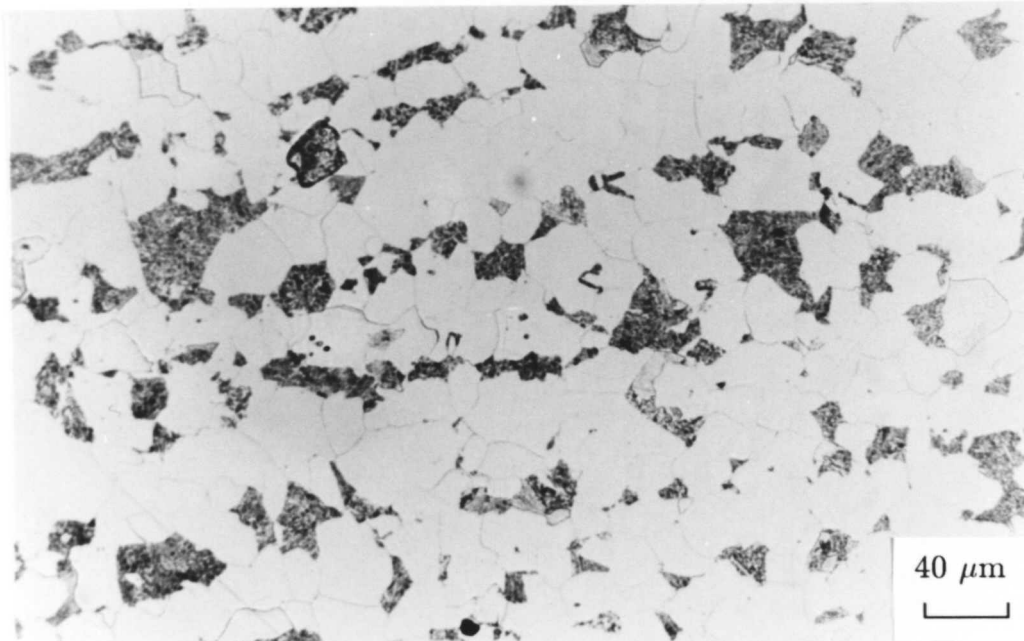
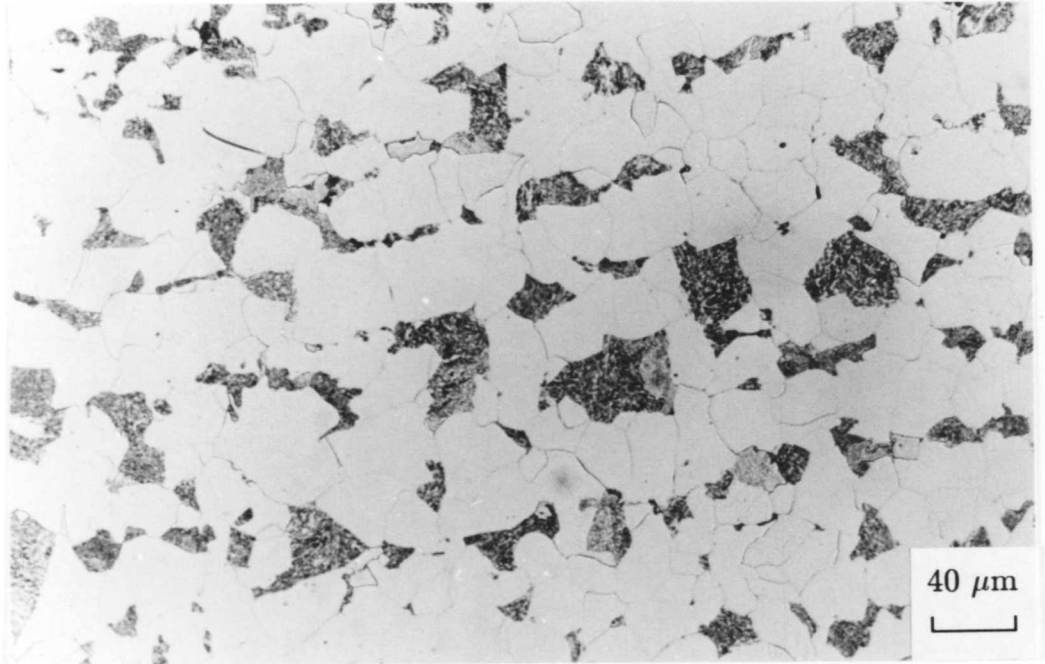


Figure 3.1: Photomicrograph of unexposed steam header material from near to header bore

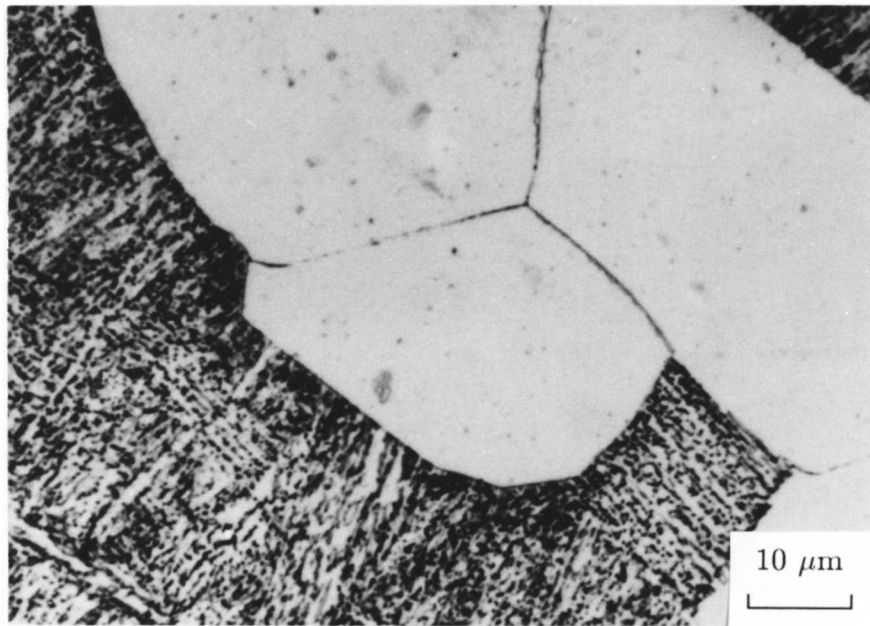
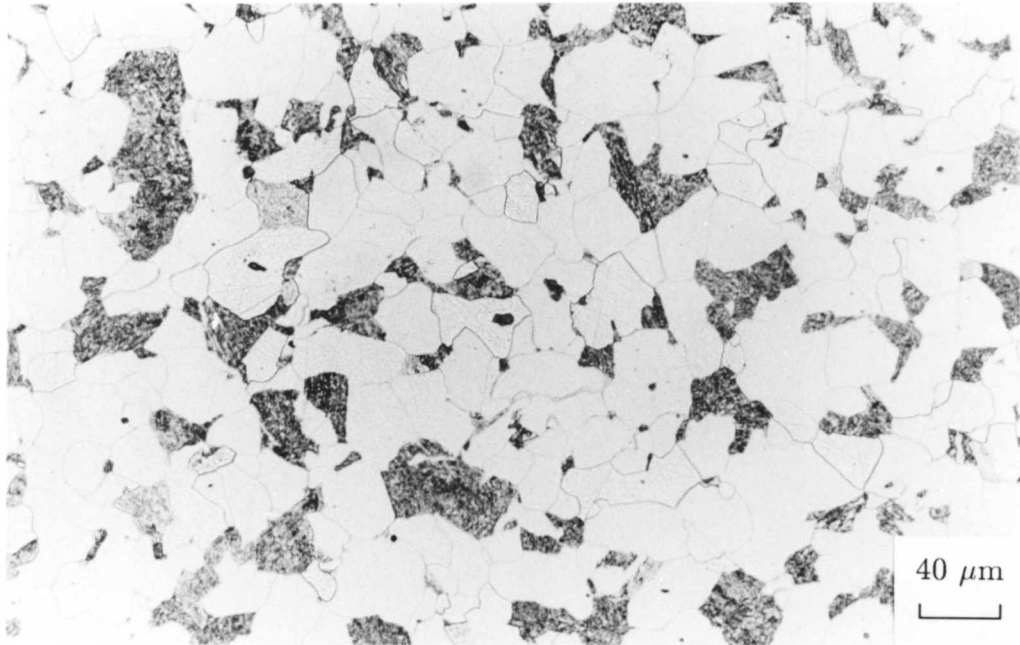
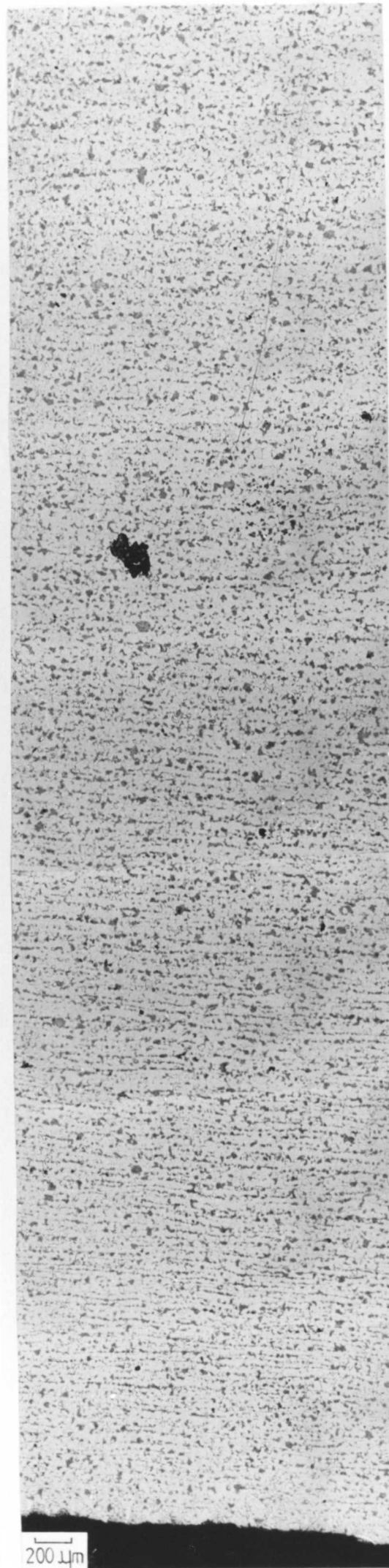


Figure 3.2: Photomicrograph of unexposed steam header material from near to outside surface

Figure 3.3:
Variations in the
microstructure
of the header in
relation to thick-
ness (transverse
section)

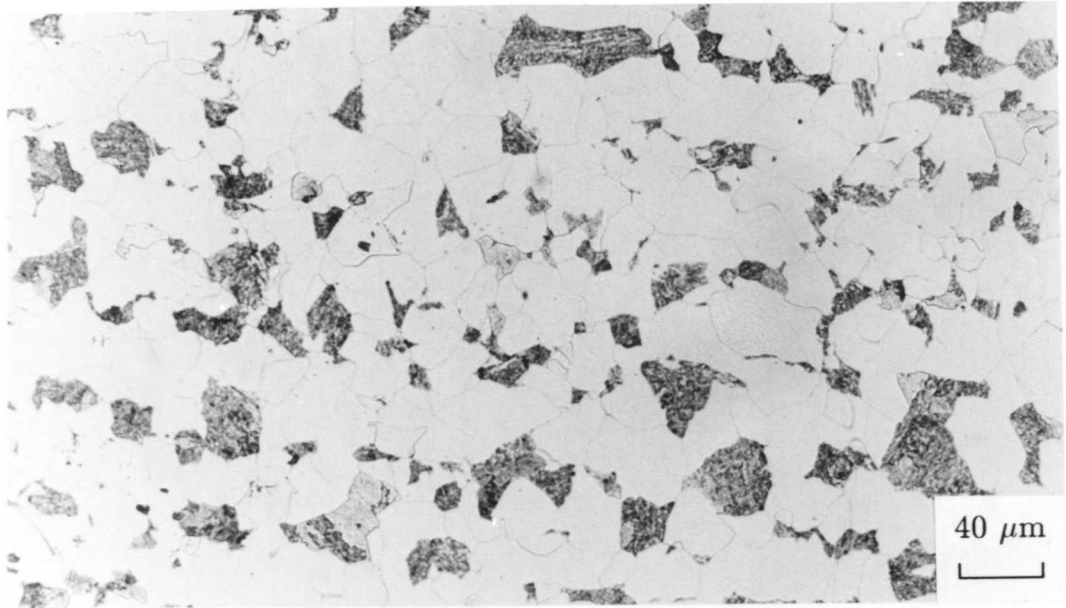


An optical examination of the microstructure alone provides insufficient data to determine with any degree of certainty the cause of the banding effect. Nevertheless, the figure illustrates that the microstructure of steam header material cannot be assumed to be homogeneous. Heterogeneity of microstructure has already been described as a significant cause of error in contemporary remanent life predictive techniques, and it is apparent that a life prediction model for this material which assumed homogeneity of physical properties would produce dubious results, given the observed large scale microstructural differences. Although physical properties, and not mere appearance, govern creep behaviour, the discontinuity of the latter casts doubt on the validity of the conventional assumption of uniformity in the former. The difficulty in quantifying any such heterogeneity, let alone relating it mechanistically to creep behaviour, makes accurate creep life prediction in artefacts with irregular microstructures more difficult.

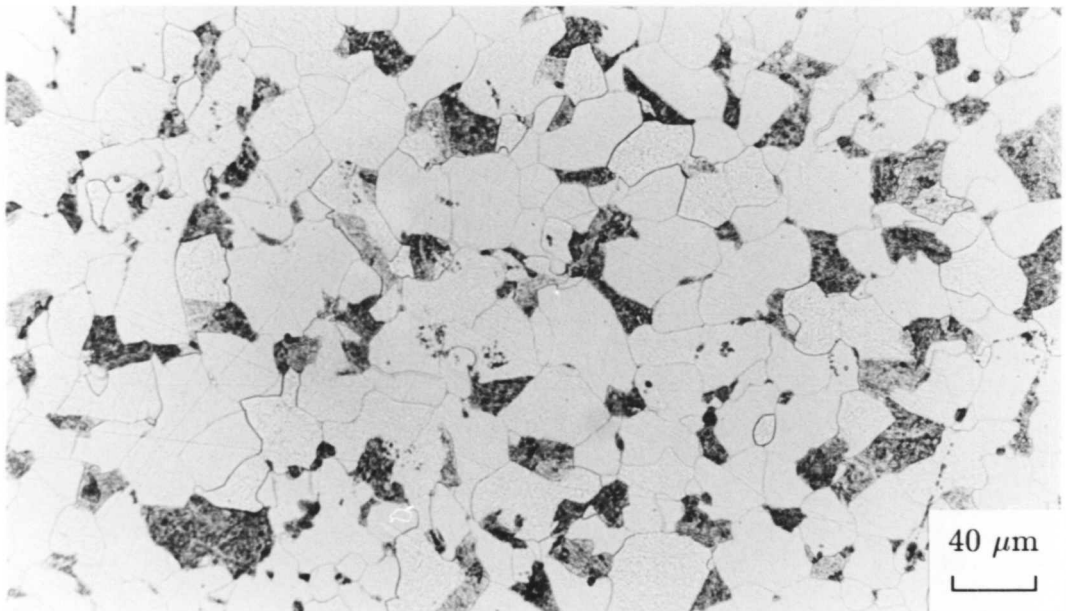
Observations of the specimens prepared from longitudinal sections of the steam header material (*i.e.*, sections cut parallel to the long axis of the pipe) were found to be similar to the observations made from the transverse sections (*i.e.*, mixed ferrite/bainite with some microstructural detail within the ferrite grains which may be suggestive of intragranular carbide precipitation) (figure 3.4).

3.3 Quantitative Metallography

A quantitative representation of the relative proportions of ferrite and bainite was obtained using a point counter. It was necessary to record 700–800 points for each area of the material before results of satisfactory statistical significance could be obtained. In order to obtain a representative sample with the microstructure partially aligned as it is in the bore region of the as-received steam header material, the data were obtained from a number of random specimen orientations. An optical specimen was given the lightest possible etching which still allowed the phases to be distinguished, as the point counting tech-



Near bore



Away from bore

Figure 3.4: Photomicrographs of unexposed steam header in longitudinal section

nique requires that measurements are made on a two dimensional section, and excessive etching so that one phase is significantly in relief would cause this condition to break down.

The microstructure was found to be 25% bainitic in the region near the bore, but with an increased percentage of bainite, 28%, near the edge. Gladman & Woodhead (1960) have shown that the standard deviation, σ_V , of the volume fraction measured by a point counting method, V_v , is given by the following relationship:

$$\left(\frac{\sigma_V}{V_v}\right)^2 = \frac{1 - V_v}{N} \quad (3.1)$$

where N is the total number of readings taken. It follows that the standard error at the 95% level, $2\sigma_V$, is determined by equation (3.2):

$$2\sigma_V = 2V_v \sqrt{\frac{1 - V_v}{N}} \quad (3.2)$$

This produces 95% confidence limits in the measured values for volume fraction of 1.4% for the bore region value and 1.6% for the outer region value; therefore, the measured difference in volume fraction is a statistically-significant feature, and a further indication of long-range microstructural inhomogeneity in the as-received steam header material.

3.4 Hardness Measurements

3.4.1 Microhardness testing

Microhardness measurements were made at different points in the material for both longitudinal and transverse section specimens. Readings for the ferritic and bainitic regions of the as-received microstructure were considered separately.

Testing was carried out on polished specimens given as light an etch as possible (so that the bainite could be distinguished, but without introducing too much surface roughness and other surface artefacts). A Leitz indenter equipped

with an indent measuring digital eyepiece device was used to quantify specimen hardness, connected to an automatic counter/printer to collect the data. The load applied to the indenter was varied to take account of the following factors.

- (i) A large indent size will reduce proportionately the error resulting from inherent inaccuracies in measurement of that size.
- (ii) In order to give a reasonable result there must be no overlap of deformation caused by the indenter into the adjacent phase, across a grain boundary, or with a region deformed by a previous indent (Sargent, 1979a). This places an upper limit on what constitutes a reasonable size of indent, and hence on the load.

In consequence, an applied load of 0.981N was used for the ferritic regions of the microstructure, and 0.2452N for the (somewhat smaller) bainitic regions.

Subtle variations in microhardness with applied load are well documented, even for polycrystalline metal specimens (the so called indentation size effect). In general, the hardness is found to be increased for the smallest applied loads, a phenomenon which can be attributed in part to surface effects, *e.g.*, work hardened surfaces during specimen preparation, oxide and other surface films *etc.*, which are more pronounced for smaller indent sizes; in part to the fact that the dislocation loops associated with smaller indents are more sharply curved and require a correspondingly higher stress to propagate (Buckle, 1973; Sargent, 1979b). As a result the readings obtained for ferritic and bainitic regions are not mutually compatible, and identical loadings for all measurements on the same microstructural feature were used so that a quantization of variation of hardness with distance for a given microstructural feature could be obtained.

3.4.2 Results

The results are illustrated schematically on figure 3.5 for both longitudinal and transverse sections expressed in terms of the distance from the header bore. Between 40 and 60 readings were taken for each point on the figure, and the

point itself represents the mean of those readings, with the scatter bars on figure 3.5 representing standard deviations in those sets of figures.

A definite trend is shown clearly by figure 3.5: the microhardness of the bainitic regions is noticeably higher towards the inside surface of the pipe (the region where banding was observed), whereas the ferritic regions show an increased microhardness towards the outside surface (where the microstructure appeared more random). The standard errors calculated for each set of data indicate that it is reasonable to conclude that sufficient readings have been taken to verify this as a real microstructural effect and not a statistical aberration.

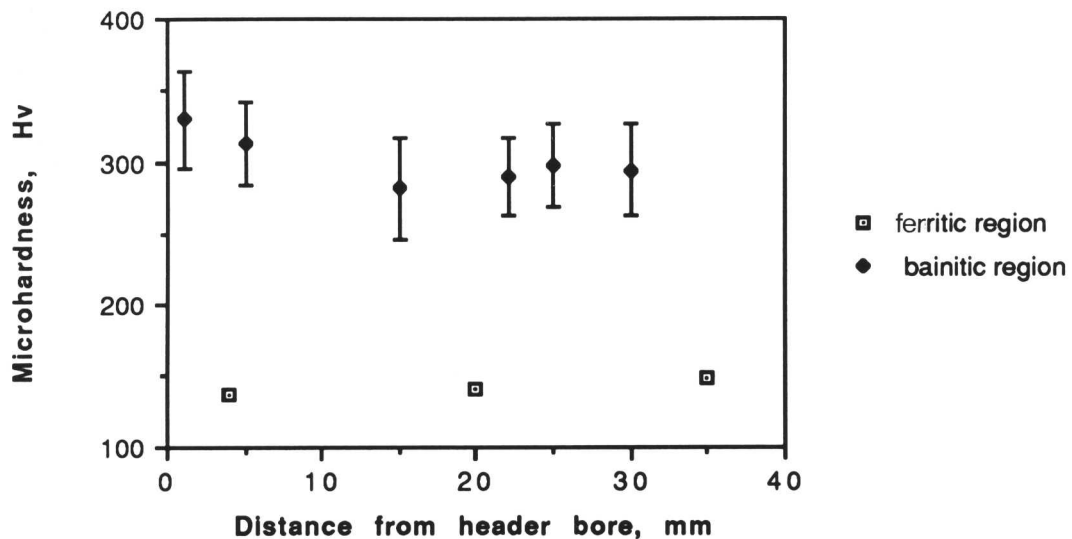


Figure 3.5: Microhardness measurements for the unexposed steam header material

3.4.3 Discussion

A lower microhardness in the ferrite could be attributable to a slower cooling rate during the initial transformation, hence a softer material, in some parts of the specimen. This would be expected to be accompanied by a larger ferrite grain size in these regions, and no such variation was observed. In a material where the ferrite grain size varies so much at adjacent points in the material, it would be very difficult to detect small systematic variations between different areas of the microstructure, so the absence of a detected variation does not definitively prove its absence; however, it is unlikely that such a small difference could be associated with any large effect.

An alternative explanation for the ferritic region could be provided by differences in distribution of carbides within the ferrite: relatively small changes in the structure and distribution of intragranular carbides, which could arise as a result of long-range chemical inhomogeneity in the original cast, would be expected to have a measurable effect on local hardness. However, metallography showed the intragranular carbide precipitates to be of a relatively uniform distribution.

The bainitic region has been shown (Section 3.3) to occupy a smaller volume fraction towards the bore of this piece of steam header than it does towards the outside surface. This would imply that the bainite contained a higher proportion of bainitic Fe_3C , more closely spaced; a microstructure which would be expected to produce a harder bainitic region, and is strongly indicative of a local variation in cooling rate between the two regions. A consideration of the likely transformation processes given the heat treatments to which the steam header had been subjected (appendix) implies that the material will be partially transformed to allotriomorphic ferrite, with bainite forming subsequently during cooling. It is possible to explain the fact that greater evidence of variations in temperature is seen in the bainite on this basis: if there was a variation in temperature during the air cool, a possibility for a component of significant thickness, then the effect on the bainitic region would be pronounced.

Studies of low-alloy ferritic steels in real systems are complicated by the possibility of both thermal variations during transformation and chemical heterogeneity. In the material examined here, the observed microstructural banding effect may well result from segregation effects within the original cast material which promoted aligned nucleation during the subsequent heat treatments, and it has been shown that local thermal and compositional variations in this material can make an appreciable difference to microstructural appearance and physical properties. Both these factors may potentially have contributed to the observed microstructure.

3.5 Energy Dispersive X-ray Analysis

3.5.1 Procedure

Microanalysis of the unexposed steam header material was carried out on a Cambridge Instruments ISI100 scanning electron microscope, which was fitted with a LINK energy dispersive X-ray analysis system. The resulting data were analysed using the LINK microanalysis programme (which includes corrections for fluorescence, atomic number, and absorption effects). A transverse section was taken and mounted in bakelite, which contained particles of graphite so that it would be electrically conducting; polished to $0.25\mu\text{m}$ diamond paste as for optical metallography; and given a very light etch in 2% nital (it was necessary to use an etchant in order to distinguish between ferrite and bainite, but to the minimum level so as to affect chemical composition as little as possible).

3.5.2 Theoretical basis of EDX technique

The EDX system collects and analyses the X-ray emission spectrum produced in the material by de-excitations of near-surface electrons which had been stimulated into an excited state by the scanning electron beam. The overall X-ray emission spectrum for the material is analysed (*e.g.*, figure 3.6), and the proportions of elements present calculated by quantification of the characteristic X-ray peaks for each element present.

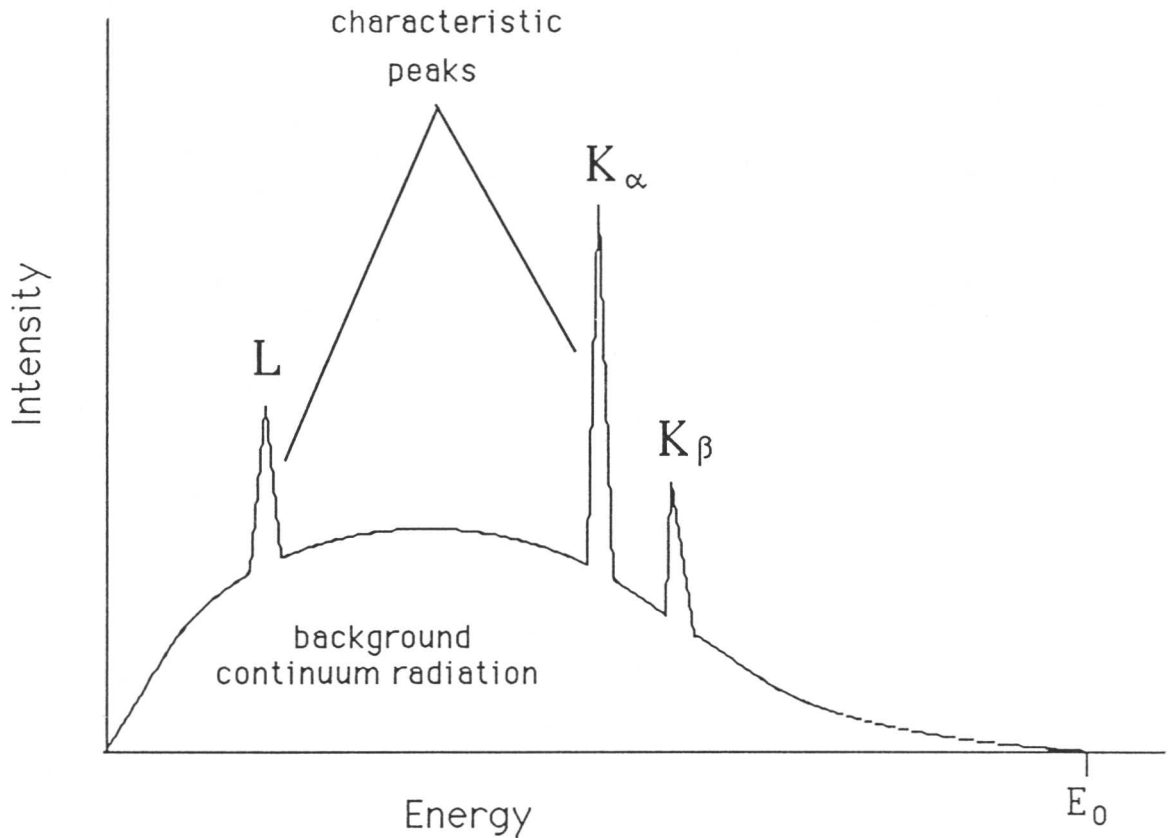


Figure 3.6: Typical X-ray emission spectrum

Note that EDX is not a surface sampling technique as it analyses emissions from a 'pear-shaped' envelope of material (figure 3.7). As a consequence, results must be treated with caution, as it is possible inadvertently to sample data from two different phases if the second phase lies just below the surface. Also, low-atomic-number emissions are absorbed by the system (see the typical spectrum), hence EDX is not a viable technique for detecting carbon, nitrogen, oxygen or hydrogen. (Russ, 1984)

3.5.3 Results

The results are presented in figure 3.8 for both the region near the bore and the region near the outside surface of the material. The spatial resolution can be considered to be approximately $10\mu\text{m}$. Mean values for each set of compositional readings for a particular point in the material were calculated, and are also

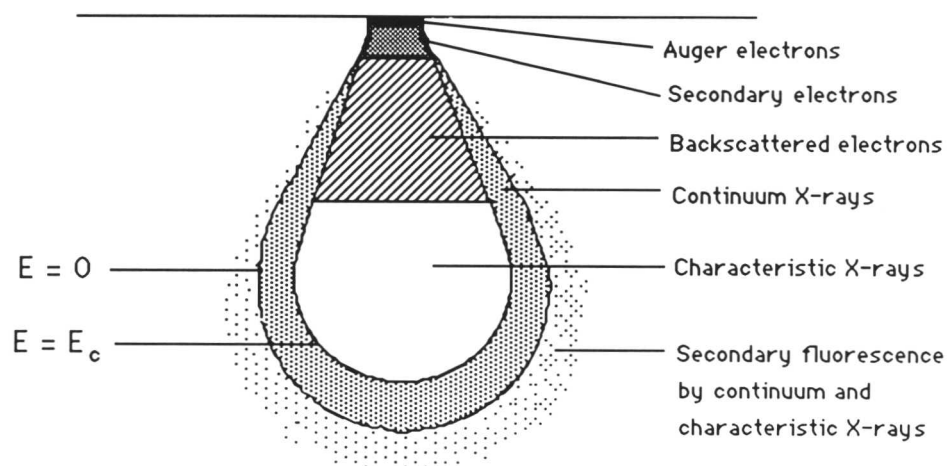


Figure 3.7: Volume sampled by EDX technique

included on figure 3.8 as horizontal lines, with the overall mean alloy composition marked on the y-axis. Standard errors in those means (calculated from the standard deviation) were all in the region ± 0.10 to ± 0.18 wt%.

It had been hoped that differences in composition between the banded and unbanded regions, which might suggest an explanation for the banding effect, would be exposed by this work. However, whilst the results are indicative of some variations in proportion of some alloying elements between ferrite and bainite, it seems impossible to draw any conclusions about small levels of local heterogeneity: the resolution of the technique is not adequate to respond to small composition changes between areas, given the large variations in composition which are apparently observed for different points of the same phase in the same area (probably due to the problems associated with the sampling envelope size mentioned above), and the values of standard error in the calculated means.

AS RECEIVED MATERIAL

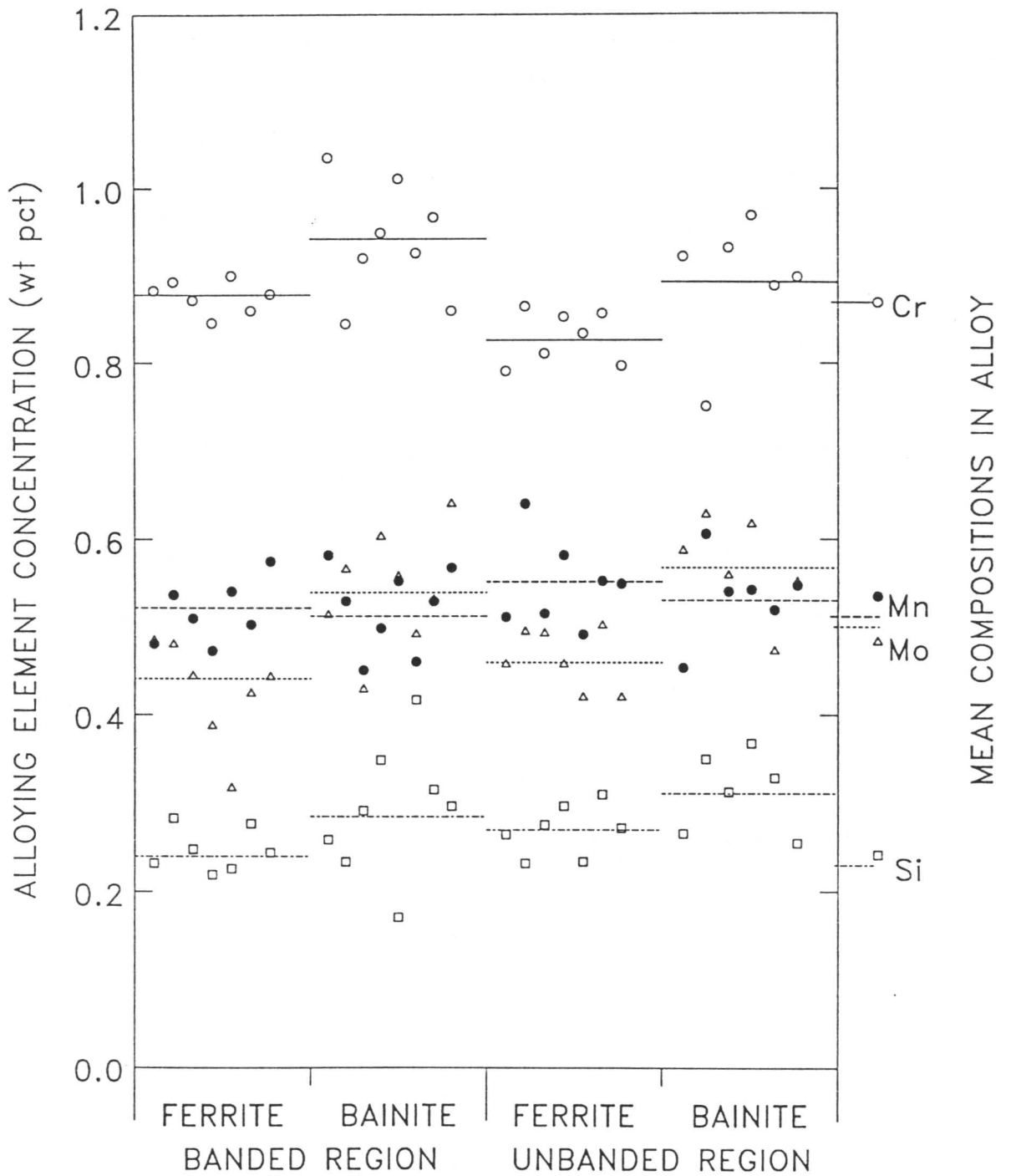


Figure 3.8: EDX compositional data for as-received steam header material

Even so, it is notable that the proportion of some alloying elements (*e.g.*, Cr and Mo) is consistently greater in the bainitic region, although by an amount which is within the error bounds. The regularity of this small variation suggests real difference is being represented, even if resolution is inadequate for the difference to be fully quantified. The EDX data is consistent with the hypothesis that some redistribution of substitutional alloying elements has taken place during ferrite formation at the point of fabrication, from ferrite to retained austenite. Such a redistribution would enrich the retained austenite, and thus the bainite which subsequently formed from the retained austenite would be similarly enriched. The silicon composition is relatively constant; in any case, if a partitioning effect were shown for this element, it would be in the other direction, from austenite to ferrite.

Moreover, the range of readings obtained is much greater for the bainitic than for the ferritic regions, and it is suggested that the larger chromium, manganese and molybdenum composition results were obtained where the volume sampled was mostly bainitic, and that results from apparently bainitic regions which are closer to those obtained from the ferrite arise because the sampled volume included an amount of allotriomorphic ferrite (perhaps just below a carbide region on the surface). This sampling volume problem would tend to mask any small differences which were present.

In conclusion, the EDX technique on the SEM is satisfactory for illustrating general compositional trends in this alloy, but the sampling volume is too large for quantitative data to be obtained on the small scale necessary to analyse compositional variations in individual carbide structures.

3.6 Summary

The microstructure of the pre-service steam header is a mixture of allotriomorphic ferrite and partially-annealed bainite, the bainite making up around 25% by volume. Observations provide evidence of inhomogeneity on both a microscopic and macroscopic scale in the as-received sample, with a suggestion of both chemical inhomogeneities in the original cast and localized temperature

variations during the heat treatments used in fabrication of the steam header section.

These observations are in agreement with much previously published work on the microstructure of low-alloy ferritic steels and the problem of inhomogeneity in steam header material. It is essential that this inhomogeneity is considered, and an attempt made to quantify its rôle in microstructural development during ageing, if an improved remanent creep life prediction model which is applicable to real systems is to be developed.

Chapter 4

MODELLING THE AUSTENITE–FERRITE TRANSFORMATION

4.1 Introduction

Phase diagrams and TTT curves are of considerable value in predicting and understanding phase changes. For this reason, calculations using a model to predict the phase boundaries and transformation start times in low-alloy steels have been performed for the compositions corresponding to those of the supplied power plant material. The procedure was repeated for an Fe–4.08Cr–0.3C (wt. %) alloy, which was used in subsequent experimental work as an alloy to study the model proposed by Bhadeshia (1989) for the ageing of bainitic cementite.

Further calculations for the power plant steel were performed to provide an illustration of the effect of variations in composition (which could arise due to segregation effects) on the TTT curves, and hence the transformation process and products. The existence of some macrosegregation in practice was shown by comparing measured compositions of two specimens taken from a real, service exposed component, both of which came from the same initial cast, but had been found to have slightly different compositions thus illustrating compositional inhomogeneity in a real system. These samples were also of the 1Cr– $\frac{1}{2}$ Mo type steel. (full details of the composition and fabrication of all these steels may be found in Appendix 1.)

The calculated data were compared with an experimentally-determined TTT curve produced by dilatometric work carried out on homogenized and reaustenitized specimens of the power plant material. The microstructures thus generated were prepared for optical examination, and a comparison made between the appearance of the regenerated microstructures and the observations made in the previous chapter of material in the as-received condition.

4.2 Theoretical Calculation of TTT Diagrams

4.2.1 The model

A computer program has been developed to generate TTT diagrams for low-alloy steels containing carbon, silicon, manganese, nickel, molybdenum, chromium and vanadium (Bhadeshia, 1982). It is based on a model to calculate reaction start times for the different austenite-ferrite reaction products at varying transformation temperatures and compositions.

'C'-curves can then be predicted for both reconstructive and displacive reactions as a function of time and temperature with a reasonable degree of accuracy; limitations are imposed because only certain alloying elements are considered, and because the approach is applicable only to low levels of substitutional alloying (typically less than about 7 wt%). The model generates reaction incubation times which are not especially sensitive to grain size, so the results are consistent for varying grain size. Provided the limitations of the low-solute approximations in the model are borne in mind, the calculations made by the program should be able to provide a reasonable quantitative guide to the effect of alloy heterogeneity on transformation rates and products.

The method was essentially developed by fitting experimental values to the general equation of incubation time proposed by Russell (1969), that is

$$\tau_s \propto \frac{T}{(\Delta F_m^v)^p D} \quad (4.1)$$

where τ_s is the incubation time taken to establish a steady nucleation rate,

T is the absolute temperature,

D is the appropriate diffusion coefficient,

ΔF_m^v is the maximum volume free energy for nucleation (and is a function of alloying element concentrations and transformation temperature),

and p is an exponential factor which depends on the nature of the nucleus (Russell showed theoretically that $p = 2$ for a coherent nucleus, $p = 3$ for an incoherent one).

Thus, two C-curves were generated, representing reconstructive and displacive transformation incubation times as a function of time and temperature in the materials under investigation. The method allows the effect of varying alloying element concentrations on τ to be studied in some detail. The TTT curves that were generated from calculations applying this model to the 1Cr- $\frac{1}{2}$ Mo type power plant steel and the Fe-4.08Cr-0.3C wt % model alloy are shown by the continuous lines on figure 4.1 and figure 4.2 respectively.

4.2.2 Long-range segregation of alloying elements

The model may also be used to calculate partition coefficients between liquid and solid, and from these the compositions corresponding to maximum solute depletion during solidification for the four power plant alloy compositions (the unexposed header material, service exposed plugs U3B1 and U4A1, and the base cast composition of the service exposed material). An estimate of the maximum solute enrichment can be obtained by reversing the calculation. TTT curves calculated for these new compositions will provide an illustration of the effect which chemical segregation could have on the transformation behaviour of the material. The calculated maximum solute depleted and maximum solute enriched compositions are presented in table 4.1, and TTT curves corresponding to those compositions for the steam header section are plotted from the computer model and superimposed on that for the original composition (the broken lines on figure 4.1) for comparison purposes.

An examination of table 4.1 also illustrates levels of compositional inhomogeneity which may be observed in practice, as shown by the differences between the measured compositions of the two service exposed plugs, U3B1 and U4A1, which were taken from the same cast. It can be suggested that the very large size of these components leads to a cooling rate during casting which is sufficiently slow to allow some redistribution of alloying elements, and produce inhomogeneity of composition.

Specimen	Compositions (wt.%)							Transformation starts, °C		
	C	Si	Mn	Ni	Mo	Cr	V	B _s	M _s	
<i>steam pipe section</i>	SD	0.12	0.16	0.38	0.00	0.25	0.72	0.00	601	483
	OC	0.12	0.23	0.51	0.00	0.50	0.87	0.00	594	474
	SE	0.12	0.33	0.68	0.00	1.00	1.05	0.00	580	458
<i>U3B1 plug</i>	SD	0.11	0.14	0.32	0.06	0.27	0.74	0.00	604	488
	OC	0.11	0.19	0.43	0.12	0.54	0.89	0.00	594	477
	SE	0.11	0.27	0.52	0.27	1.10	1.08	0.00	578	459
<i>U4A1 plug</i>	SD	0.13	0.16	0.39	0.06	0.26	0.84	0.00	595	475
	OC	0.13	0.22	0.52	0.13	0.53	1.02	0.00	581	461
	SE	0.13	0.31	0.69	0.29	1.06	1.24	0.00	566	442
<i>base header cast</i>	SD	0.13	0.18	0.41	0.07	0.27	0.84	0.00	594	474
	OC	0.13	0.25	0.55	0.14	0.54	1.01	0.00	580	460
	SE	0.13	0.35	0.73	0.31	1.10	1.22	0.00	559	438

OC denotes the base composition of each material, and SD and SE denote results for solute depleted and enriched compositions (for maximum segregation)

Table 4.1: Theoretical analysis of effects of segregation

4.2.3 Discussion

It is hoped that the predicted TTT diagrams will be of value when used together with heat treatment experiments to monitor the transformation as it proceeds, and microanalysis in order to determine the levels of segregation of alloying elements and the effect of this on the resulting development of microstructure.

Although segregation effects on the TTT curves for the power plant material are apparently small the effect on microstructure may be exaggerated. Depending on the cooling processes used, the nature of the transformation products (both which form first and their relative proportions) could change. Segregation is known to be considerable in these materials in practice, both on a microscopic level, and macroscopically with variations in different parts

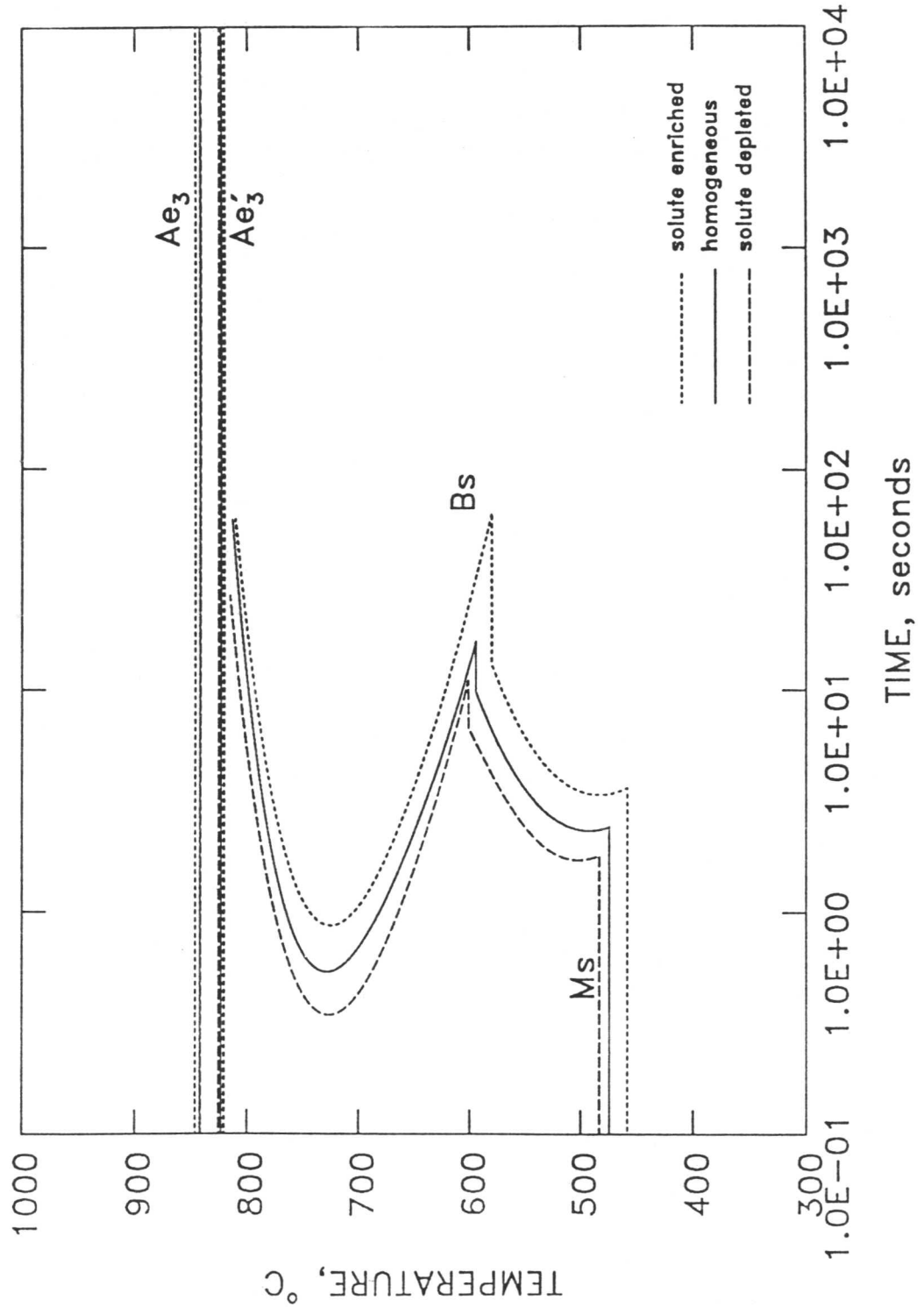


Figure 4.1: Calculated isothermal TTT diagram for the unexposed steam header material

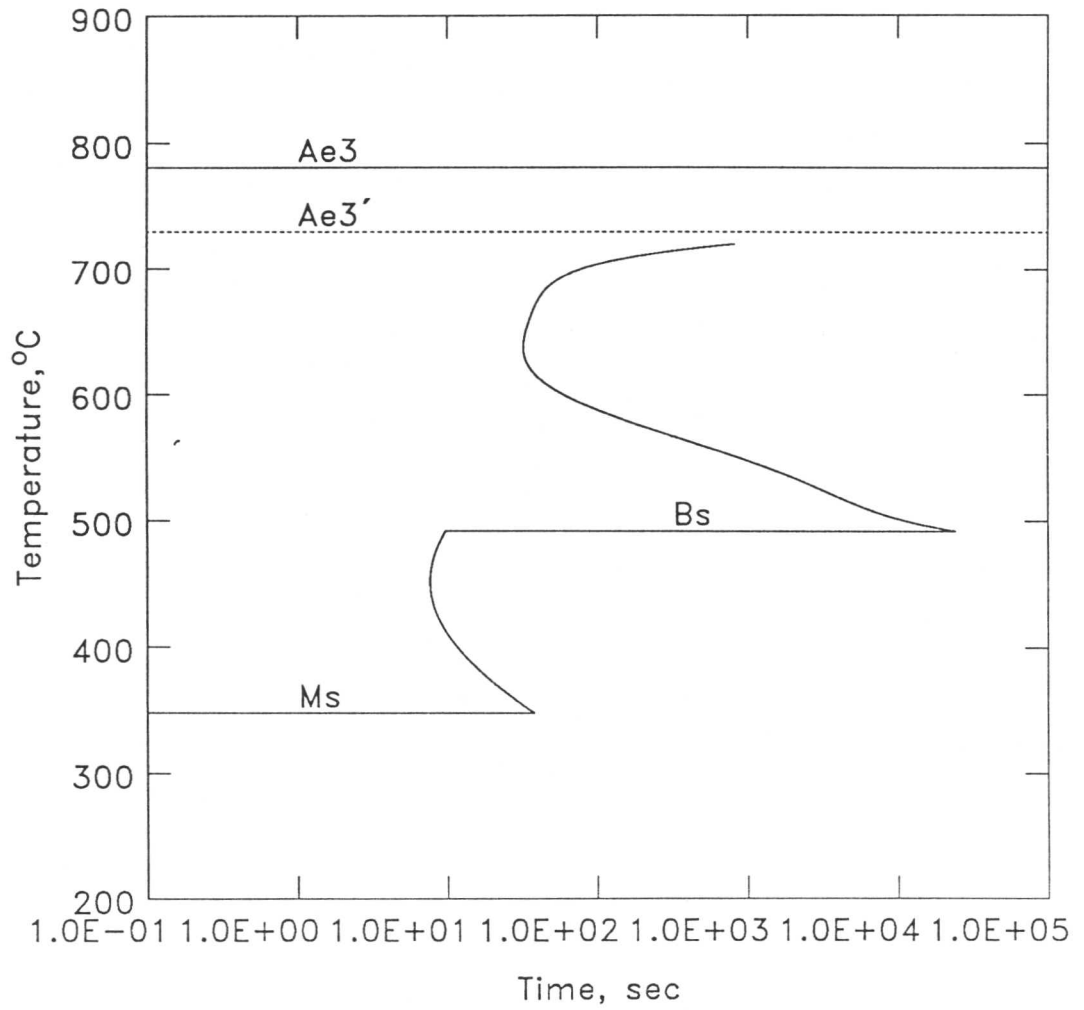


Figure 4.2: Calculated isothermal TTT diagram for the Fe-4.08Cr-0.3C (wt %) model alloy

of a cast ingot (for example, see the differences in composition between U3B1 and U4A1 plugs – both from the same cast – in the appendix). As a result, obtaining an idea (even if only approximate) of the effect of segregation on the transformation in low-alloy ferritic steels of these compositions is of considerable value.

4.3 Calculation of Phase Diagrams

4.3.1 The model

A computer program has been developed based on thermodynamic models proposed by Bhadeshia (1981a). This provides a procedure to enable the T_0 , T'_0 and Ae'_3 curves to be calculated for the alloy compositions under consideration.

T_0 is defined as the temperature at which α and γ of the same composition have the same free energy (Zener, 1946). It lies between the Ae_1 and Ae_3 temperatures which define the limits of the $\alpha + \gamma$ two phase field. Above T_0 ferrite growth can only occur accompanied by a change in composition. Bainite has been observed to form via a displacive mechanism with associated invariant plane strain shape change; the curve for T'_0 is the T_0 curve modified to take account of the 400 Jmol^{-1} strain energy accompanying the IPS. The displacive bainite transformation mechanism implies that no composition change occurs during transformation, which is therefore impossible above this temperature.

Ae'_3 is the equivalent to Ae_3 (the curve representing the boundary between the $\alpha + \gamma/\gamma$ phase fields), but modified to apply to the para-equilibrium situation. This differs from the Ae_3 temperature because for paraE no redistribution of substitutional alloying elements occurs during transformation, and the substitutional atom to iron atom ratio is constant throughout the material.

4.3.2 Calculated results

The T_0 , T'_0 and Ae'_3 curves were calculated for alloying element concentrations corresponding to that in the unexposed steam header material and in the Fe-4.08Cr-0.3C (wt %) model alloy. These are represented graphically in figure 4.3 and 4.4, as a function of carbon content.

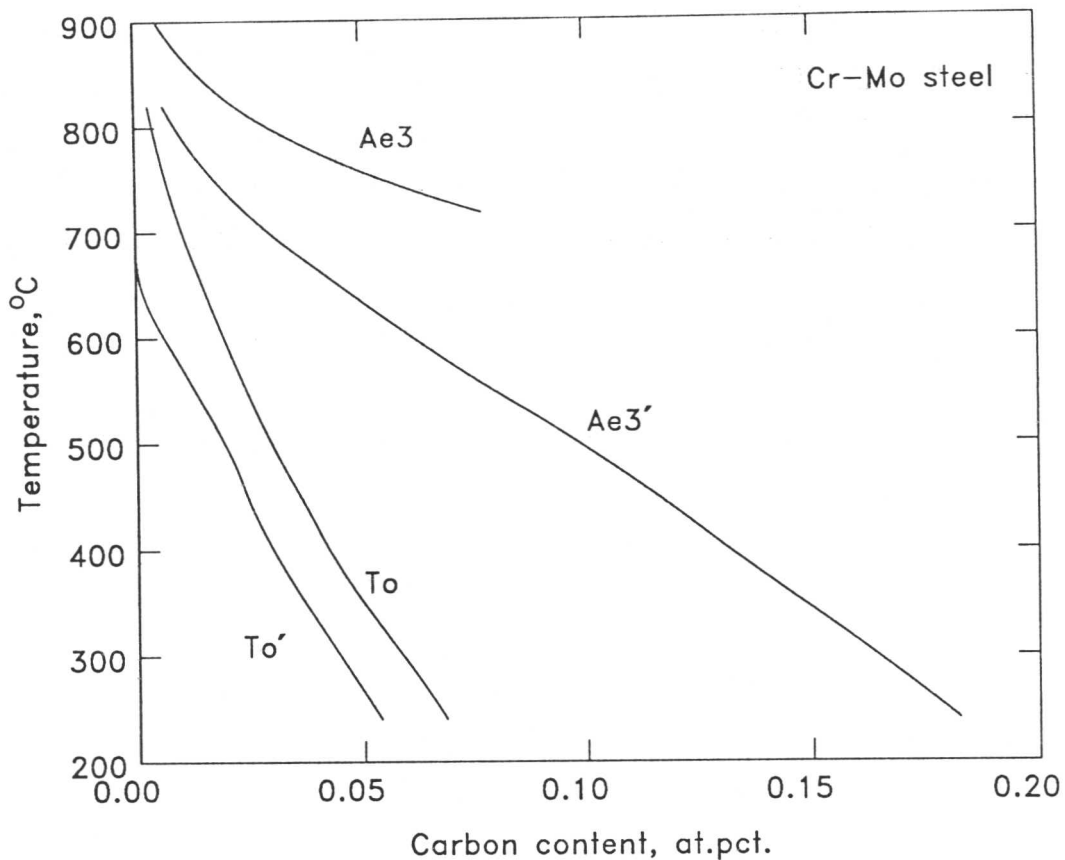


Figure 4.3: Calculated T_0 , T'_0 and Ae'_3 curves for the $1\text{Cr}-\frac{1}{2}\text{Mo}$ as-received power plant material

4.4 Heat Treatments on Steam Header Section

4.4.1 Aims of experimental work

It was the intention of this work to try to recreate the microstructure of a pre-service steam header material (based as closely as possible on the observations discussed earlier which were made of specimens from the actual pre-service material) by repeating the heat treatments used in fabrication on regenerated material. The procedure was designed to enable all the austenite-ferrite transformation processes in this alloy to be studied in some detail, and thus give a sound basis on which to determine the heat treatments necessary to reproduce the starting microstructure and conduct subsequent microstructural assessment when the material was aged to model service conditions.

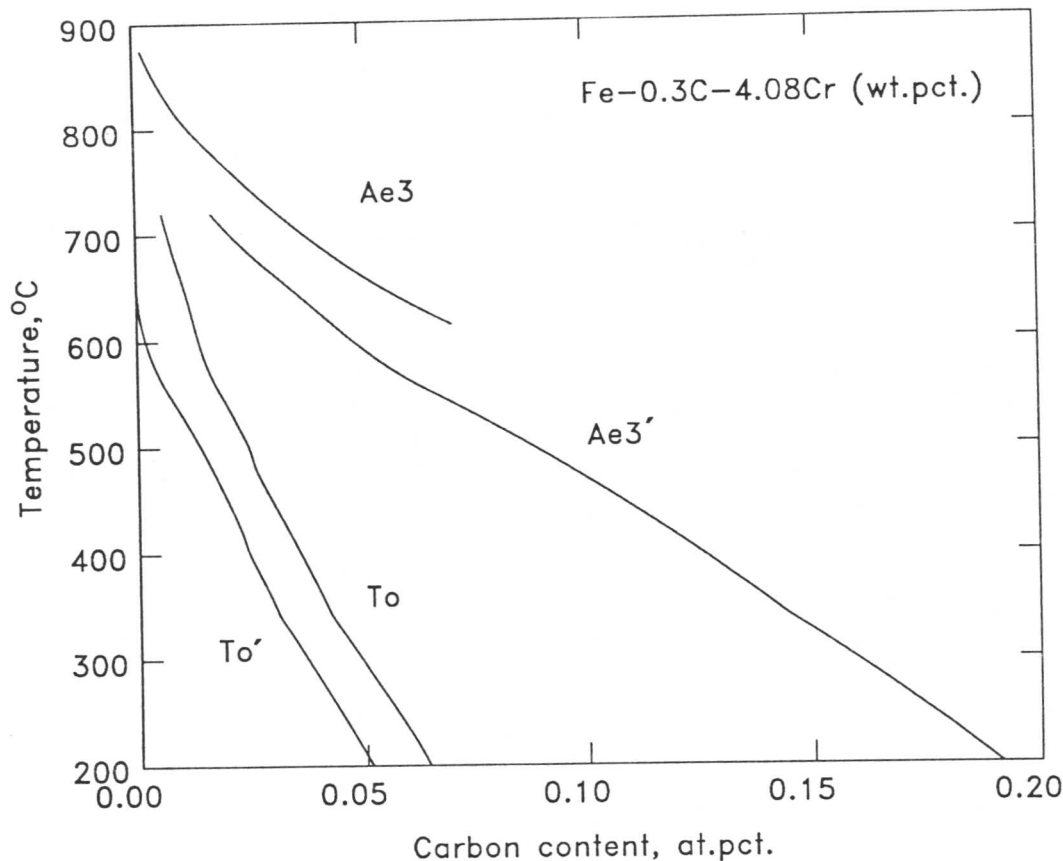


Figure 4.4: Calculated T_0 , T'_0 and Ae'_3 curves for the Fe-4.08Cr-0.3C (wt %) alloy

To this end a large number of 3mm diameter rods were machined from the steam header section. These rods were sealed in a quartz tube, which had been evacuated and had a partial pressure of argon (160 mm Hg) inserted to prevent the loss of carbon from the surface due to vaporization; homogenized by heating in a tube furnace at a temperature of 1250°C for 3 days; and then air cooled, still inside the sealed tubes to prevent environmental attack on the surface during cooling.

It was the intention of the procedure to model thick-section material using a 3 mm diameter rod, so it was essential that any surface nucleation effects should be kept to a minimum if the results were to be at all representative. (In a steam header the low surface to volume ratio renders surface effects negligible, whereas for small rods they could be significant.) As a result all specimens were nickel

plated before heat treatment. The treatment involved two processes: an initial striking and subsequent plating. The striking solution consisted of 250g NiSO₄ and 27ml of conc. H₂SO₄ made up to 1 litre by addition of the appropriate quantity of distilled water. Striking was carried out for 3 minutes at 50°C and a current density of 775mAcm⁻². The plating solution was 140g NiSO₄, 140g Na₂SO₄, 15g ammonium chloride and 20g boric acid made up to 1 litre in distilled water. Plating was carried out for 15 minutes at 50°C and a current density of 40mAcm⁻².

4.4.2 High-speed dilatometer

This machine was used to carry out the austenitizations and transformations back to ferrite on the homogenized steam header material. It operates by measuring and recording the length change which takes place in the specimen under test as the temperature is varied. This allows the transformation to be monitored, by recording the volume expansion that takes place as austenite is transformed to ferrite.

The set up of the dilatometer is illustrated schematically in figure 4.5. The specimen is fixed between two quartz tubes, one of which is static, and the other free to move as the specimen expands or contracts; the latter tube is attached to a linear transducer, which enables length change to be recorded. Heating is achieved by use of an RF induction coil which enables quite rapid heating rates to be obtained. The specimen is enclosed in another quartz tube to prevent contact with the coil, and also to act as a safety barrier in the event of an equipment malfunction causing the specimen to melt. The surface temperature of the specimen is monitored by means of a Pt Pt-10wt%Rh thermocouple which is spot welded to the surface near the centre of the specimen length. The specimens are sufficiently small that it is reasonable to assume that the temperature is uniform throughout at the heating and cooling rates that the dilatometer produces. Helium is used to increase the cooling rate, by providing an inert quenching fluid should it be required; it may also be used to provide an inert atmosphere if a high vacuum is not desirable.

The procedure used to operate the dilatometer was as follows:

- (i) Before use the dilatometer transducer had been calibrated using a platinum specimen of accurately known thermal expansivity, so that data produced by the transducer for the steel specimens could be converted to accurate length change values.
- (ii) The specimen was set up as in figure 4.5.
- (iii) The transducer was 'tuned' by use of the attached micrometer (see figure 4.5) so that a suitable magnification for the chart recorder could be set, and temperature and length change pens on the chart recorder were zeroed.
- (iv) After pumping down to a good vacuum the specimen was raised to the austenitizing temperature and held there for a set austenitization period. Cooling was effected either by using a 'data-trak' program drum (for continuous cooling) or by quenching using the helium flux until the desired temperature was reached, and then holding at temperature (for isothermal transformation).

4.4.3 Heat treatments

Homogenized and nickel-plated specimens were given heat treatments over a range of temperatures and time scales. All of the specimens for isothermal transformation were first austenitized for 10 minutes at 1100°C, then quenched to the required isothermal temperature using the helium flux. Isothermal transformation temperatures were in the range 750°C to 450°C, allowing all transformation products from allotriomorphic ferrite to martensite to be produced, and transformation times were in the range 30 minutes to 2 hours. After completion of the desired transformation time, the material was allowed to cool by switching off the RF coil (note that for such small specimens this amounted to a fairly rapid quench). The dilatometer apparatus enabled readings for temperature and length (which could be converted to relative length change using the length at ambient temperature) to be taken at suitable time intervals. These data were collected directly onto computer disc for subsequent processing.

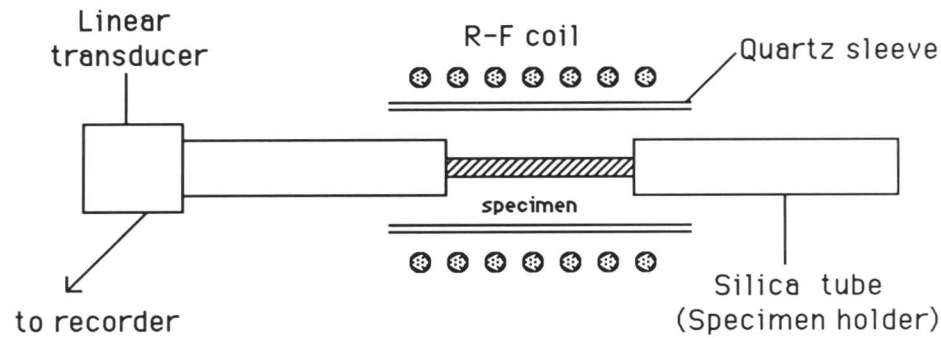
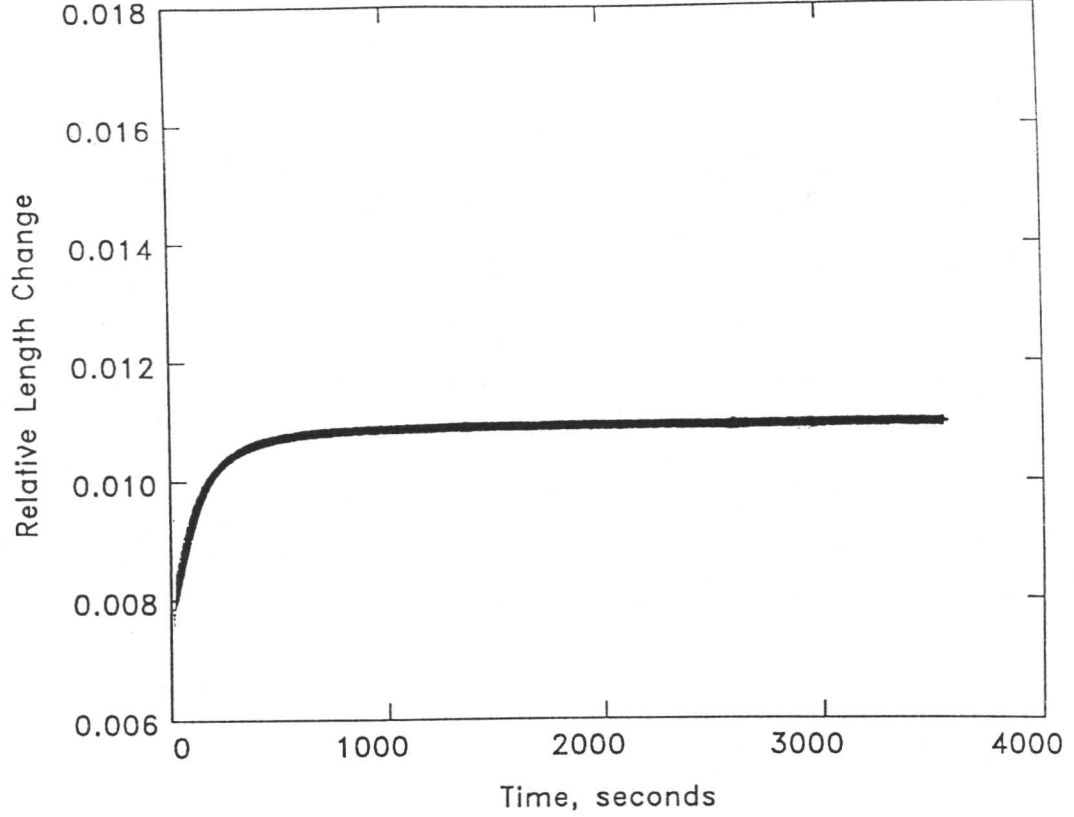


Figure 4.5: Dilatometer arrangement

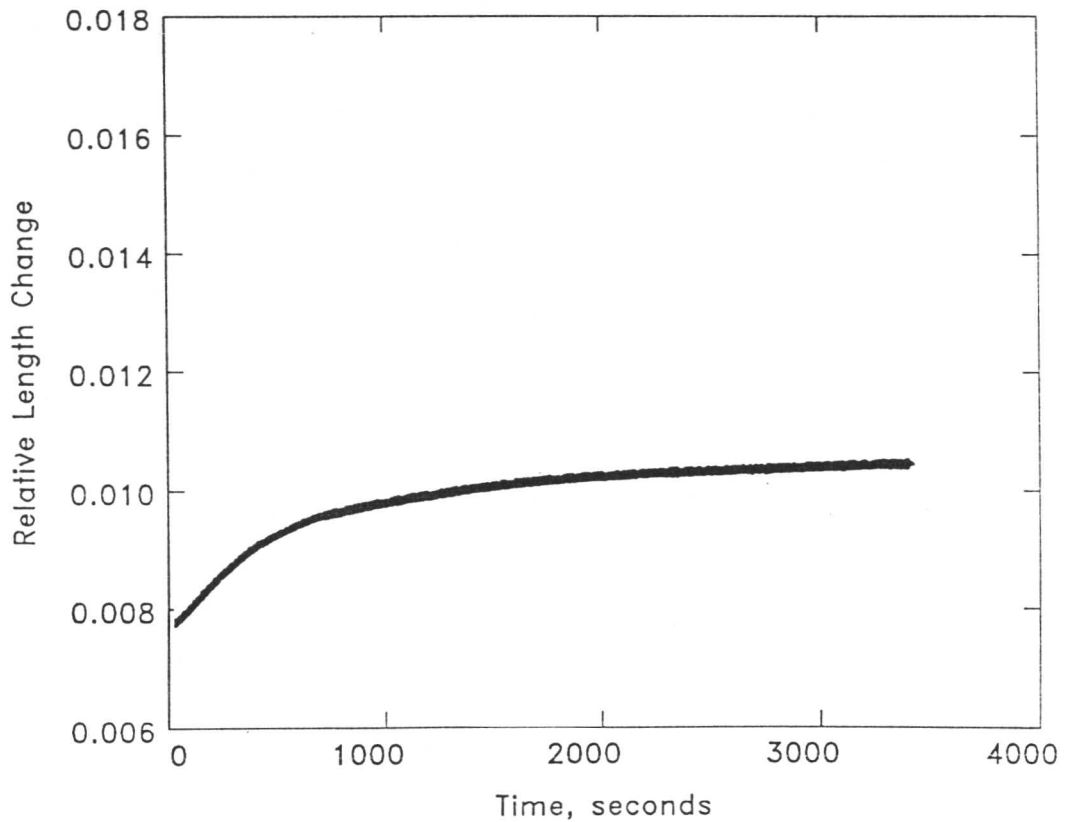
4.5 Results of Dilatometric Experiments

4.5.1 Processing of dilatometric data

Graphs illustrating the observed length change during the course of the transformation were obtained from the recorded data. The lower density of the ferritic structures compared with austenite manifests itself in a length extension as the transformation proceeds, and can be detected by the transducer. Typical examples of such plots are given in figure 4.6, each data point having been collected at one second intervals in all four cases. The data were processed to determine the transformation start time and the volume fraction transformed at a given temperature; the latter was determined both by direct measurement using a point counting technique, and by calculation from dilatometric length change data. These calculations are discussed in detail below, and the processed dilatometric data are presented in table 4.2. The rapid progress of the martensitic transformation compared to transformations above M_s is clearly illustrated by figure 4.6(d).

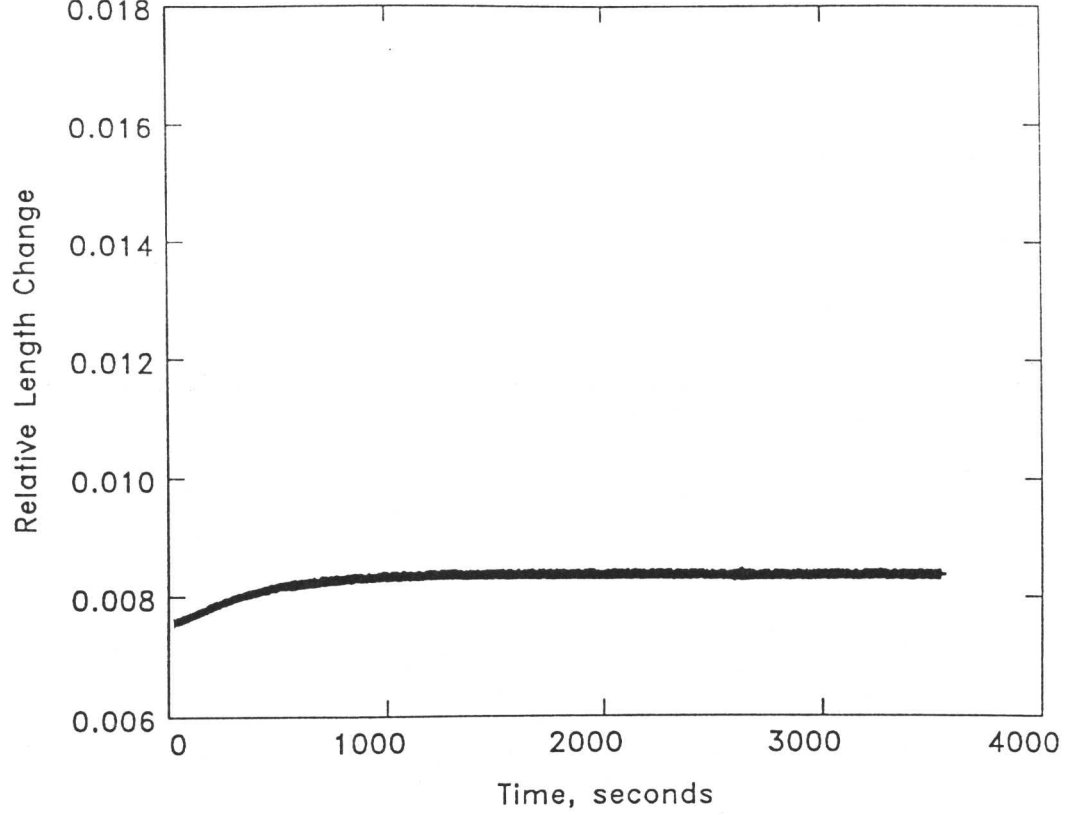


(a) 1 hour @ 735°C

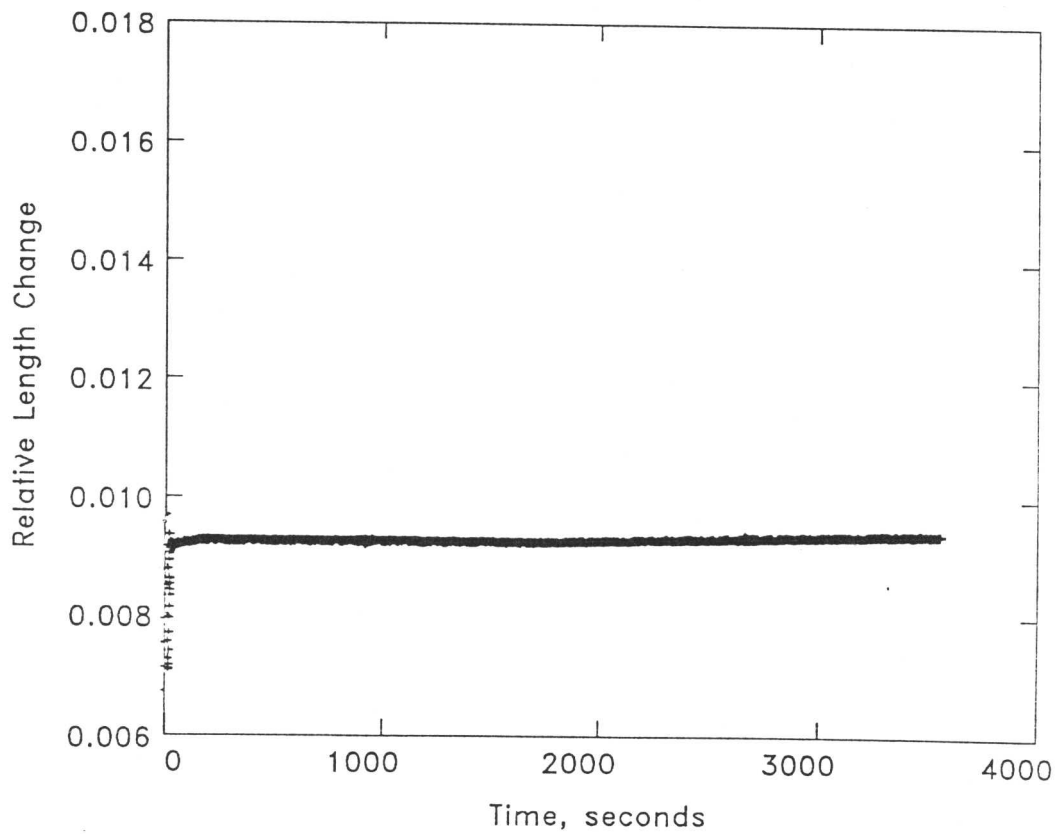


(b) 1 hour @ 647°C

Figure 4.6: Typical dilatometric relative length change vs time plots for isothermal heat treatments carried out on the 1Cr- $\frac{1}{2}$ Mo power plant steel



(c) 1 hour @ 547°C



(d) 1 hour @ 453°C

Figure 4.6: Typical dilatometric relative length change vs time plots for isothermal heat treatments carried out on the 1Cr- $\frac{1}{2}$ Mo power plant steel

4.5.2 Transformation incubation times

It was possible to extract the data points applying to the early stages of each experimental run and plot graphs of length *versus* time for these limited periods. From such plots the time taken for the reaction to commence (the point at which the length began to increase at constant temperature) could be determined with reasonable accuracy. A temperature vs. time plot of the same period was also required in order to ascertain the time which elapsed during the experimental run before the desired isothermal temperature was reached; this must be subtracted from the total time to give a correct incubation time for that particular transformation temperature. The procedure is illustrated in figure 4.7. Note that the difficulty in determining exactly the point at which a length change at constant temperature (*i.e.*, a transformation from austenite to ferrite) first occurred can be considered to introduce an error of the order of several seconds to the tabulated incubation times. Those dilatometry runs in which no discernible period of time elapsed at the transformation temperature before a length change was observed (*i.e.*, the transformation start was, within the limits imposed by the technique, effectively instantaneous) are denoted on table 4.2 by ** in the incubation time column.

4.5.3 Determination of expansion coefficients

In order to translate relative length changes to volume fraction of transformed product it is necessary to determine the thermal expansion coefficients of both parent (austenite) and product (ferrite) phases, denoted by e_γ and e_α respectively. This was achieved by performing a continuous cooling dilatometry run for both ferritic and austenitic examples of the homogenized steam header material. The ferritic specimen was held for two hours at 800°C to try to ensure that it was fully spherodized.

The situation is complicated by the fact that the thermal expansion coefficient for ferrite in low-alloy steel materials are known to show an appreciable temperature dependence (Coleman & Rowley, 1973). Typical examples of this non-linearity in thermal expansion as observed in materials commonly used in

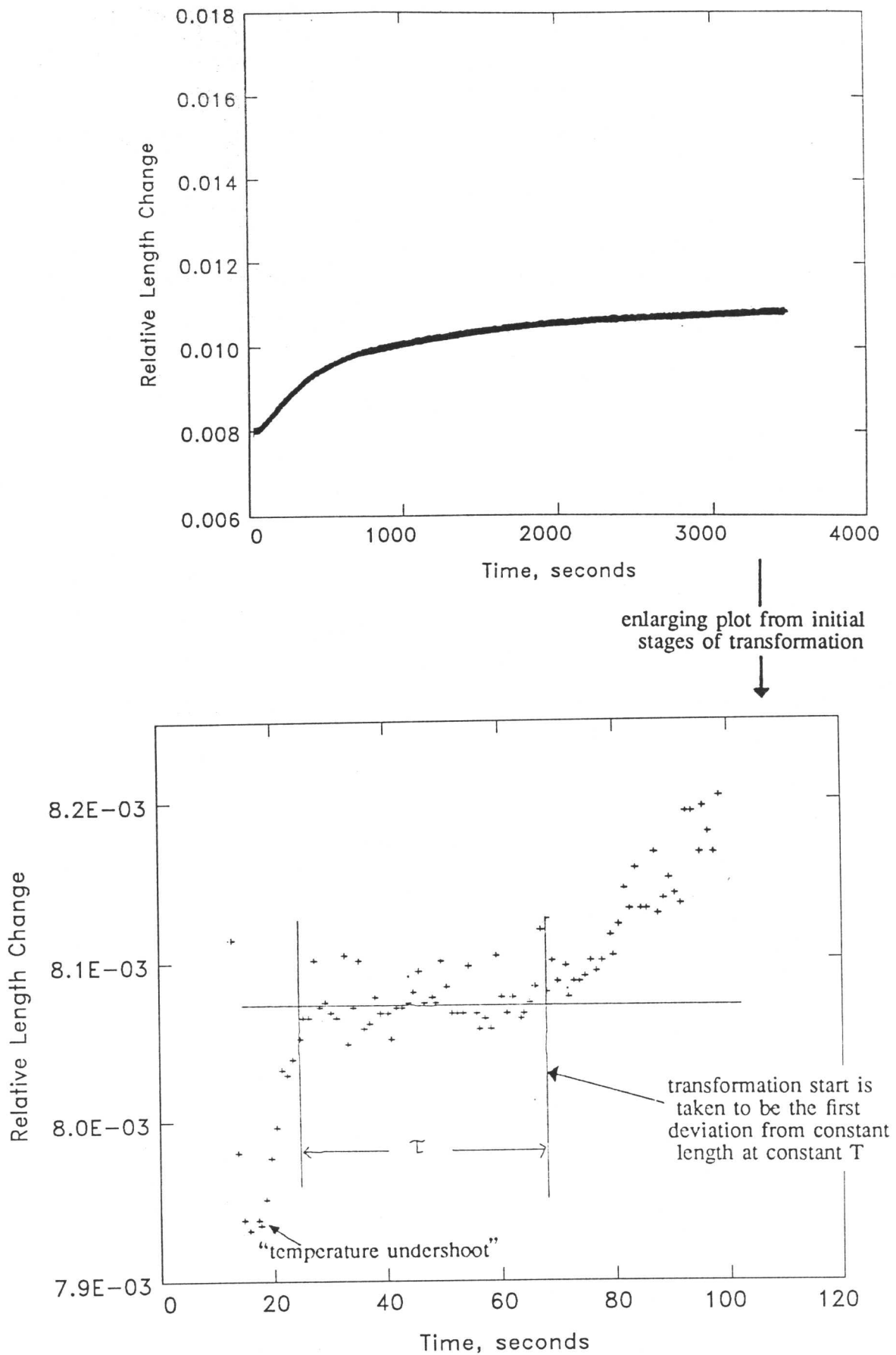


Figure 4.7: Determining transformation incubation times from dilatometric data

T_{iso}	t_{iso}	cooling time	τ	volume fraction of transformed region	
				measured	calculated
770°C	1 hr	15°C	85s	0.65	0.57
751°C	1 hr	15°C	30s	0.60	0.57
735°C	1 hr	12°C	10s	0.78	0.72
722°C	1 hr	11°C	4s	0.63	0.79
715°C	1 hr	10°C	**	0.80	0.85
703°C	1 hr	10°C	**	0.74	0.85
698°C	1 hr	20°C	3s	0.82	0.78
676°C	1 hr	10°C	3s	0.82	0.86
674°C	1 hr	12°C	13s	0.72	0.79
669°C	1 hr	20°C	5s	0.81	0.84
647°C	1 hr	12°C	30s	0.79	0.84
622°C	1 hr	8°C	16s	0.60	0.52
610°C	1 hr	8°C	12s	0.60	0.57
591°C	1 hr	12°C	22s	0.60	0.53
576°C	1 hr	15°C	70s	-	0.15
555°C	1 hr	6°C	20s	-	0.12
542°C	1 hr	10°C	36s	-	0.24
525°C	1 hr	8°C	12s	-	0.25
510°C	1 hr	12°C	7s	-	0.25
499°C	1 hr	15°C	15s	-	0.31
475°C	1 hr	5°C	**	all martensite	
453°C	1 hr	8°C	**	all martensite	
740°C	30 mins	12°C	3s	0.78	0.75
734°C	30 mins	15°C	9s	0.79	0.82
720°C	30 mins	15°C	**	0.82	0.79
703°C	30 mins	7°C	**	0.85	0.93
680°C	30 mins	12°C	2s	0.73	0.86
661°C	30 mins	10°C	25s	0.60	0.57
630°C	30 mins	12°C	18s	0.50	0.42
606°C	30 mins	10°C	80s	0.48	0.53
580°C	30 mins	12°C	44s	0.48	0.42
530°C	30 mins	15°C	12s	-	0.15
730°C	2 hrs	8°C	28s	0.88	0.92
693°C	2 hrs	10°C	**	0.90	0.93
640°C	2 hrs	7°C	15s	0.88	0.85
621°C	2 hrs	12°C	19s	0.72	0.88

Table 4.2: Dilatometric data produced for the 1Cr- $\frac{1}{2}$ Mo power plant steel during isothermal austenite-ferrite heat treatments

power plant construction are shown in table 4.3 and represented as a function of the temperature range on figure 4.8 (Darbyshire & Knight, 1977).

Temperature Interval °C	25 to 100	25 to 200	25 to 300	25 to 400	25 to 500	25 to 600	25 to 700
$\frac{1}{2}\text{Cr}\frac{1}{2}\text{Mo}\frac{1}{4}\text{V}$	12.02	12.55	13.20	13.80	14.36	14.90	15.31
$2\frac{1}{4}\text{Cr}1\text{Mo}$	11.75	12.21	12.77	13.30	13.81	14.31	14.73
$1\text{Cr}\frac{1}{2}\text{Mo}$	12.02	12.26	12.88	13.46	14.04	14.57	14.99
Mild Steel	12.22	12.78	13.39	13.94	14.49	15.05	15.47

Table 4.3: Mean coefficient of linear thermal expansion (in $\text{K}^{-1} \times 10^{-6}$) for some typical power plant steels (Darbyshire and Knight, 1977)

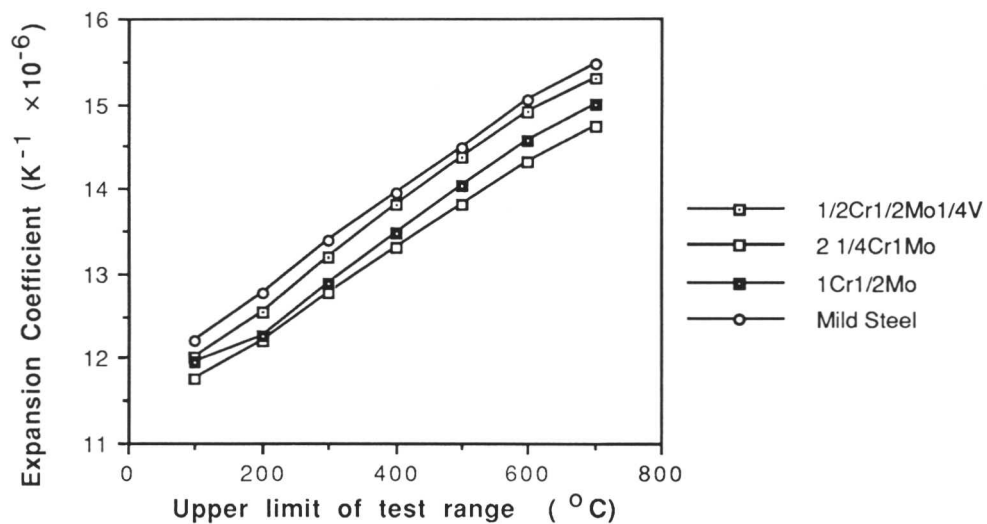


Figure 4.8: Variation as a function of T_{test} of the coefficient of linear thermal expansion (in $\text{K}^{-1} \times 10^{-6}$) measured over a range $25^\circ\text{C} - T_{\text{test}}$ for some typical power plant steels (Darbyshire and Knight, 1977)

The measured expansion coefficient for the steam header material will thus be expected to depend on the range of temperatures over which it is determined; hence, values appropriate to several temperature ranges have been obtained for the ferritic thermal expansion coefficients, as can be seen from table 4.4. These results are also presented graphically (figure 4.9) to illustrate the variation of thermal expansion coefficient with temperature in the steam header material used in this study. The initial length of the specimen is measured using a micrometer at ambient temperature, (T_{amb}); the specimen is then fully spherodized at around 800°C in all cases before being allowed to stabilize at the required test temperature, (T_{test}), at which point the length is determined from dilatometric data; then cooled slowly to T_{amb} in order to allow the linear thermal expansion coefficient specific to the range $T_{amb}-T_{test}$ to be determined.

Temperature Interval °C	25 to 100	25 to 200	25 to 300	25 to 400	25 to 500	25 to 600	25 to 700
Value of e_{α}	11.90	13.07	13.27	14.11	14.73	14.99	15.60
Value of e_{γ}	33.1						

Table 4.4: Mean coefficient of linear thermal expansion (in $K^{-1} \times 10^{-6}$) as determined from dilatometric experiments carried out using the 1Cr- $\frac{1}{2}$ Mo type power plant steel

4.5.4 Measuring volume fraction of transformed material

Two approaches were used to obtain these results. Firstly, optical specimens were prepared, polished down to 0.25 μ m diamond paste, and etched in a solution of 2% nital. The region which had remained untransformed at the end of the dilatometer run was clearly visible as a martensitic region, the product of retained austenite during the period of rapid specimen cooling after the furnace was switched off at the end of the run. This observable difference allows a systematic point-counting method to be used to determine the relative

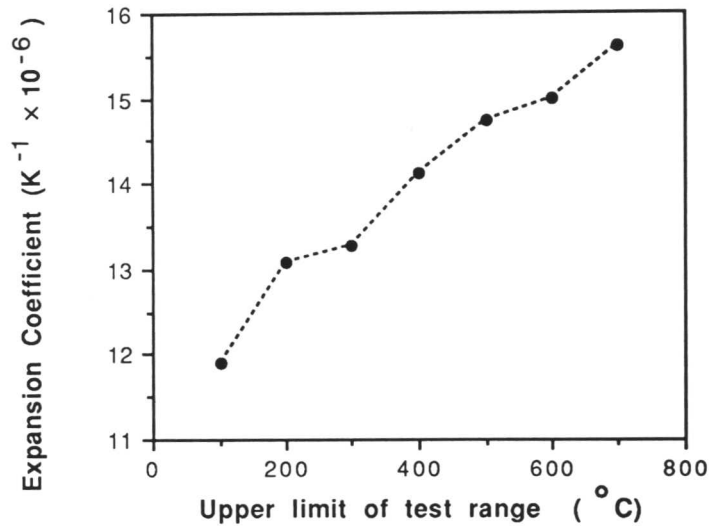


Figure 4.9: Experimentally-determined coefficients of linear thermal expansion for the 1Cr- $\frac{1}{2}$ Mo steam header steel : variation as a function of T_{test} when measured over the range room temperature - T_{test}

proportions of transformed and untransformed regions. This produces an area fraction, which can be considered equivalent to a volume fraction provided the microstructure shows no systematic variation with orientation (if such an orientation relationship did apply, then the area fraction would vary depending on the plane of section and could not be extrapolated with confidence to a volume fraction).

The approach to error analysis which was used for measurements on the as-received microstructure (Gladman & Woodhead, 1960) was used here, giving a 95% confidence limit, $2\sigma_V$, as:

$$2\sigma_V = 2V_v \sqrt{\frac{1 - V_v}{N}} \quad (4.2)$$

The number of readings, N , was selected on this basis to give $2\sigma_V = 0.03$ as the typical uncertainty in the measured volume fraction, which required $N = 400$ – 600 depending on the magnitude of V_v .

The hypothetical dimensions of a 100% ferritic specimen at the transformation temperature can be calculated using the expansion coefficients and the measured length of the rod at ambient temperature. The dilatometer apparatus records specimen length at the start of transformation, when it is 100% austenitic having been fully reaustenitized at 1100°C , and at the end of the run (immediately before quenching to ambient temperature). Now that specimen length for the fully-ferritic, fully-austenitic, and partially-transformed conditions are known, volume fractions of the two phases in the transformed specimen can be calculated, as illustrated by figure 4.10. These results are compared with point counting data in table (4.2) and figure 4.10.

The non-linearity of expansion coefficient with temperature (see above) must be considered: if calculated volume fractions are to be accurate, then a value of expansion coefficient must be appropriate to the isothermal transformation temperature. That is to say, the linear expansion coefficient so used should have been determined experimentally over the range of temperatures ambient – T_{iso} .

4.5.5 Limitations imposed by experimental procedure

The cooling system, although rapid, is not instantaneous. Despite the use of an RF coil heating system (which means that the change in ‘furnace’ temperature is effectively instantaneous), and the helium inert gas quench, the cooling profile during the transition from T_{reaus} to T_{iso} tended to have a form such as that illustrated in figure 4.12, with up to 20 seconds elapsing between the start of the cooling from the austenitizing temperature and the achievement of a stable transformation temperature, and an overshoot of 10 – 20°C below the isothermal temperature. Reduction of the former (by increasing the flow of the helium quench gas) only served to increase the latter, which is highly undesirable. This feature of the apparatus makes time at which T_{iso} is reached determinable only

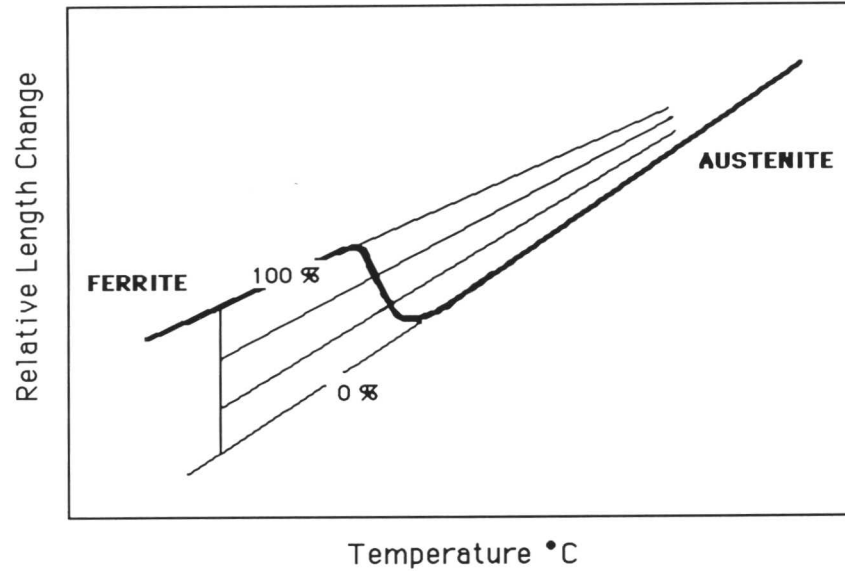


Figure 4.10: Illustration of the procedure followed to determine the volume fraction of the transformed region from dilatometric relative length change vs temperature curves in the 1Cr- $\frac{1}{2}$ Mo power plant steel

to within an accuracy of the order of a couple of seconds, and this is significant at temperatures where the incubation time, τ , is of a similar order of magnitude. Incubation times in the 1Cr- $\frac{1}{2}$ Mo power plant material are predicted to be extremely small at the nose of the upper C curve (around 720°C).

Furthermore, the rapid commencement of the austenite-ferrite transformation in the vicinity of this temperature, coupled with limited cooling rate obtained from the dilatometer in practice, can cause partial transformation to ferrite during cooling through the nose region to isothermal transformation temperatures below 720°C. In this case, the measured incubation times will not be in accordance with theory as the microstructure is already partially ferritic before T_{iso} is reached, which can be expected to retard the onset of the transformation at T_{iso} , so that the measured incubation time is greater than the theoretical τ ,

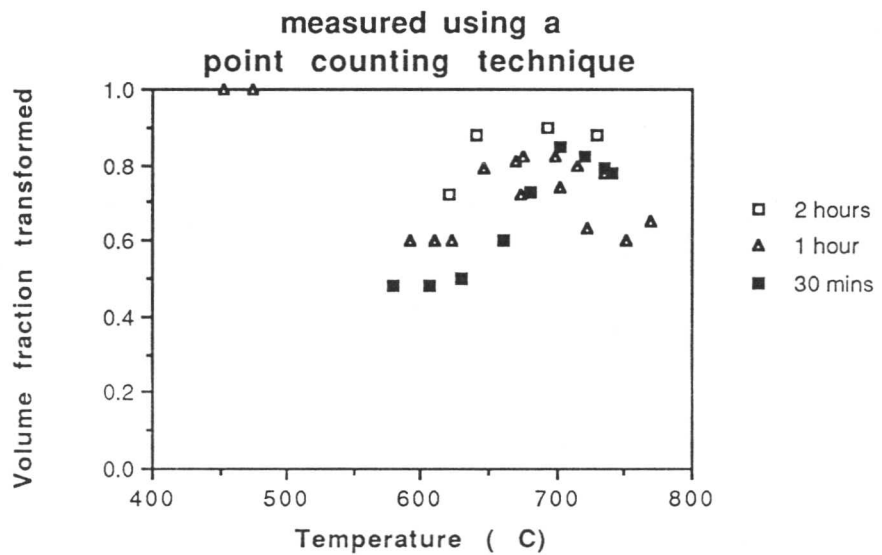
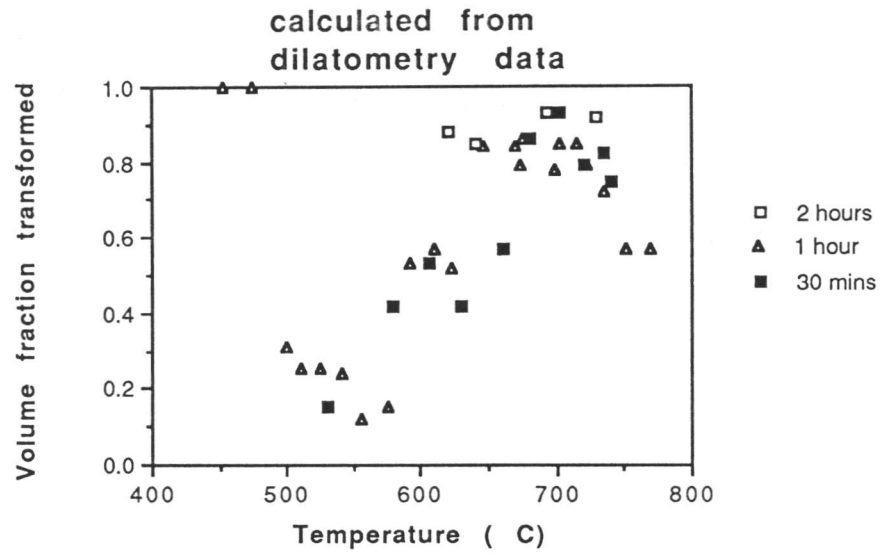


Figure 4.11: Variation of volume fraction of transformed material with transformation temperature for dilatometric experiments on the 1Cr- $\frac{1}{2}$ Mo power plant steel

possibly by an appreciable amount. In any case, it would render the collected data invalid.

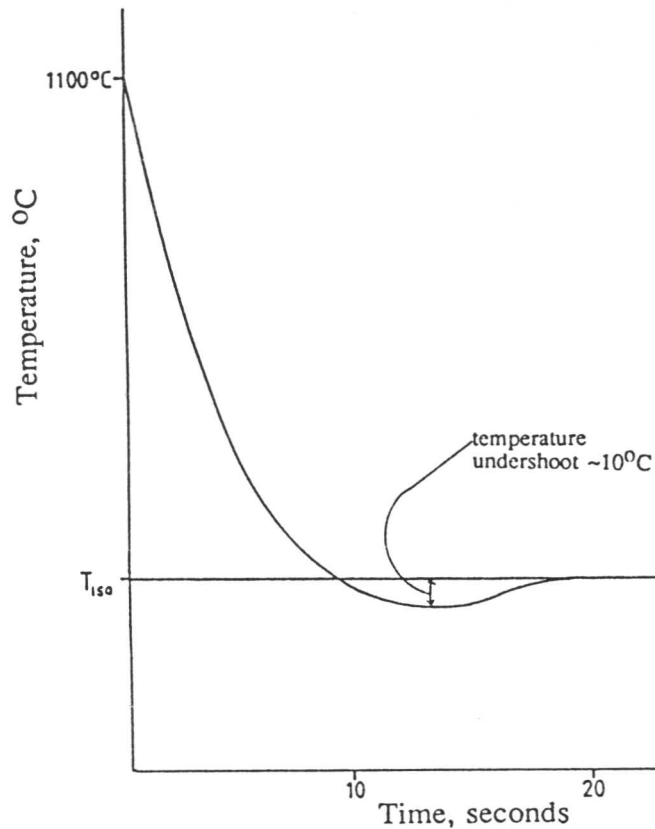


Figure 4.12: Typical cooling curve from austenite to isothermal temperature

It is essential to examine a plot of length vs temperature (figure 4.13) to determine that cooling rates are adequate to avoid this difficulty. These plots should be essentially linear in nature as the specimen is cooled towards T_{150} if the length contraction is entirely due to the thermal contraction of austenite: a deviation from linearity would be attributable to the transformation volume change occurring during cooling, making the heat treatment invalid.

Examples of the plots used for this purpose are presented in figure 4.13. It is noticeable that in the second case (at an isothermal temperature of 535°C) deviation from linearity (*i.e.*, deviation from the case where only the thermal contraction of austenite is being observed) has occurred before t_{150} is reached,

whereas the transformation at 720°C exhibits no such problem. This is suggestive of the volume increase associated with the transition from austenite to ferrite having taken place to some extent during cooling in the former case. Included in figure 4.13 is a plot to illustrate that the undershoot of T_{iso} during cooling, which was found to be an inevitable feature of the apparatus, does not necessarily render the result invalid (the transformation run at 700°C, where the absence of any deviation from a linear plot except at T_{iso} confirms that the results produced during this experimental run should be acceptable). The transformation runs where conclusive evidence for prior reaction was found from length change–time plots must be discarded as the experiments failed to produce truly isothermal conditions, but all results where the length vs temperature plots were linear during cooling should be genuinely representative, and are included in table (4.2).

The suspicion that prior transformation may be taking place in some cases was investigated by repeating the isothermal transformations over short time periods for some temperatures. The transformation time was chosen so as to be intermediate between the theoretically-predicted and dilatometrically-measured reaction incubation times, and the material was given a rapid quench. The presence of small colonies of allotriomorphic ferrite within the martensite (figure 4.14) provides confirmation that transformation took place before the measured incubation time, presumably during cooling to T_{iso} through around 720°C where α formation occurs at its most rapid rate. As a consequence, the transformation proceeds more slowly once the desired temperature is reached, and the apparent incubation time is invalid.

The solution to this problem could be to increase the rate of cooling from austenite to the isothermal temperature by using hollow specimens to which a helium line can be attached directly; helium passed through the specimen in this way will produce a much more efficient quench than the method of simply flooding the vacuum chamber. Unfortunately, such a procedure increases the specimen surface area, and hence the risk of surface nucleation effects creating spurious results, as the nickel plating procedure is not perfectly efficient

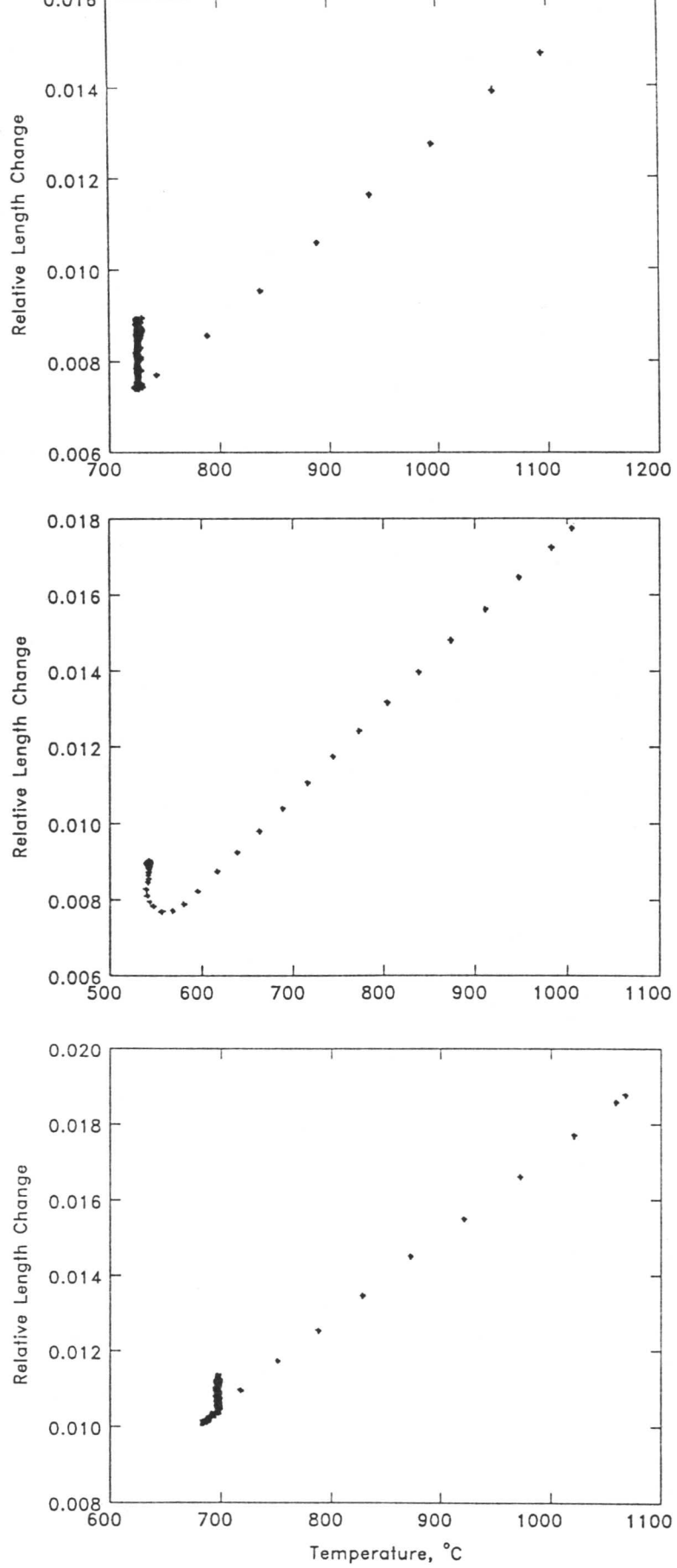


Figure 4.13: Length versus temperature plots for 1Cr- $\frac{1}{2}$ Mo steel isothermal heat treatments

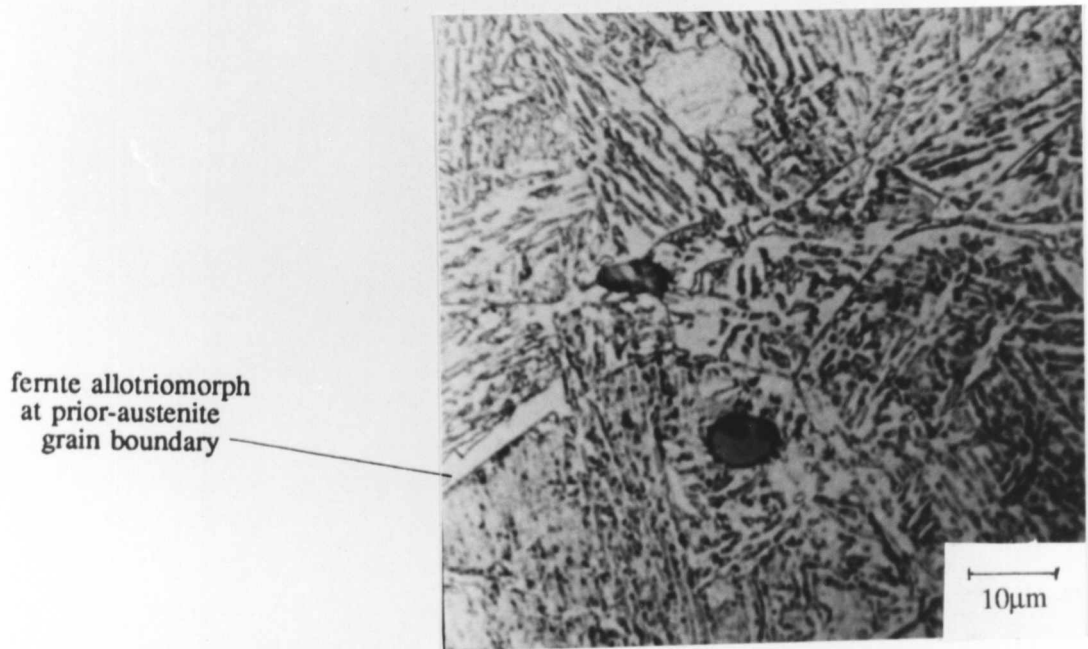


Figure 4.14: Evidence of initiation of transformation to ferrite during cooling to T_{iso} , negating the validity of the value for τ subsequently calculated from dilatometric data collected at the isothermal temperature

at preventing this, especially on internal surfaces. If such a modification is not practicable, an alternative method such as using a molten-tin bath quench could be employed, although this is less desirable as the excellent data collection facilities provided by the dilatometer would be lost. In this study, the procedure followed has been to vary the rate of helium quenching to try to produce the maximum cooling rate which retains a reasonably clean stop at the isothermal temperature, and to abort those runs which do not achieve this. This approach appears to have proved satisfactory.

4.5.6 A comparison of experimental and theoretical TTT curves

The results obtained from dilatometric data (see table (4.2)) are used to construct an experimental isothermal TTT curve (figure 4.15). It is clear that whilst some points on the graph illustrate good agreement with the theoretical TTT curve generated using Russel's equations, in some cases the fit is poor, especially at isothermal transformation temperatures lying above the nose of the upper C curve. The consideration of the limitations and errors associated with the dilatometric technique has been made above, and some of the factors noted in that section may be responsible for some of this lack of agreement. In essence, the cooling rate available in the system is insufficient entirely to eliminate a suspicion of some transformation occurring before T_{iso} is reached, but on the whole theoretical and experimental values of τ are reasonably close.

An attempt was made to construct a TTT curve based on the experimental incubation times, and this is presented in figure 4.16. This curve, however, does not represent a best-fit through the measured values for τ , but was subject to certain constraints to give the final form a degree of physical significance: the regions above and below the kinetic bainite start temperature were considered separately, and curves fitted to both sets of points; and the upper curve was forced to be asymptotic to the Ae'_3 curve, and was further constrained to take on the familiar C-curve shape. Within these constraints, best-fit splined curves were drawn through both sets of points, and combined to produce figure 4.16. These somewhat arbitrary limits were found to be necessary to produce a curve of meaningful form, but, in consequence, the TTT curve produced in figure 4.16

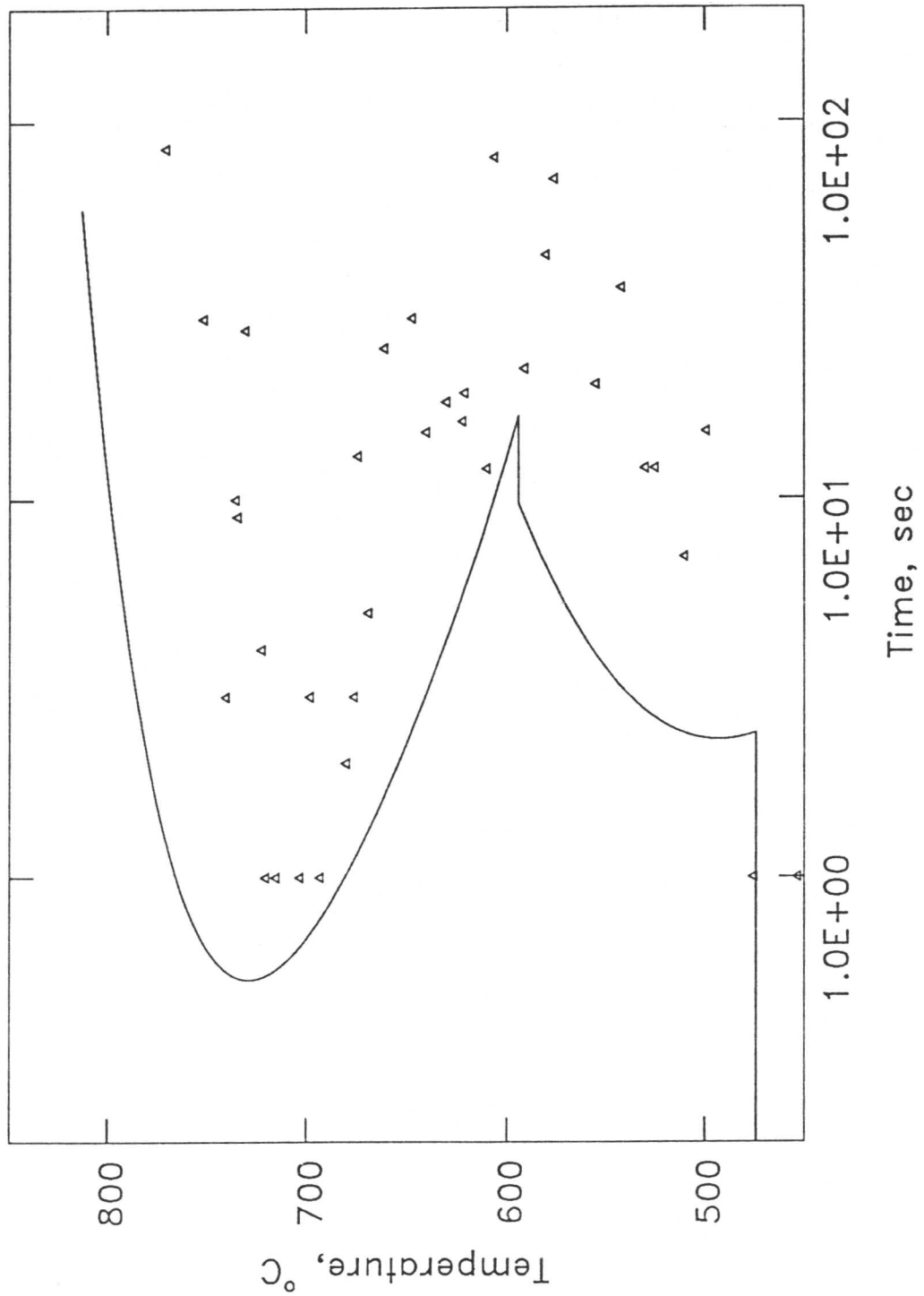


Figure 4.15: Experimentally-determined values for incubation time in comparison with the theoretically-determined TTT curve for the 1Cr- $\frac{1}{2}$ Mo type steam header steel

cannot be said to be a true representation of the experimental data, but rather an approximate illustration of the physical significance of those data.

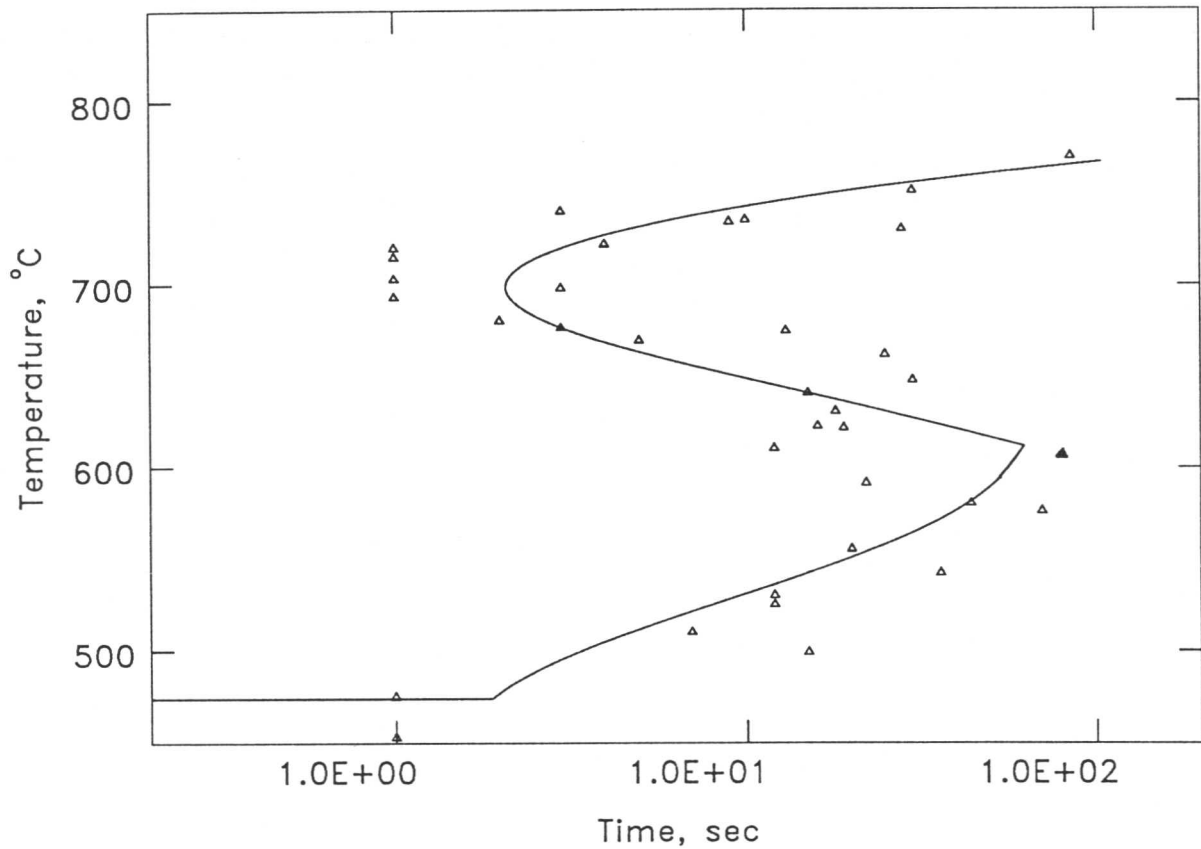


Figure 4.16: TTT curve for 1Cr- $\frac{1}{2}$ Mo type steam header steel determined from experimental data

The TTT curve constructed to represent measured τ is compared with that constructed using Russell's equations in figure 4.17, and shows reasonable agreement with the theoretical prediction.

It may be observed on the graphs that there is particularly noticeable deviation from the theoretically-constructed curve above 720°C. At this temperature, transformation during cooling is unlikely (except in the case of a large temperature undershoot). However, Bhadeshia's program is based on nucleation equations derived by Russell (1969) which are known to be of dubious accuracy for small reaction driving forces and longer incubation times. This is in

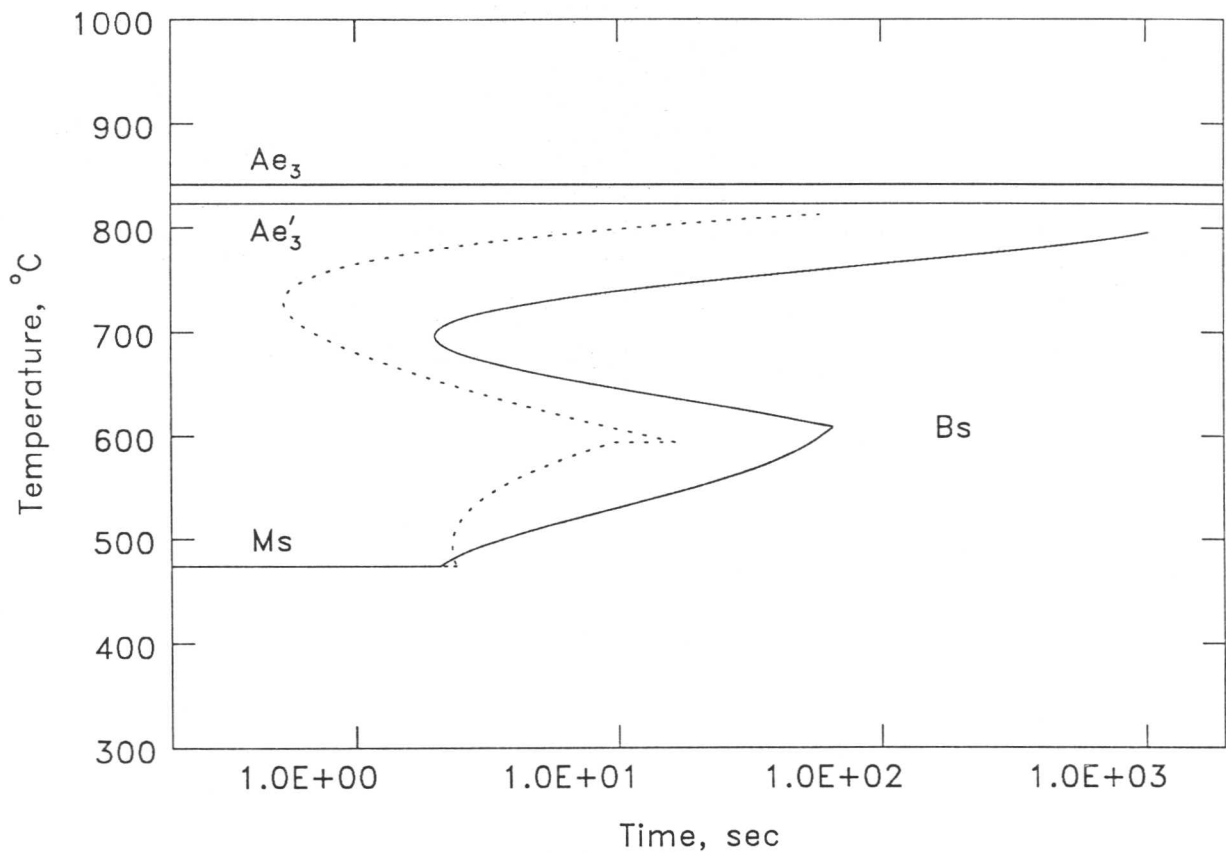


Figure 4.17: A comparison between TTT curves constructed from dilatometric data and calculations based on Russell's equations for the 1Cr- $\frac{1}{2}$ Mo type steam header steel

keeping with the fact that experimental incubation times are consistently longer than those generated by the computer model in the region above 720°C, where Russell's equations cannot rigorously be applied.

4.6 Metallographic Examination of Heat Treated Specimens

4.6.1 Microscopy

The specimens which were prepared of samples from the full range of isothermal transformation temperatures and times, and employed for point counting volume fraction measurement (above), were also examined optically. This was done using an Olympus reflected light microscope, with Ilford FP4 (100 ASA) film used to record the observations. A selection of optical micrographs is pre-

sented in figure 4.18, illustrating the range of transformation products from allotriomorphic ferrite, through bainite, to martensite.

It is notable that on an optical scale is that there was an absence of carbide precipitation within the ferrite of the kind which had been present in the as-received steam header material. In these materials optical evidence for such particles is rarely seen until appreciable ageing has occurred to allow coarsening, or, at the very least, the stress relief heat treatment which is given to pre-service steam header components; hence, any precipitates which would be present in the transformed specimen would be of such a fine scale as to be beyond optical resolution, if present at all.

It can be seen from the micrographs that these microstructures are not always straightforward in interpretation, particularly in relation to the eventual product of the residual austenite which remained after completion of the isothermal transformation run. It can be seen from micrographs obtained from specimens transformed at the higher isothermal temperatures (where the bulk of the material had transformed to allotriomorphic ferrite) that the residual austenite has subsequently decomposed to a mixture of bainite and martensite. This is a consequence of the fact that specimens were air cooled after isothermal transformation (that is to say, at the end of the isothermal transformation the vacuum chamber of the dilatometer was simply opened to air), giving a moderately slow cooling rate; hence some bainite formation was possible from the untransformed austenite before M_s was reached. Lower temperature bainitic microstructures were particularly difficult to analyse: the remaining austenitic regions after transformation could be found as a mixed microstructure of bainite, martensite and even retained austenite (given sufficiently high carbon enrichment of the untransformed region during bainite formation), products which are practically indistinguishable optically, in any case indistinguishable with accuracy. Optical determination of volume fraction transformed was then impracticable for the bainitic microstructures; consequently, measured volume fractions are not presented for this temperature regime in the table of results.

4.6.2 Energy-dispersive X-ray analysis

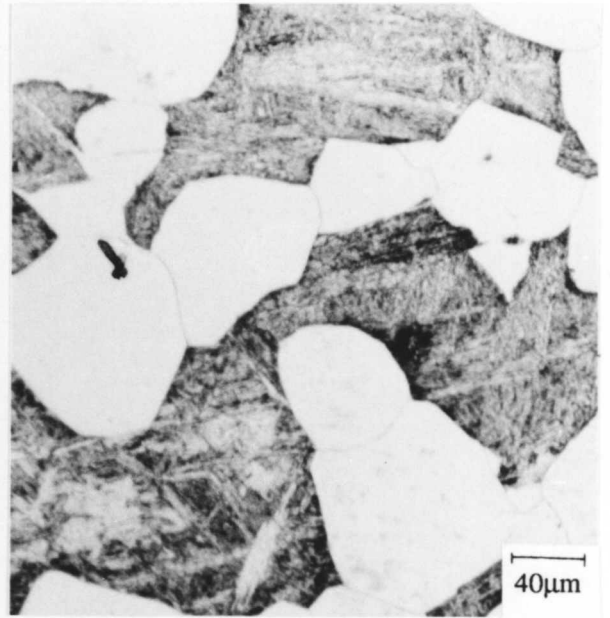
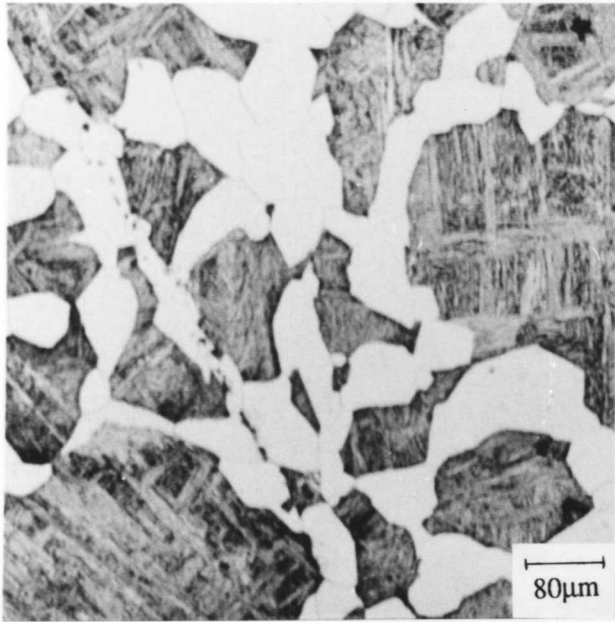
EDX traces were obtained for chromium, manganese, molybdenum and silicon contents for both transformed and untransformed regions in the heat treated steel. The EDX analysis was performed on the ISI100 scanning electron microscope, using the same procedure as for the as-received steam header material, so that results could be compared; they are represented on 4.19.

The figure shows a small difference in composition between allotriomorphic ferrite and martensite with respect to substitutional alloying elements at the highest transformation temperature. In this respect, it shows a similarity to the as-received material, which had also been heat treated at a relatively high temperature (Appendix). Such an effect indicates some redistribution of substitutional alloying elements during transformation at the higher transformation temperature from ferrite to retained austenite (from which the martensite forms on cooling). The scatter in results for a given material is large, however probably due to the large sampling volume (figure 3.14) resulting, in some cases, in a compositional reading being obtained in part from a phase other than the desired one; the accuracy of the data is correspondingly limited, and insufficient for the results to be considered to provide conclusive evidence of redistribution during transformation.

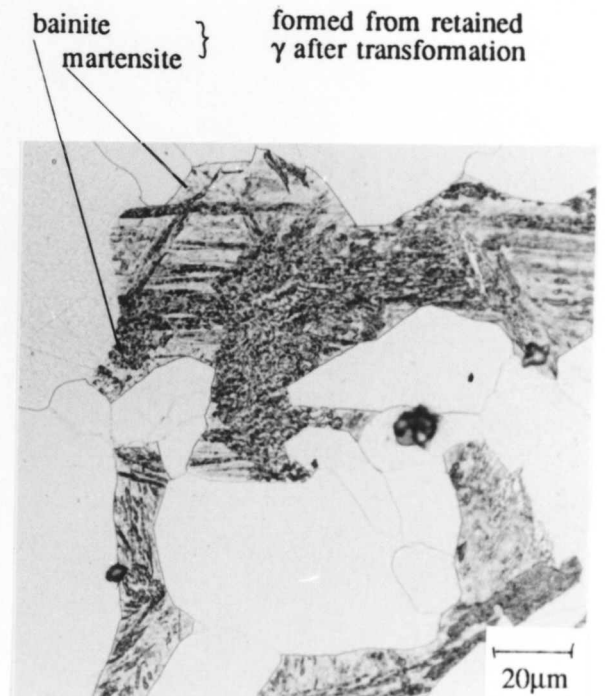
At lower isothermal transformation temperatures, there is no evidence of a difference in substitutional alloying element concentrations between the ferrite and retained austenite, suggestive of a paraequilibrium mechanism for ferrite formation at these temperatures which would be consistent with expectations as undercooling is increased.

4.7 Summary

The austenite–ferrite transformation in the $1\text{Cr}-\frac{1}{2}\text{Mo}$ type steam header steel has been examined carefully using both dilatometric experiments and predictive theory. The transformation behaviour was found to be typical of that expected for a low-alloy, low-carbon steel, producing allotriomorphic ferrite, bainite, and martensite depending on the degree of undercooling from the austenite phase

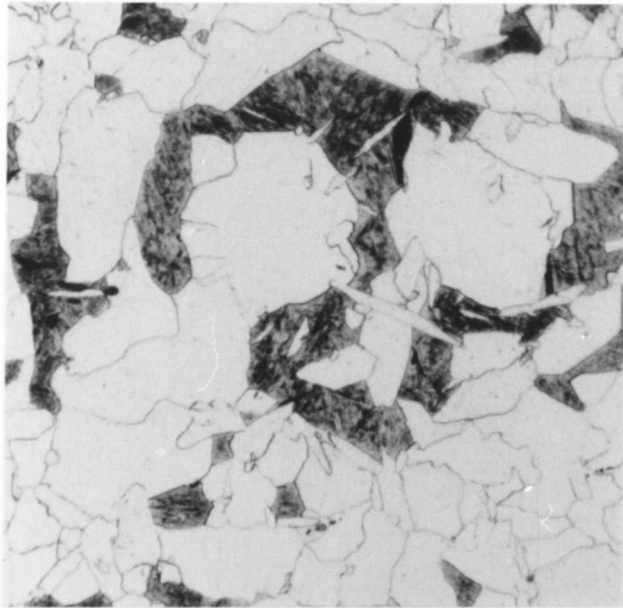


(a) 1 hour @ 750°C



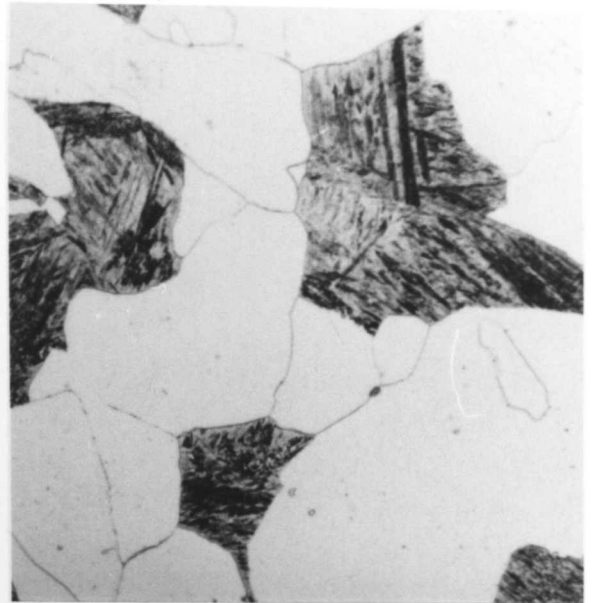
(b) 30 minutes @ 735°C

Figure 4.18 (a) Optical micrographs of heat treated steels

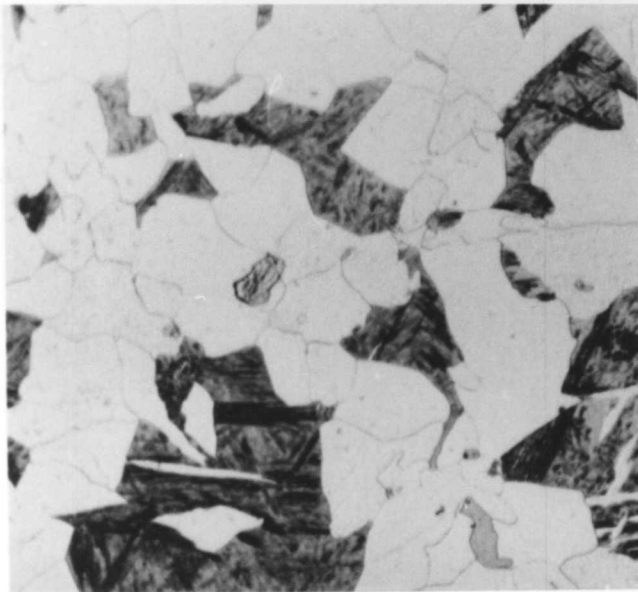


(c) 30 minutes @ 720°C

40µm



20µm



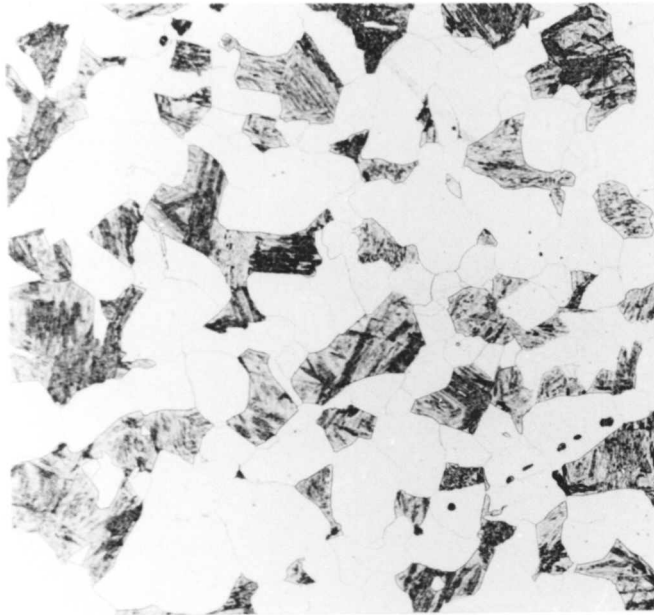
(d) 1 hour @ 700°C

40µm



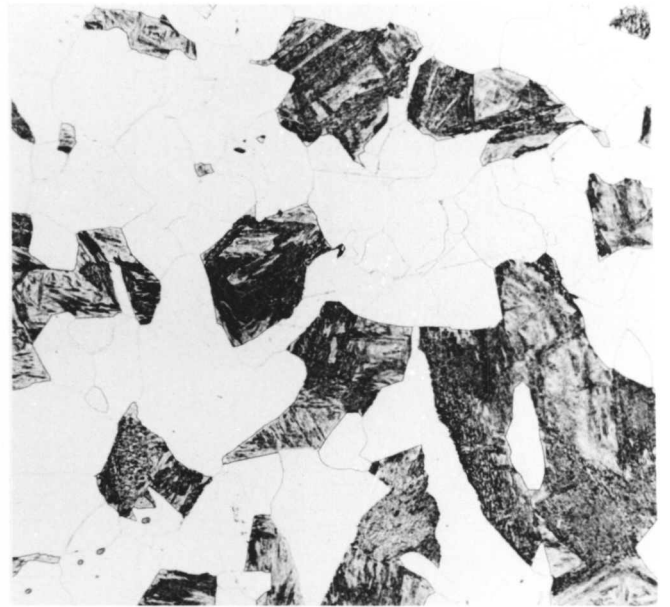
20µm

Figure 4.18 (b) Optical micrographs of heat treated steels

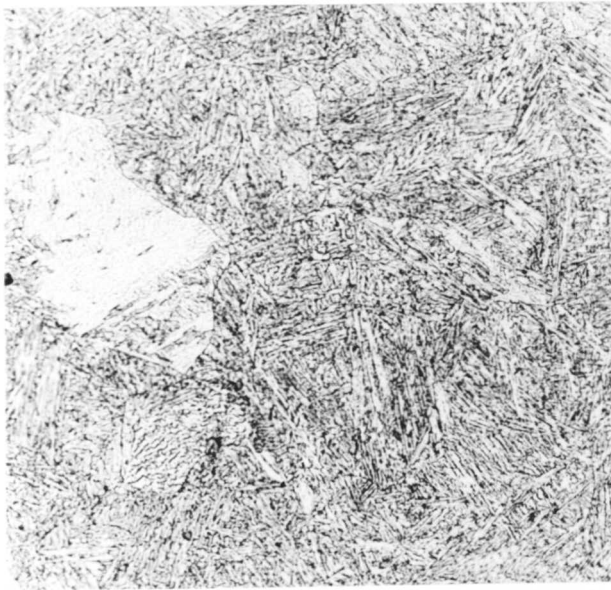


(e) 1 hour @ 650°C

40μm

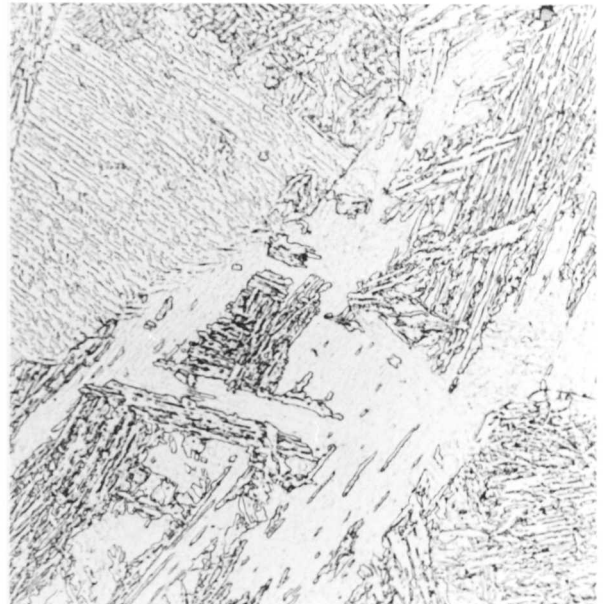


20μm



(f) 1 hour @ 550°C

40μm



20μm

Figure 4.18 (c) Optical micrographs of heat treated steels



(g) 1 hour @ 500°C

40μm



20μm

Figure 4.18 (d) Optical micrographs of heat treated steels

field. The theoretical modelling of the transformation was also carried out using the composition of the Fe–4.08Cr–0.3C (wt.%) model alloy.

An experimental TTT curve for the transformation has been constructed, and was found to show the standard, two-C-curve form, with a pronounced bay region at around the bainite start temperature. Measurements of the volume fraction transformed to ferrite at different temperatures for a given time were also made; these were found to be typical for a low-alloy steel, and, in the case of bainitic ferrite, to illustrate the incomplete reaction phenomenon. Coefficients of linear thermal expansion were determined for the material, illustrating the non-linearity of ϵ_α with temperature typical of low-alloy ferritic steels.

The knowledge of the austenite–ferrite transformation in the 1Cr– $\frac{1}{2}$ Mo type steam header steel which was obtained by this work may be used in the production of regenerated bainitic and mixed ferritic/bainitic microstructures for the ageing experiments which are described in subsequent chapters.

HEAT TREATED MATERIAL

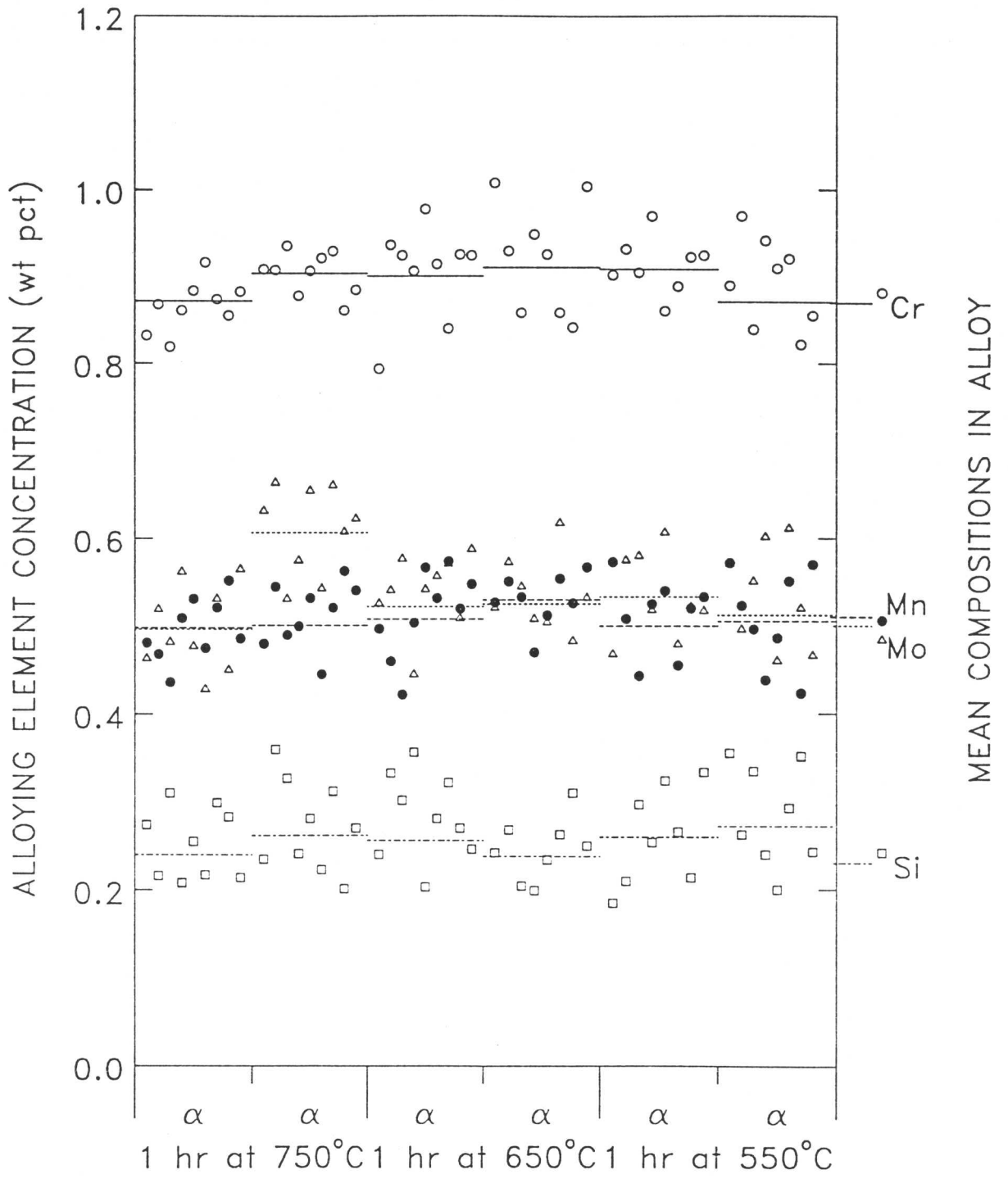


Figure 4.19: EDX results from heat treated steel specimens

Chapter 5

AGEING OF BAINITIC MICROSTRUCTURES: EXPERIMENTAL PROCEDURE

5.1 Introduction

An extensive programme involving the ageing of bainitic and mixed allotriomorphic ferrite / bainite microstructures has been carried out. Specimens have been aged over several temperatures over a range of $\sim 50^\circ\text{C}$ either side of the fossil fuelled boiler system service temperature (*i.e.*, 565°C). The aged specimens have been studied in order to determine the effect of the ageing treatment on their composition (with particular reference to the theoretical model for ageing of θ which was discussed in Chapter 2), microstructure and physical properties. The experimental procedure involved is outlined below.

5.2 Programme of Heat Treatments

Two materials were used with the following compositions (wt. %):

	C	Si	Mn	Cr	Mo	Fe
1	0.30	0.00	0.00	4.08	0.00	bal.
2	0.12	0.23	0.51	0.87	0.50	bal. ¹

Steel 1 was chosen as a model ternary alloy to give an initially simple system of cementite so that the technique could be developed and the theory tested in a controlled manner. Steel 2 is a power plant material and can be expected to give a more complex, and more typically realistic, system of various alloy carbides as well as cementite.

For the second steel (the power plant material), two microstructures have been produced: fully bainitic and a mixture of allotriomorphic ferrite and approx. 25% bainite. The latter microstructure corresponds to that generally observed in actual power plant materials, and will be produced by reference to the

¹ With the exception of negligible levels of sulphur and phosphorus, details of which can be found in the appendix

transformation modelling work which was described earlier. It differs from the as-received material in that it has not been given a subsequent stress-relieving heat treatment following transformation, as it is the intention of the current work to investigate the enrichment of cementite from a precisely known starting composition in order to test recent theory. It is established that bainitic cementite forms with negligible redistribution of substitutional alloying elements, so that it has an initial composition, c_0^θ , which is accurately known; however, the stress-relief heat treatment would introduce significant ageing, so that c_0^θ for the subsequent lower-temperature ageing treatments would not be known so precisely.

5.2.1 Generation of model microstructures

In the case of steel 1, the microstructure was generated by austenitizing at 1100°C for 10 minutes, followed by isothermal transformation to lower bainite at 420°C for 10 minutes. A bainitic microstructure from steel 2 was also generated isothermally, in this case transformed at 530°C for 1 hour. As was noted earlier, the absence of partitioning of substitutionals during bainite formation means that bainitic cementite can be assumed to have substitutional alloy concentrations in the same ratio as those in the alloy as a whole, with a stoichiometric carbon concentration.

The mixed microstructure was generated by performing a partial isothermal transformation at 720°C for 30 minutes, followed by an isothermal treatment of 1 hour at 500°C to transform the remaining austenite to bainite. The temperature of the first half of the treatment was chosen on the basis of the dilatometry in the current work modelling the $\gamma \rightarrow \alpha$ transformation which suggested that such a treatment would produce around 75% transformation to allotriomorphic ferrite. The actual quantity of bainite was measured using a point counting technique with approximately 2000 readings taken, which produced a volume fraction for bainite of $29.1 \pm 1.0\%$ (error is a 95% confidence limit derived using the same procedure as previously).

It was also felt that the undercooling would be sufficient to ensure that the ferrite formed via a paraE mechanism, so that, with no partitioning of substitu-

tionals, the substitutional composition of the retained austenite and transformed ferrite would both be \bar{c} . Thence, as bainitic cementite forms from remaining austenite with no diffusion of substitutionals, it should be safe to assume that the substitutional cementite contents are as \bar{c} , with a stoichiometric carbon concentration. This supposition was confirmed by EDX analysis of cementite particles in unaged specimens, which produced mean compositions of \bar{c} .

Heat treatments were carried out in a fluidized bed set to the isothermal transformation temperature. This method produces a reasonably rapid transition from the austenitizing to the isothermal temperature. The material was sealed in quartz tubes under an appropriate partial pressure of argon to maintain an inert atmosphere at the surface. The temperature must be monitored carefully at the exact point at which the transforming material is placed, to guard against any fluctuations of temperature with distance within the fluidized bed system.

5.2.2 Ageing procedure

The fully-bainitic microstructures were aged at 510°C, 565°C and 625°C, and the partially-bainitic microstructure generated from the power plant steel was aged at 565°C to compare with the fully-bainitic one, giving a total of 7 series of heat treatments. Specimens consisted mostly of 3mm diameter machined rods of approximately 3cm in length. These could then be used both as a source for thin foil work, and for mounting for optical examination and replica production. Ageing was carried out with the specimens sealed in quartz tubes with an inert argon atmosphere.

Material was removed from the furnace at periodic intervals for ageing times of up to a year (*i.e.*, approx 8000 hours).

A careful analysis of the stability of furnace temperature was made in order to obtain a measure of potential experimental error which could be introduced from this source. This involved measuring the furnace temperature at intervals over a period of time, using a Pt-Pt-10%Rh bimetallic thermocouple. The results are represented graphically on figure 5.1.

onto a specimen produced in a manner similar to the procedure described above for optical metallography. The aged material is mounted in acrylic, polished down to 0.25 micron diamond paste, and then given a very light etch in 2% nital to expose the carbide particles. This primary etch should be barely visible optically.

The specimen thus prepared is then placed in a carbon evaporator (see schematic of figure 5.2). The evaporator chamber is evacuated down to a maximum of 2×10^{-4} torr. Resistance heating of high-purity graphite rods is used to evaporate off carbon, which is then deposited onto the specimen below in the form of an amorphous carbon film. The heating effect is achieved by ensuring that one of the rods narrows to less than 1mm in diameter at the point of contact with the other (which has a flat surface) (see figure 5.2). Contact is maintained as carbon evaporates by applying a light force to the narrow-ended rod provided by the spring loading system. It is important to ensure that the surface of the mounted specimen is clean and free from grease to ensure good adhesion of the deposited carbon. This is achieved by washing the specimen in industrial methylated spirits (IMS) immediately prior to insertion into the vacuum system. Carbon is deposited from a height of 10 cm directly above the specimen surface to obtain as even a coverage as possible.

The depth of the layer of carbon is gauged roughly by its apparent colour, which is due to interference effects. As an aid to determining this clearly, a glass microscope slide covering a piece of paper, and with an oil drop on it was placed alongside the specimen. The depth of deposit was judged by comparing the part of the slide under the drop (hence without a carbon deposit) with the rest of the slide.

The carbon layer is found to adhere to those carbide particles which were exposed by the initial light etch. It can thus be loosened from the specimen surface by etching away the ferrite matrix, and hence be removed with the carbides still attached, but without any of the ferrite matrix.

The agent used to etch the replica free from the specimen surface was 10% nital. The specimen was scored with a razor blade into squares around 2mm

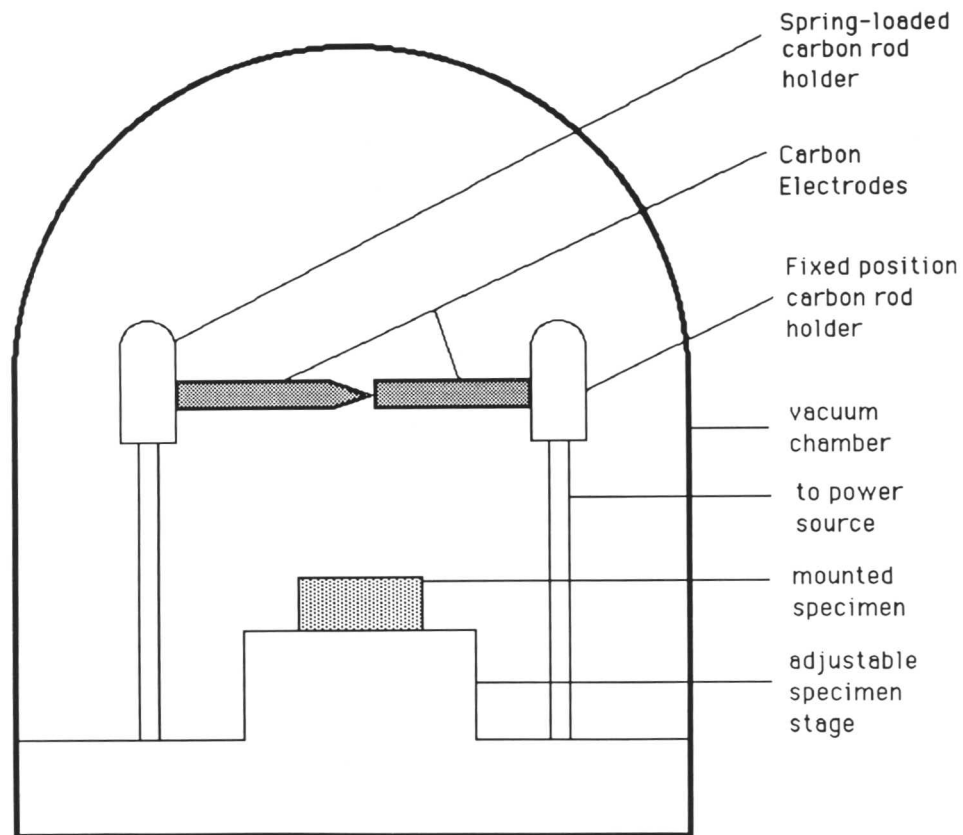


Figure 5.2: Schematic diagram of the carbon evaporator apparatus

across to allow reasonable access for the etchant to bare metal surface, and to ensure that the carbon replica pieces would be of manageable size. The specimen was then placed in the nital and the etching process speeded up by making the specimen cathodic with a 3V potential difference across it.

As soon as the carbon layer had worked almost free of the metal surface, the specimen was washed in ethanol, and the fragments of carbon layer were floated clear of the surface using the surface tension provided by a 50% ethanol / 50% distilled water mixture. It was found that the use of just distilled water for this purpose, as some authorities report, gave too pronounced a surface tension effect, leading to folding over of the replica which was then rendered useless.

Each replica was then collected onto a 3mm, 200 square mesh copper grid and was then ready for analysis in the electron microscope.

5.3.2 The replica technique

The replica technique was chosen because it enables the carbide particles to be analysed in isolation, eliminating any problems which could be caused by interference from signals emanating from the matrix, effects which may be associated with alternative techniques (such as microanalysis of thin foils). This would be a particular problem given the small size of the carbides under analysis. It is likely that the use of thin foils would lead to spurious results, as the spreading and depth of penetration of the EDX beam would mean that a significant part of the spectrum produced would have arisen in the ferrite matrix, and that the compositions extrapolated from the spectra would then be unrepresentative of the actual compositions of the carbides.

These problems can effectively be eliminated by the use of replicas, where no material from the matrix is present, and also the carbon layer is very thin, and hence effectively electron transparent. As a result, the EDX spectrum produced from the replica consists solely of signals from the carbide being tested (with the exception of a very small carbon response and an inevitable background copper signal from the copper grid which can be safely ignored with no loss of accuracy provided copper is not an element under consideration in the carbide analysis). The spectrum can thus be considered to give a true analysis (to within the limits of experimental error and noise) of the composition of the bainitic cementite and other carbide particles under investigation.

5.3.3 Thin foil microscopy

Although the vast majority of this study was conducted using extraction replicas, some thin foils were produced. The primary purpose of examining thin foils was to ensure that the extracted carbides in the replica were representative of the true microstructure. Where necessary, discs were prepared from 3mm diameter cylinders of specimen, initially cut to roughly 0.25mm thick; ground down to 0.05mm on wet 600 grade SiC paper; and jet polished using a twin-jet

electropolisher, with a polishing solution of 5% perchloric acid 25% glycerol (by volume) in ethanol at room temperature, and 40V applied voltage. A Phillips EM400T electron microscope was used for the examination, with an operating accelerating voltage of 120kV.

5.3.4 Procedure for EDX analysis

The replicas were taken and analysed on a Philips 400T transmission electron microscope using the energy-dispersive X-ray analysis (EDX) technique, with 120 kV accelerating voltage, with the specimen orientated at a 30° angle to the detector. The microscope was fitted with a Link EDX analysis system, and the spectra were collected and processed using the Link microanalysis program (which includes corrections for atomic number, absorption and fluorescence effects).

Spurious signals from the system were reduced by using a beryllium specimen holder ($Z = 4$, so the EDX signal from the holder is negligible), although some spurious X-rays arising from the copper grids on which the replicas were mounted could not be eliminated entirely.

Around 30 cementite particles were analysed from each ageing treatment, 'selected' as randomly as reasonably possible from the replica. This number of analyses was found to give data of reasonable statistical significance except at very short ageing times. In each case the EDX spectrum was collected over a 200 s livetime. Micrographs were also taken for each particle from which a spectrum was obtained so that a measure of size could be made.

Diffraction patterns were obtained in order to check that only cementite was being analysed, and to identify any other alloy carbides which may appear after longer ageing times.

5.3.5 Measurement of x_θ

To test a model for the ageing process, such as that producing equation (2.9), it is necessary to obtain a representative indication of particle thickness for each precipitate. For this purpose, a mean linear intercept, \bar{L} was measured from each micrograph.

The mean linear intercept measurement was obtained manually from the appropriate TEM plate. This was done by using a computer program to generate a graph consisting of a random array of straight lines, which was then laid across the TEM plate. The lengths of the various intercepts thus created could be read off to produce a mean linear intercept. A statistical standard error analysis led to the conclusion that around 20 intercepts gave a reasonably accurate value for each mean linear intercept value, with a 95% confidence limit in the measured \bar{L} of the order of $\pm 0.15\text{--}0.20\mu\text{m}$.

It was felt that the mean linear intercept provided the most appropriate measure of the effective mean diffusion length in the cementite particle. The x_θ value in the theoretical model which assumes a cementite slab of infinite length and constant thickness, will thus be best represented by the measured value for \bar{L} in any subsequent analysis.

5.4 Interpretation of Microanalytical Data

5.4.1 Statistical Analysis of Data

Data interpretation involves performing regression analyses to test the correlation of the collected data to several of the predictions which can be deduced from equation (2.9):

- (i) $(c - \bar{c})$ proportional to $1/x_\theta$ at constant t ;
- (ii) $(c - \bar{c})$ proportional to $(\text{time})^{1/2}$ for constant x_θ ;
- (iii) $(c - \bar{c})(x_\theta)$ proportional to $(\text{time})^{1/2}$.

The last two were also tested against the $(\text{time})^{1/3}$ relationship proposed by Afrouz *et al.* (1983) for purposes of comparison.

The best fit $(c - \bar{c})$ v. x_θ^{-1} was also generated in the regression analysis and a statistical significance test performed on the data. This test consisted of fitting the regression coefficient (*i.e.*, the gradient of the best fit line) against the null hypothesis that the true gradient was zero (*i.e.*, no size effect), using a

statistical standard a t-distribution. The t-value thus generated was compared with statistical tables to determine the appropriate confidence limit.

The above statistical analyses were carried out using a computer program for multiple regression analysis using a subroutine from the Numerical Algorithms Group (NAG) numerical analysis package to generate the values for the Pearson product-moment correlation coefficient between x_{θ}^{-1} and $(c - \bar{c})$, and the t-value attributable to the data (and similarly for the $(c - \bar{c})(x_{\theta})$ versus $(\text{time})^{1/2}$ plot). The significance levels quoted in the data presented in the results sections were produced by reading off the t-values produced from the collected data using this procedure and comparing with statistical tables for the t-distribution.

The importance of obtaining a measurement of the statistical significance of any quantitative analysis of analytical electron microscopy, so that results can be processed with reasonable confidence that they are representative, is well documented, e.g. Senior (1988). Senior uses a similar statistical procedure to the one described above in order to determine the sample size required to give significant results. It should be noted, however, that the situation in the quoted reference is not directly analogous to that for the present work,² even though a t-distribution analysis is also used, and the work is referred to primarily as an illustration of the caution required in interpretation of these types of data.

In this work a sample size of about 30 readings per ageing treatment has been used (see above) as this is considered to give tolerable levels of experimental uncertainty in the $(c - \bar{c})$ v. x_{θ}^{-1} analysis, whilst producing plenty of data for the analysis of composition change versus time (a larger sample size would increase the accuracy of the former analysis, but at the expense of the latter). This

² Senior's study consisted of an attempt to quantify the relative proportions of two distinct types of precipitate occurring simultaneously in a microstructure using the EDX technique. The statistical analysis produced a figure for the uncertainty in these measured proportions. In the case of the current project only a single type of particle (*i.e.*, cementite) is analysed, and the level of significance quoted is that associated with the proposed relationship between the composition of various of these particles and an independent variable (*e.g.*, the precipitate size).

sample size is found to produce adequate significance levels for the $(c - \bar{c}) v. x_{\theta}^{-1}$ analysis, at least for specimens from longer ageing times (where the size effect becomes reasonably pronounced).

It is also apparent from equation (2.9) that an approximate activation energy for the diffusion process can be determined provided that data is available over a range of temperatures (because most of the temperature dependence of the Bhadeshia model is attributable to D_{α}). These were also determined for each set of heat treatments.

5.4.2 Inaccuracies in EDX measurement due to matrix effects

The essence of the EDX technique lies in the ability to extrapolate relative X-ray signal intensities for two elements within a specimen (say, I_A/I_B) to the relative concentration of the elements present (C_A/C_B), in accordance with equation (5.1), below (Cliff and Lorimer, 1975), where k_{AB} is a constant for constant accelerating voltage and specimen thickness.

$$\frac{C_A}{C_B} = k_{AB} \frac{I_A}{I_B} \quad (5.1)$$

Factors affecting the proportionality between the two are therefore of considerable concern, and care must be taken to quantify and if necessary correct for such factors before the compositional data produced by the technique can be used. Consideration is given to two such problems: unequal level of absorption of different X-ray emissions (from different elements) by the specimen; and fluorescence within the specimen.

5.4.2.1 Absorption

The Link system used in analysing the EDX spectra includes a routine to make a correction for matrix absorption from specimen thickness and density. A brief consideration of the physical situation is given below.

The relationship between the observed intensity of signal from an element A present in the specimen, I'_A , and the real intensity of emission which would

be observed in the absence of any absorption, I_A , follows the exponential law as equation (5.2).

$$I'_A = I_A \exp\{-(\mu/\rho)_{\text{spec}}^A \rho x\} \quad (5.2)$$

where x is the distance the signal travels through the material, ρ is the density of the material, ϕ_A is a measurement of the attenuation of incident electron energy during its passage through the material, and $(\mu/\rho)_{\text{spec}}^A$ is the mass absorption coefficient for X-ray emission attributable to element A for the whole specimen, obtained as a sum over all elements in the specimen of $c_i(\mu/\rho)_i^A$, where c_i and $(\mu/\rho)_i^A$ are the weight fraction and mass absorption coefficient associated with the element i .

In a practical situation for a specimen of finite thickness, d , Goldstein *et al.* (1977) thus propose equation (5.3) for the relationship between I'_A and I_A .

$$\frac{I'_A}{I_A} = \frac{1}{d} \int_0^d \phi_A(\rho x) \exp\{-(\mu/\rho)_{\text{spec}}^A \csc(\psi) \rho x\} dx \quad (5.3)$$

where ψ is the take-off angle, and, for practical purposes, is assumed to fit the relationship

$$\csc(\psi) = \frac{1}{\sin \alpha \cos \theta + \cos \alpha \sin \beta} \quad (5.4)$$

where α is the tilt angle, θ is the angle between the detector and tilt axes, and β is the elevation of the detector, which is zero for Philips instruments such as the one used in the current work.

If it is assumed that the electrons lose negligible energy during passage through the specimen (that is to say, the rate of production of X-ray photons is constant through the thickness d), then $\phi(\rho x) = 1$ (Cliff and Lorimer, 1975). Thus equation (5.3) can then be reduced to equation (5.5). This assumption is generally considered a reasonable approximation in thin films, although for slightly thicker specimens it may break down.

$$\frac{I'_A}{I_A} = \frac{1 - \exp\{-(\mu/\rho)_{\text{spec}}^A \csc(\psi)\rho d\}}{(\mu/\rho)_{\text{spec}}^A \csc(\psi)\rho} \quad (5.5)$$

A correction factor for intensity ratios can then be obtained by combining the above equation with an identical equation for an element B. This approach allows the ratio I_A/I_B to be quantified as equation (5.6), which makes it apparent that the effect of absorption depends on the difference between the mass absorption coefficients for the two elements, as well as on specimen density and thickness.

$$\frac{I_A}{I_B} = \frac{I'_A}{I'_B} \times \frac{(\mu/\rho)_{\text{spec}}^A (1 - \exp\{-(\mu/\rho)_{\text{spec}}^A \csc(\psi)\rho d\})}{(\mu/\rho)_{\text{spec}}^B (1 - \exp\{-(\mu/\rho)_{\text{spec}}^B \csc(\psi)\rho d\})} \quad (5.6)$$

A further approximation has been proposed by Lorimer (1975) assuming a mean path length for an emitted X-ray between absorption events of $d/2$. The use of this approximation simplifies the evaluation of equation (5.3), producing equation (5.7) below.

$$\frac{I'_A}{I_A} = \exp\{-(\mu/\rho)_{\text{spec}}^A \csc(\psi)\rho(d/2)\} \quad (5.7)$$

The use of this further approximation produces the correction factor for observed against true concentrations as in equation (5.8).

$$\frac{I_A}{I_B} = \frac{I'_A}{I'_B} \times \exp\{-[(\mu/\rho)_{\text{spec}}^B - (\mu/\rho)_{\text{spec}}^A] \csc(\psi)\rho(d/2)\} \quad (5.8)$$

The practical problem in quantifying absorption thus becomes one of obtaining reasonable estimates for ρ and d , or alternatively a figure for the combination ρd the “effective mass path length”. The latter approach is easier in

some practical situations, as it may be possible to obtain a value for the effective mass path length directly from the spectra. This is generally done by either comparing K and L lines from a given element of reasonable concentration within the specimen (which requires that the K and L lines have appreciably different absorption behaviour, requiring $Z > 27$ in practice), or taking a series of spectra from the same area at slightly different tilts to produce a series of data with known relative path lengths (which requires a specimen of clearly known geometry). In this project neither approach for the determination of ρd would be practicable, and estimates of density and thickness are made separately.

5.4.2.2 Fluorescence

Fluorescence effects in EDX microanalysis can arise either from the continuum or from a characteristic line. It is generally held that continuum fluorescence is likely to present a serious problem only in bulk samples, and can reasonably be ignored for thin foils, where continuum fluorescence will be sufficiently small to be trivial compared with other sources of error.

In the case of characteristic fluorescence some problems have been reported even for thin foils, notably for $\text{Cr}K_\alpha$ radiation for low chromium concentrations in iron (Lorimer *et al.*, 1977, see figure 5.3). The levels of fluorescence found were smaller than for bulk specimens, but still appreciable at chromium concentrations of below about 10%, with the measured chromium composition being overestimated by a factor of 30% for a chromium concentration of 1%. This result was obtained from a thin foil which Lorimer estimated to have a thickness of around 2000\AA and hence may be of relevance to this work. Lorimer further suggested that, in thin foils, the degree of this effect would vary as $d \log d$, which approximates to d at small values, where d is the specimen thickness.

In order to quantify the problem for the experimental conditions applying in this case, EDX spectra for the as-transformed bainitic microstructure were considered in detail, as it was known that these should have a composition of (\bar{c}) . Measurements made on the $1\text{Cr}-\frac{1}{2}\text{Mo}$ type steel were found to give a mean value for chromium composition which exceeded \bar{c} by 0.08 at%, or about 10% of the expected value (see tables 6.1–3), which compares with a statistical

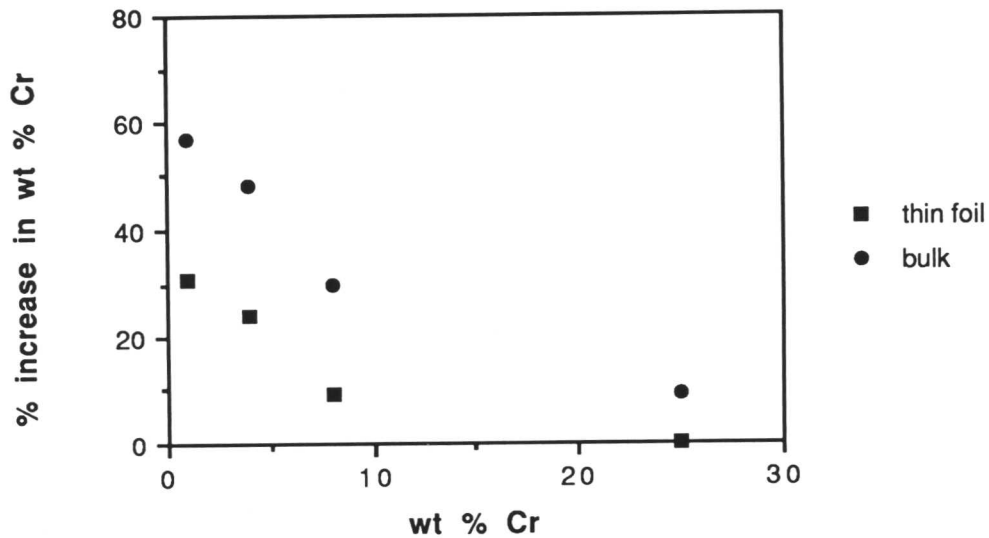


Figure 5.3: Variation in % increase in Cr concentration as a function of Cr concentration for EDX analysis of bulk and thin film specimens (Lorimer *et al.*, 1977)

standard error which was found typically to be of the order of 0.5 at% for these EDX spectra. If Lorimer's relationship for specimen thickness holds, given x_θ which mostly lie between 0.1 and 0.2 μm , then an overestimate attributable to fluorescence for particles of these two sizes can be estimated to be of the order of +0.05 at% and +0.10 at% respectively, a difference which is much less than (and in the reverse direction to) the predicted size effect for all but the shortest ageing times.

In view of the fact that the observed systematic error is relatively small compared with other uncertainties in these EDX measurements, that the effect is exaggerated at small values of c^θ , so accuracy will improve with enrichment during ageing, and that it is difficult to measure x_θ accurately whilst collecting the spectra, it is unlikely that any attempt to allow for this apparent effect will yield a significant improvement in accuracy.

Problems caused by characteristic fluorescence with manganese and molyb-

denum have not been reported, and any such effect can be expected to be trivial in the case of these elements.

5.4.3 Inaccuracies in EDX measurement due to spurious effects

5.4.3.1 Instrumental sources

Spurious X-rays which do not arise from a single event in the specimen by the central electron beam have been attributed to several instrumental factors (Goldstein & Williams, 1978).

- (i) Bremsstrahlung radiation from the condenser apertures and electrons uncollimated by the condenser may generate X-rays from both the specimen and its surroundings.
- (ii) Electrons scattered in the chamber can generate a signal from specimen or surroundings.
- (iii) X-rays can be generated in the specimen or surroundings by electrons scattered from the specimen.
- (iv) X-rays generated within the specimen can cause fluorescence of the surroundings.
- (v) In the case of extraction replicas, X-rays may be produced by the copper grid used to support the specimen.

Effects (ii)–(iv) can be reduced to a trivial level by appropriate experimental practice (consistent electron beam, shielding of the specimen with low-atomic-number materials – hence the beryllium holder – *etc.*). The fifth effect is only a problem if copper is also present in the material (in which case a different grid could be used), otherwise the spurious Cu signal may be safely ignored. However, it is important to maintain vigilance to ensure that these effects do not constitute a serious problem in the collected data.

5.4.3.2 Specimen based sources

Spurious results in EDX analysis have been reported in a number of cases as arising from problems in the specimen. In particular, variation in specimen

thickness is liable to give variable results. This will arise in part because any difficulty in determining an accurate specimen thickness will introduce an error into any estimate of the magnitude of thickness dependent effects (fluorescence and absorption). In addition, it has been suggested that enrichment of one species relative to another in a surface film (such as an oxide layer), will produce further variations of EDX spectra with specimen thickness (Morris, Davies & Treverton, 1977).

Spurious results arising from foreign species at the specimen preparation stage have also been documented (*e.g.*, residues from etching and polishing solutions), emphasizing the need for care in replica preparation: high-purity carbon rods were used as the evaporation source; the optical specimens were scrupulously cleaned before insertion into the evaporator (which is also essential for good carbon film adhesion); and the replicas were thoroughly washed in pure ethanol before the lifting stage (in the ethanol / distilled water solution) to remove etching residues.

5.4.4 Stochastic scatter in EDX measurements

Even when systematic errors in the EDX results, such as could arise from absorption, fluorescence, spurious X-rays *etc.*, have been accounted for, an individual EDX composition will be subject to an error attributable to stochastic scatter in the X-ray signal intensity (both background and characteristic). The EDX spectrum analysis program makes an estimate of this error on the basis of the observed noise in the collected spectrum, enabling the problem to be quantified approximately, and the scatter can be reduced by extending the time period over which the spectrum is collected, to increase the signal : noise ratio.

In practice, the composition which is measured from an EDX spectrum, c_{obs}^{θ} will be related to the actual composition, c_{real}^{θ} , by equation (5.9)

$$c_{\text{obs}}^{\theta} = c_{\text{real}}^{\theta} \pm x \quad (5.9)$$

where x is a factor representative of the stochastic scatter in the observed signal intensity at the characteristic frequency under analysis. The stochastic nature

of the error imposed on individual measurements by this factor means that confidence limits in the measured mean composition for a given ageing time can be increased by the standard expedient of increasing the number of measurements taken from specimens aged to that time (hence, approximately 30 particles were measured at each ageing time in the current work).

It is evident that, where the characteristic-peak intensity is small (for a small concentration of the element concerned), and the noise in the background signal is of a similar order of magnitude, it is possible that the stochastic scatter in c^θ is larger than the magnitude of c^θ , which will produce an occasional negative result for the concentration of the element when the spectrum is analysed. Such a result indicates that the X-ray intensity at the characteristic frequency in that particular spectrum is less than that which would be expected from background radiation alone, as a result of the stochastic noise in the background signal.

A negative value for c^θ is clearly of no physical significance as a composition, and results obtained from specimens where this problem arises must be treated with considerable suspicion; the true composition is so small as to be of a similar order of magnitude to the resolution of the technique. Nevertheless, because such results arise from a random process inherent in the EDX technique, it is necessary that they be included when mean compositions are calculated from a large number of observed c^θ values. In the current work, where substitutional alloying content is relatively small at short ageing times, conditions were set as carefully as possible to reduce the stochastic scatter to a minimum (by ensuring that the error in each reading, which was calculated by the analysis program from the spectrum and was, in effect, an estimate of this scatter, remained small). In consequence, the number of spectra which produced negative values for a composition was kept small, although such results were occasionally obtained, and were retained for analysis for the above reason.

Chapter 6

AGEING OF BAINITIC MICROSTRUCTURES:

Fe–Cr–Mo POWER PLANT STEEL

6.1 EDX Compositional Data

6.1.1 Procedure

The EDX microanalytical data for the series of heat treatments done on the 1Cr– $\frac{1}{2}$ Mo power plant steel were collected and analysed, in accordance with the procedure described in the previous chapter, by comparison with the simple analytical solution of equation (2.9). This equation is used extensively in the following pages, so it is reproduced below, as equation (6.1), for ease of reference:

$$t_c = \frac{\pi[x_\theta(c^\theta - \bar{c})]^2}{16D_\alpha(\bar{c} - c^{\alpha\theta})^2} \quad (6.1)$$

where t_c is the time to reach cementite of concentration c^θ ,

\bar{c} is the mean alloy composition,

x_θ is the cementite particle size,

$c^{\alpha\theta}$ is the composition of α in equilibrium with θ ,

and D_α is the diffusivity in ferrite.

Measurements for particle size and degree of enrichment for a given ageing time are processed by a regression analysis for $(c - \bar{c})$ versus $1/x_\theta$, and the results are presented in table 6.1 for the series of specimens aged at 510°C, in table 6.2 for specimens aged at 565°C, and in table 6.3 for specimens aged at 625°C. In all three cases the initial microstructures had been generated by heat treatments prior to tempering to be fully bainitic. It should be noted that the units used in the table are μm for x_θ (the measured mean linear intercept) and at.% of total

substitutionals¹ for $(c - \bar{c})$, and that the data presented for the best fit produced from the regression procedure will be consequently in similar non-standard units.

6.1.2 Accuracy of EDX data for the elements present

The accuracy of EDX data is found to be dependent, to some extent, on the substitutional element under investigation. The tables of experimental data show relatively better agreement to proportionality of $(c - \bar{c})$ to x_θ^{-1} for chromium and manganese than for molybdenum, especially at shorter ageing times; observed molybdenum compositions are substantively greater than \bar{c} at zero time, and higher than the analytical model predicts after ageing; and nothing of statistical significance is obtained when the regression analysis is performed on the silicon data.

(i) Chromium and manganese

The characteristic K_α peaks for these two elements are well defined, reasonably large, and readily distinguished from signals produced by the other elements present. The equilibrium partition coefficient between cementite and ferrite, $c^{\theta\alpha}/c^{\alpha\theta}$, is much greater than unity in both cases; therefore diffusion in ferrite should be the controlling process, and appreciable enrichment will occur reasonably quickly, making the observed random variations in measured c_0^θ (as-transformed cementite compositions) trivial relative to $(c - \bar{c})$. In consequence, the EDX composition measurements are well representative of real cementite compositions.

(ii) Molybdenum

Molybdenum analysis uses the L peaks, as the energy required to produce K de-excitations is too large. It is well established that the spread of the molybdenum characteristic coupled with its proximity in the spectrum to the sulphur K_α

¹ For much of this work, c^θ is expressed as an atomic percentage of the substitutional elements only, excluding carbon. This facilitates development of models for processes where diffusion only in the substitutional lattice is of concern, and is also in accordance with EDX methods which do not detect carbon. Atomic percentages are used so that conversion to an absolute (*i.e.*, inclusive of carbon) value is done by way of a simple linear relationship, assuming stoichiometric carbon content of cementite.

signal can cause the two to become difficult to distinguish in spectra from steels containing both elements (as did the steel in the current work, see appendix). This could be the cause of the non-zero as-transformed value for $(c - \bar{c})$. Furthermore, the molybdenum peak intensity is appreciably less than those from chromium and manganese (in part because the molybdenum content is lower), resulting in a poorer characteristic-signal to background-continuum-noise ratio which could be detrimental to the accuracy of the determined composition, and the larger atomic number differential between iron and molybdenum than between iron and the other substitutionals would exaggerate any errors inherent in the correction.

It can also be noted that $c^{\theta\alpha}/c^{\alpha\theta}$ is not so large for molybdenum as for chromium and manganese, and that the diffusion coefficient is less; therefore, the enrichment process is slower and any experimental errors which are present will remain significant relative to $(c - \bar{c})$ for longer ageing times.

(iii) Silicon

Silicon differs from the other elements under investigation in that $c^{\theta\alpha}/c^{\alpha\theta}$ is less than unity, so that silicon rapidly passes into ferrite from cementite. Any reading obtained for silicon in cementite will be too small to be experimentally significant given the possible scatter. Consequently, although silicon EDX measured compositions are presented for completeness, the data are of inadequate accuracy for further analysis.

6.2 Variation of Composition Change with Particle Size

Typical examples of sets of compositional measurements for a given heat treatment, plotted against x_{θ}^{-1} in accordance with equation (6.1), are presented in figure 6.1(a)–(e). Each point on these graphs represents the measured composition and size of an individual cementite particle in the aged specimen.

6.2.1 The as-transformed condition

Bainitic carbides are expected to form with negligible partitioning of substitutional alloying elements during transformation (section 2.2). Nevertheless, it is

also noticeable in figure 6.1(a) that in the as-transformed state larger particles appear to show a trend to slightly higher compositions, in contrast to the situation for aged specimens where smaller particles have enriched to a greater degree. Similar trends have been found for the as-transformed specimens in other series in this steel, as is illustrated by figure 6.2.

Where this effect is observed for chromium, it may be attributable to the fluorescence effect noted by Lorimer *et al.*(1977) and discussed in the previous chapter, but similar results are observed for manganese and molybdenum concentrations. A tentative explanation is offered that this effect is due to the fact that the larger particles of cementite formed first, and hence have undergone a little enrichment even at the low transformation temperatures. However, although the effect is plausible, it is very small, and of low statistical significance, and disappears rapidly as soon as the ageing treatments and the associated general enrichment process begin. It would inevitably disappear rapidly, because of the increased enrichment rate of smaller particles relative to larger ones that is predicted by equation (6.1).

6.2.2 Variation as ageing time increases

Rearranging equation (6.1) to give the relationship in equation (6.2), it can be seen that, for a given time, the change in composition of cementite, $(c^\theta - \bar{c}) \propto 1/x_\theta$, the mean linear intercept.

$$(c^\theta - \bar{c}) = \frac{t_c^{1/2}}{x_\theta} \frac{4D_\alpha^{1/2}(c^{\alpha\theta} - \bar{c})}{\pi^{1/2}} \quad (6.2)$$

where $4D_\alpha^{1/2}(c^{\alpha\theta} - \bar{c})/\pi^{1/2}$ is constant for a given material at a fixed temperature.

It is apparent in the data presented in the tables for the $(c - \bar{c}) \text{ v } x_\theta$ that, as the ageing time was increased, the correlation coefficient which is calculated for this predicted size effect (*i.e.*, $(c - \bar{c})$ versus $1/x_\theta$) shows a general improvement with prolonged ageing. The trend is most clearly exhibited by chromium, less so by manganese due to the lower degree of enrichment, and rather poorly by molybdenum as a consequence of the problems noted above which are attached

to obtaining accurate EDX data for this element. No particular pattern is shown for silicon, which, in any case, is more soluble in ferrite, and hence will tend to partition in the opposite direction to the other substitutional alloying elements at a rate which is not governed by the rate of diffusion in ferrite, so that equation (6.1) would not apply.

The gradient of the best fit line also shows a general trend of increasing with time. This is again in accordance with the size effect predicted by the theory behind equation (6.1): smaller particles would be expected to increase in composition more rapidly, such that the effect of particle size on composition change becomes more marked with increased ageing time. A semi-empirical illustration of this feature is given below (section 6.2.4). The t-distribution significance test on the regression analysis also generates a generally increasing level of significance to the calculated best fit gradient. This acts as further confirmation that a size effect is present. These trends are also illustrated by the plots in figure 6.1(a–e).

It can be seen from the figures that individual measured compositions are scattered around the theoretically expected composition to some degree. The distribution around \bar{c} in the as-transformed condition suggests that this is probably, at least in part, a statistical fluctuation associated with the EDX technique; it is known from theory that bainite forms with negligible substitutional redistribution, so that c_0 for the cementite particles should be very close to \bar{c} . This scatter tends to be more marked for smaller particles, where a weaker intensity of signal would lead to a higher signal to noise ratio which would exaggerate any such effect.

A comparison of compositions for earlier and later aged specimens in figure 6.1 suggests that the degree of scatter shown by individual values of c^θ for a particular ageing time is greater for longer ageing times. It should be emphasized that the simple analytical model does not account for any soft impingement, where the diffusion fields of adjacent particles overlap cause a slowing down in the rate of diffusion. Nor does the model account for irregular interparticle spacing of the type which was observed experimentally; it considers a single,

‘average’ particle with a similarly averaged ferrite region adjacent to it. In effect, to apply the model to a multi-precipitate system is to assume that both the cementite particle size and particle distribution are uniform, which is known not to be the case. In reality, more closely spaced cementite particles will be subject to soft impingement effects after a shorter ageing time than will those which are more widely spaced. It is probable that, at longer ageing times and higher temperatures where soft impingement in the ferrite becomes of significance, some of the c^θ measurements will be obtained from (more closely-spaced) particles where the effect is larger, resulting in a lower c^θ than that predicted by the model; whereas more widely-spaced particles may continue to fit the analytical model. This would add a systematic scatter to the experimental statistical scatter at longer ageing times, in keeping with the actual scatter of data which is seen in the experimental c^θ distributions (figure 6.1(a-e)).

The intercept of the best fit line with the y-axis on the $(c - \bar{c})$ versus $1/x_\theta$ plot) was also noted. This corresponds to $x_\theta = \infty$ so has no physical significance, but it can be seen intuitively that an infinitely large particle will show zero mean enrichment by diffusion of a species at a finite rate for all finite ageing times. If this intercept ceases to be at \bar{c} then it is evident that equation (6.1) no longer describes the situation entirely.

It was found that the best-fit line intercept with the y-axis was zero to within the bounds of experimental accuracy except at the longest ageing times, where a small positive value was consistently observed. It appears that $(c - \bar{c})$ ceases to be strictly proportional to x_θ^{-1} , although a marked size effect is still observed.

It is suggested that this deviation from the predictions of equation (6.1) may arise from the way that the analytical model considers the structure to be of the form of one slab of cementite, of thickness x_θ , in slabs of ferrite whose size is calculated from the lever rule, and does not include a consideration of soft impingement. It is possible that smaller cementite particles will be associated with smaller ferritic sub-units, in which case they will be more closely spaced. Thus, the onset of significant levels of soft impingement could affect the enrich-

ment of smaller cementite particles sooner than larger ones. A slowing down of the enrichment rate of the smaller particles relative to the large ones due to soft impingement would lead to a non-linearity in $(c - \bar{c})$ versus x_θ^{-1} , and a tendency for the intercept of the best fit line with $x_\theta^{-1} = 0$ to be non-zero. In any case, the onset of soft impingement means that equation (6.1) cannot rigorously be applied.

It is also possible that the problem arises in part as a consequence of particle coarsening, which the analytical model ignores, but which seemed to be occurring to a small degree from x_θ measurements. As a result of coarsening during ageing, it is not strictly correct to compare $x_\theta = 0.15\mu\text{m}$ (for instance) at zero time and large ageing time under the assumption that the data represents the same particle. It can be assumed that, where particle coarsening is taking place, enrichment of a given particle will have occurred at a more rapid rate during the early stages of ageing when the relevant cementite particle was smaller; hence, some deviation from strict proportionality in the $(c - \bar{c})$ versus x_θ^{-1} relation can be expected.

6.2.3 Mixed microstructure

The data for the approximately 30% bainitic / 70% allotriomorphic ferrite microstructure aged at 565°C are presented in table 6.4. It is immediately apparent that the cementite enrichment rate is more rapid than for the fully-bainitic case at this temperature, especially in the early stages of ageing. This can be attributed in part to the fact that the cementite particle size tends to be slightly smaller than was the case for the fully-bainitic microstructure, which equation (6.1) predicts should lead to an increased rate of enrichment. Furthermore, it can be assumed that carbon partitions into the retained austenite during formation of the allotriomorphic ferrite phase, whereas the relative proportions of substitutional alloying elements and iron remain the same; hence, the 30% bainitic region will contain almost all the carbon. This leads to a much greater carbon concentration in α_b than was the case for the fully-bainitic microstructure, and a correspondingly increased value for V_θ in this region. In order to maintain equilibrium partitioning into an increased volume fraction of cementite, it is

clear that both $c^{\alpha\theta}$ and $c^{\theta\alpha}$ will be reduced compared with the fully-bainitic case, increasing the driving force for the rate-controlling process of diffusion in the ferrite ($(\bar{c} - c^{\alpha\theta})$ in equation (6.1)) and thus reducing t_c .

Apart from the difference in enrichment rate, general trends in the data are similar to the fully-bainitic case, although the statistical scatter associated with single measurements of composition change in the mixed microstructure is generally found to be greater. This may be due to the smaller particle size: throughout the work values of $(c^\theta - \bar{c})$ appeared to be less reliable for smaller cementite particles. In consequence, despite the more rapid enrichment rate, correlation to the predicted size effect is much the same as in the case of the fully-bainitic microstructure aged at 565°C.

It can be seen intuitively, and from equation (6.1), that reducing x_θ and increasing V_θ will lead to a much reduced x_α , or inter-cementite spacing. Consequently, soft impingement can be expected to occur earlier, so that the problems associated with it (above) will become significant at relatively shorter ageing times. This may explain the fact that the correlation of the $(c - \bar{c}) \propto x_\theta^{-1}$ relationship ceases to improve (and in some cases deteriorates) at longer ageing times, and that the enrichment rate of the molybdenum in particular appears to slow at longer ageing times. Nevertheless, a general trend of improved agreement with equation (6.1) is exhibited by the data as ageing proceeds.

CHROMIUM at 510°C						
Ageing time (hours)	No of points	Mean c change (at %)	Mean x_θ μm	Data from best fit $(c - \bar{c}) \text{ v } x_\theta$		
				correlation	gradient	significance
0	31	0.06	0.161	-0.10	-0.033	<0.90
2	28	-0.02	0.149	0.11	0.022	<0.90
6	34	0.46	0.148	0.29	0.076	0.90
12	26	0.34	0.155	0.28	0.068	<0.90
24	30	0.28	0.149	-0.12	-0.032	<0.90
48	28	0.58	0.157	0.45	0.098	0.95
96	34	0.58	0.169	0.19	0.056	<0.90
168	27	0.92	0.160	0.43	0.144	0.95
336	28	1.49	0.162	0.56	0.138	0.98
672	31	1.99	0.157	0.59	0.163	0.99
1008	27	2.22	0.163	0.54	0.141	0.95
1344	32	2.23	0.169	0.57	0.149	0.98
2016	30	2.36	0.166	0.55	0.177	0.98
2688	28	2.72	0.158	0.56	0.192	0.98
4032	34	2.81	0.162	0.54	0.232	0.99
6240	27	3.89	0.171	0.61	0.283	0.99
8064	28	4.47	0.173	0.52	0.245	0.98

Table 6.1 (a) Fe–Cr–Mo power plant steel, initially with a fully-bainitic microstructure, aged at 510°C. EDX analysis data obtained for chromium content of cementite.

MANGANESE at 510°C						
Ageing time (hours)	No of points	Mean c change (at %)	Mean x_θ μm	Data from best fit $(c - \bar{c})$ v x_θ		
				correlation	gradient	significance
0	31	0.00	0.161	0.10	0.024	<0.90
2	28	0.04	0.149	-0.18	-0.025	<0.90
6	34	0.24	0.148	0.36	0.073	0.90
12	26	0.24	0.155	0.47	0.092	0.95
24	30	0.35	0.149	0.10	0.021	<0.90
48	28	0.41	0.157	0.43	0.087	0.95
96	34	0.24	0.169	0.17	0.041	<0.90
168	27	0.66	0.160	0.28	0.068	<0.90
336	28	0.58	0.162	0.42	0.042	0.90
672	31	0.78	0.157	0.46	0.062	0.95
1008	27	0.72	0.163	0.48	0.058	0.95
1344	32	0.79	0.169	0.53	0.088	0.99
2016	30	0.88	0.166	0.52	0.100	0.95
2688	28	1.00	0.158	0.37	0.114	0.90
4032	34	1.13	0.162	0.39	0.092	0.95
6240	27	1.26	0.171	0.52	0.121	0.98
8064	28	1.66	0.173	0.54	0.144	0.99

Table 6.1 (b) Fe–Cr–Mo power plant steel, initially with a fully-bainitic microstructure, aged at 510°C. EDX analysis data obtained for manganese content of cementite.

MOLYBDENUM at 510°C						
Ageing time (hours)	No of points	Mean c change (at %)	Mean x_θ μm	Data from best fit $(c - \bar{c}) \text{ v } x_\theta$		
				correlation	gradient	significance
0	31	0.42	0.161	0.00	0.001	<0.90
2	28	0.21	0.149	-0.05	-0.007	<0.90
6	34	0.54	0.148	0.34	0.101	0.95
12	26	0.55	0.155	-0.35	-0.103	0.90
24	30	0.34	0.149	-0.22	-0.061	<0.90
48	28	0.60	0.157	0.07	0.017	<0.90
96	34	0.39	0.169	0.00	0.000	<0.90
168	27	0.54	0.160	0.13	0.039	<0.90
336	28	0.35	0.162	-0.10	-0.017	<0.90
672	31	0.46	0.157	0.22	0.048	<0.90
1008	27	0.79	0.163	0.30	0.066	<0.90
1344	32	0.58	0.169	0.00	0.003	<0.90
2016	30	0.49	0.166	0.48	0.126	0.90
2688	28	0.89	0.158	0.19	0.044	<0.90
4032	34	0.67	0.162	0.29	0.055	0.90
6240	27	0.88	0.171	0.42	0.080	0.95
8064	28	1.02	0.173	0.42	0.125	0.95

Table 6.1 (c) Fe–Cr–Mo power plant steel, initially with a fully-bainitic microstructure, aged at 510°C. EDX analysis data obtained for molybdenum content of cementite.

SILICON at 510°C						
Ageing time (hours)	No of points	Mean c change (at %)	Mean x_θ μm	Data from best fit ($c - \bar{c}$) v x_θ		
				correlation	gradient	significance
0	31	-0.20	0.161	-0.21	-0.036	<0.90
2	28	-0.17	0.149	0.12	0.014	<0.90
6	34	-0.08	0.148	0.01	0.002	<0.90
12	26	-0.31	0.155	0.07	0.012	<0.90
24	30	-0.28	0.149	0.07	0.018	<0.90
48	28	-0.13	0.157	-0.07	-0.009	<0.90
96	34	-0.40	0.169	0.10	0.018	<0.90
168	27	-0.21	0.160	-0.10	-0.017	<0.90
336	28	-0.28	0.162	0.25	0.037	<0.90
672	31	-0.16	0.157	-0.24	-0.044	<0.90
1008	27	-0.23	0.163	-0.28	-0.044	<0.90
1344	32	-0.16	0.169	-0.05	-0.011	<0.90
2016	30	-0.19	0.166	-0.20	-0.020	<0.90
2688	28	-0.20	0.158	-0.38	-0.074	0.90
4032	34	-0.26	0.162	0.12	0.023	<0.90
6240	27	-0.25	0.171	-0.06	-0.009	<0.90
8064	28	-0.28	0.173	0.32	0.063	0.90

Table 6.1 (d) Fe-Cr-Mo power plant steel, initially with a fully-bainitic microstructure, aged at 510°C. EDX analysis data obtained for silicon content of cementite.

CHROMIUM at 565°C						
Ageing time (hours)	No of points	Mean c change (at %)	Mean x_θ μm	Data from best fit $(c - \bar{c}) \text{ v } x_\theta$		
				correlation	gradient	significance
0	34	0.11	0.160	-0.10	-0.021	<0.90
1	26	0.53	0.165	-0.12	-0.032	<0.90
4	29	0.54	0.149	0.11	0.019	<0.90
8	29	0.50	0.156	0.29	0.087	0.95
12	37	0.59	0.160	0.35	0.062	0.95
24	32	0.65	0.173	0.20	0.068	<0.90
48	27	1.19	0.159	0.42	0.136	0.95
96	31	1.67	0.167	0.52	0.151	0.98
168	30	1.77	0.162	0.57	0.201	0.99
336	31	1.89	0.171	0.38	0.186	0.90
672	26	3.09	0.163	0.40	0.175	0.90
1344	31	3.70	0.177	0.45	0.264	0.98
2688	29	3.53	0.170	0.47	0.247	0.95
4032	32	4.00	0.180	0.46	0.302	0.98
7002	27	4.69	0.174	0.54	0.331	0.99

Table 6.2 (a) Fe-Cr-Mo power plant steel, initially with a fully-bainitic microstructure, aged at 565°C. EDX analysis data obtained for chromium content of cementite.

MANGANESE at 565°C						
Ageing time (hours)	No of points	Mean c change (at %)	Mean x_θ μm	Data from best fit $(c - \bar{c})$ v x_θ		
				correlation	gradient	significance
0	34	0.05	0.160	-0.11	-0.024	<0.90
1	26	0.23	0.165	-0.02	-0.009	<0.90
4	29	0.33	0.149	-0.05	-0.007	<0.90
8	29	0.30	0.156	0.13	0.025	<0.90
12	37	0.33	0.160	0.28	0.037	0.90
24	32	0.41	0.173	0.48	0.152	0.98
48	27	0.74	0.159	0.29	0.133	0.90
96	31	1.06	0.167	0.42	0.080	0.95
168	30	0.86	0.162	0.58	0.118	0.99
336	31	1.37	0.171	0.28	0.172	<0.90
672	26	1.17	0.163	0.49	0.156	0.99
1344	31	1.92	0.177	0.50	0.187	0.98
2688	29	1.97	0.170	0.56	0.207	0.99
4032	32	2.41	0.180	0.38	0.149	0.95
7002	27	3.08	0.174	0.55	0.177	0.98

Table 6.2 (b) Fe–Cr–Mo power plant steel, initially with a fully-bainitic microstructure, aged at 565°C. EDX analysis data obtained for manganese content of cementite.

MOLYBDENUM at 565°C						
Ageing time (hours)	No of points	Mean c change (at %)	Mean x_θ μm	Data from best fit $(c - \bar{c}) \text{ v } x_\theta$		
				correlation	gradient	significance
0	34	0.67	0.160	-0.13	-0.036	<0.90
1	26	0.82	0.165	0.09	0.037	<0.90
4	29	0.31	0.149	0.06	0.012	<0.90
8	29	0.14	0.156	0.07	0.019	<0.90
12	37	0.49	0.160	-0.04	-0.007	<0.90
24	32	0.46	0.173	0.11	0.036	<0.90
48	27	0.31	0.159	0.13	0.046	<0.90
96	31	0.79	0.167	0.29	0.080	<0.90
168	30	0.64	0.162	0.18	0.052	<0.90
336	31	0.84	0.171	0.34	0.075	0.90
672	26	1.03	0.163	0.06	0.026	<0.90
1344	31	0.76	0.177	0.43	0.112	0.98
2688	29	1.30	0.170	-0.31	-0.075	<0.90
4032	32	0.89	0.180	0.42	0.170	0.98
7002	27	1.40	0.174	0.02	0.007	<0.90

Table 6.2 (c) Fe–Cr–Mo power plant steel, initially with a fully-bainitic microstructure, aged at 565°C. EDX analysis data obtained for molybdenum content of cementite.

SILICON at 565°C						
Ageing time (hours)	No of points	Mean c change (at %)	Mean x_θ μ m	Data from best fit ($c - \bar{c}$) v x_θ		
				correlation	gradient	significance
0	34	-0.25	0.160	0.25	-0.051	<0.90
1	26	-0.33	0.165	0.02	0.004	<0.90
4	29	-0.12	0.149	0.02	0.007	<0.90
8	29	-0.44	0.156	-0.18	-0.029	<0.90
12	37	-0.09	0.160	-0.13	-0.010	<0.90
24	32	-0.06	0.173	-0.20	-0.046	<0.90
48	27	-0.39	0.164	-0.16	-0.038	<0.90
96	31	-0.16	0.167	0.01	0.002	<0.90
168	30	-0.38	0.162	-0.29	-0.058	0.90
336	31	-0.40	0.171	-0.24	-0.045	<0.90
672	26	-0.40	0.163	-0.18	-0.039	<0.90
1344	31	-0.23	0.177	-0.25	-0.064	<0.90
2688	29	-0.43	0.170	-0.23	-0.046	<0.90
4032	32	-0.22	0.180	-0.13	-0.031	<0.90
7002	27	-0.37	0.174	0.13	0.028	<0.90

Table 6.2 (d) Fe-Cr-Mo power plant steel, initially with a fully-bainitic microstructure, aged at 565°C. EDX analysis data obtained for silicon content of cementite.

CHROMIUM at 625°C						
Ageing time (hours)	No of points	Mean c change (at %)	Mean x_θ μm	Data from best fit $(c - \bar{c})$ v x_θ		
				correlation	gradient	significance
0	27	0.07	0.154	-0.05	-0.016	<0.90
1	28	0.20	0.140	0.22	0.069	<0.90
2	30	0.40	0.166	0.27	0.060	<0.90
4	32	0.89	0.156	0.35	0.082	0.90
8	29	1.37	0.152	0.48	0.124	0.98
12	32	1.88	0.161	0.40	0.154	0.95
24	25	1.76	0.155	0.56	0.215	0.98
48	31	2.86	0.176	0.57	0.258	0.99
96	30	2.95	0.162	0.54	0.293	0.98
168	28	3.30	0.181	0.46	0.298	0.95
336	32	4.57	0.183	0.62	0.319	0.99
672	29	5.78	0.176	0.59	0.348	0.99
1344	31	6.16	0.188	0.66	0.358	0.99
2688	30	6.81	0.190	0.60	0.296	0.95
4032	26	7.93	0.177	0.50	0.308	0.95
6048	29	8.69	0.186	0.48	0.382	0.98

Table 6.3 (a) Fe–Cr–Mo power plant steel, initially with a fully-bainitic microstructure, aged at 625°C. EDX analysis data obtained for chromium content of cementite.

MANGANESE at 625°C						
Ageing time (hours)	No of points	Mean c change (at %)	Mean x_θ μm	Data from best fit $(c - \bar{c})$ v x_θ		
				correlation	gradient	significance
0	27	0.03	0.154	-0.19	-0.029	<0.90
1	28	0.14	0.140	0.21	0.049	<0.90
2	30	0.17	0.166	0.29	0.031	<0.90
4	32	0.74	0.156	0.46	0.068	0.90
8	29	0.68	0.152	0.50	0.099	0.95
12	32	0.85	0.161	0.51	0.091	0.98
24	25	1.13	0.155	0.47	0.086	0.98
48	31	1.32	0.176	0.40	0.094	0.95
96	30	0.80	0.162	0.34	0.090	0.90
168	28	1.70	0.181	0.23	0.068	<0.90
336	32	1.49	0.183	0.48	0.107	0.98
672	29	1.76	0.176	0.58	0.178	0.99
1344	31	2.23	0.188	0.41	0.095	0.95
2688	30	2.72	0.190	0.52	0.167	0.98
4032	26	3.41	0.177	0.51	0.190	0.99
6048	29	3.45	0.186	0.37	0.164	0.95

Table 6.3 (b) Fe–Cr–Mo power plant steel, initially with a fully-bainitic microstructure, aged at 625°C. EDX analysis data obtained for manganese content of cementite.

MOLYBDENUM at 625°C						
Ageing time (hours)	No of points	Mean c change (at %)	Mean x_θ μm	Data from best fit $(c - \bar{c}) \text{ v } x_\theta$		
				correlation	gradient	significance
0	27	0.42	0.154	-0.22	-0.070	<0.90
1	28	0.64	0.140	0.06	0.024	<0.90
2	30	0.41	0.146	-0.36	-0.155	<0.90
4	32	0.73	0.156	0.32	0.040	<0.90
8	29	0.29	0.152	-0.04	-0.007	<0.90
12	32	0.95	0.161	0.13	0.017	<0.90
24	25	0.58	0.155	0.20	0.047	<0.90
48	31	0.83	0.176	0.10	0.025	<0.90
96	30	0.41	0.162	-0.19	-0.043	<0.90
168	28	0.91	0.181	0.33	0.084	0.90
336	32	1.07	0.183	0.35	0.078	0.90
672	29	0.53	0.176	0.35	0.096	0.90
1344	31	0.89	0.188	0.43	0.115	0.95
2688	30	1.19	0.190	0.62	0.216	0.99
4032	26	1.02	0.177	0.10	0.035	<0.90
6048	29	1.60	0.186	0.39	0.005	<0.90

Table 6.3 (c) Fe–Cr–Mo power plant steel, initially with a fully-bainitic microstructure, aged at 625°C. EDX analysis data obtained for molybdenum content of cementite.

SILICON at 625°C						
Ageing time (hours)	No of points	Mean c change (at %)	Mean x_θ μm	Data from best fit $(c - \bar{c}) \text{ v } x_\theta$		
				correlation	gradient	significance
0	27	-0.20	0.154	0.09	0.019	<0.90
1	28	-0.38	0.140	-0.13	-0.019	<0.90
2	30	-0.11	0.166	0.11	0.018	<0.90
4	32	-0.35	0.156	0.20	0.025	<0.90
8	29	-0.26	0.152	0.16	0.025	<0.90
12	32	-0.21	0.161	-0.18	-0.027	<0.90
24	25	-0.38	0.155	-0.25	-0.033	<0.90
48	31	-0.26	0.176	0.16	0.029	<0.90
96	30	-0.38	0.162	-0.39	-0.074	0.90
168	28	-0.26	0.181	0.13	0.020	<0.90
336	32	-0.30	0.183	-0.03	-0.004	<0.90
672	29	-0.26	0.176	-0.07	-0.010	<0.90
1344	31	-0.38	0.188	-0.36	-0.080	0.90
2688	30	-0.27	0.190	-0.30	-0.040	<0.90
4032	26	-0.39	0.177	0.26	0.052	<0.90
6048	29	-0.14	0.186	-0.03	-0.007	<0.90

Table 6.3 (d) Fe-Cr-Mo power plant steel, initially with a fully-bainitic microstructure, aged at 625°C. EDX analysis data obtained for silicon content of cementite.

CHROMIUM at 565°C						
Ageing time (hours)	No of points	Mean c change (at %)	Mean x_θ μm	Data from best fit $(c - \bar{c})$ v x_θ		
				correlation	gradient	significance
0	29	0.15	0.150	-0.02	-0.040	<0.90
1	26	0.49	0.146	0.31	0.052	<0.90
2	27	0.35	0.140	0.03	0.006	<0.90
4	32	0.82	0.143	0.13	0.027	<0.90
12	32	0.87	0.150	0.38	0.077	0.95
24	28	1.30	0.164	0.25	0.082	<0.90
48	28	1.97	0.145	0.61	0.214	0.99
96	31	2.73	0.152	0.61	0.260	0.99
168	27	3.54	0.152	0.59	0.296	0.99
336	27	4.37	0.135	0.47	0.350	0.98
672	29	4.46	0.150	0.28	0.210	<0.90
1344	31	4.82	0.157	0.62	0.447	0.99
2688	26	5.79	0.152	0.51	0.357	0.98
5376	31	6.53	0.156	0.43	0.443	0.95

Table 6.4 (a) Fe–Cr–Mo power plant steel, initially with a mixed ferritic and bainitic microstructure, aged at 565°C. EDX analysis data obtained for chromium content of cementite.

MANGANESE at 565°C						
Ageing time (hours)	No of points	Mean c change (at %)	Mean x_θ μ m	Data from best fit ($c - \bar{c}$) v x_θ		
				correlation	gradient	significance
0	29	0.03	0.150	-0.21	-0.039	<0.90
1	26	0.41	0.146	0.07	0.007	<0.90
2	27	0.32	0.140	0.14	0.014	<0.90
4	32	0.32	0.143	0.05	0.004	<0.90
12	32	0.40	0.150	0.40	0.044	0.95
24	28	0.95	0.164	0.30	0.057	<0.90
48	28	0.89	0.145	0.67	0.149	0.95
96	31	0.98	0.152	0.48	0.108	0.95
168	27	1.20	0.152	0.61	0.163	0.99
336	27	2.18	0.135	0.40	0.083	0.90
672	29	2.71	0.150	0.22	0.086	<0.90
1344	31	2.56	0.157	0.49	0.196	0.98
2688	26	2.60	0.152	0.34	0.200	0.90
5376	31	3.75	0.156	0.60	0.151	0.99

Table 6.4 (b) Fe–Cr–Mo power plant steel, initially with a mixed ferritic and bainitic microstructure, aged at 565°C. EDX analysis data obtained for manganese content of cementite.

MOLYBDENUM at 565°C						
Ageing time (hours)	No of points	Mean c change (at %)	Mean x_θ μm	Data from best fit ($c - \bar{c}$) v x_θ		
				correlation	gradient	significance
0	29	0.38	0.150	-0.25	-0.055	<0.90
1	26	0.62	0.146	-0.10	-0.018	<0.90
2	27	0.56	0.140	-0.13	-0.020	<0.90
4	32	0.56	0.143	0.13	0.020	<0.90
12	32	0.80	0.150	0.10	0.016	<0.90
24	28	0.97	0.164	0.17	0.045	<0.90
48	28	0.61	0.145	0.45	0.111	0.95
96	31	0.56	0.152	0.22	0.050	<0.90
168	27	1.17	0.152	0.59	0.152	0.98
336	27	1.02	0.135	0.67	0.170	0.99
672	29	0.77	0.150	-0.18	-0.048	<0.90
1344	31	1.28	0.157	0.22	0.090	<0.90
2688	26	1.39	0.152	0.34	0.104	<0.90
5376	31	1.44	0.156	0.61	0.213	0.99

Table 6.4 (c) Fe-Cr-Mo power plant steel, initially with a mixed ferritic and bainitic microstructure, aged at 565°C. EDX analysis data obtained for molybdenum content of cementite.

SILICON at 565°C						
Ageing time (hours)	No of points	Mean c change (at %)	Mean x_θ μm	Data from best fit $(c - \bar{c}) \text{ v } x_\theta$		
				correlation	gradient	significance
0	29	-0.39	0.150	0.20	0.030	<0.90
1	26	-0.29	0.146	0.17	0.018	<0.90
2	27	-0.21	0.140	0.26	0.026	<0.90
4	32	-0.40	0.143	-0.10	-0.011	<0.90
12	32	-0.23	0.150	-0.03	-0.003	<0.90
24	28	-0.36	0.164	0.10	0.012	<0.90
48	28	-0.21	0.145	0.15	0.010	<0.90
96	31	-0.39	0.152	0.23	0.009	<0.90
168	27	-0.10	0.152	0.09	0.012	<0.90
336	27	-0.37	0.135	-0.46	-0.039	0.95
672	29	-0.19	0.150	0.33	0.040	<0.90
1344	31	-0.51	0.157	-0.08	-0.012	0.98
2688	26	-0.28	0.152	-0.15	-0.016	<0.90
5376	31	-0.32	0.156	-0.14	-0.020	<0.90

Table 6.4 (d) Fe-Cr-Mo power plant steel, initially with a mixed ferritic and bainitic microstructure, aged at 565°C. EDX analysis data obtained for silicon content of cementite.

Fe-Cr-Mo STEEL AFTER 8 HOURS AT 565 °C

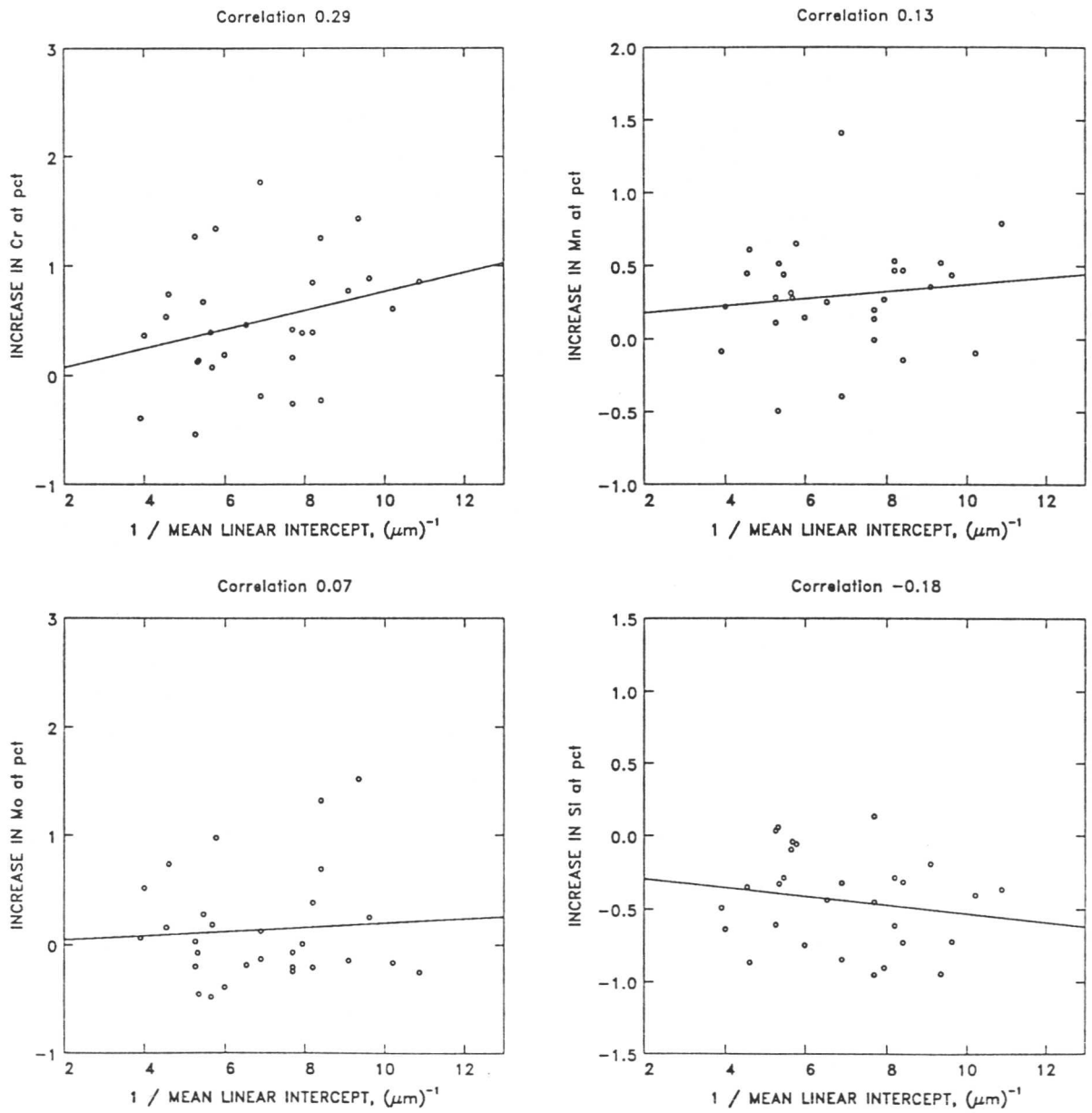


Figure 6.1(b): EDX microanalytical data for steel 1

Fe-Cr-Mo STEEL AFTER 48 HOURS AT 565 °C

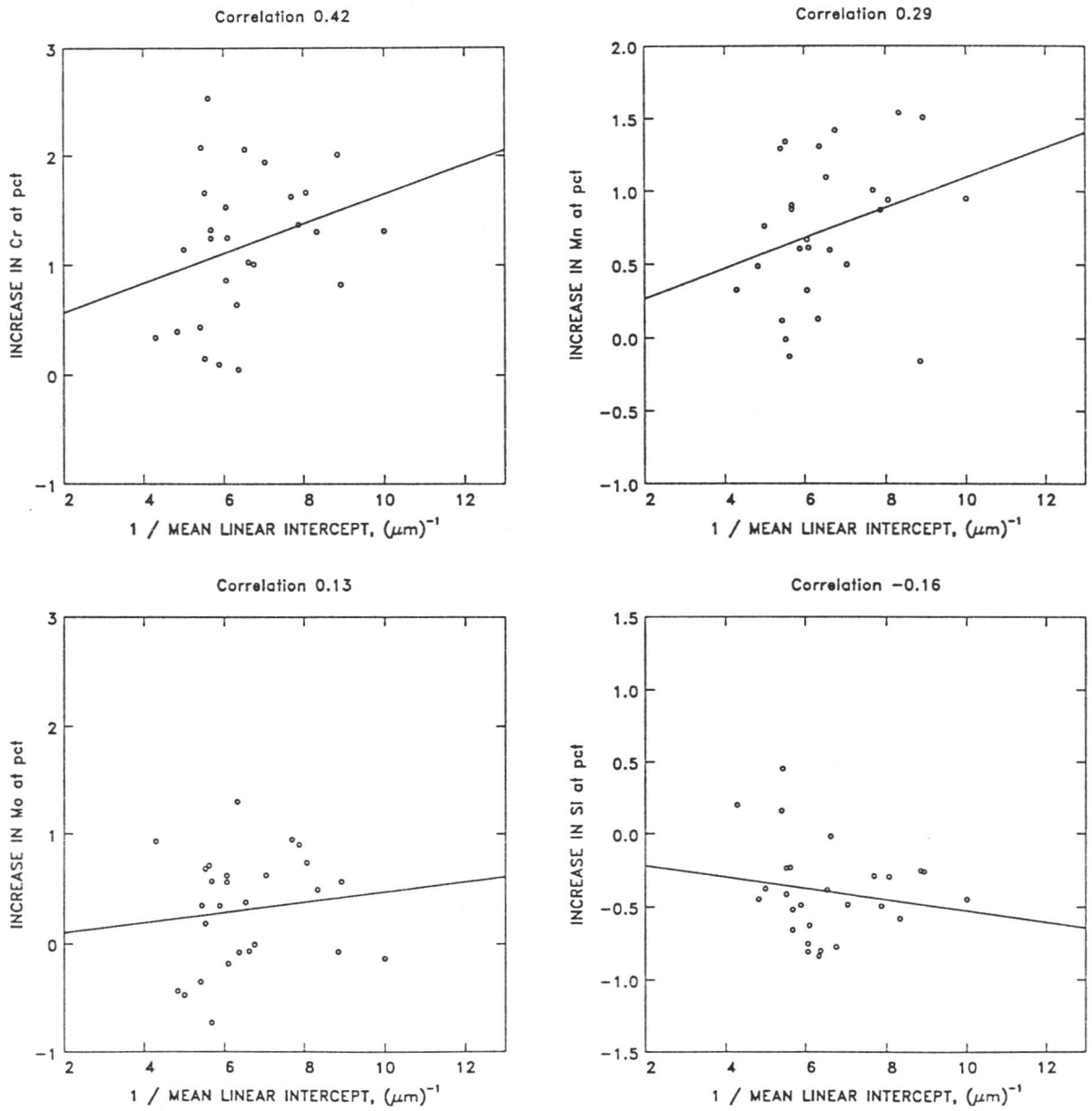


Figure 6.1(c): EDX microanalytical data for steel 1

Fe-Cr-Mo STEEL AFTER 4 WEEKS AT 565 °C

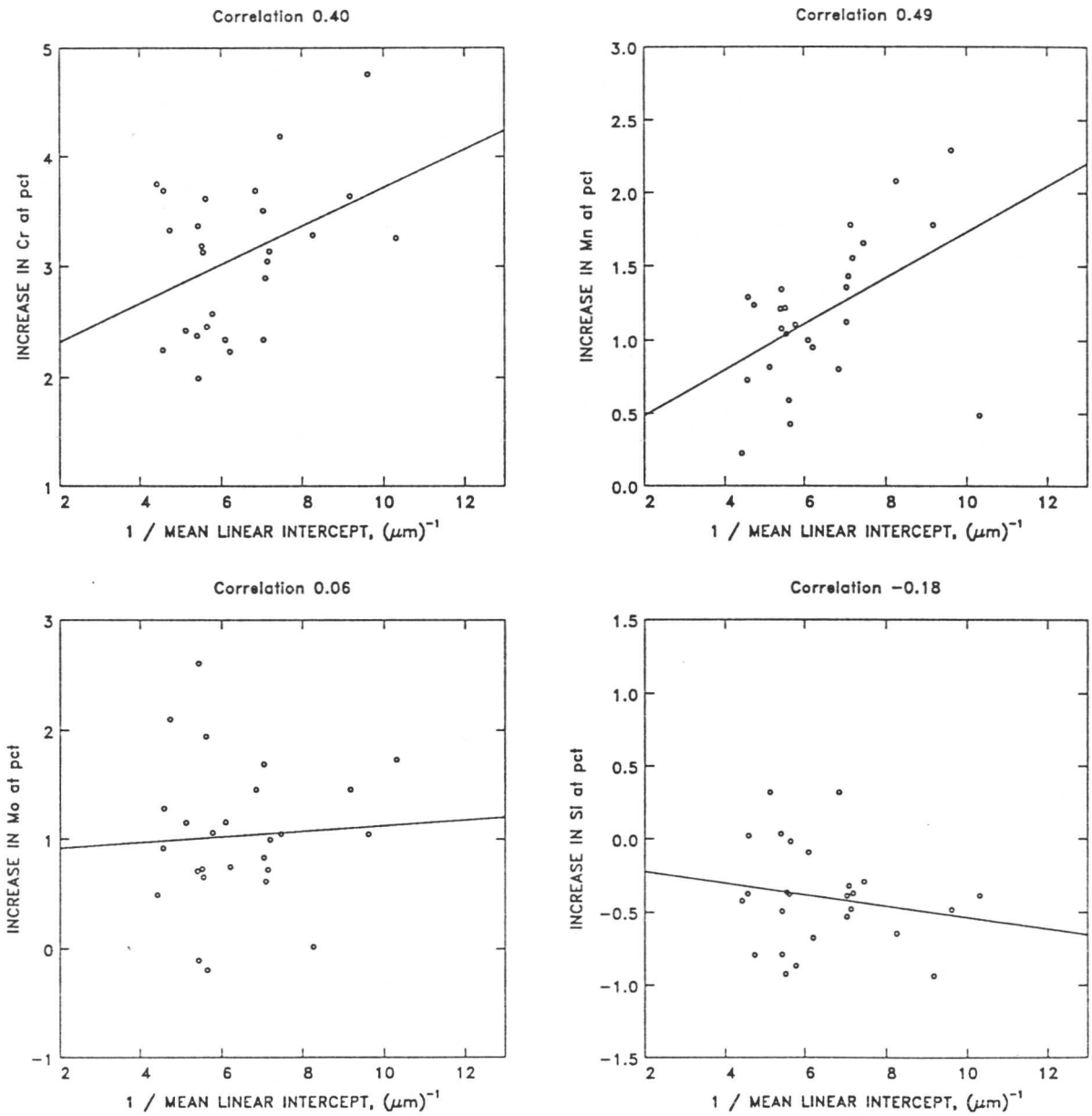


Figure 6.1(d): EDX microanalytical data for steel 1

Fe-Cr-Mo STEEL AFTER 42 WEEKS AT 565 °C

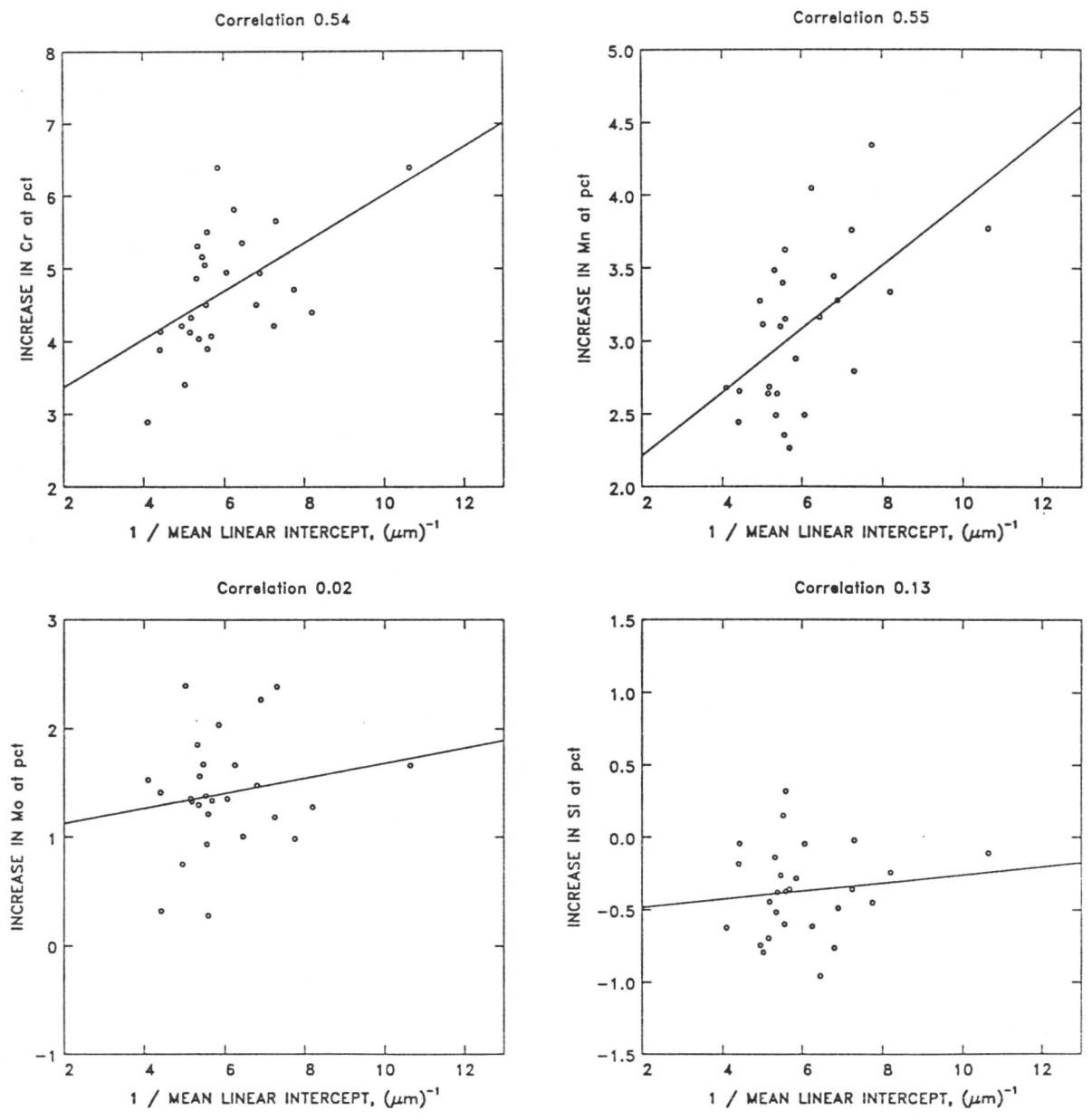


Figure 6.1(e): EDX microanalytical data for steel 1

Fe-Cr-Mo STEEL, AS TRANSFORMED

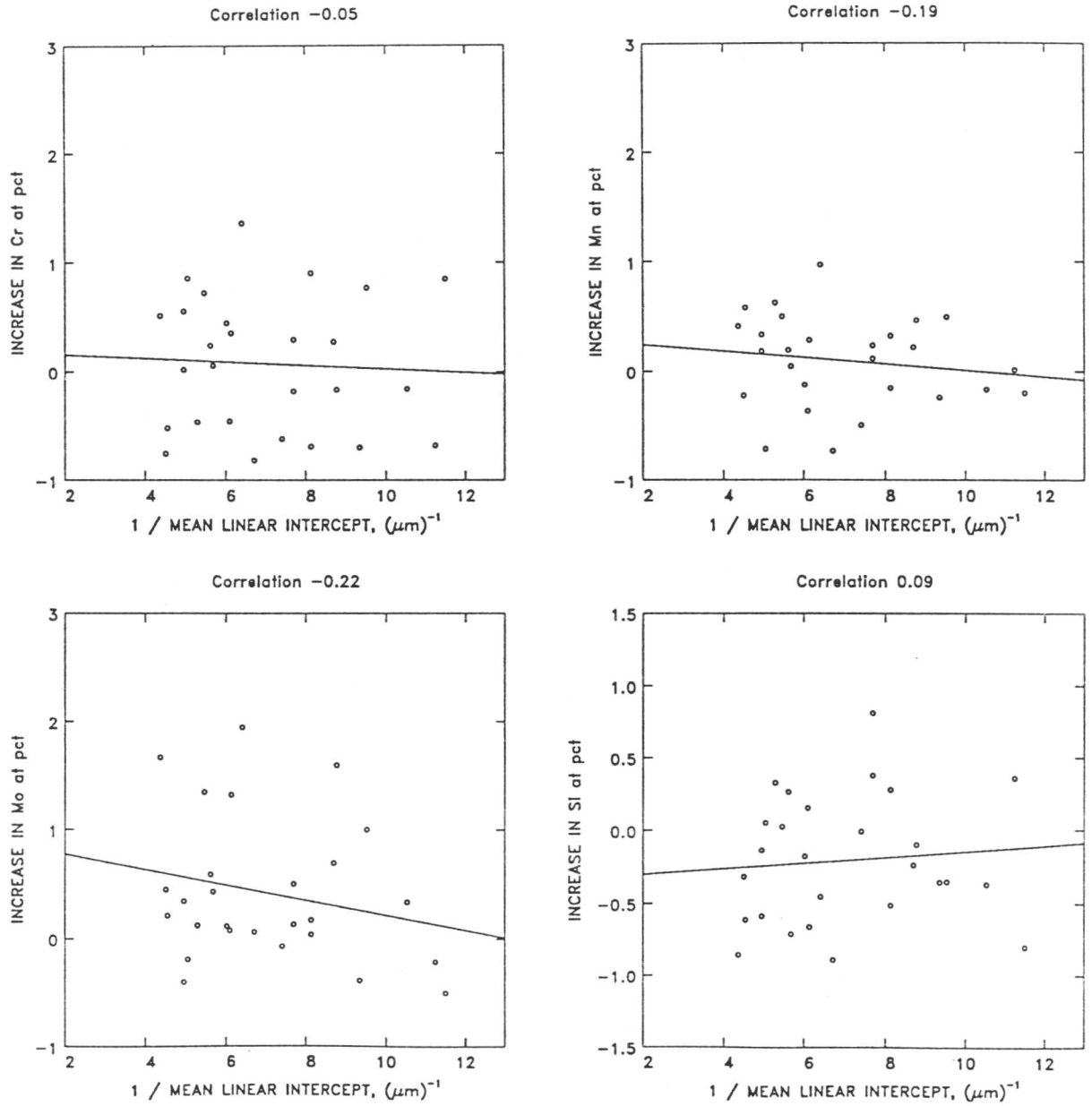


Figure 6.2: EDX microanalytical data for unaged specimens

Fe-Cr-Mo STEEL, AS TRANSFORMED

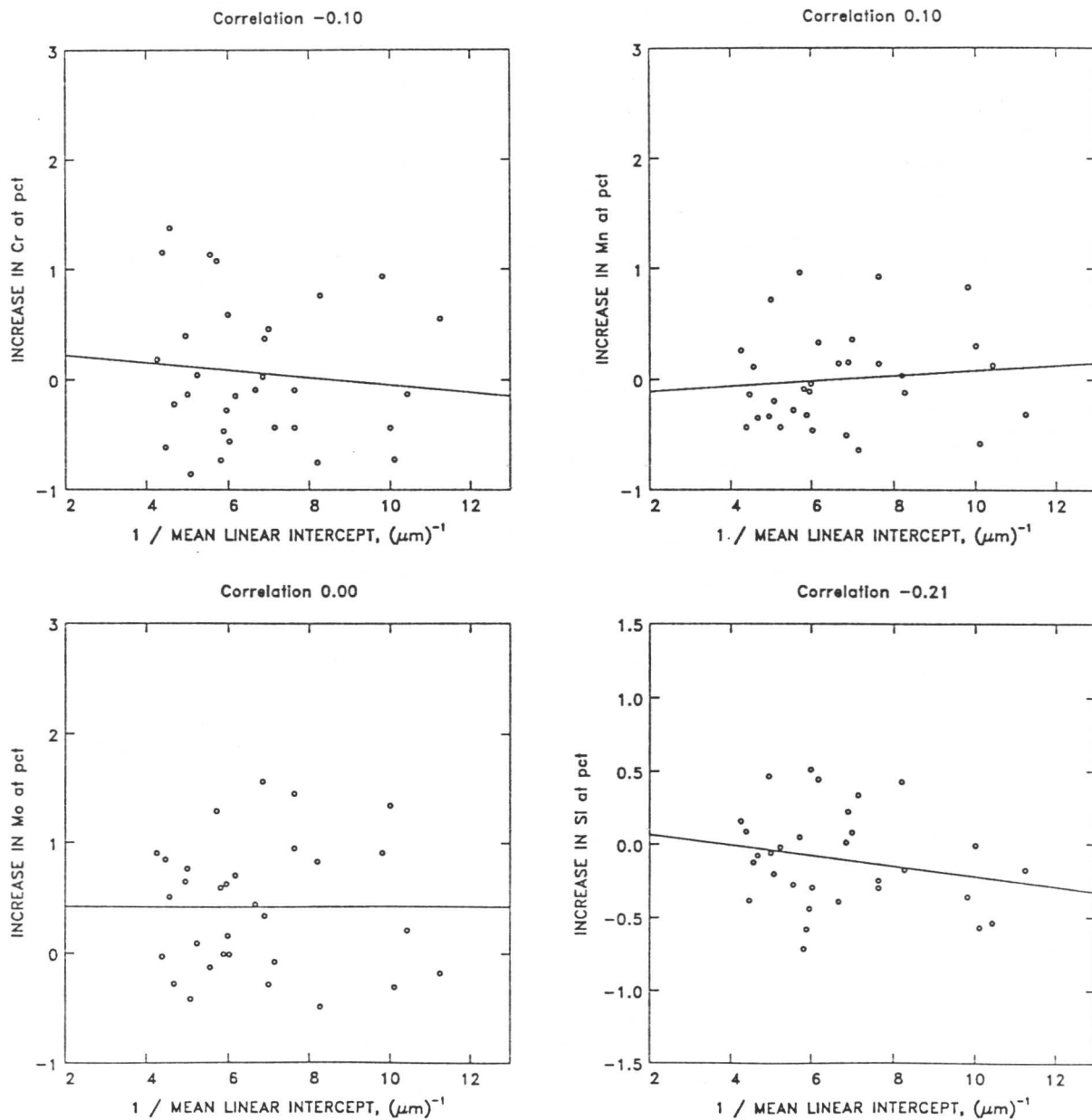


Figure 6.2: EDX microanalytical data for unaged specimens

6.2.4 Effect of particle size on ageing behaviour of cementite

It has been noted that the analytical model (equation (6.1)) predicts that differing x_θ will affect the rate of enrichment of cementite, and that such a size effect was observed experimentally for composition measurements made on particles of varied x_θ at a particular ageing time. The model also predicts that the rate of enrichment at a particular temperature will also be affected by mean particle size, and an attempt was made to illustrate this effect using the collected composition data.

To this end, values representative of the experimental data were obtained for $x_\theta = 0.100\mu\text{m}$, $0.180\mu\text{m}$, and $0.260\mu\text{m}$ (which were chosen arbitrarily as being representative of the smaller, mean, and larger sizes of cementite observed), from the best fit lines on each by $(c - \bar{c})$ versus $1/x_\theta$ plot that had been calculated earlier using a regression analysis. This was done by taking these three values for x_θ on a $(c - \bar{c})$ versus $1/x_\theta$ plot, and extrapolating from the best fit line to determine the corresponding value of composition change; these could then be plotted against time to give an approximate indication of the fact that smaller cementite particle size was associated with larger degrees of enrichment. The extrapolation procedure is illustrated in figure 6.3.

It is important to realize that such values were not direct experimental results, but were rather a representation of the experimental data: the analysis relies on a complete absence of coarsening for its assumption that data for the same x_θ at different ageing times are comparable, as the development of individual cementite particles during ageing is impossible to follow. We know that this assumption is not strictly true, so the analysis must be considered with reservations, although the current work has shown coarsening to be of less significance than diffusion on the enrichment process.

Calculations were carried out using enrichment data for all four elements, but only those for chromium and manganese are presented here and used in subsequent analysis. Silicon was ignored because of the lack of statistical significance which could be attached to the small measured composition values as a result of the inherent statistical scatter in the EDX technique, and because

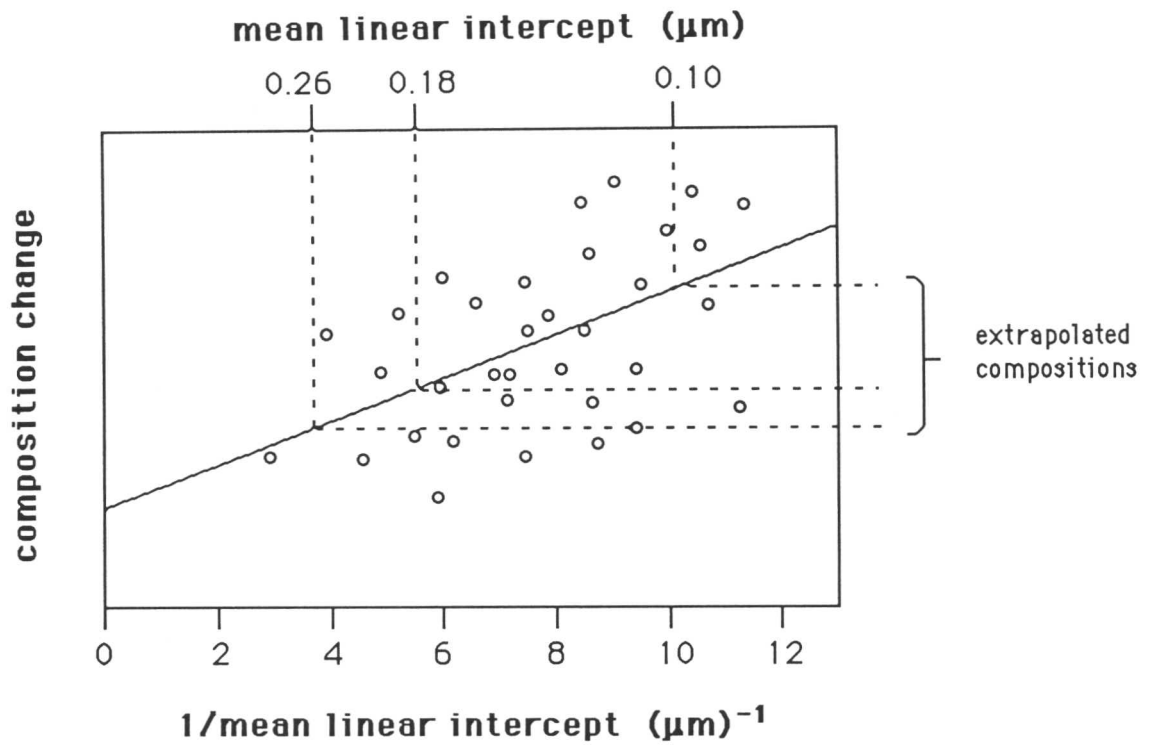


Figure 6.3: Method of extrapolation to produce values representative of experimentally-obtained compositions illustrating the effect of variations in x_θ on rate of enrichment of cementite

it partitions from cementite to ferrite, so that the relationship in equation (6.1) does not apply; and molybdenum because the large scatter and suspicion of overlap with the sulphur K line made the data similarly unreliable, as discussed in Section 6.1. The resulting extrapolated values of cementite composition are presented in tables 6.5–6.7 for the three ageing temperatures for the fully-bainitic microstructure, and in table 6.8 for the partially-bainitic microstructure aged at 565°C.

Graphs were plotted for the data obtained for chromium and manganese (the two alloying elements which showed a statistically-significant size effect) against $(\text{time})^{1/2}$, the relationship predicted by equation (6.1), and are presented in figure 6.4 and 6.5 for the fully-bainitic case, and figure 6.6 for the partially-bainitic case.

Ageing time (hours)	Experimental data ($c - \bar{c}$) intercepts at:		
	0.100 μm	0.180 μm	0.260 μm
CHROMIUM			
0	-0.07	0.08	0.14
2	0.05	-0.05	-0.08
6	0.71	0.37	0.24
12	0.58	0.28	0.16
24	0.17	0.32	0.37
48	0.94	0.50	0.33
96	0.81	0.56	0.46
168	1.46	0.82	0.57
336	2.02	1.40	1.17
672	2.58	1.86	1.58
1008	2.76	2.14	1.90
1344	2.84	2.18	1.92
2016	3.06	2.28	1.97
2688	3.42	2.57	2.24
4032	3.70	2.67	2.27
6240	5.07	3.81	3.32
8064	5.50	4.41	4.00
MANGANESE			
0	0.09	-0.02	-0.06
2	-0.04	0.07	0.11
6	0.48	0.15	0.03
12	0.57	0.16	0.00
24	0.42	0.33	0.29
48	0.73	0.34	0.19
96	0.41	0.23	0.16
168	0.92	0.61	0.50
336	0.74	0.55	0.48
672	1.01	0.73	0.62
1008	0.94	0.69	0.59
1344	1.15	0.76	0.61
2016	1.28	0.83	0.66
2688	1.42	0.91	0.72
4032	1.48	1.07	0.92
6240	1.76	1.22	1.02
8064	2.27	1.63	1.38

Table 6.5: Representative experimental values for varying x_θ in Fe-Cr-Mo power plant steel aged at 510°C

Ageing time (hours)	Experimental data ($c - \bar{c}$) intercepts at:		
	0.100 μm	0.180 μm	0.260 μm
CHROMIUM			
0	0.03	0.12	0.16
1	0.40	0.55	0.60
4	0.60	0.52	0.49
8	0.81	0.43	0.28
12	0.82	0.55	0.44
24	0.94	0.63	0.52
48	1.69	1.09	0.86
96	2.28	1.60	1.35
168	2.54	1.65	1.30
336	2.66	1.84	1.52
672	3.77	2.99	2.69
1344	4.85	3.68	3.22
2688	4.55	3.45	3.03
4032	5.34	4.00	3.48
7002	6.10	4.63	4.06
MANGANESE			
0	-0.04	0.07	0.11
1	0.19	0.23	0.25
4	0.31	0.34	0.35
8	0.39	0.28	0.24
12	0.47	0.30	0.24
24	1.05	0.38	0.12
48	1.23	0.64	0.42
96	1.38	1.03	0.89
168	1.31	0.79	0.59
336	2.08	1.32	1.03
672	1.77	1.08	0.81
1344	2.73	1.90	1.58
2688	2.82	1.90	1.55
4032	3.07	2.41	2.16
7002	3.83	3.05	2.74

Table 6.6: Representative experimental values for varying x_θ in Fe-Cr-Mo power plant steel aged at 565°C

Ageing time (hours)	Experimental data ($c - \bar{c}$) intercepts at:		
	0.100 μm	0.180 μm	0.260 μm
CHROMIUM			
0	0.01	0.09	0.11
1	0.40	0.09	-0.03
2	0.64	0.37	0.27
4	1.18	0.82	0.68
8	1.79	1.24	1.03
12	2.46	1.78	1.52
24	2.52	1.57	1.20
48	3.97	2.83	2.39
96	4.07	2.77	2.27
168	4.63	3.31	2.80
336	6.02	4.60	4.05
672	7.28	5.74	5.14
1344	7.84	6.24	5.63
2688	8.21	6.90	6.39
4032	9.27	7.90	7.37
6048	10.46	8.76	8.11
MANGANESE			
0	-0.07	0.06	0.11
1	0.28	0.06	-0.02
2	0.29	0.16	0.10
4	0.98	0.68	0.57
8	1.02	0.58	0.41
12	1.19	0.79	0.63
24	1.44	1.05	0.91
48	1.73	1.31	1.15
96	1.14	0.74	0.59
168	2.00	1.70	1.59
336	1.98	1.50	1.32
672	2.53	1.74	1.43
1344	2.67	2.25	2.09
2688	3.51	2.77	2.48
4032	4.24	3.39	3.07
6048	4.04	3.31	3.03

Table 6.7: Representative experimental values for varying x_θ in Fe–Cr–Mo power plant steel aged at 625°C

Ageing time (hours)	Experimental data ($c - \bar{c}$) intercepts at:		
	0.100 μm	0.180 μm	0.260 μm
CHROMIUM			
0	0.02	0.19	0.26
1	0.65	0.42	0.33
2	0.37	0.34	0.33
4	0.90	0.78	0.74
12	1.13	0.78	0.65
24	1.62	1.26	1.12
48	2.63	1.68	1.32
96	3.62	2.46	2.02
168	4.55	3.24	2.73
336	5.28	3.72	3.12
672	5.16	4.23	3.87
1344	6.44	4.46	3.69
2688	7.01	5.42	4.81
5376	8.12	6.15	5.39
MANGANESE			
0	-0.10	0.07	0.14
1	0.43	0.40	0.39
2	0.36	0.30	0.27
4	0.33	0.31	0.31
12	0.55	0.35	0.28
24	1.17	0.92	0.82
48	1.35	0.69	0.44
96	1.35	0.87	0.68
168	1.76	1.03	0.75
336	2.40	2.03	1.88
672	3.00	2.61	2.47
1344	3.27	2.40	2.07
2688	3.28	2.40	2.05
5376	4.29	3.62	3.36

Table 6.8: Representative experimental values for varying x_θ in Fe–Cr–Mo power plant steel with a mixed starting microstructure aged at 565°C

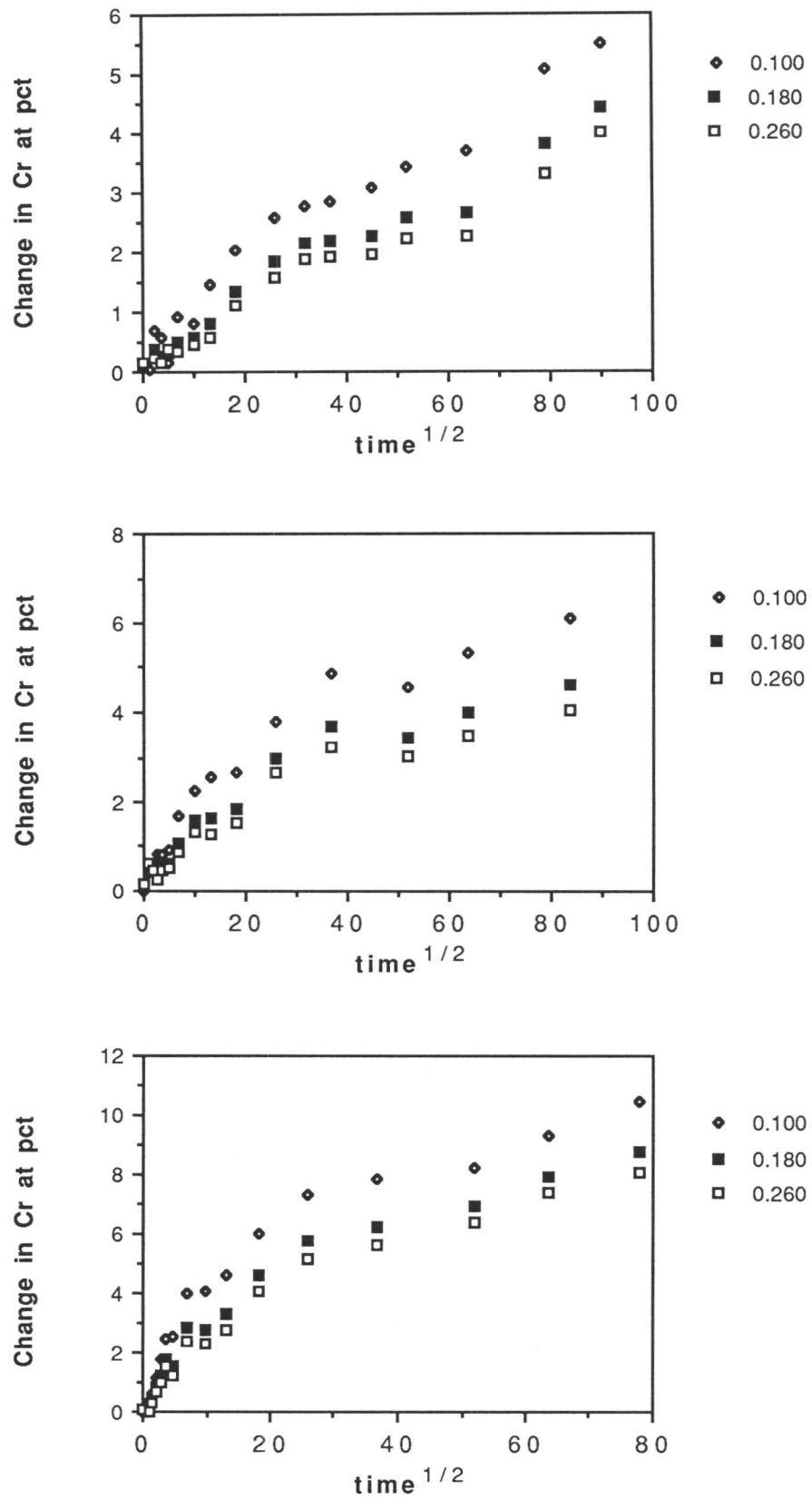


Figure 6.4: A representation of experimental data for chromium enrichment compared for varying x_θ in the fully-bainitic 1Cr- $\frac{1}{2}$ Mo type power plant steel

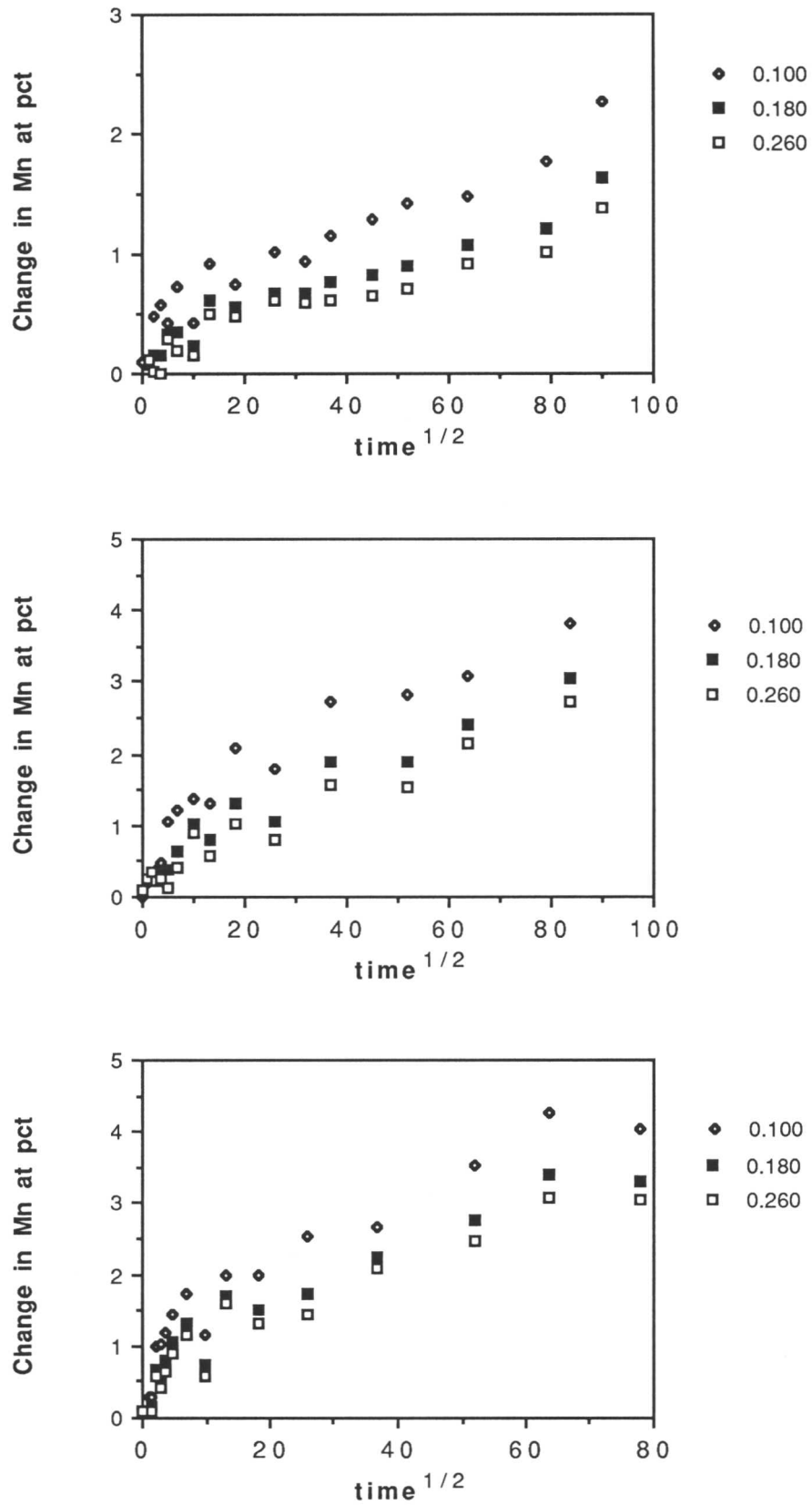


Figure 6.5: A representation of experimental data for manganese enrichment compared for varying x_θ in the fully-bainitic 1Cr- $\frac{1}{2}$ Mo type power plant steel

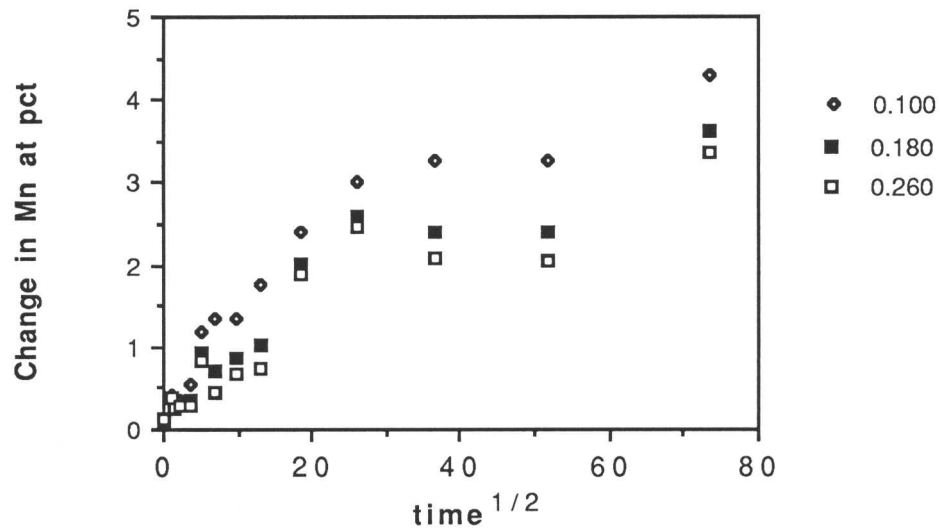
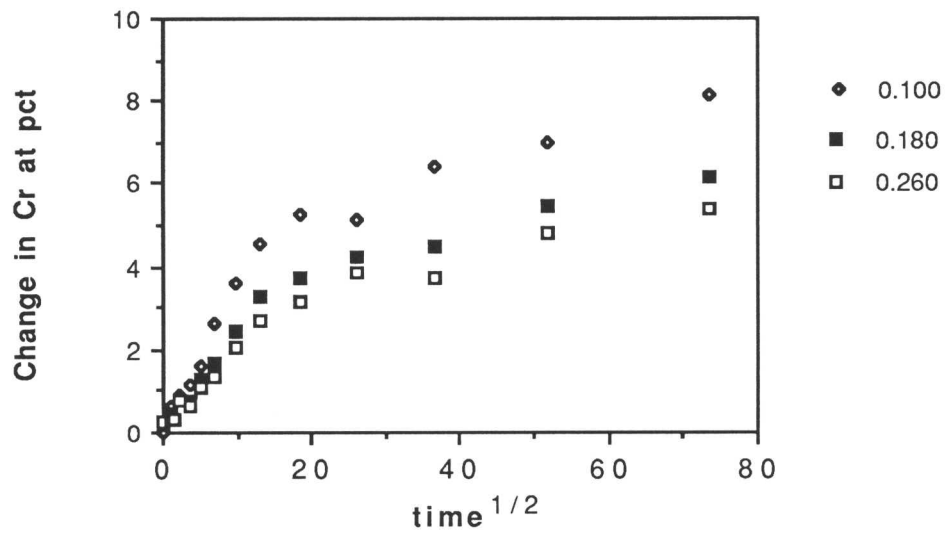


Figure 6.6: A representation of experimental data for the enrichment of cementite with chromium and manganese compared for varying x_θ in the ferritic/bainitic $1\text{Cr}-\frac{1}{2}\text{Mo}$ type power plant steel

6.2.5 Summary

This analysis provides an illustration that the size effect predicted by equation (6.1) is present in the experimental data for this alloy. The correlation of experimental data to theory generally increases as ageing time is increased. At longer ageing times, especially at the higher temperature, there is a tendency for the correlation to get slightly poorer, which suggests that the approximations in the analytical model are beginning to break down, but in general the fit with equation (6.1) is reasonable, and a statistically-significant $(c - \bar{c}) \propto x_\theta^{-1}$ relationship has been shown for the ageing data in this alloy.

6.3 Variation of c^θ with Time: Analytical Approach

6.3.1 Analysis of results

It is evident from equation (6.1) and equation (6.2) that the analytical model for diffusion-controlled enrichment of cementite predicts a variation of cementite composition with $(\text{time})^{1/2}$ for a constant x_θ , and that this is at variance with industrial practice, in which an empirical $(\text{time})^{1/3}$ relationship is generally applied. The collected data are analysed here for both relationships. A further regression analysis is performed for the more rigorous relationship derived from equation (6.1), which suggests the mean value of the product of composition change and particle size, $\Sigma(c - \bar{c})(x_\theta)/N$, where N is the number of individual particles measured, at a given time, should vary as $(\text{time})^{1/2}$; $\Sigma(c - \bar{c})(x_\theta)/N$ is not analysed against $(\text{time})^{1/3}$ as such a relationship could have no physical significance. The correlation between experimental data and the theoretical model, together with that for the empirical method, is presented in table 6.9 below. Graphical representations of composition change versus $(\text{time})^{1/2}$ for the four temperature/microstructure combinations are presented in figures 6.7–6.10.

It can be seen from the figures and the table that the collected mean composition data generally fits the linearity with $(\text{time})^{1/2}$ predicted by equation (6.2) better at short and medium ageing times. For the longest ageing times at higher

temperatures there is a tendency to deviation from this linearity. This may well be indicative of the onset of significant levels of soft impingement between the diffusion fields of different cementite particles, which would be expected to be of greater importance under conditions of increased ageing temperature and time, but which cannot be predicted by the analytical model. Such effects would reduce the diffusion rate in ferrite, and hence the rate of enrichment, so that a composition versus (time)ⁿ relationship would tend in practice to fit $n > 2$. This may explain why the purely empirical (time)^{1/3} relationship frequently used in industrial practice met with some success.

It has been noted that in the case of the mixed microstructure, the increase in the effective carbon composition, and hence V_θ , which is caused by partition of that element into the retained austenite when the allotriomorphic ferrite forms, and the concomitant reduction in x_α , would be expected to lead to an earlier significant soft impingement effect. It is evident that this deviation from a strict (time)^{1/2} is especially marked in the case of the mixed microstructure (figure 6.10), which supports the supposition that a slowing down of diffusion rates within ferrite due to soft impingement is a factor in the observed non-linearity at longer ageing times.

It can be noted from table 6.9 that correlation to both (time)ⁿ relationships is fairly similar. On the basis of this simple analysis alone no conclusion could rigorously be made within meaningful confidence limits. Nevertheless, when account is taken of the slight variation in x_θ between different samples (*i.e.*, the data are analysed for a $\Sigma(c - \bar{c})(x_\theta)/N$ vs (time)^{1/2} relationship), the agreement is consistently better than it is with (time)^{1/3}.

It appears that equation (6.1) describes the experimental situation rather well. Chromium and manganese are found to show better correlation to theory than molybdenum, suggesting that the larger degree of scatter in the molybdenum composition measurement has once more led to a less conclusive result for that element.

Ageing temp. °C	R ² correlation of experimental data to:		
	$(c - \bar{c})$ v. $t^{1/2}$	$(c - \bar{c})x_{\theta}$ v. $t^{1/2}$	$(c - \bar{c})$ v. $t^{1/3}$
	(chromium)		
510	0.96	0.97	0.97
565	0.89	0.95	0.94
625	0.88	0.93	0.91
565 30% α_b	0.86	0.91	0.93
	(manganese)		
510	0.93	0.97	0.95
565	0.94	0.96	0.86
625	0.88	0.92	0.88
565 30% α_b	0.87	0.90	0.92
	(molybdenum)		
510	0.64	0.70	0.61
565	0.61	0.73	0.58
625	0.64	0.59	0.57
565 30% α_b	0.58	0.63	0.51

Table 6.9: Correlation coefficients between experimental data for the Fe–Cr–Mo Steel and the three methods to analyse $(c - \bar{c})$ versus a function of (time)

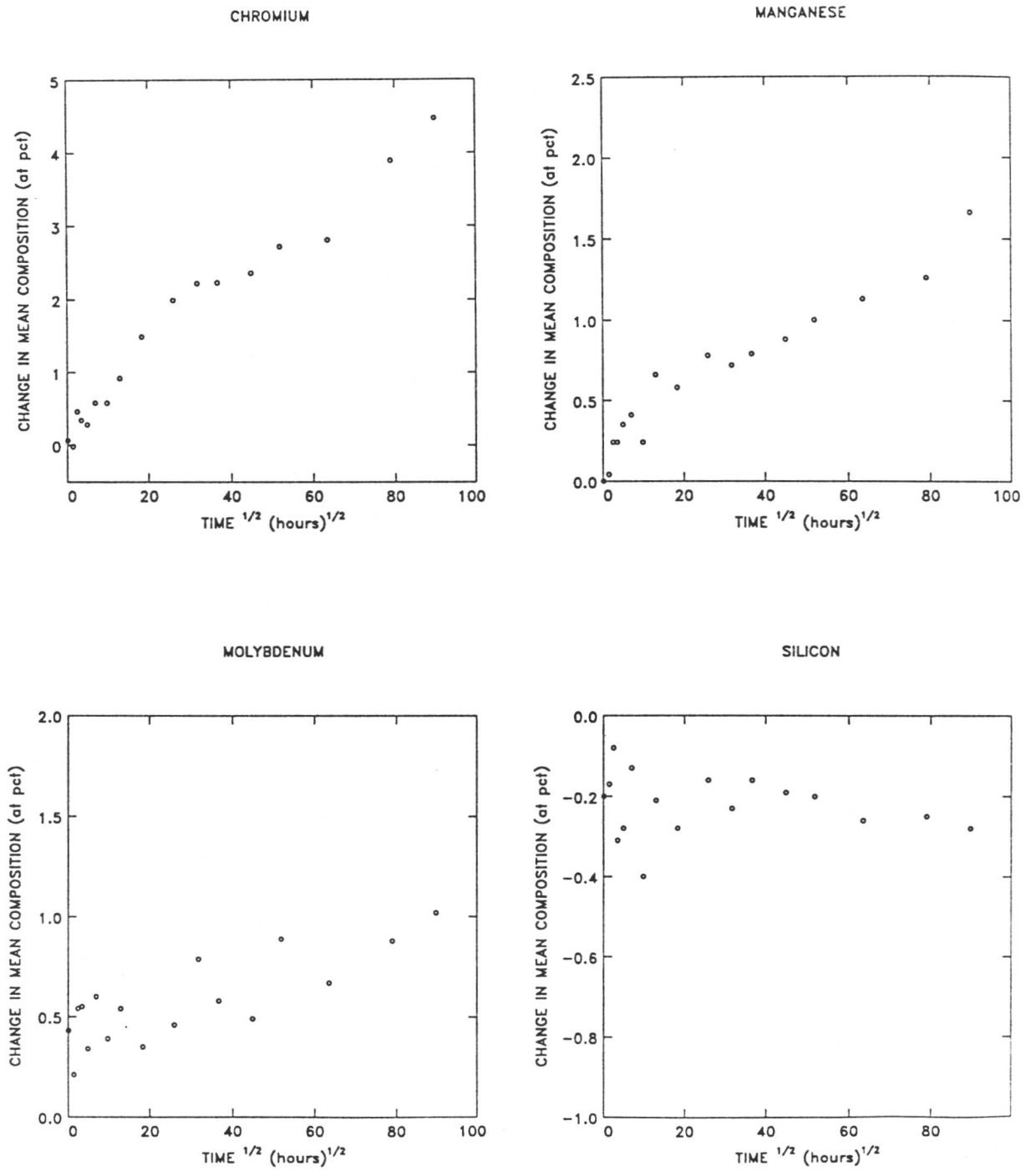


Figure 6.7: Mean $(c - \bar{c})$ versus ageing time for the Fe-Cr-Mo power plant steel, initially having a fully-bainitic starting microstructure, aged at 510°C.

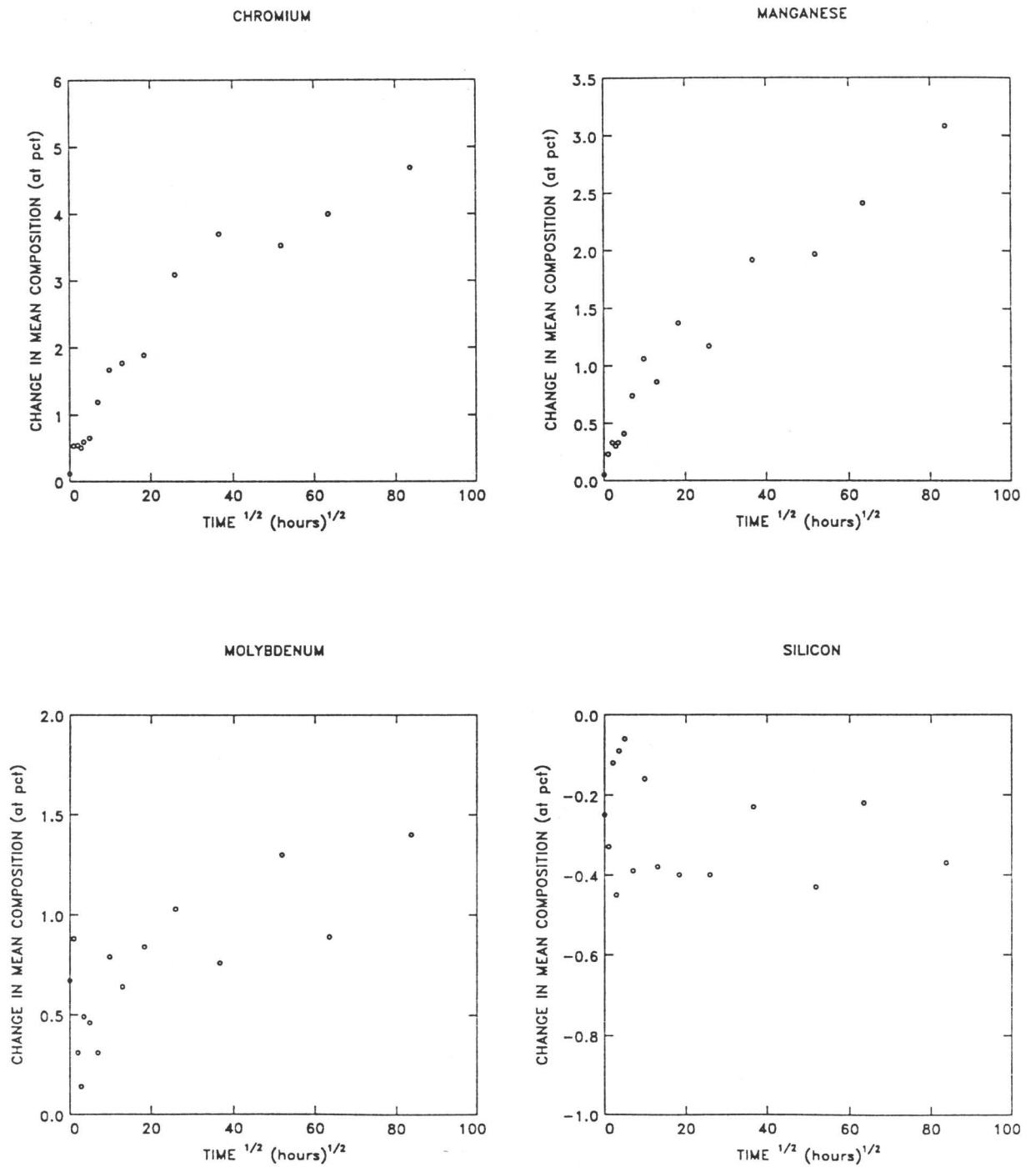


Figure 6.8: Mean ($c - \bar{c}$) versus ageing time for the Fe-Cr-Mo power plant steel, having a fully-bainitic starting microstructure, aged at 565°C.

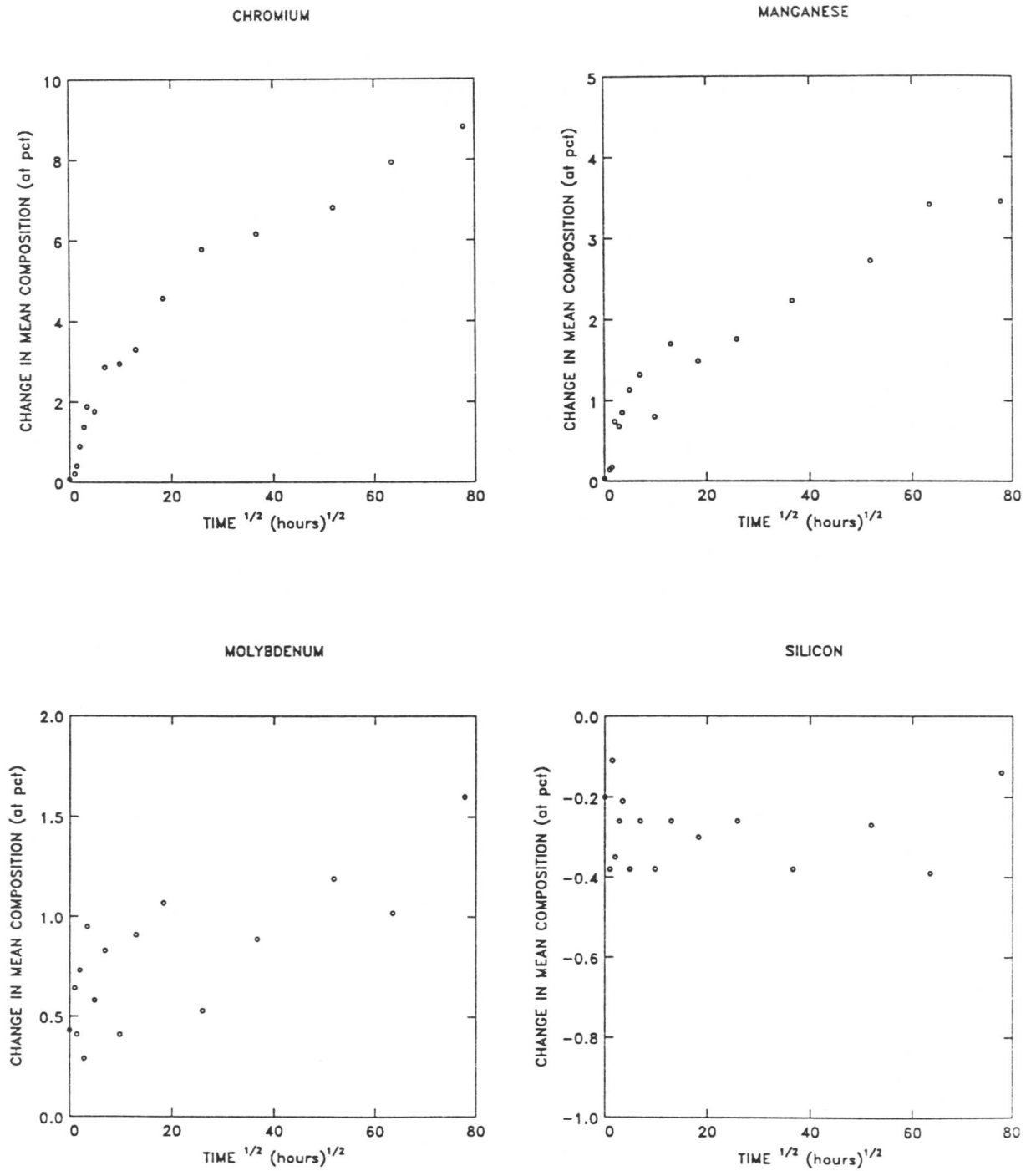


Figure 6.9: Mean $(c - \bar{c})$ versus ageing time for the Fe-Cr-Mo power plant steel, having a fully-bainitic starting microstructure, aged at 625°C.

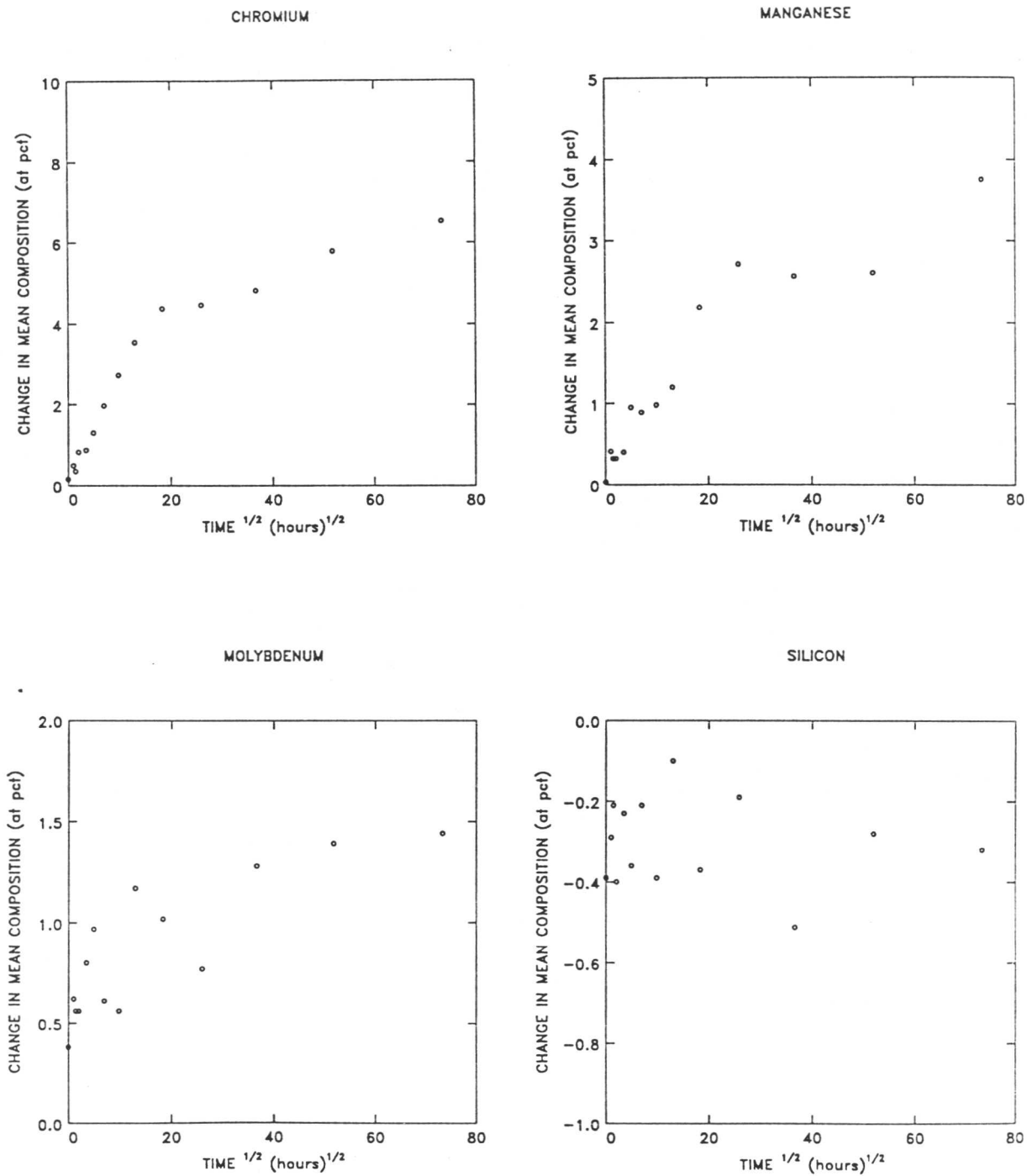


Figure 6.10: Mean $(c - \bar{c})$ versus ageing time for the Fe-Cr-Mo power plant steel, initially having a mixture of allotriomorphic ferrite and bainite as a starting microstructure, aged at 565°C.

6.3.2 Diffusion coefficients

Rearranging equation (6.1) enables the gradient of the $(c - \bar{c})(x_\theta)$ versus $(\text{time})^{1/2}$ graph to be used to produce values for the diffusion coefficient of the alloying elements under consideration:

$$x_\theta(\bar{c} - c^\theta) = \frac{4D^{1/2}(c^{\alpha\theta} - \bar{c})t^{1/2}}{\pi^{1/2}} \quad (6.3)$$

\Rightarrow gradient of $(c - \bar{c})(x_\theta)$ v. $t^{1/2}$ line:

$$\frac{4D^{1/2}(c^{\alpha\theta} - \bar{c})}{\pi^{1/2}} \quad (6.4)$$

In a general case, if the partition coefficient for a given element Z between cementite and ferrite (k_z) is known, a value for $c^{\alpha\theta}$ can be calculated from equation (6.5) and equation (6.6) with V_θ , the volume fraction of cementite, being calculated from the lever rule assuming a stoichiometric carbon concentration in cementite.

$$\bar{c} = c^{\theta\alpha}V_\theta + (c^{\theta\alpha}/k_z) - (c^{\theta\alpha}V_\theta/k_z) \quad (6.5)$$

$$k_z = \frac{c^{\theta\alpha}}{c^{\alpha\theta}} \quad (6.6)$$

However, in the case of the power plant material, equilibrium cementite and ferrite compositions and volume fractions were calculated using the MTDATA computer package which was developed by the National Physical Laboratory (NPL). The method used by the MTDATA package involves a large database of accurate composition measurements from simple, extensively-studied systems, from which data for more complex systems are extrapolated. The results obtained by applying this method to the four temperature/microstructure combinations under test are presented in table 6.10. Two values of $c^{\theta\alpha}$ (in atomic percent) are presented: $c_{sub}^{\theta\alpha}$ is the equilibrium concentration of an element in cementite as a percentage of the total substitutional content only, and $c_{all}^{\theta\alpha}$ is the

concentration including carbon; hence, it is the former value which corresponds to the method used for presenting the experimental data.

It should be noted that the values for the bainitic region of the mixed microstructure were generated by assuming that all of the carbon had partitioned to that region when allotriomorphic ferrite formed, but that the relative proportions of substitutional elements had remained the same.

Temp (K)	Element	V_θ (pct)	equilibrium compositions				
			weight pct		atomic pct		
			$c^{\alpha\theta}$	$c^{\theta\alpha}$	$c^{\alpha\theta}$	$c_{all}^{\theta\alpha}$	$c_{sub}^{\theta\alpha}$
783	chromium	1.67	0.34	30.2	0.36	25.9	34.5
	manganese		0.30	11.9	0.31	9.7	12.9
	molybdenum		0.43	4.3	0.25	2.1	2.8
838	chromium	1.66	0.43	25.3	0.46	21.7	29.0
	manganese		0.35	9.3	0.36	7.6	10.1
	molybdenum		0.43	4.2	0.25	2.0	2.6
898	chromium	1.63	0.52	20.7	0.55	17.8	23.8
	manganese		0.40	6.9	0.40	5.6	7.5
	molybdenum		0.44	3.8	0.26	1.8	2.4
838 30% α_b	chromium	5.63	0.19	11.3	0.20	9.9	13.2
	manganese		0.18	4.4	0.19	4.6	6.1
	molybdenum		0.24	4.4	0.14	2.1	2.8

Table 6.10: Calculated equilibrium compositions for a cementite/ferrite mixture in the Fe–Cr–Mo power plant steel at the temperatures used for ageing

Substituting values for these parameters into equation (6.3) generates experimental measurements for D_{Cr} and D_{Mn} , which are presented in table 6.11 and table 6.12. The scatter in the EDX data for molybdenum and silicon is such that meaningful diffusion coefficients cannot be obtained from this approach. These are compared with the reported values for tracer diffusion coefficients (obtained from the 57th edition of the CRC handbook) (see the tables). Fair agreement is found between the experimentally-determined and published values for both chromium and manganese at all three temperatures.

The simple analytical method used to generate these values is only valid before soft impingement occurs in the ferrite. In calculating diffusion coefficients, only those values of $(c - \bar{c})(x_\theta)$ prior to soft impingement should be used, but the analytical model makes no prediction of the time when soft impingement starts to be of substantive influence on the ageing process. It was decided that, in the $(c - \bar{c})(x_\theta)$ versus $(\text{time})^{1/2}$ plot at 625°C, where appreciable deviation from linearity at the longest ageing time suggested the possibility of soft impingement, diffusion coefficients should be calculated using data from the linear region only (which in all cases is the major part of the data), disregarding those points at longer ageing times where a slowing down of the enrichment rate suggests a soft impingement regime to which the model does not apply.

A more representative interdiffusion coefficient is also calculated using a procedure described by Fridberg *et al.* (1969). They propose that for practical purposes the diffusion coefficient of an alloying element can be described by the self diffusion coefficient of iron modified by a scale factor independent of temperature, but varying regularly with atomic number. This method produces values for the interdiffusion coefficient which are given in table 6.11 and table 6.12.

These calculated values are in good agreement with that derived from the experimental data and equation (6.1), indicating that the experimental regime so far is one for which equation equation (6.1) holds.

A similar analysis can be performed on the measured x_θ data using equation (6.7), which provides a value for the diffusion coefficient based on coarsening theory:

$$D = \frac{(r^3 - r_0^3)9RT}{8\sigma^{\theta\alpha}c^{\alpha\theta}V_\theta t} \quad (6.7)$$

where r is the particle size, r_0 is the initial particle size, and $\sigma^{\theta\alpha}$ is the surface energy, taken from Puls and Kirkaldy (1972) to be 0.7 Jm⁻². These calculated values are also presented in the tables.

When the experimental data are used in this equation, the calculated diffusion coefficients differ from the reported values by at least an order of magni-

Method of calculation	Diffusion coefficients (m^2s^{-1})		
	at 510°C	at 565°C	at 625°C
Experimental (equation (6.3)) <i>all</i> α_b :	1.19×10^{-20}	7.07×10^{-20}	3.11×10^{-19}
30% α_b :	-	9.36×10^{-20}	-
Interdiffusion (from Fridberg)	1.22×10^{-20}	1.37×10^{-19}	1.37×10^{-18}
Tracer (from CRC)	2.26×10^{-20}	2.56×10^{-19}	2.57×10^{-18}
coarsening theory	3.83×10^{-21}	6.22×10^{-21}	9.79×10^{-21}

Table 6.11: Analysis of $(c - \bar{c})(x_\theta)$ versus $(\text{time})^{1/2}$ plot for chromium in the Fe–Cr–Mo power plant steel

Method of calculation	Diffusion coefficients (m^2s^{-1})		
	at 510°C	at 565°C	at 625°C
Experimental (equation (6.3)) <i>all</i> α_b :	1.58×10^{-20}	9.97×10^{-20}	3.77×10^{-19}
30% α_b :	-	8.76×10^{-20}	-
Interdiffusion (from Fridberg)	9.50×10^{-21}	1.07×10^{-19}	1.06×10^{-18}
Tracer (from CRC)	7.77×10^{-20}	7.11×10^{-19}	5.85×10^{-18}
coarsening theory	3.92×10^{-21}	6.45×10^{-21}	1.21×10^{-20}

Table 6.12: Analysis of $(c - \bar{c})(x_\theta)$ versus $(\text{time})^{1/2}$ plot for manganese in the Fe–Cr–Mo power plant steel

tude; indeed, with the mixed-microstructure data, no coarsening was observed, so that this calculation is meaningless. As expected, this suggests that diffusion of substitutional alloying elements from the supersaturated ferrite phase is the dominant process, with cementite coarsening theory inapplicable in this case.

The process being studied here is really one where the cementite and ferrite are approaching their equilibrium compositions.

6.4 Theoretical Modelling of the Ageing Process

6.4.1 Correlation of experimental data to the $(c - \bar{c}) \propto 1/x_\theta$ relationship

As noted above, a consistent increase in the expected composition change versus particle size correlation is observed, but with the correlation coefficient only rising to around 0.5 after many weeks of ageing treatment. Based on intuition, the correlation coefficient was expected to rise rapidly once the mean solute content of the particles rose to levels above which the variations noted in c_θ at time = 0 for different particles became negligible. This expectation that the correlation coefficients should rapidly approach unity was tested by the development of a simple computer model for the ageing process.

The computer model of the ageing problem utilized a large (400 point) starting dataset of a distribution of cementite sizes and compositions in keeping with the initial size and composition distributions measured from as-transformed and unaged specimens. The data points are then 'aged' by the computer program in accordance with equation (6.3). The program then selects random selection of a point from the set of 'aged particles' 30 times in order to simulate experimental procedure, and derives the mean composition ($\Sigma(c_\theta - \bar{c})/n$) and the correlation coefficient of the data to the $(c - \bar{c}) \propto 1/x_\theta$ relationship. When this procedure is carried out for a whole series of time periods, and the data analysed along the same lines as the real experimental data, the model predicts a correlation coefficient for the $(c - \bar{c}) \propto 1/x_\theta$ relationship which rises rapidly to unity as soon as $(c - \bar{c})$ becomes large relative to the observed random variation in c_θ at zero time. The approach of the correlation coefficient to unity when the model is applied is found to be much more rapid in the model than in the experimental case, suggesting that another contributory factor exists in practice.

6.4.2 Statistical scatter in EDX readings

The nature of energy dispersive X-ray analysis is that the signal is produced when electrons within the atoms of the material under test, which have been energized into an excited state, return to their ground state in a process which is stochastic. The result therefore suffers from an unavoidable statistical error, though this can be minimized by detecting a large number of events. It is, however, impractical to collect data for excessively prolonged periods in order to accumulate a large signal to reduce the error, especially in programmes such as the current one when a large number of particles has to be analysed; the period of time over which events are observed must, of necessity, be a compromise between accuracy and practicality.

If our computer model is to be relatable to the practical situation, it must include a statistical noise to allow for the fact that the analysed chemistry of a given particle does not necessarily correspond to its true chemistry. This statistical scatter is assumed to have a normal distribution about the calculated true cementite composition, and a standard deviation of 0.5 at. % for chromium and manganese, 0.8 for molybdenum and 0.5 for silicon. These values for the standard deviation were chosen on the basis of experimental data gathered by repeated analysis of a single particle. The analysis illustrates that a scatter of this order of magnitude was inherently associated with the EDX technique, and the observed data showing statistical scatter are presented on figure 6.11. The program used to generate the data is included for reference in Appendix 2.

6.4.3 Data generated using the computer model

The new computer-generated data which included an allowance for the statistical scatter inevitable to the technique were interpreted using the regression procedures described earlier in the same way as the experimentally-obtained compositions had been. Thence, a comparison was made with the earlier computer-generated data where no such allowance for statistical scatter had been made, and with the compositions obtained experimentally.

SINGLE PARTICLE AFTER 1 HOUR AT 565 °C

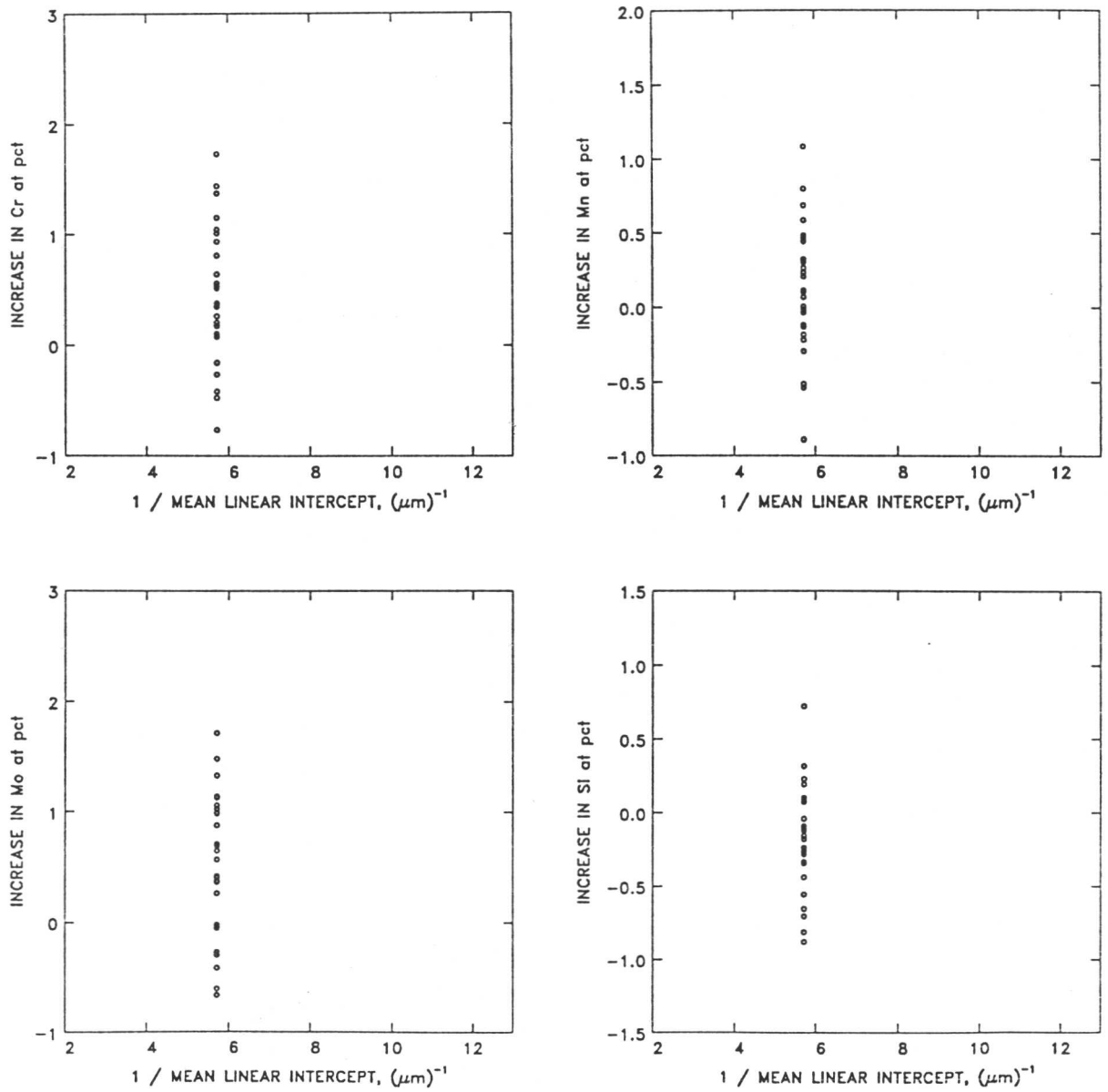


Figure 6.11: Repeated microanalysis on single particle to illustrate the statistical scatter inherent in the EDX technique

Regression analyses on the computer-generated data including scatter produced results very similar to those produced when experimental compositions were analysed, and were found to be in much better agreement with the experimental data than the computer-generated data without a statistical scatter element had been. Correlation coefficients for the $c - \bar{c}$ versus $1/x_\theta$ relationship can be obtained by carrying out the regression analysis on the compositional data obtained from both computer models. An expected value for the correlation coefficient at a particular ageing time, given the assumption that equation (6.3) holds but is masked to some degree by this statistical scatter, can be generated by repeating the regression procedure a number of times for computer-generated compositions for each ageing time, and taking the mean value of the correlation coefficients thus produced. These values, along with those obtained from experimental concentration measurements, are presented in figure 6.12–6.14.

It is of great significance that the correlation coefficients obtained from analysis of the experimental data and the computer-generated, with-scatter data are so similar, except at the longest ageing times and higher temperatures. In effect, this means that the experimental data is almost entirely explained by two factors: the size effect predicted in equation (6.2), and a statistical scatter in the EDX technique which has been both observed experimentally and modelled here.

The results demonstrate clearly that a strong particle size effect exists, whereby enrichment occurs at a faster rate when the cementite particle size is diminished. The strength of this effect is, however, masked by a statistical scatter in the microanalysis technique, especially when $(c^\theta - \bar{c})$ is relatively small.

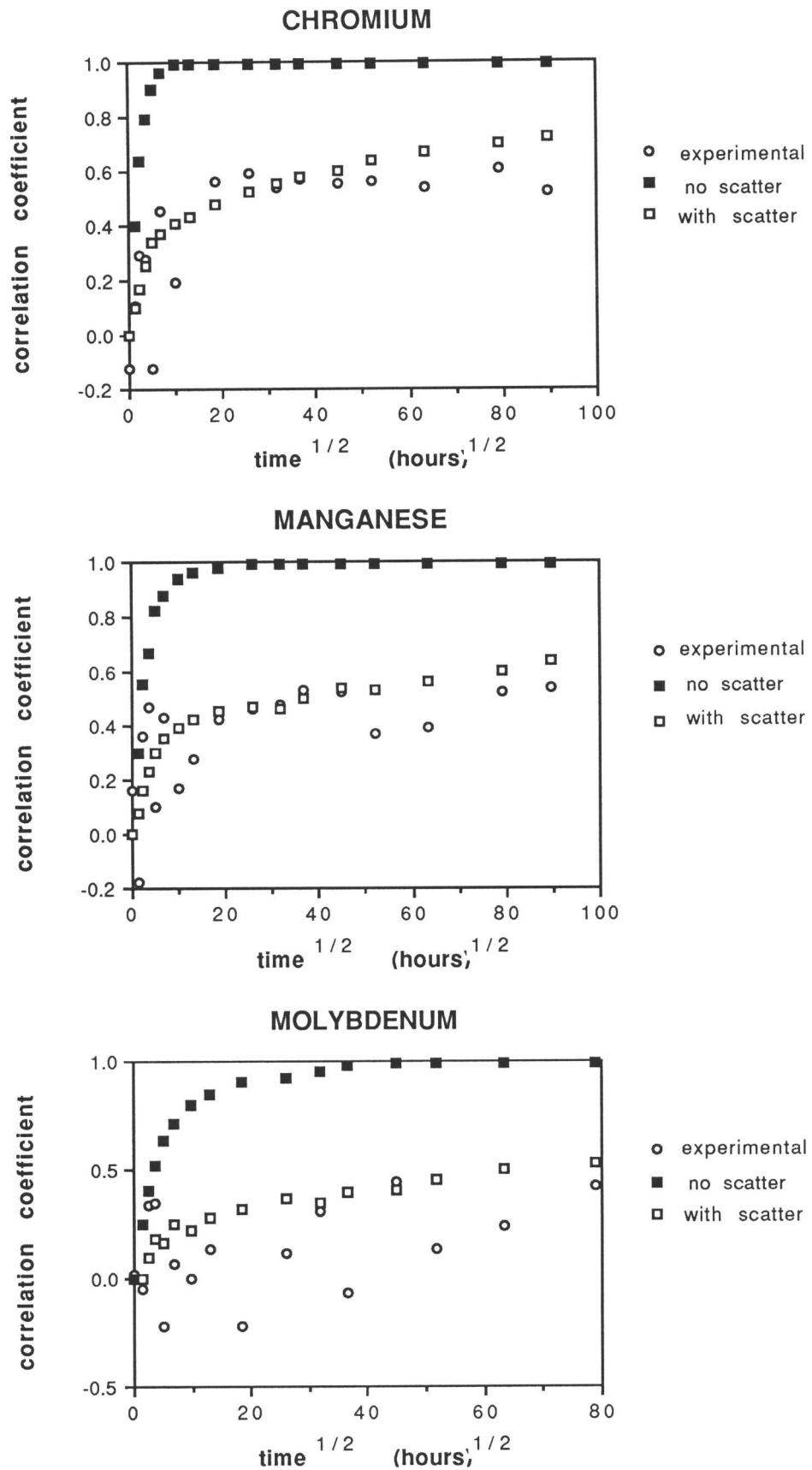


Figure 6.12: A comparison of correlation coefficients for the $(c - \bar{c}) \propto 1/x_\theta$ relationship obtained experimentally and generated by the computer model for an ageing temperature of 510°C

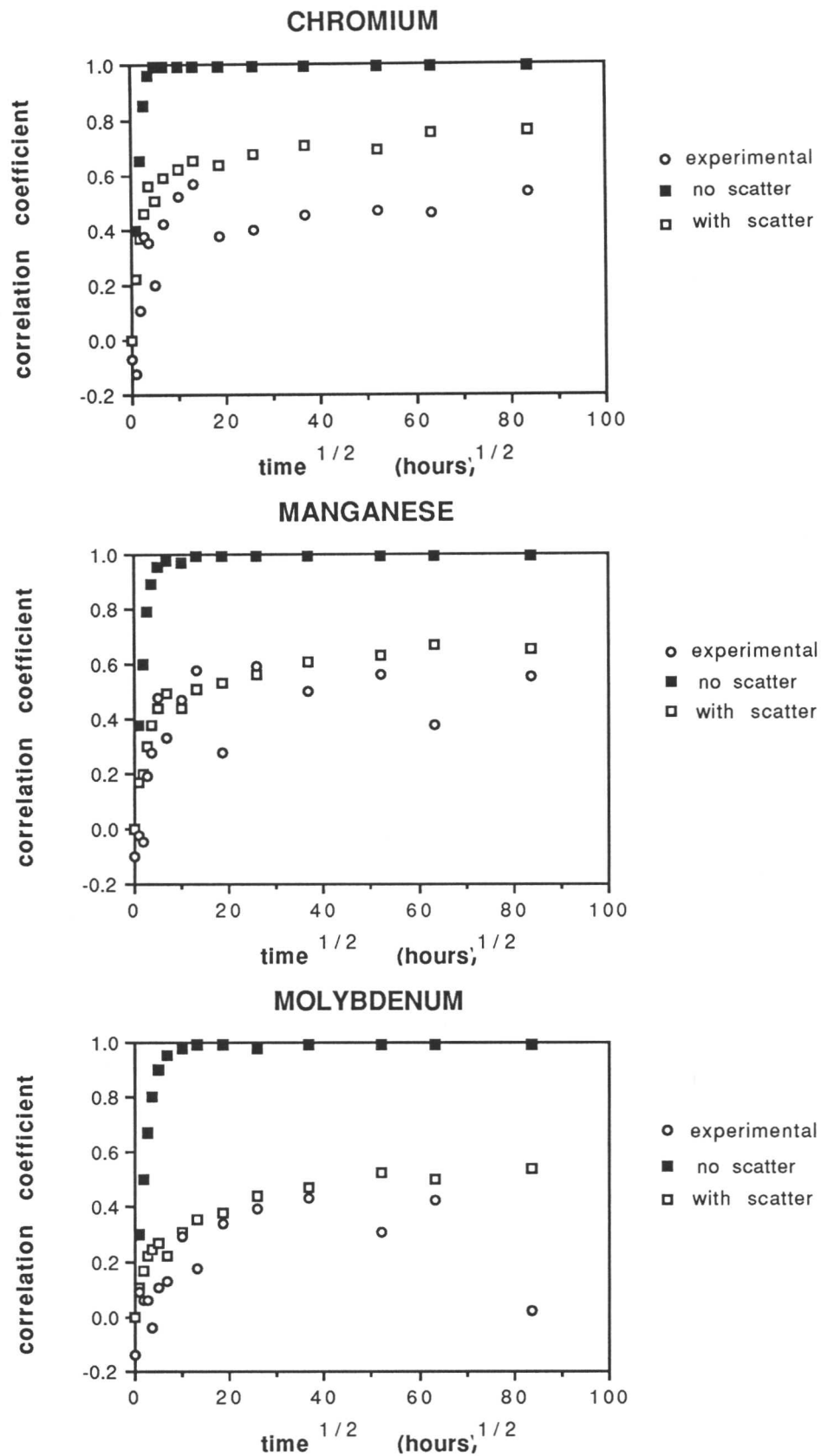


Figure 6.13: A comparison of correlation coefficients for the $(c - \bar{c}) \propto 1/x_\theta$ relationship obtained experimentally and generated by the computer model for an ageing temperature of 565°C

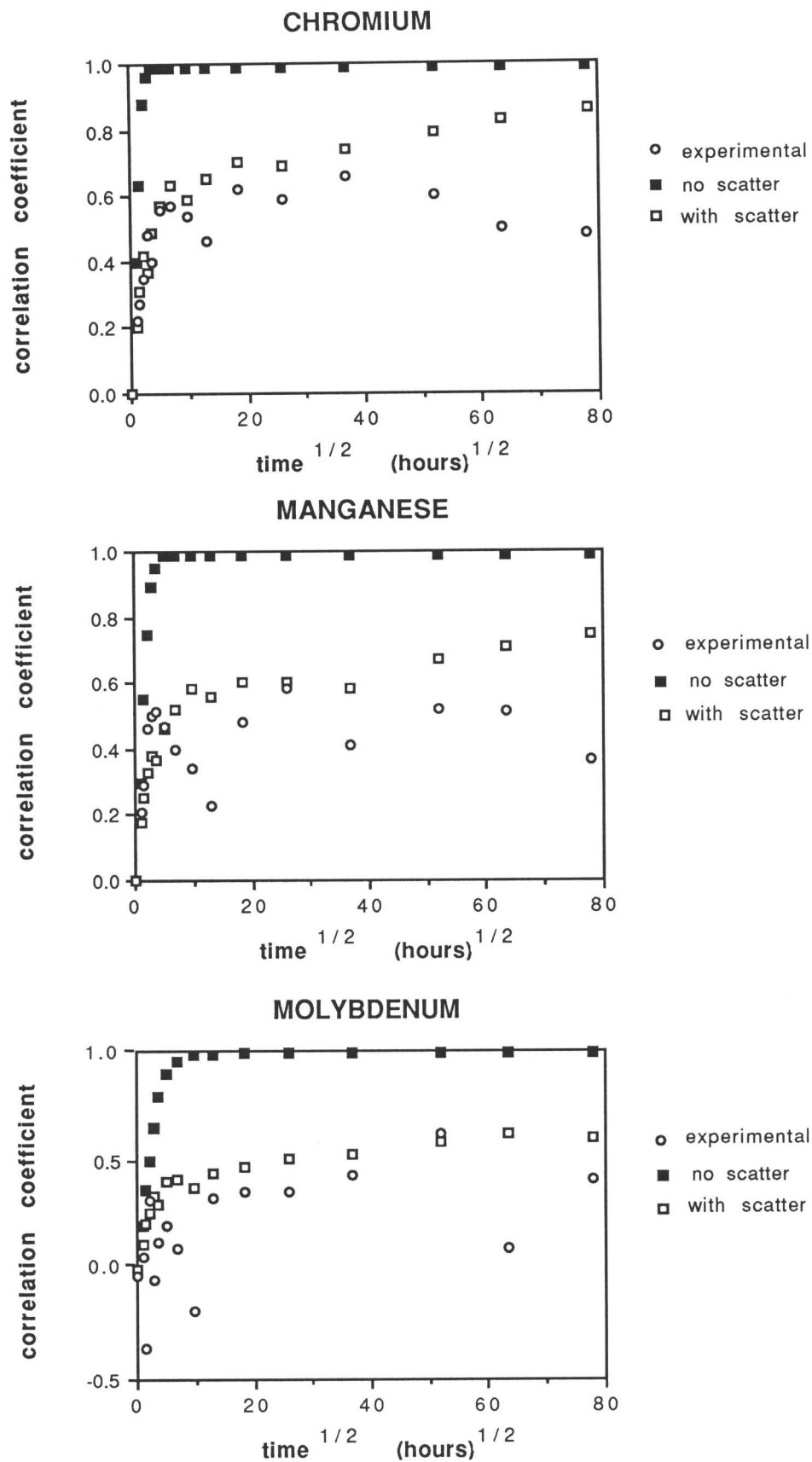


Figure 6.14: A comparison of correlation coefficients for the $(c - \bar{c}) \propto 1/x_\theta$ relationship obtained experimentally and generated by the computer model for an ageing temperature of 625°C

6.5 A Finite Element Analysis of the Ageing Process

6.5.1 Limitations of the analytical method

The current work and Bhadeshia's analysis (1989) of existing data have shown that an analytical model for the behaviour of bainitic cementite during ageing shows a reasonable agreement with experimental data, and, in particular, is an improvement on the largely empirical methods used formerly. Nevertheless, the analytical method fails to consider two important factors in a diffusion process. First, at longer ageing times the diffusion fields within ferrite associated with different cementite particles will overlap to a degree which will eventually have a significant effect on the enrichment rate, by slowing down the rate-controlling process of diffusion in ferrite. This phenomenon is referred to a soft impingement. Second, the analytical approach does not allow for a coupling of the fluxes in the two phases. As a result, a numerical method which produces a representation of the concentration profile with time and distance, and couples the fluxes across the α/θ interface is to be preferred. Bhadeshia (1989) uses a finite difference approach to achieve this, based on a procedure from Crank (1975).

6.5.2 The finite difference model

The material is treated as a complete diffusion couple between a slab of cementite of thickness x_θ , and a slab of ferrite of thickness x_α , such that:

$$\frac{x_\theta}{(2x_\alpha + x_\theta)} = V_\theta \quad (6.8)$$

Bhadeshia notes that V_θ , the volume fraction of cementite, can be calculated by application of the lever rule to \bar{c} and the $\alpha/\alpha + \theta$ and $\theta/\alpha + \theta$ phase boundaries in the iron carbon system as:

$$V_\theta = \frac{(\bar{c} - c^{\alpha\theta})}{(c^{\theta\alpha} - c^{\alpha\theta})} \quad (6.9)$$

with \bar{c} , $c^{\theta\alpha}$, and $c^{\alpha\theta}$ representing the same values as they did in the analytical approach. However, values for V_θ have already been produced using the MTDATA package, and these are used in the subsequent analysis.

Crank (1975) notes that the use of non-dimensional variables in analytical solutions frequently leads to simplification of subsequent computation. He proposes that suitable variables for a plane sheet of thickness l would be of the form $X = x/l$, $T = Dt/l^2$, and $C = c/c_0$. In consequence, Bhadeshia proposes the following for the case of cementite in ferrite:

$$\text{Distance} \quad X = x/x_\theta \quad (6.10)$$

$$\text{Concentration} \quad C = c/\bar{c} \quad (6.11)$$

$$\text{Time} \quad T' = Dt/(x_\theta)^2 \quad (6.12)$$

Hence, a non-dimensional version of the diffusion equation,

$$\frac{\partial c}{\partial t} = D \frac{\partial^2 c}{\partial x^2} \quad (6.13)$$

can be produced:

$$\frac{\partial C}{\partial T'} = \frac{\partial^2 C}{\partial X^2} \quad (6.14)$$

The analysis divides ferrite and cementite into a notional number of small slices, so that the X - T' space consists of a grid of rectangles of side lengths δX and $\delta T'$, as figure 6.15. Each grid point can be given the coordinates $\{i\delta X, j\delta T'\}$, at which the normalized composition is $C_{i,j}$. The Crank method uses Taylor series expansions of the normalized diffusion equation (6.14), so that:

$$C_{i,j+1} = C_{i,j} + \delta T' \left(\frac{\partial C}{\partial T'} \right)_{i,j} + 1/2(\delta T')^2 \left(\frac{\partial^2 C}{\partial T'^2} \right)_{i,j} + \dots \quad (6.15)$$

from which it follows that:

$$\left(\frac{\partial C}{\partial T'} \right)_{i,j} = \frac{C_{i,j+1} - C_{i,j}}{\delta T'} + O(\delta T') \quad (6.16)$$

where $O(\delta T')$ signifies that the leading term to have been neglected in producing the above by dividing through the previous equation is of the order of $\delta T'$.

Similarly, Taylor series expansions of equation (6.14) in the X direction for constant T' produce:

$$C_{i+1,j} = C_{i,j} + \delta X \left(\frac{\partial C}{\partial X} \right)_{i,j} + 1/2(\delta X)^2 \left(\frac{\partial^2 C}{\partial X^2} \right)_{i,j} + \dots \quad (6.17)$$

$$C_{i-1,j} = C_{i,j} - \delta X \left(\frac{\partial C}{\partial X} \right)_{i,j} + 1/2(\delta X)^2 \left(\frac{\partial^2 C}{\partial X^2} \right)_{i,j} - \dots \quad (6.18)$$

On adding the above:

$$\left(\frac{\partial^2 C}{\partial X^2} \right)_{i,j} = \frac{C_{i+1,j} - 2C_{i,j} + C_{i-1,j}}{(\delta X)^2} + O(\delta X)^2 \quad (6.19)$$

Bhadeshia (1989) notes that in the materials and at the temperatures under consideration, partition coefficients are large, so that the redistribution of elements is controlled by rate of diffusion in ferrite to the α/θ interface, except at very long times where c^θ approaches saturation. Equations (6.16) and (6.19) may then be substituted into the non-dimensional diffusion relationship (equation 6.14), to give an explicit finite difference formula for the rate-controlling case of diffusion in ferrite:

$$C_{1,j+1}^\alpha = C_{i,j}^\alpha + r(C_{i-1,j}^\alpha - 2C_{i,j}^\alpha + C_{i+1,j}^\alpha) \quad (6.20)$$

where $r = \delta T' / (\delta X)^2$. The value of r is determined in a semi-empirical way as a compromise between accuracy and computing time; Bhadeshia sets it to 0.4.

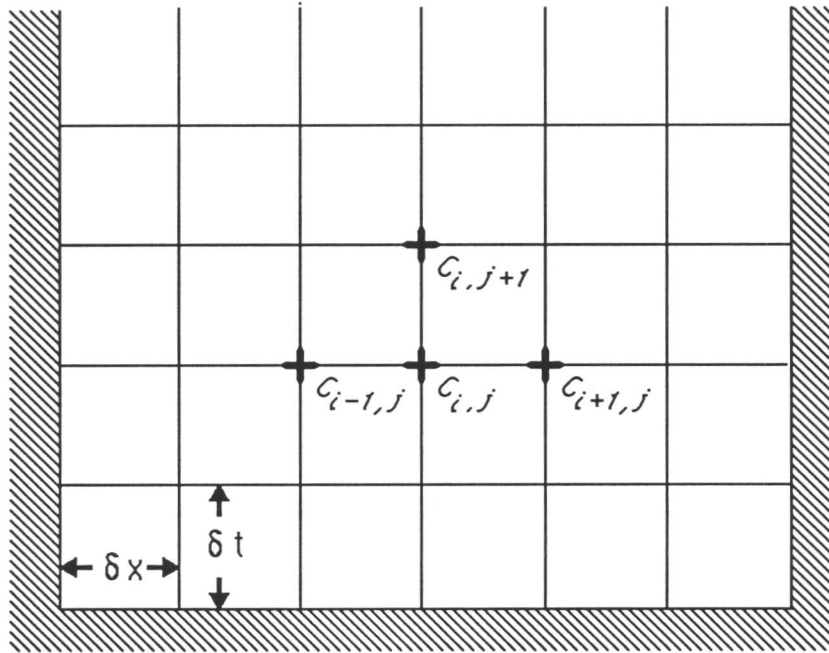


Figure 6.15: Representation of compositions in the $X-T'$ space (Crank, 1975)

A computer program was then developed to use the above equation to determine $C_{i,j}$ for times up to the ageing time required. Initial conditions were set such that $C_{i,0}^\alpha$ was $c^{\alpha\theta}/\bar{c}$ for $i = 0$, and 1 for all $i > 0$. This is a satisfactory approximation when T' is small relative to ageing time, as the algorithm quickly produces a realistic composition profile; however, if the normalized time slice is large (at low temperatures), it may not be appropriate. The program couples diffusion processes in cementite and ferrite to ensure no build up of solute at the interface, *i.e.*, $C_{0,j}^\theta$ is determined by:

$$D_\theta(C_{0,j}^\theta - C_{1,j}^\theta) = D_\alpha(C_{1,j}^\alpha - C_{0,j}^\alpha) \quad (6.21)$$

where D_θ and D_α are the diffusion coefficients in cementite and ferrite which this analysis assumes to be equal, $C_{0,j}^\theta$ and $C_{0,j}^\alpha$ are the normalized interface compositions in cementite and ferrite, and $C_{1,j}^\theta$ and $C_{1,j}^\alpha$ are the normalized compositions in cementite and ferrite at the point one finite distance element away from the interface.

6.5.3 Change of composition profile with time

Bhadeshia's analysis divides up the cementite and the ferrite into a number (n) of finite elements of thickness x_s such that:

$$\begin{aligned}n_\theta &= x_\theta/2x_s \\n_\alpha &= x_\alpha/x_s\end{aligned}\tag{6.22}$$

In this way, the finite difference model can be used to produce composition profiles for the ferrite region (the area whose diffusion rate is the rate controlling step for enrichment of cementite). Typical profiles for four distinct cases are reproduced in figure 6.16 for chromium in the 1Cr- $\frac{1}{2}$ Mo steel, with a 565°C ageing temperature and x_θ of 0.180 μ m (in keeping with the value typically found by experiment). The full 220 element plot range represents one half thickness of a hypothetical ferrite plate.

Profile 1 (after 5 hours) illustrates that in the early stages of ageing the model predicts that most of the ferrite is still at \bar{c} , with only the region nearest the θ/α interface denuded of chromium. Note that the composition of the first slice is greater than $c^{\alpha\theta}$ by a noticeable amount in the very early stages of this analysis. This is a consequence of the initial assumption of slice compositions, namely $C_{i,0}^\alpha = c^{\alpha\theta}/\bar{c}$ for $i = 0$, and 1 for all $i > 0$, rather than of fundamental significance: T' and X are large relative to the ageing time, so that the algorithm has not completely settled down to a smooth curve, but this is trivial during the long ageing times employed in practice.

Profile 2 (after 100 hours) shows a typical case during which cementite enrichment should take place as (time)^{1/2}: diffusion through ferrite to the interface is the rate controlling step, and no soft impingement has occurred to slow it down ($C_{i,j}$ for large j remains 1, which is to say c^α in these regions is \bar{c} , or 0.91 atomic pct).

Profile 3 (after 1000 hours) shows the case where an observable degree of soft impingement has almost occurred, where $C_{i,j} = 1$ for only the largest j approaching n_α , so that, at the half thickness of the ferrite plate, the diffusion

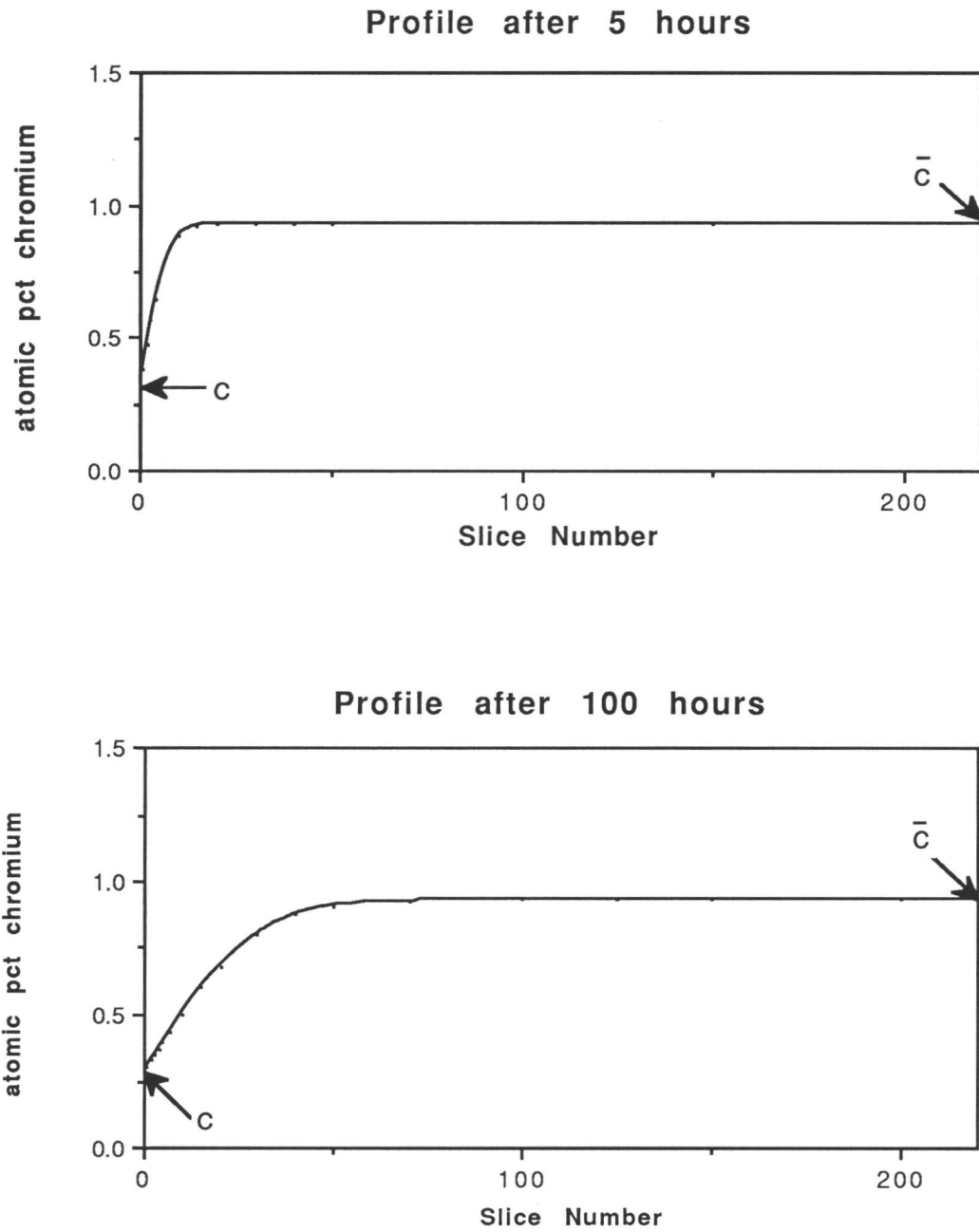


Figure 6.16: Finite element modelling of chromium composition within ferrite for the 1Cr- $\frac{1}{2}$ Mo steel aged at 565°C

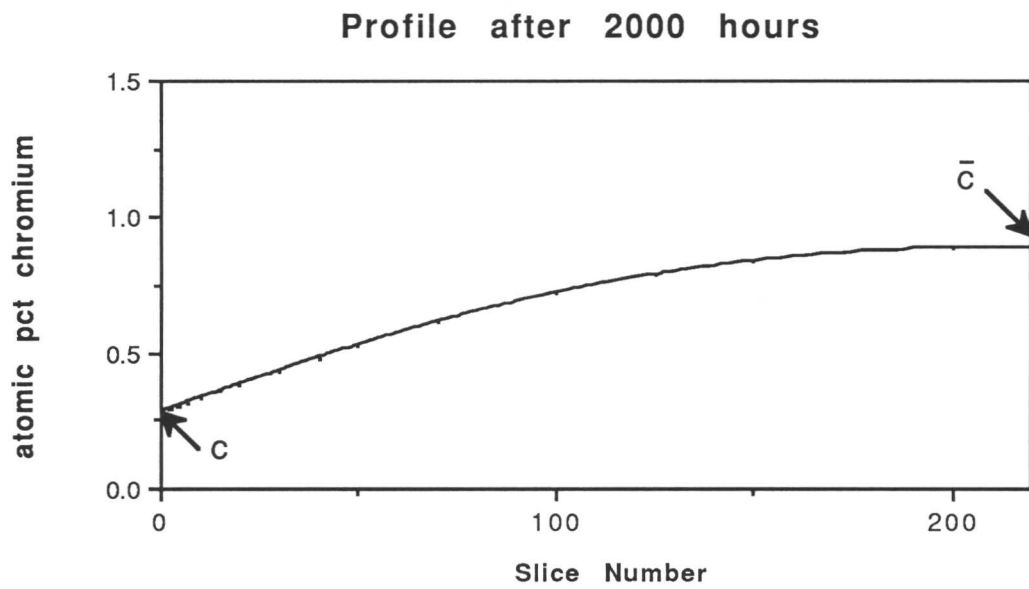
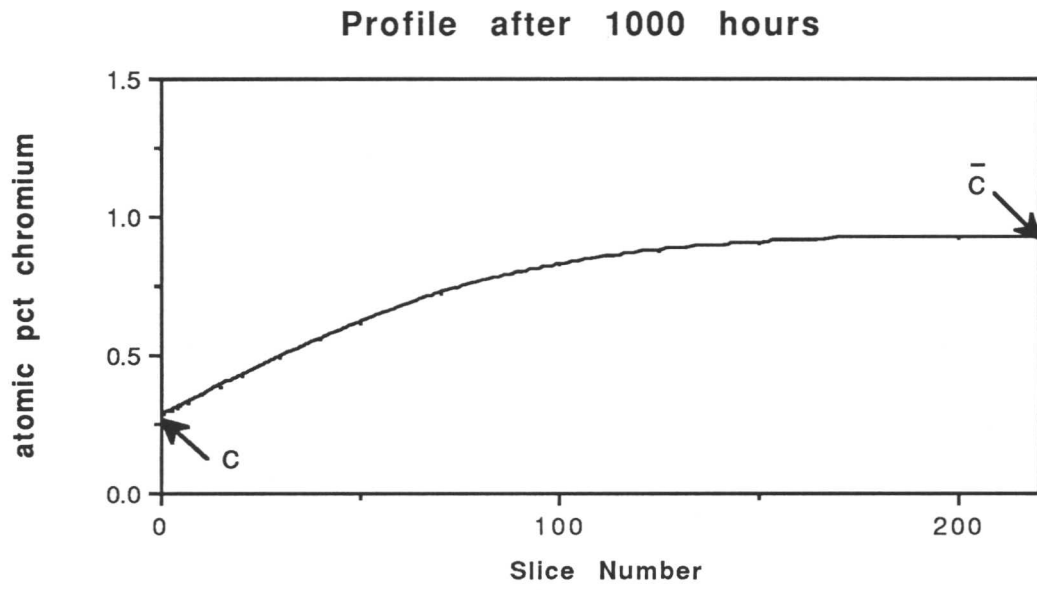


Figure 6.16: Finite element modelling of chromium composition within ferrite for the 1Cr- $\frac{1}{2}$ Mo steel aged at 565°C

profile is almost interfering with the diffusion field associated with the next cementite particle. The program is set to detect soft impingement at a 1% level of overlap of diffusion fields, which is to say that $C_{n\alpha,j} \leq 0.99$, but this is entirely arbitrary and the program can be used to determine the time at which soft impingement at any other level of diffusion field overlap commences.

Profile 4 shows the case after the onset of soft impingement. The fluxes of solute in the ferrite will be slowed slightly; therefore, the enrichment of cementite will occur at a concomitantly smaller rate, and enrichment will no longer be expected to fit a strictly $(\text{time})^{1/2}$ relationship.

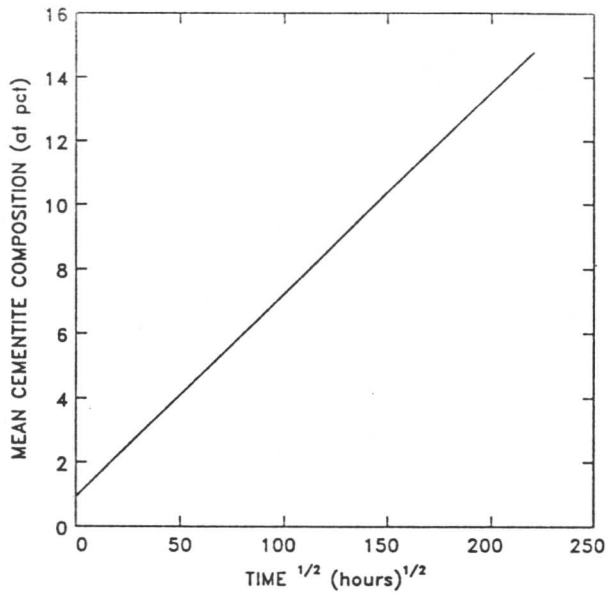
6.6 Variation of c^θ with Time: Finite Difference Approach

6.6.1 *The onset of soft impingement and its effect*

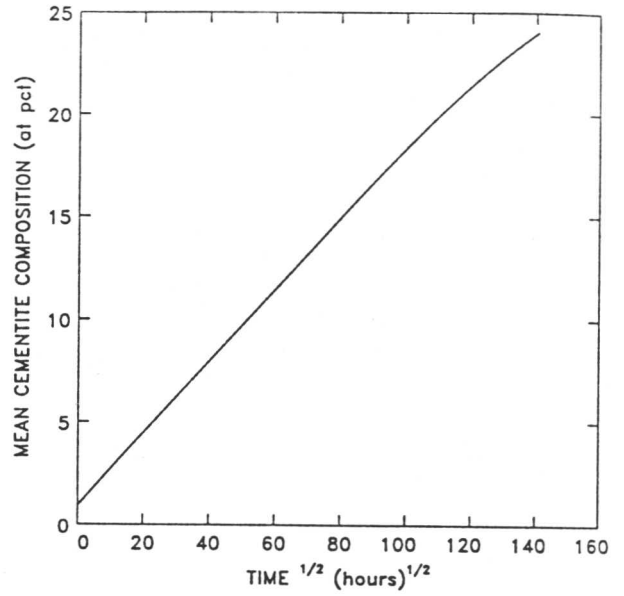
The analytical approach of Section 6.3 enabled the $(\text{time})^{1/2}$ relationship to be tested against experimental data, showing good agreement in the early stages. A decreased enrichment rate was found at longer time scales, however, and it was tentatively suggested that this could be caused by either soft impingement reducing the diffusion fluxes in the rate-controlling ferrite case, or by alloy carbide precipitation. No microscopic evidence was found for the latter in this alloy; the finite difference model enables us to consider the former.

To this end, calculations were carried out using the finite difference model to determine how c^θ varied with time, and, in particular, the occurrence and effect of soft impingement. Values of x_θ for the fully-bainitic and partially-bainitic microstructures were taken as $0.180\mu\text{m}$ and $0.150\mu\text{m}$ respectively, these being typical of the particle sizes obtained experimentally, and Bhadeshia's program was modified to use interdiffusion coefficients, which were shown in section 6.3 to be more representative of what was occurring experimentally. Predicted $(c - \bar{c})$ versus $(\text{time})^{1/2}$ plots are presented for chromium, manganese and molybdenum in figure 6.17–6.19. Note that the flattening of the predicted curves for the fully-bainitic microstructure at 625°C , and for the mixed microstructure, correspond to saturation of cementite. At this point, both cementite and ferrite should be at their equilibrium compositions.

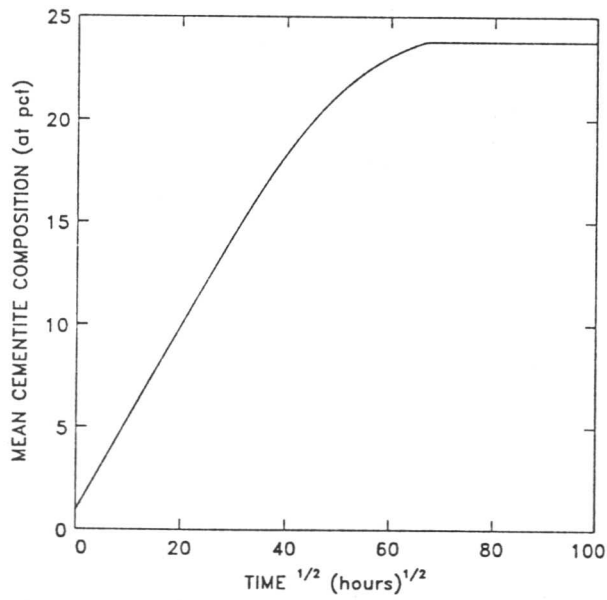
Fe-Cr-Mo STEEL AGED AT 510 °C : Cr



Fe-Cr-Mo STEEL AGED AT 565 °C : Cr



Fe-Cr-Mo STEEL AGED AT 625 °C : Cr



MIXED MICROSTRUCTURE Cr-Mo STEEL AGED AT 565 °C : Cr

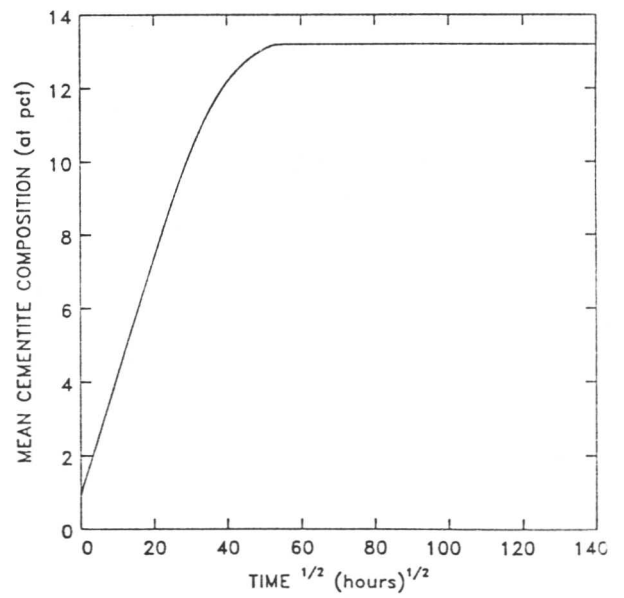


Figure 6.17: Finite difference predictions of $(c - \bar{c})$ versus $(\text{ageing time})^{1/2}$ for chromium in the Fe-Cr-Mo power plant steel

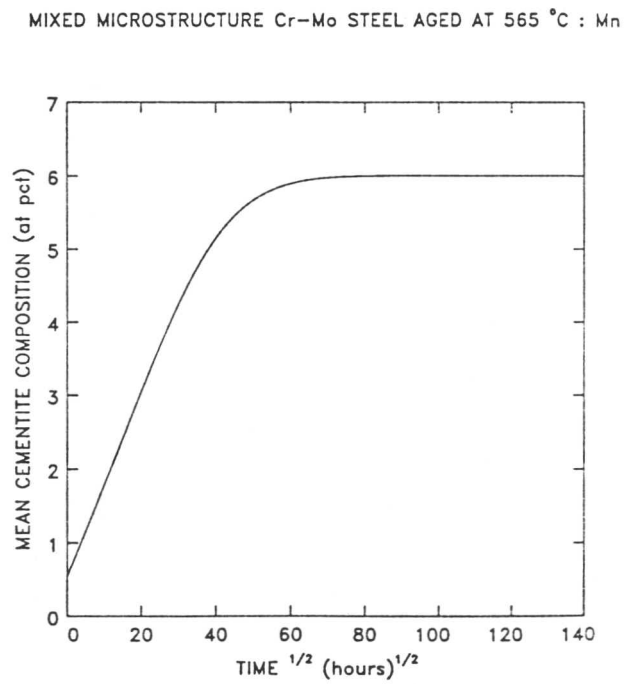
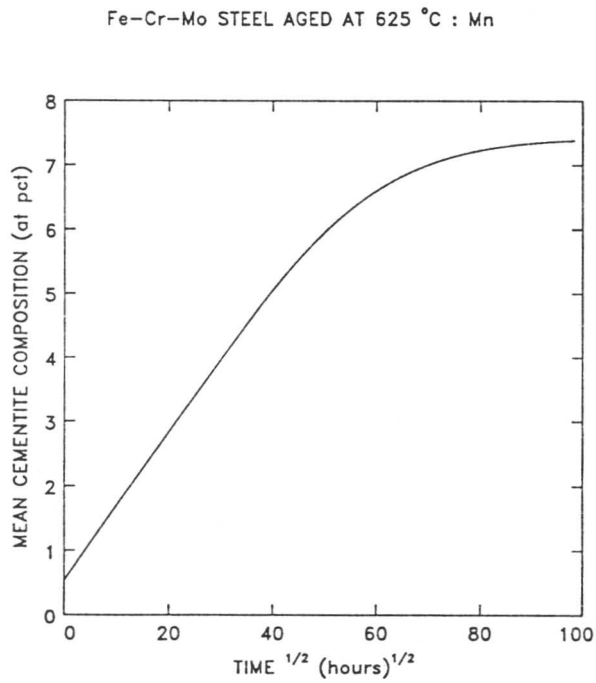
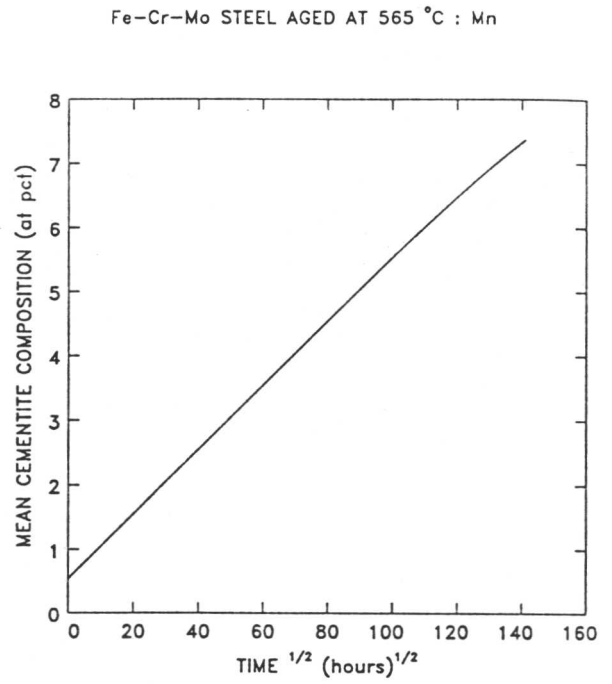
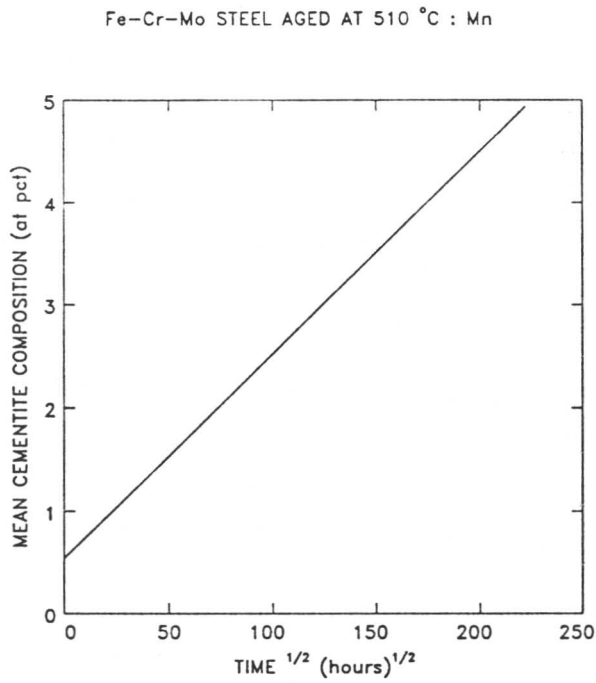


Figure 6.18: Finite difference predictions of $(c - \bar{c})$ versus (ageing time)^{1/2} for manganese in the Fe-Cr-Mo power plant steel

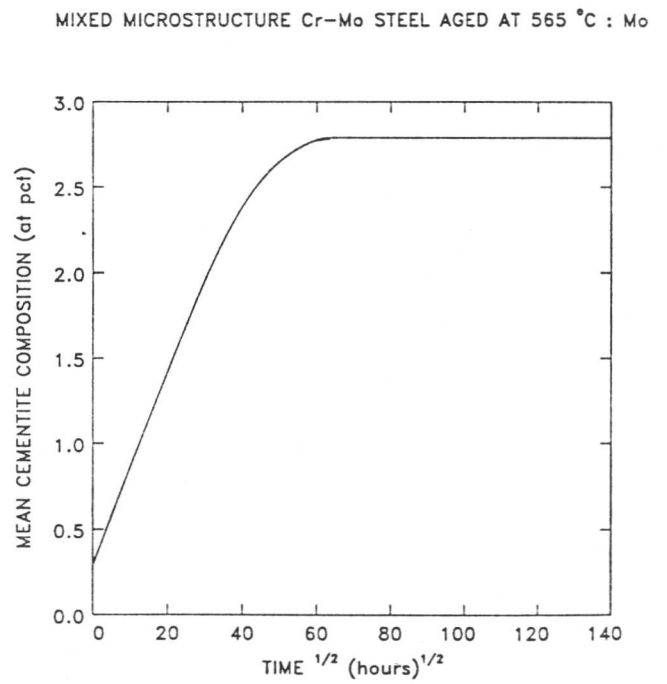
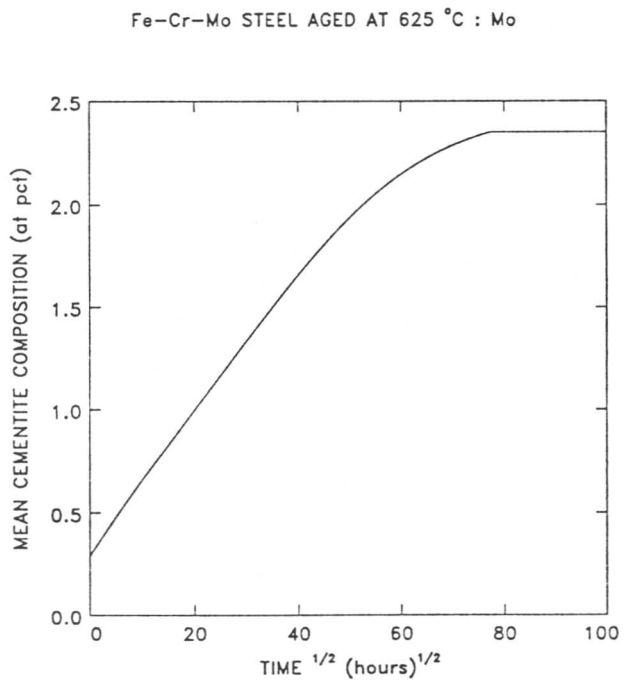
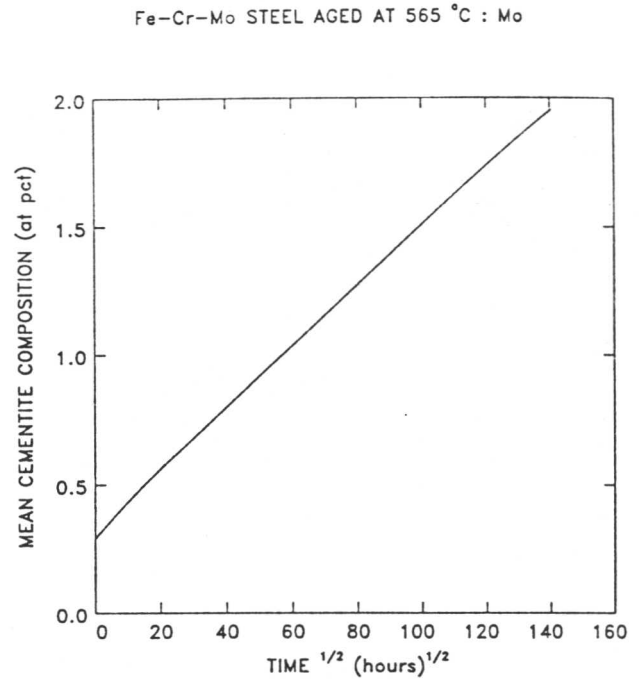
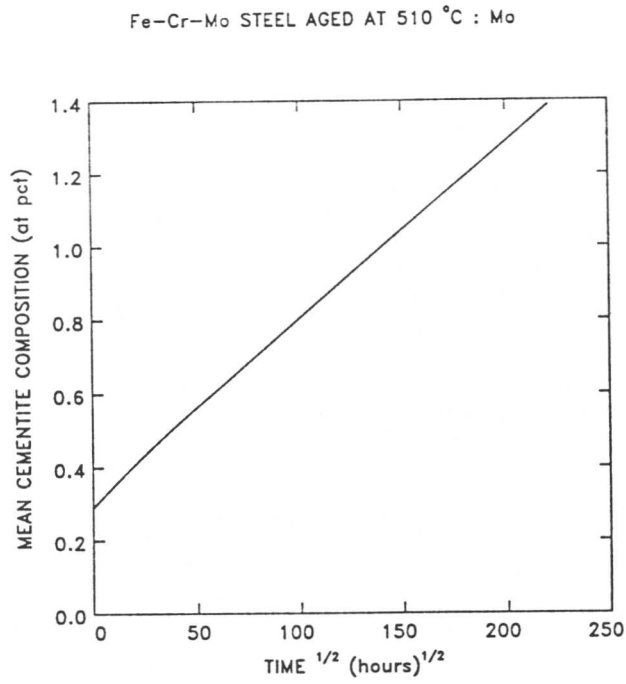


Figure 6.19: Finite difference predictions of $(c - \bar{c})$ versus (ageing time)^{1/2} for molybdenum in the Fe-Cr-Mo power plant steel

The finite difference program was initially set to register soft impingement at a 1% level, which is to say that the overlap of diffusion fields is considered to be of physical significance when $C_{n_{\alpha,j}}$, the normalized value for composition at the mid-point of the hypothetical ferrite slab, falls below 0.99. This level is entirely arbitrary, and, in consequence, predicted soft impingement times for 1%, 2%, 5% and 10% were calculated, and are shown in table 6.13, for $x_{\theta} = 0.180\mu\text{m}$. A comparison of table 6.13 with the $(c - \bar{c})$ versus (ageing time)^{1/2} finite element curves suggests that a marked deviation from linearity in $(c - \bar{c})$ versus (ageing time)^{1/2} is not really shown until the 5–10% level. At this point, the overlap of diffusion fields becomes important in determining the diffusion rates within the ferrite, and hence the rate of enrichment of cementite.

The experimental data for chromium and manganese composition vs ageing time are compared with finite difference composition versus ageing time curves on figure 6.20 and figure 6.21 respectively. Finite difference curves were generated using two values of D_{α} : the reported values for interdiffusion coefficient from Fridberg *et al.* (1969), and the values of D_{α} which were calculated from equation (6.3) to be representative of the experimental c^{θ} data.

Both the graphs and the table illustrate that measured data for $(c - \bar{c})$ levels off to some degree, and ceases to fit a (time)^{1/2} relationship, somewhat earlier than predicted by the soft impingement model; the model predicts negligible deviation from linearity over the time-scales and temperatures employed in this project. It is nevertheless suggested that the slowing down of enrichment rate at longer times may in part be due to such an effect. The Bhadeshia model assumes that all cementite and ferrite is notionally swept into two slabs, with the analysis obtaining x_{θ} from the experimentally-determined \bar{x}_{θ} , and calculating x_{α} , the half thickness of the ferrite slab, from the relationship

$$\frac{x_{\theta}}{(2x_{\alpha} + x_{\theta})} = V_{\theta} \quad (6.23)$$

with V_{θ} being obtained from the lever rule assuming a stoichiometric cementite composition as was explained in Chapter 2. This may be representative of a situation where cementite and bainite comprise a regular array of consistently sized

Ageing temp. °C	Predicted time for soft impingement (hours)			
	1% level	2% level	5% level	10% level
	(chromium)			
510	27051	32551	44010	59083
565	2563	3109	4252	5791
625	281	342	474	661
565 30% α_b	118	144	199	278
	(manganese)			
510	39077	47770	66691	93247
565	3825	4724	6732	9686
625	443	555	814	1222
565 30% α_b	160	201	294	441
	(molybdenum)			
510	52096	64806	93863	137997
565	5633	7086	10525	16039
625	607	776	1194	1918
565 30% α_b	267	341	525	844

Table 6.13: Predicted time for the onset of various levels of soft impingement in ferrite using the finite difference model and experimentally-determined values of x_θ for the Fe–Cr–Mo power plant steel

plates, but, in practice, both cementite particle size and separation will vary, a factor for which the model makes no allowance. This will lead to a practical situation where the diffusion fields of those particles more closely spaced than average will interfere on a shorter time scale than that predicted by the model.

A rigorous analysis of a real system on a finite element basis, necessitating the consideration of coupling of diffusion fields from a large number of variously-sized and randomly-distributed particles, and the extension of the model from one to three dimensions will be a major undertaking; but some idea of the effect of decreased particle spacing can be obtained from figure 6.22. The figure was

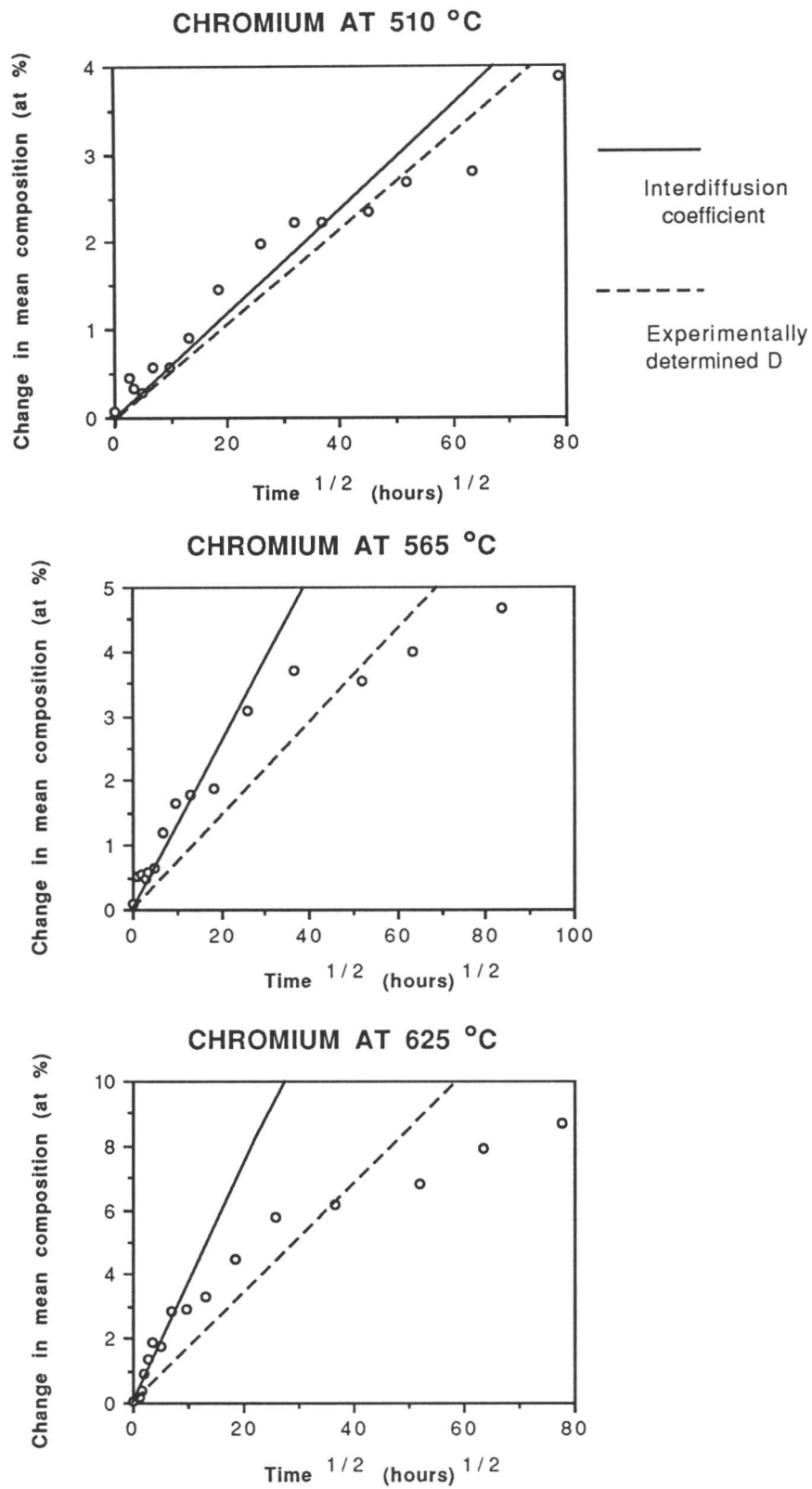


Figure 6.20: A comparison between experimental cementite enrichment results for chromium in the Fe-Cr-Mo power plant steel and the two finite difference predictions of $(c - \bar{c})$ versus $(\text{ageing time})^{1/2}$ obtained by using the experimentally-determined and the reported values for D_α

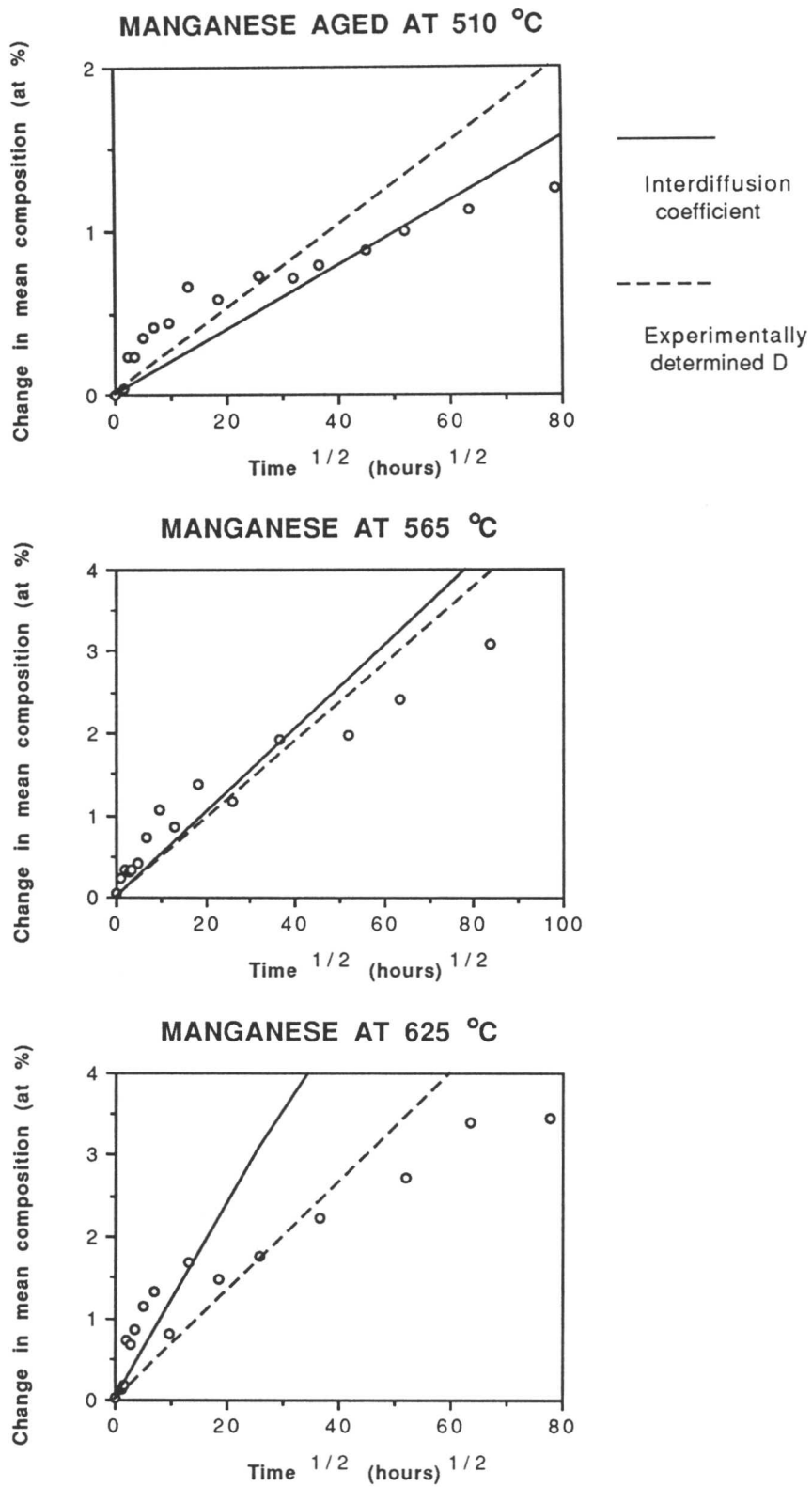


Figure 6.21: A comparison between experimental cementite enrichment results for manganese in the Fe-Cr-Mo power plant steel and the two finite difference predictions of $(c - \bar{c})$ versus $(\text{ageing time})^{1/2}$ obtained by using the experimentally-determined and the reported values for D_α

generated by performing finite element calculations for the composition change in chromium aged at 565°C, using the typical experimental x_θ value of 0.180 μm . In addition to the standard analysis, which set x_α on the basis of equation (6.23), curves were also calculated with the half-thickness of the ferrite slab set to $x_\alpha/2$, $x_\alpha/3$, and $x_\alpha/4$, in all cases keeping the other parameters constant.

It can be seen from figure 6.22 that this somewhat arbitrary adjustment to the ferrite thickness has a dramatic effect on the value of c^θ predicted by finite element analysis. This suggests strongly that it is likely that some particles will be affected by soft impingement over the time-scale and temperatures in these experiments, which would explain the observed deviation from linearity of a $(c^\theta - \bar{c})$ vs $(\text{time})^{1/2}$ plot at longer ageing times.

It is also apparent that a slowing down of enrichment rate due to soft impingement in the ferrite, by affecting small particles as well as large ones, would introduce an uncertainty into any size effect, and may be a partial explanation of the observation that the magnitude $(c - \bar{c})$ vs x_θ^{-1} size effect was not as large as predicted by equation (6.3) at higher temperatures and longer ageing times.

It should be emphasized that the flattening of the composition vs $(\text{time})^{1/2}$ curves in the $x_\alpha/3$ and $x_\alpha/4$ cases is not due to saturation of cementite, but rather to the loss of chromium from the ferritic region.

6.7 Alloy carbide precipitates

Calculations have been performed to determine the thermodynamically-stable carbide structures at the three ageing temperatures, and the relative proportions and equilibrium compositions of those phases. These were done using the MTDATA computer package which was developed by the National Physical Laboratory (NPL). The package models multicomponent systems using a database of carefully determined results from simpler systems.

The results of this calculation are presented in table 6.14, which shows that the stable carbide in this alloy at all three ageing temperatures is M_{23}C_6 . This is the species which may be expected to precipitate out in preference to cementite for prolonged ageing, but, as noted earlier, no significant evidence of

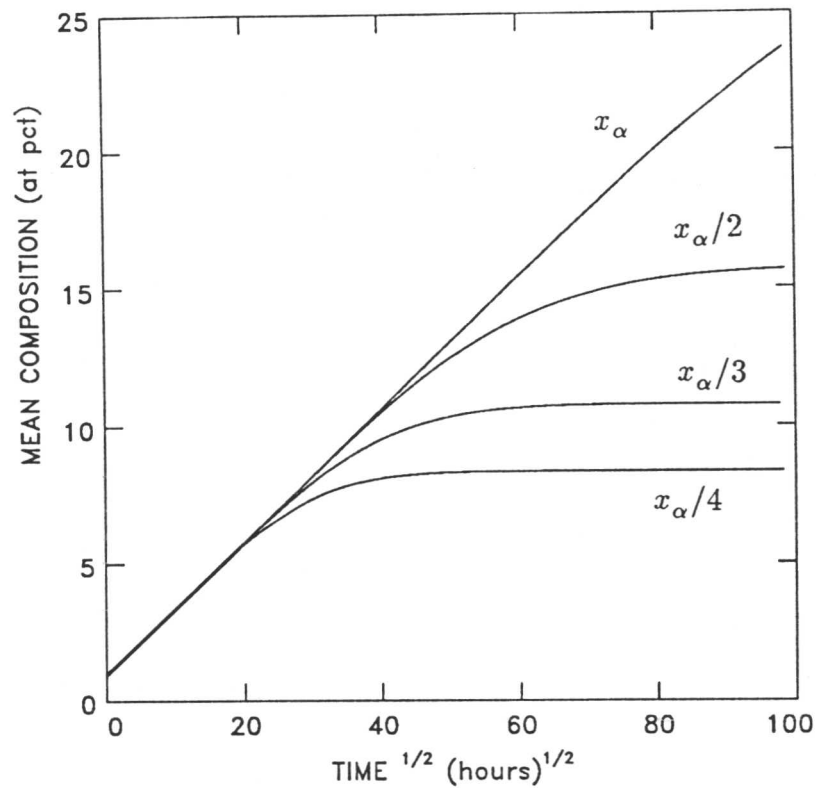


Figure 6.22: The effect of variation in ferrite thickness on a finite element analysis of the ageing of a $0.180\mu\text{m}$ cementite particle at 565°C for the $1\text{Cr}-\frac{1}{2}\text{Mo}$ type steel

this has been found in these experiments, and it appears that a longer timescale is required for the process to occur.

6.8 Summary

The measurement of cementite composition during ageing of bainitic microstructures in a $1\text{Cr}-\frac{1}{2}\text{Mo}$ type power plant steel provides evidence that the analytical model proposed by Bhadeshia (1989) (see equation (6.3)) is a good model of the real behaviour of this material before the onset of soft impingement. Cementite enrichment was found to show good agreement with the $(\text{time})^{1/2}$ relationship that the model predicted, a prediction which is at variance with frequent industrial practice where an empirical $(\text{time})^{1/3}$ relation has been preferred. In particular, the values for D_α which were calculated from enrichment data us-

Temp (K)	Equilibrium phases	Composition (wt %)					
		Fe	Cr	Mn	Mo	Si	C
783	97.59% α	98.95	0.24	0.52	0.02	0.24	0.00
	2.41% $M_{23}C_6$	48.97	26.27	0.00	19.78	0.00	4.98
838	97.59% α	98.86	0.33	0.52	0.03	0.24	0.00
	2.41% $M_{23}C_6$	52.65	22.89	0.00	19.49	0.00	4.97
898	97.59% α	98.75	0.42	0.52	0.05	0.24	0.00
	2.41% $M_{23}C_6$	56.78	19.43	0.00	19.49	0.00	4.97
838 30% α_b	93.34% α	99.37	0.13	0.23	0.00	0.24	0.00
	3.31% θ	77.23	8.69	7.30	0.05	0.00	6.74
	0.37% M_7C_3	36.78	39.74	13.98	0.81	0.00	8.68
	2.96% $M_{23}C_6$	67.93	10.50	0.00	16.59	0.00	4.98

Table 6.14: Calculated equilibrium phase compositions for the Fe–Cr–Mo power plant steel at the temperatures used for ageing

ing equation (6.3) can be considered strong evidence in support of the model. Furthermore, individual values of c^θ at a given time are found to vary with cementite particle size such that $(c - \bar{c}) \propto x_\theta^{-1}$, as predicted by equation (6.3). This size effect has been shown to be of particular significance once the limitations imposed on such an analysis by the unavoidable statistical scatter concomitant with the EDX technique is considered.

It can be concluded that, in this material, the mechanism effecting enrichment of cementite is predominantly diffusion of substitutional alloying elements through the ferrite to the α/θ interface. Although some evidence of cementite coarsening was found, this process does not appear to play a major rôle in the enrichment of those particles.

The finite element model analysis fits the data very well before a significant level of soft impingement occurs, and gives some quantitative prediction of the effect of soft impingement, although refinements are necessary if the variation in size and irregular distribution of cementite particles that is found in practice is to be considered properly. The experimental results suggest, in particular, that the lack of account taken by the finite element analysis of variation in

interparticle distances may be a particular problem, with some slowing down of the rate of enrichment occurring early than the model predicts in practice.

A full analysis taking account of non-uniform particle distributions, changes to cementite morphology (enlargement and shape change), and the interaction of diffusion fields in ferrite associated with many cementite particles of differing x_θ is necessary if a model which can fully quantify the later stages of ageing and the approach to saturation in real materials is to be developed. To do this rigorously would be a major undertaking, and in the mean time, the current analysis provides a good representation of the cementite enrichment processes in aged bainitic cementite in these materials.

Chapter 7

AGEING OF BAINITIC MICROSTRUCTURES:

FULLY-BAINITIC Fe–Cr MODEL ALLOY

7.1 EDX Compositional Data

The experiments described in the previous chapter were also carried out on a Fe–4.08Cr–0.3C (wt%) alloy. This steel was chosen to give a simple ternary system to contrast with the multiple alloying elements of the real power plant steel. The higher substitutional content should also encourage the formation of alloy carbides so that the effect of this on the ageing process can be studied over a more manageable timescale.

The EDX microanalytical data were collected and analysed as before, the analysis being applied only to results from cementite particles. In practice, other alloy carbides were found to precipitate after relatively short ageing times, and these precipitates are considered in a later section. It was also found that the cementite had disappeared entirely soon after this secondary precipitation commenced, presumably going back into solution to allow precipitation of the nearer-equilibrium species. This accounts for the fact that the maximum ageing time at each temperature in the c^θ analysis was much shorter than had been the case with the 1Cr– $\frac{1}{2}$ Mo steel; the cementite was no longer present in the microstructure.

Results obtained from plotting $(c - \bar{c})$ vs $1/x_\theta$ are presented in table 7.1 for the series of specimens aged at 510°C, in table 7.2 for specimens aged at 565°C, and in table 7.3 for specimens aged at 625°C. The initial microstructures were fully bainitic for all three ageing temperatures. The data in the table are once again presented for convenience in units of μm for x_θ and at.% for $(c - \bar{c})$. Only those compositional data which were obtained from cementite are presented in these tables. It was found in this alloy that during ageing the cementite was replaced by other carbides, a process which is discussed later in the chapter.

7.2 Variation of Composition Change with Particle Size

At short ageing times, the results obtained when the regression analysis for the $(c - \bar{c}) \propto x_{\theta}^{-1}$ relationship (as predicted by equation (6.1)) is carried out for EDX compositional data for each ageing treatment show similar trends to those for the power plant steel: as ageing time increases, the correlation coefficient which is calculated for the predicted size effect (*i.e.*, $(c - \bar{c})$ versus $1/x_{\theta}$) improves; the calculated best fit gradient generally increases, indicating that the magnitude of the size effect is becoming more marked; and the statistical significance attributable to the size effect increases. Illustrations of the effect in the model alloy are provided by the plots in figure 7.1(a-c).

It is evident that these effects occur over a much more rapid time-scale than was the case for the 1Cr- $\frac{1}{2}$ Mo material, a consequence of the higher substitutional content, which results in a greater imbalance between the \bar{c} concentration of chromium in the two phases in the as-transformed condition and the equilibrium chromium concentrations, and a consequent increase in the driving force for the diffusion process.

As the ageing time is increased, the correlation of experimental data to the $(c - \bar{c}) \propto x_{\theta}^{-1}$ relationship, which was never very great, becomes poorer once more. It appears that the relationship is breaking down. This is not surprising in view of the fact that the situation is no longer a diffusion problem alone: the precipitation of alloy carbides and the disappearance of cementite are also occurring, so the analytical diffusion model cannot describe the situation in practice. Nevertheless, it can be said that during the early stages of ageing, where negligible alloy carbide precipitation is observed, the existence of the size effect predicted by equation (6.1) suggests that cementite enrichment is effected by a diffusion process, controlled by the rate of diffusion in the ferrite phase, and driven by the concentration difference between the initial ferrite composition (\bar{c}) and the equilibrium ferrite composition; in this respect, the process is similar to that found in the case of the power plant steel.

Ageing time (hours)	No of points	Mean c change (at %)	Mean x_θ μm	Data from best fit $(c - \bar{c}) \propto x_\theta^{-1}$		
				correlation	gradient	significance
0	31	0.33	0.174	-0.02	-0.010	<0.90
1	29	0.25	0.173	0.02	0.021	<0.90
3	30	1.33	0.182	0.10	0.118	<0.90
6	31	0.94	0.179	0.20	0.122	<0.90
12	31	1.57	0.176	0.13	0.139	<0.90
24	27	1.09	0.177	0.24	0.233	0.90
48	29	1.90	0.169	0.33	0.262	0.95
96	29	1.62	0.162	0.22	0.156	<0.90
168	33	1.99	0.150	0.19	0.148	<0.90

Table 7.1: Fe-4.08Cr-0.3C (wt.%) model alloy, with a fully-bainitic initial microstructure, aged at 510°C.

Ageing time (hours)	No of points	Mean c change (at %)	Mean x_θ μm	Data from best fit $(c - \bar{c}) \propto x_\theta^{-1}$		
				correlation	gradient	significance
0	36	0.32	0.173	-0.14	-0.067	<0.90
1	29	0.40	0.191	-0.17	-0.188	<0.90
2	32	1.44	0.193	0.11	0.117	<0.90
4	32	2.27	0.166	0.31	0.326	0.90
8	30	2.01	0.143	0.41	0.227	0.95
24	28	2.36	0.156	0.12	0.241	<0.90

Table 7.2: Fe-4.08Cr-0.3C (wt.%) model alloy, with a fully-bainitic initial microstructure, aged at 565°C.

Ageing time (hours)	No of points	Mean c change (at %)	Mean x_θ μm	Data from best fit $(c - \bar{c}) \text{ v } x_\theta^{-1}$		
				correlation	gradient	significance
0	28	0.13	0.154	-0.23	-0.151	<0.90
1	29	0.85	0.160	0.06	0.036	<0.90
2	28	1.50	0.154	0.37	0.284	0.98
4	31	2.42	0.158	0.11	0.123	<0.90
8	26	2.60	0.138	-0.06	-0.028	<0.90

Table 7.3: Fe-4.08Cr-0.3C (wt.%) model alloy, with a fully-bainitic initial microstructure, aged at 625°C.

Fe-Cr STEEL, AS TRANSFORMED

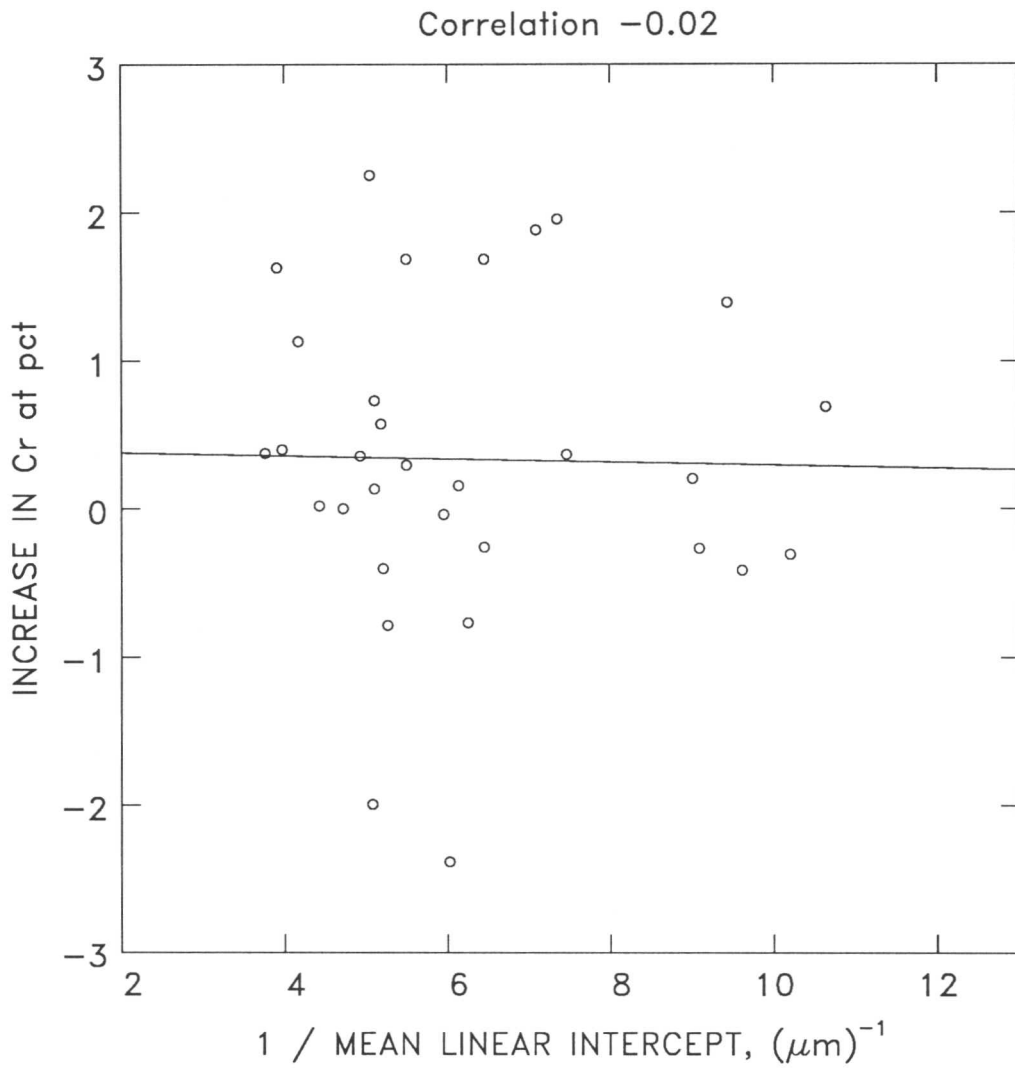


Figure 7.1(a): EDX microanalytical data for the Fe-Cr steel

Fe-Cr STEEL AFTER 12 HOURS AT 510 °C

Correlation 0.13

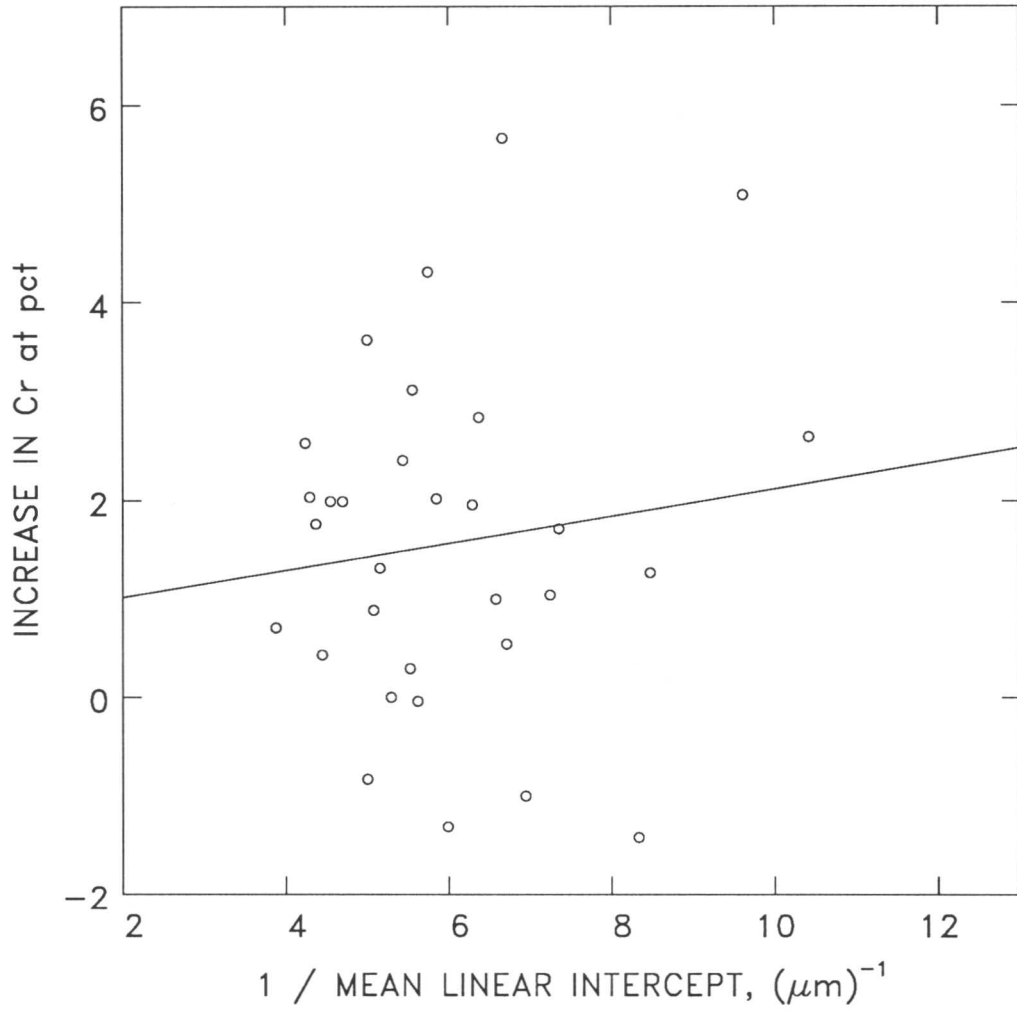


Figure 7.1(b): EDX microanalytical data for the Fe-Cr steel

Fe-Cr STEEL AFTER 1 WEEK AT 510 °C

Correlation 0.19

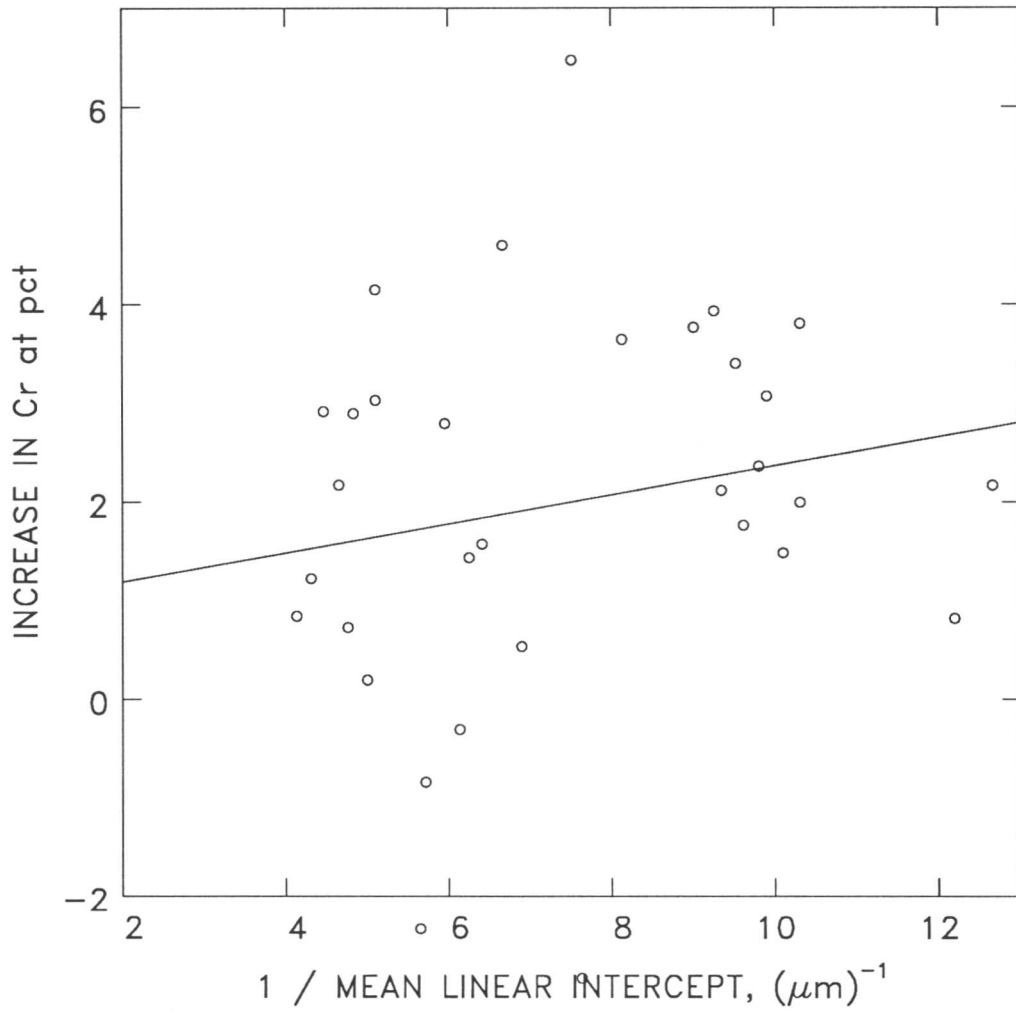


Figure 7.1(c): EDX microanalytical data for the Fe-Cr steel

7.3 Variation of c^θ with Time

The finite difference analysis outlined in the previous chapter was carried out for this material. A representative value for x_θ , the mean cementite thickness, was taken, on the basis of experimental data, to be $0.18\mu\text{m}$. Equilibrium compositions for ferrite and cementite, and V_θ , were obtained from the MTDATA package as before, and are presented in table 7.4.

As was the case in the previous chapter, the equilibrium chromium concentration in the carbide is expressed both as a true atomic percent (inclusive of carbon), $c_{all}^{\theta\alpha}$, and as an atomic percent considering only substitutional elements (Cr and Fe), $c_{sub}^{\theta\alpha}$. The latter value is calculated for compatibility with measured data as EDX only detects the chromium and iron.

Temp (K)	V_θ (pct)	equilibrium compositions				
		weight pct		atomic pct		
		$c^{\alpha\theta}$	$c^{\theta\alpha}$	$c^{\alpha\theta}$	$c_{all}^{\theta\alpha}$	$c_{sub}^{\theta\alpha}$
783	4.18	1.05	72.3	1.13	59.2	78.9
838	4.18	1.34	65.4	1.44	53.8	71.7
898	4.17	1.68	57.7	1.80	47.8	63.7

Table 7.4: Calculated equilibrium chromium concentrations for a cementite/ferrite mixture in the Fe–Cr steel at the temperatures used for ageing

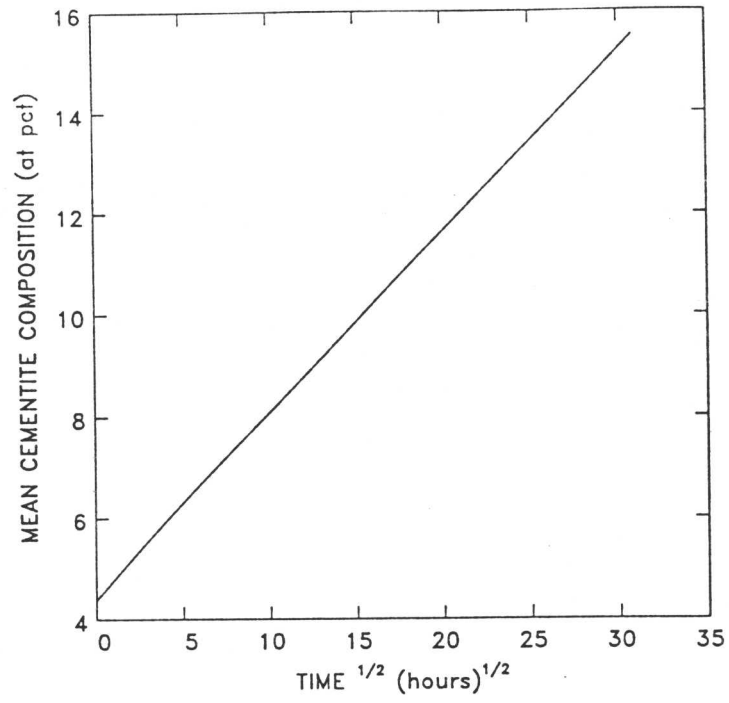
When the finite difference predictions for $(c^\theta - \bar{c})$ vs $(\text{time})^{1/2}$ (figure 7.2–figure 7.4) are compared with experimental data plotted to the same relationship (figure 7.5) it is apparent that the enrichment rate was substantially slower in practice than predicted by the model, even at ageing times preceding those at which significant evidence of secondary precipitation was found. The differences are especially marked at 565°C and 625°C ; at 510°C the experimentally-measured enrichment rate, although lower than prediction, is of a similar order of magnitude. It seems reasonable to conclude from this observation that, even at the early stages of ageing, some secondary precipitation had occurred;

thence, the finite difference prediction for the composition profile of ferrite no longer represented the true situation, in which some solute atoms were associated with carbide particles within the ferrite, and the model could not be applied.

Nevertheless, appreciable enrichment of cementite with chromium was observed during the early stages of ageing. This observation, and the fact that a size effect (such that smaller particles had enriched more than larger at a given ageing time) was observed combine to suggest that diffusion of chromium through ferrite into cementite does take place, although at a reduced rate owing to the simultaneous precipitation of more thermodynamically-stable chromium-rich carbides. This produces some correlation of the experimental data with the diffusion model, although the agreement is relatively poor as the true situation on a microscopic level is much more complex than the simple, diffusion-only model assumes. As the newly-precipitated carbides grow at the expense of cementite, even this limited correlation ceases, and subsequently the cementite is found to disappear altogether.

It can be concluded that an analysis of bainitic cementite composition carried out in association with a diffusion-based model for enrichment of cementite will only be of value in the determination of the thermal history of an aged specimen in the absence of precipitation of a second carbide species (as was the case for the power plant steel). In this case, the presence of secondary precipitation means that the diffusion-based model alone is inadequate to describe the situation; hence, cementite compositions are not relatable to the ageing time and temperature regime on this basis.

Fe-4.08Cr STEEL AGED AT 510 °C



Fe-4.08Cr STEEL AGED AT 510 °C

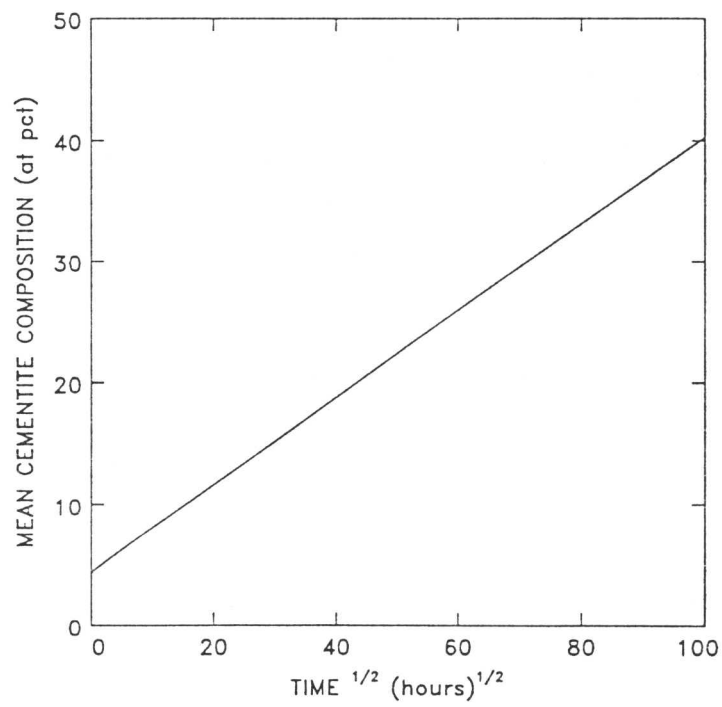
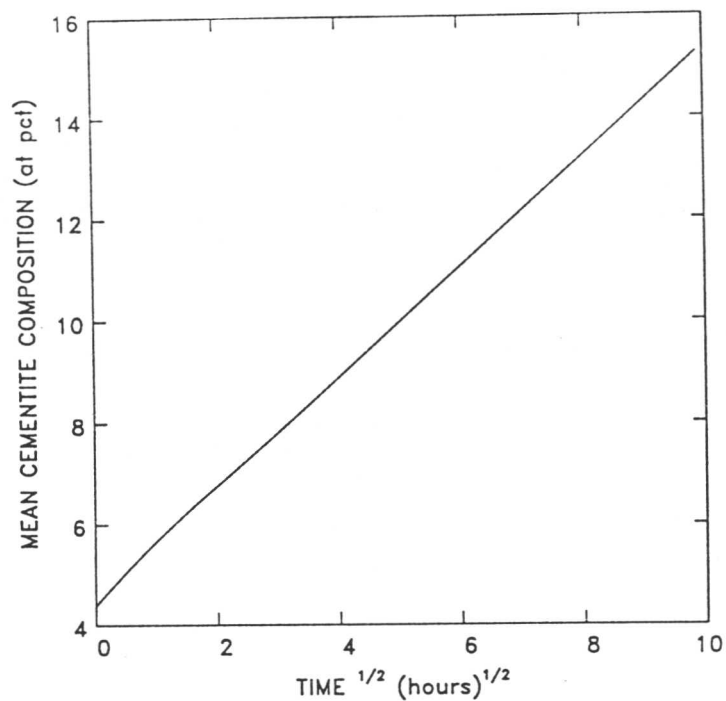


Figure 7.2: Finite difference predictions of $(c - \bar{c})$ versus $(\text{ageing time})^{1/2}$ in the Fe-Cr steel aged at 510 °C

Fe-4.08Cr STEEL AGED AT 565 °C



Fe-4.08Cr STEEL AGED AT 565 °C

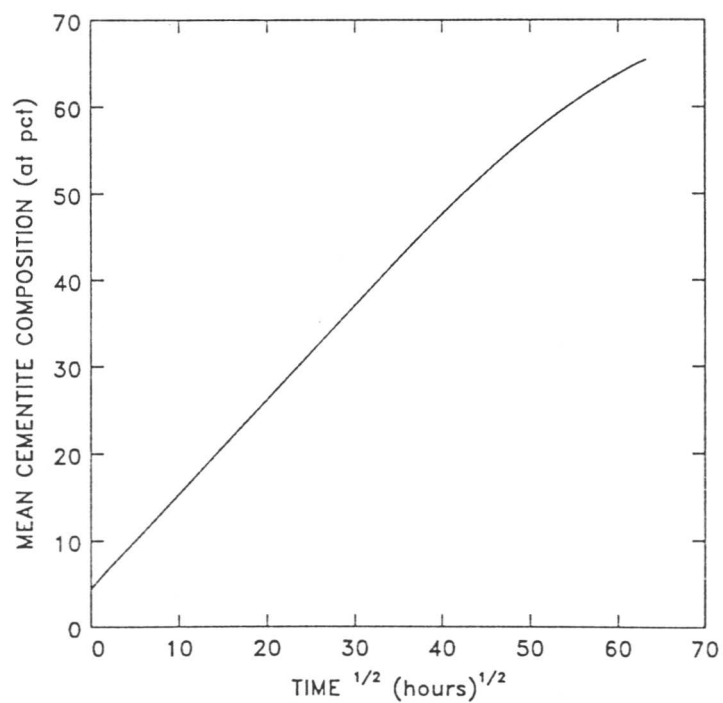
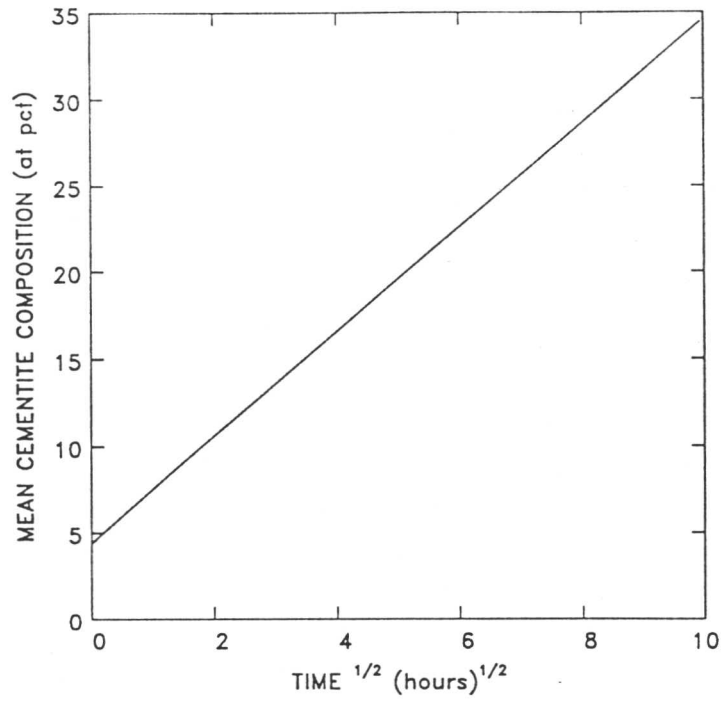


Figure 7.3: Finite difference predictions of $(c - \bar{c})$ versus $(\text{ageing time})^{1/2}$ in the Fe-Cr steel aged at 565 °C

Fe-4.08Cr STEEL AGED AT 625 °C



Fe-4.08Cr STEEL AGED AT 625 °C

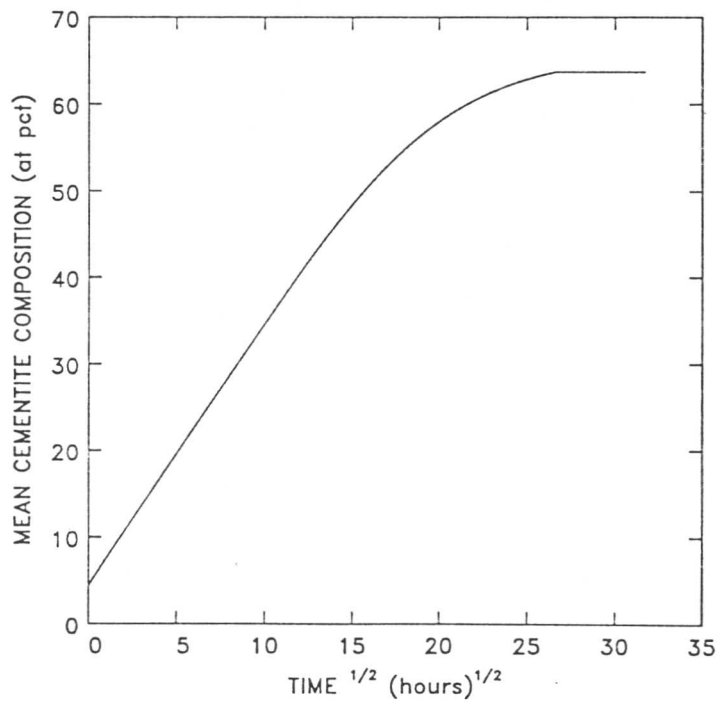


Figure 7.4: Finite difference predictions of $(c - \bar{c})$ versus $(\text{ageing time})^{1/2}$ in the Fe-Cr steel aged at 625 °C

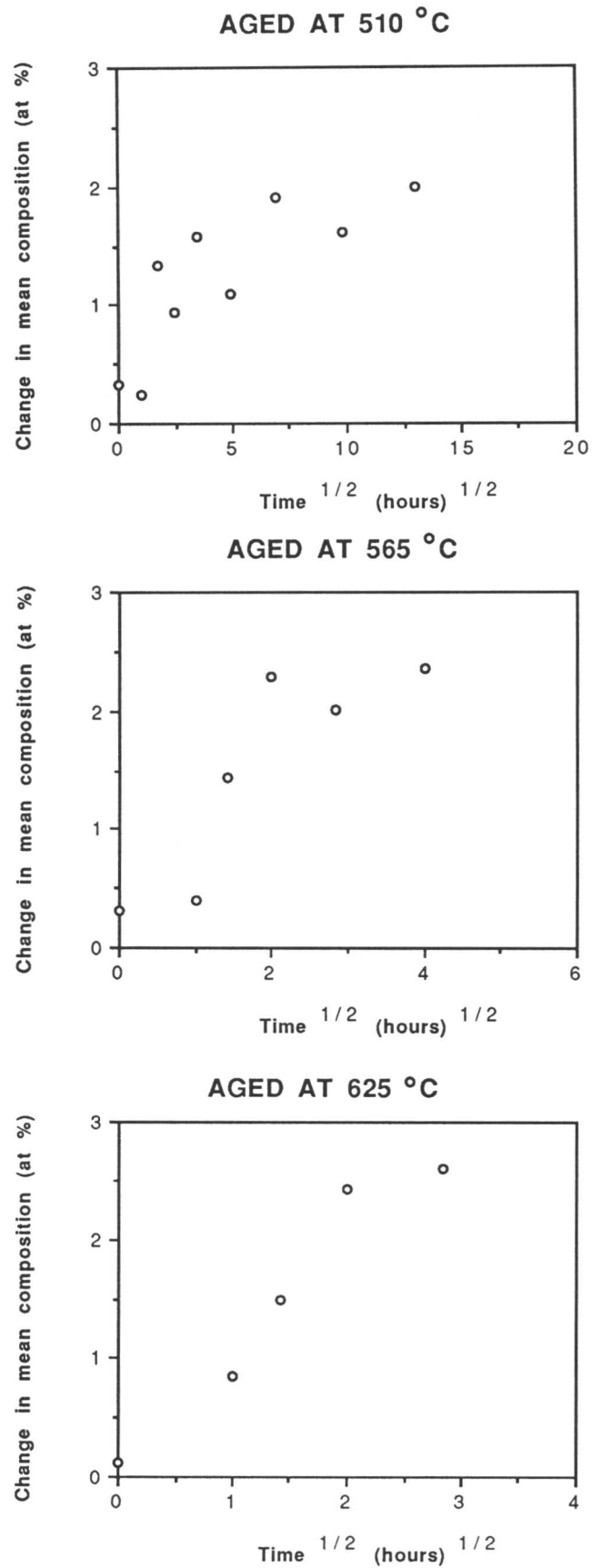


Figure 7.5: Means of measured values of $(c-\bar{c})$ at a given ageing time plotted versus $(\text{ageing time})^{1/2}$ in the Fe-Cr steel

7.4 Alloy carbide precipitates

7.4.1 Calculated equilibrium phases and compositions

Calculations were performed to determine the thermodynamically-stable carbide structures at the three ageing temperatures, and their relative proportions and equilibrium compositions, to be compared subsequently with values measured using EDX analysis of aged specimens. These compositions and volume fractions were determined using the MTDATA computer package in the same manner as previously. The results of these calculations are presented in table 7.5, which shows that the stable carbide in this alloy at all three ageing temperatures is M_7C_3 . As the equilibrium phase, this is the carbide which may be expected to form eventually, but not necessarily as the first non-cementite precipitate to form, which may be some sort of intermediate species, and not necessarily of equilibrium composition.

Temp (K)	Equilibrium phases	Composition (wt %)			At% ratio	
		Fe	Cr	C	Fe/Fe+Cr	Cr/Fe+Cr
783	96.76% α	98.74	1.26	0.00	98.65	1.35
	3.34% M_7C_3	5.58	85.45	8.96	5.74	94.26
838	96.75% α	98.64	1.36	0.00	98.54	1.46
	3.35% M_7C_3	8.45	82.59	8.97	8.69	91.31
898	96.73% α	98.75	1.42	0.00	98.48	1.52
	3.37% M_7C_3	11.20	79.82	8.98	11.56	88.44

Table 7.5: MTDATA calculations showing the equilibrium phases, and the compositions of those phases, in the Fe–Cr steel at the three ageing temperatures used

7.4.2 EDX compositional measurements

The non-cementite precipitates were analysed for composition as the cementite had been. Two ageing times were used at each temperature, the first corresponding to the time at which significant levels of precipitate other than cementite

were first observed, and the second after a much greater degree of ageing, to test whether the secondary precipitation took place at around equilibrium, or at a non-equilibrium concentration followed by enrichment. Around 60 particles were analysed in all six cases.

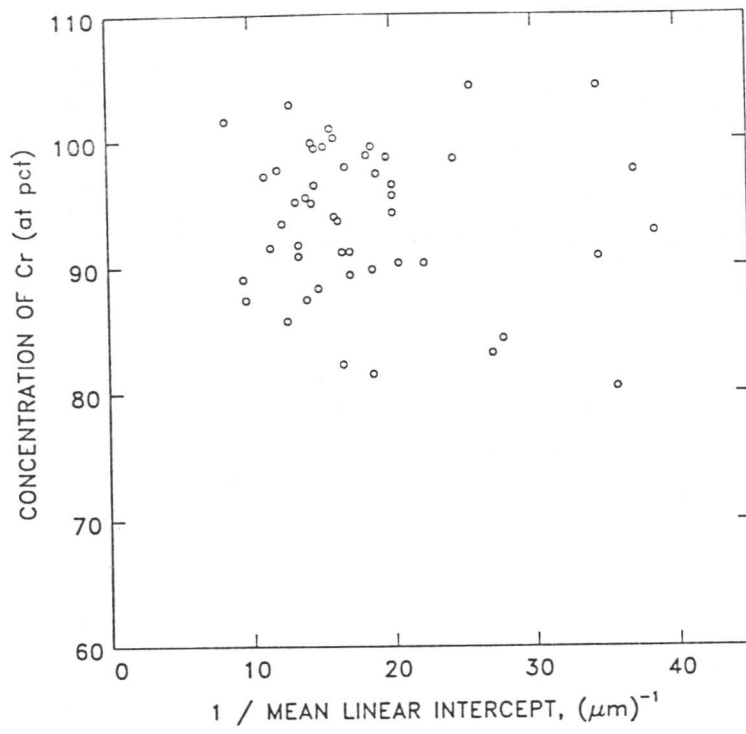
The mean values of chromium concentration (expressed as a percentage of substitutionals only, *i.e.*, chromium and iron) and particle size were calculated from the data, and are presented in table 7.6. It is evident that compositions are very close to those predicted for the equilibrium M_7C_3 phase by the MTDATA package at both the shorter and the longer ageing times. It appears that M_7C_3 precipitates and grows at a sufficiently slow rate to allow sufficient diffusion of substitutional atoms for the maintenance of an approximately equilibrium composition. Consequently, an analysis of particles precipitated in this fashion will not give any indication of the thermal history or degree of ageing to which the material has been subjected.

Temp (K)	short ageing			long ageing		
	time (hours)	particle size, μm	Cr/Fe+Cr at% ratio	time (hours)	particle size, μm	Cr/Fe+Cr at% ratio
783	24	0.061	91.75	672	0.079	91.70
838	16	0.064	88.72	672	0.061	87.71
898	8	0.059	83.11	336	0.074	87.50

Table 7.6: Mean measured chromium concentrations for the non-cementite particles in the Fe–Cr steel

Individual particle compositions were also plotted against particle size for each temperature (see figures 7.6–7.8). No relationship between composition and particle size was observed in the data, which is in accordance with the supposition that the nucleation and growth of the M_7C_3 particles occurred at roughly equilibrium compositions. It can be seen on the figures that the scatter of individual compositions about the mean is generally greater than it was for cementite, which may be a real effect, suggesting that M_7C_3 will tolerate a greater deviation from equilibrium than M_3C .

AFTER 24 HOURS AT 510 °C



AFTER 4 WEEKS AT 510 °C

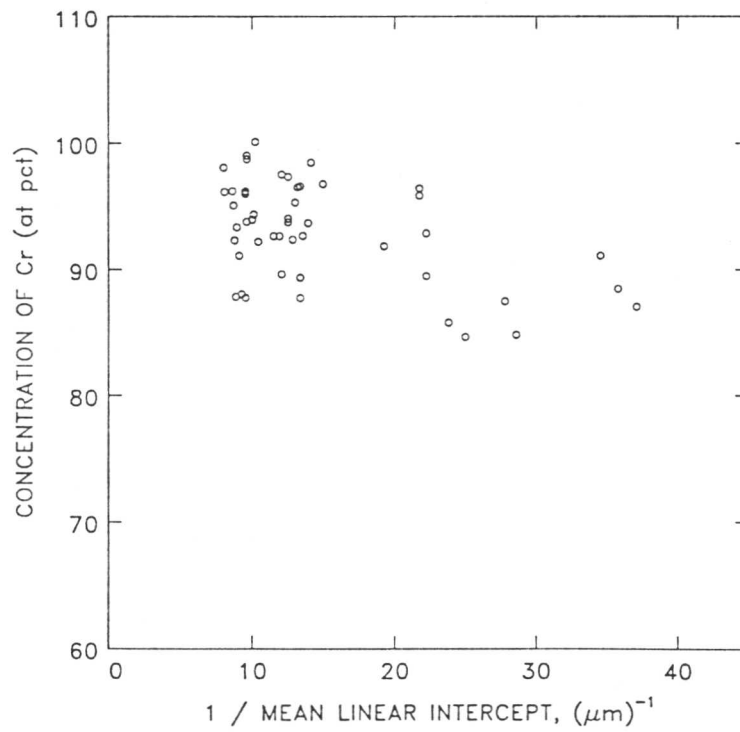
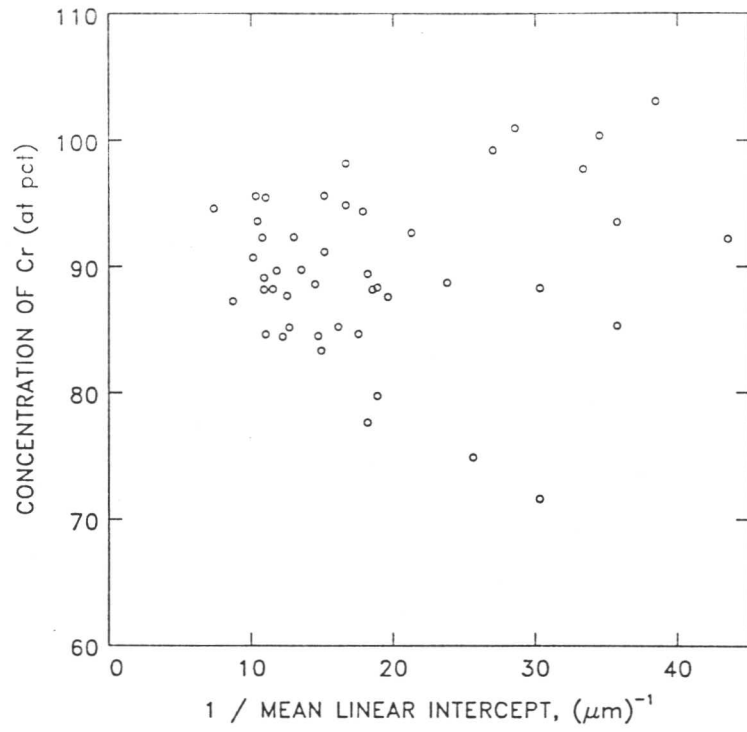


Figure 7.6: Measured compositions of M_7C_3 particles in the Fe-Cr steel aged at 510°C

AFTER 16 HOURS AT 565 °C



AFTER 4 WEEKS AT 565 °C

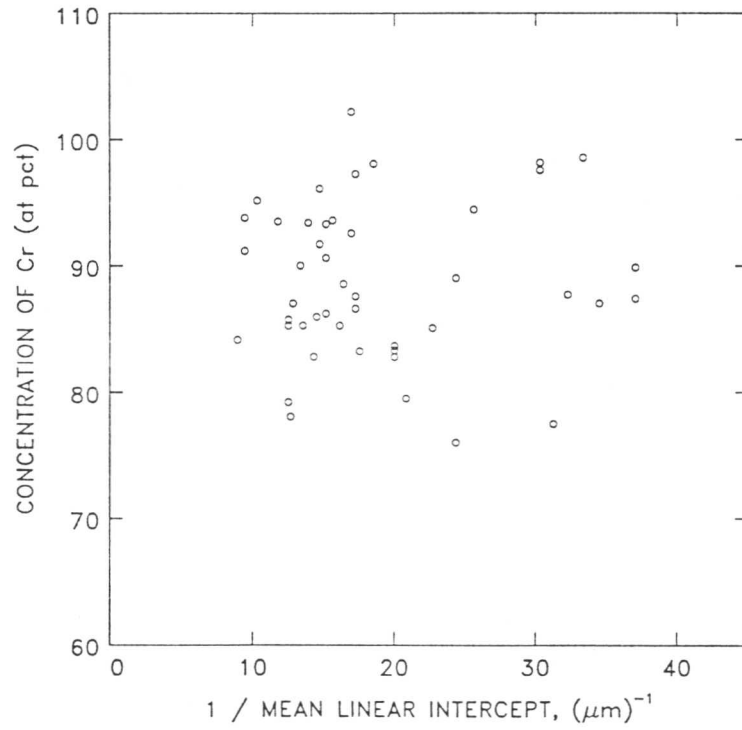
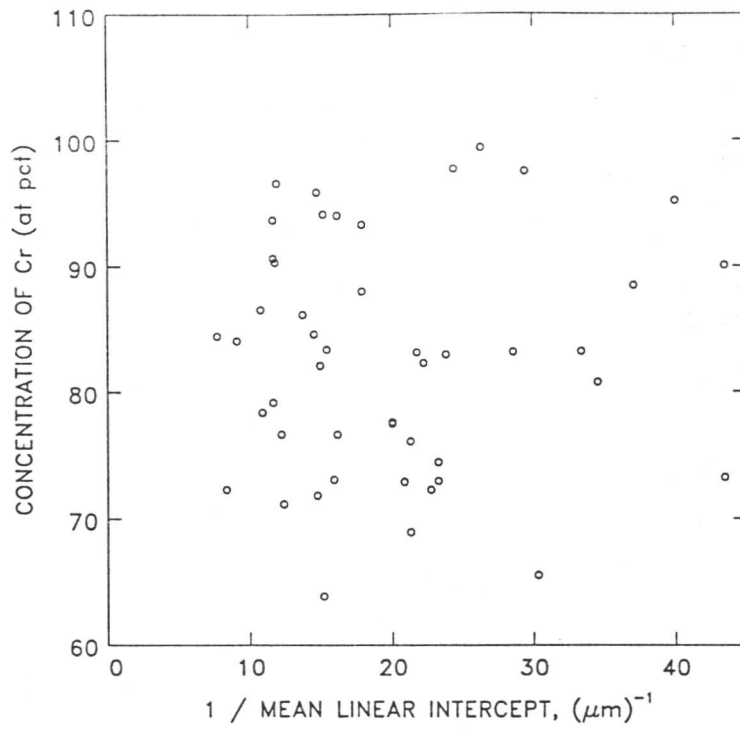


Figure 7.7: Measured compositions of M_7C_3 particles in the Fe-Cr steel aged at 565 °C

AFTER 8 HOURS AT 625 °C



AFTER 2 WEEKS AT 625 °C

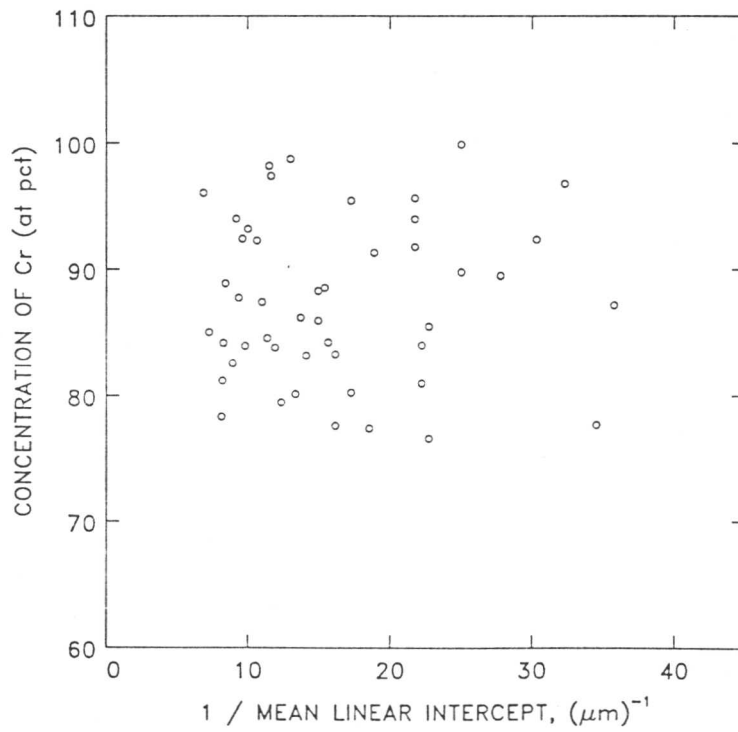


Figure 7.8: Measured compositions of M_7C_3 particles in the Fe-Cr steel aged at 625°C

Note that the occasional EDX result producing an apparent chromium : chromium+iron ratio of greater than 100% has to be included as it is a consequence of stochastic scatter in the X-ray process (iron content is so small that the associated signal is of the same order of magnitude as background noise, giving rise to the possibility of a negative value for iron content, hence a value for the normalized chromium content which exceeds 100%; see section 5.4.4 for a more detailed discussion of this problem).

7.5 Summary

The bainitic microstructures generated from this material were found during ageing to undergo simultaneous enrichment of cementite with chromium and precipitation of chromium rich carbides. The secondary precipitation appeared to occur in the ferrite matrix independent of cementite, which continued to enrich to some degree during the early stages of ageing. This process will denude the surrounding ferrite region of chromium, which would be expected to suppress chromium carbide precipitation and may explain the fact that this secondary precipitation appeared to occur away from the cementite.

Although enrichment of cementite was observed, the cementite enrichment rate was found to be significantly slower than predictions from the finite difference model, which can be explained by the effect of the secondary precipitation on the enrichment-rate-controlling process of diffusion of substitutional alloying elements within ferrite. Furthermore, at later stages of ageing, the metastable cementite phase was found redissolve at the expense of the more thermodynamically-stable M_7C_3 . Consequently, the model cannot be used to relate ageing time and temperature to degree of enrichment of cementite in this material; nor can the cementite composition be used as an indicator of thermal history on which to base a remanent life estimate in components manufactured from materials in which significant secondary precipitation occurs.

EDX analysis of the secondary precipitate indicated that it formed with a composition which was close to the equilibrium, in accordance with predictions

made from the MTDATA database. As a result, the composition of M_7C_3 cannot relate to ageing time, and any model which was intended to relate microstructure to thermal history in this material would need to be based on subsequent coarsening of the secondary precipitate, rather than enrichment.

It is evident that the diffusion-based model for enrichment of cementite is relatable to the thermal history of the material only for those alloys where no significant secondary precipitation is observed in the bainitic region, but the metastable cementite phase is retained for the full ageing period. Where secondary precipitation is occurring, it will interfere with the diffusion process, making the enrichment model inapplicable to the physical situation.

Chapter 8

SUMMARY

8.1 Composition Changes During Ageing of Bainitic Cementite

8.1.1 The simple analytical model

A model was tested for the enrichment of bainitic cementite during ageing, which was derived by considering a single cementite slab in a semi-infinite ferrite matrix, and considering diffusion within ferrite to be the enrichment-rate-controlling process. This model relies on the absence of any soft impingement within ferrite, or coarsening of cementite.

Experimental measurement of changes in cementite composition during ageing of bainitic microstructures in a 1Cr- $\frac{1}{2}$ Mo type power plant steel provides evidence that the model successfully describes the enrichment behaviour of this material providing the ageing time is not so large that soft impingement in the ferrite becomes significant. In particular, the experimental data agreed with the model in that:

- (i) The degree of cementite enrichment was found to be in accordance with a (time)^{1/2} relationship as expected from the model, which differs from frequent industrial practice where an empirical (time)^{1/3} relation has been preferred.
- (ii) Individual values of c^θ at a given ageing time are found to be dependent on cementite particle size, such that $(c - \bar{c}) \propto x_\theta^{-1}$, in accordance with the analytical model. Furthermore, the limited correlation shown between experimental data and prediction for this size effect has been explained as arising from stochastic scatter concomitant with the EDX technique. If the limitations thus imposed on such an analysis are considered, then the correlation between experimental data and the $(c - \bar{c}) \propto x_\theta^{-1}$ relationship is strong.

- (iii) The enrichment rate, obtained from the gradient of a graph of $(c - \bar{c})$ vs $(\text{time})^{1/2}$, can be used to produce a diffusion coefficient corresponding to the experimental data. The calculated values of D_α were very close to previously reported values of interdiffusion coefficient for chromium and manganese.

At longer ageing times, this linearity with $(\text{time})^{1/2}$ tended to break down, and the enrichment rate slowed, which is strongly suggestive of soft impingement within ferrite causing a reduction in the rate of diffusion of substitutional alloying elements to the cementite particles. This effect was noted after a timescale of months at 565°C, rather than the years these materials experience in service in power plant, so an analysis which allows for soft impingement is necessary to model the remanent life problem. Nevertheless, the analytical model provides an excellent description of cementite ageing prior to the onset of significant levels of soft impingement, and it can be concluded that cementite enrichment is primarily effected by diffusion of substitutional alloying elements through the ferrite to the α/γ interface, driven by the excess of substitutionals in the ferrite phase.

8.1.2 The finite difference model

The finite difference model was developed to include an analysis of the effect of soft impingement in ferrite on the enrichment rate. The model was found to be in excellent agreement with experimental results before a significant level of soft impingement occurred, and to give a reasonable estimate of the time after which soft impingement had a substantive effect on the enrichment rate. However, the slowing down of cementite enrichment at longer stages of ageing was somewhat greater than expected, and it is suspected that this arises from the failure of the model to account for the variation in size and irregular distribution of cementite particles that is found in practice.

If the finite element model is to be improved so that more accurate predictions can be made for the real situation, the following refinements can be proposed:

- (i) Account should be taken of non-uniform particle distributions and sizes, especially to allow for the fact that soft impingement will become significant at an earlier stage for more closely spaced particles. Adapting the model to consider a large number of different particles would lead to a huge increase in the computing time required, and would also necessitate a proper analysis of the interaction between diffusion fields in ferrite associated with many cementite particles, as the procedure used by the present form of the model of reflection at the last finite element in the ferrite could not be applied.
- (ii) An allowance should be made of changes to cementite morphology (enlargement and shape change) during ageing. Although the degree of coarsening observed in these experiments was small, and diffusion in ferrite shown to be the dominant process, over the timescales used, some change in cementite morphology can be expected to occur during the long ageing times which these materials are subjected to in industrial use. It is desirable that the effect of these changes on the enrichment process can be modelled.

If these limitations are borne in mind, the current analysis can provide an adequate model for the cementite enrichment processes during ageing of bainitic cementite in these materials.

8.2 Remanent Life Prediction

8.2.1 The engineering problem of remanent life prediction

It is suspected that a significant proportion of the high-temperature, high-pressure steam plant in contemporary power generation may be replaced unnecessarily, owing to the lack of an accurate method of determining the amount of potential life remaining in a component, and the resultant need for large safety factors. It has been suggested that this uncertainty arises from three principal sources:

- (i) The absence of a rigorous mechanistic model for microstructural degradation and creep damage accumulation in these materials during service.

- (ii) Large fluctuations which occur in practice in the pressure and temperature conditions to which the component is subjected.
- (iii) Problems in accurately measuring those pressure and temperature conditions.

8.2.2 Applicability of current work to remanent life prediction

It has been proposed that problems (ii) and (iii) could largely be eliminated if a model predicting to a high enough degree of accuracy the ageing behaviour of the material could be developed: analysis would then provide an indication of the thermal history of the component without the difficulties of constant on-plant monitoring of conditions.

It is evident that the limitations in the current model at the later stages of ageing which were uncovered in this work make it impossible to relate a cementite composition to an ageing regime with the required degree of accuracy at present. Nevertheless, significant groundwork for research into this problem has been made by advancing a procedure which models the early stages of ageing very successfully, and by illustrating the problems which must be addressed before the later stages of ageing can be similarly modelled.

REFERENCES

- Aaronson, H.I., 1962, "Decomposition of Austenite by Diffusional Processes", Interscience, New York, pp. 387-546
- Aaronson, H.I., Laird, C. and Kinsman, K.R., 1970, "Phase Transformations", ASM, Metals Park, Ohio, pp. 313-396
- Afrouz, A.M., Collins, M.J. and Pilkington, R., 1983, *Metals Tech.*, **10**, 461
- Ashby, M.F. and Ebeling, R., 1966, *Trans. Met. Sci. AIME*, **236**, 1396
- Atkinson, C., Aaron, H.B., Kinsman, K.R. and Aaronson, H.I. [Atkinson *et al.*], 1973, *Met. Trans.*, **4**, 783
- Ballinger, N.K. and Honeycombe, R.W.K., 1980, *Met. Sci.*, **14**, 121
- Balluffi, R.W. and Siegle, L.L., 1957, *Acta Metall.*, **5**, 449
- Batte, A.D. and Honeycombe, R.W.K., 1973, *J. Iron and Steel Inst.*, **211**, 284
- Berry, F.G. and Honeycombe, R.W.K., 1970, *Metall. Trans.*, **1**, 3279
- Bhadeshia, H.K.D.H. and Edmonds, D.V., 1979, *Metall. Trans.*, **10A**, 895
- Bhadeshia, H.K.D.H. and Edmonds, D.V., 1980, *Acta Metall.*, **28**, 1265
- Bhadeshia, H.K.D.H. and Waugh, A.R., 1982, *Acta Metall.*, **30**, 775
- Bhadeshia, H.K.D.H., 1980, *Acta Metall.*, **28**, 1103
- Bhadeshia, H.K.D.H., 1981a, *Acta Metall.*, **29**, 1117
- Bhadeshia, H.K.D.H., 1981b, *Met. Sci.*, **15**, 175
- Bhadeshia, H.K.D.H., 1982, *Met. Sci.*, **16**, 159
- Bhadeshia, H.K.D.H., 1985, *Progress in Materials Sci.*, **29**, 321
- Bhadeshia, H.K.D.H., 1988, Phase Transformations '87, (*Conf. Proc.*), Inst. of Metals, London, p. 309
- Bhadeshia, H.K.D.H., 1989, *Mat. Sci. Tech.*, **5**, 131
- Borggren, K. and Huntley, P., 1984, 2nd Int. Conf. on Creep & Frac. of Eng. Mats., (*Conf. Proc.*), Swansea, **2**, 1251
- Buckle, H., 1973, "The Science of Hardness Testing and its Research Applications", ASM, Metals Park, Ohio, pp. 453-485
- Campbell, K. and Honeycombe, R.W.K., 1974, *Met. Sci.*, **8**, 197
- Cane, B.J. and Browne, R.J., 1982, *Int. J. Pressure Vessels and Piping*, **10**, 11

- Cane, B.J. and Needham, N.G., 1983, *Advances in Life Prediction*, (*Conf. Proc.*), ASME, Albany, N.Y.
- Cane, B.J. and Townsend, R.D., 1984, CEGB Report No. TPRD/L/2674/N84
- Cane, B.J. and Williams, J.A., 1987, *Int. Mat. Review*, **32**, 241
- Cane, B.J. and Williams, K.R., 1979, *Int. Conf. of Mechanical Behaviour of Mats.*, (*Conf. Proc.*), Cambridge, **2**, 255
- Cane, B.J., 1978, *Matl. Sci. and Eng.*, **35**, 229
- Cane, B.J., 1979, 3rd Int. Conf. Mech. Behaviour of Matls, (*Conf. Proc.*), **2**, 173
- Cane, B.J., 1983, *High Temperature Tech.*, **1**, 4
- Cane, B.J., 1986, *Materials Forum*, **9**, 5
- Carruthers, R.B. and Collins, M.J., 1981,, “Quantitative Microanalysis With High Spatial Resolution”, (*Conf. Proc.*), Institute of Metals, London
- Carruthers, R.B. and Collins, M.J., 1983, *Metal Science*, **17**, 107
- CEGB, 1982, Procedure for boiler header creep life assessment, GOM101A
- Chance, J. and Ridley, N., 1981, *Metall. Trans.*, **12A**, 1205
- Christian, J.W. and Edmonds D.V., 1984, “Phase Transformations in Ferrous Alloys”, Met. Soc. AIME, New York, pp. 293–325
- Cliff, G. and Lorimer, G.W., 1972, 5th European Congress on Electron Microscopy, (*Conf. Proc.*), Bristol I. O. P., 140
- Cliff, G. and Lorimer, G.W., 1975, *J. Microscopy*, **103**, 203
- Coleman, M.C. and Rowley, T., 1973, CEGB Note No. RD/M/N 710
- Coleman, M.C., Parker, J.D., Walters, D.J. and Williams, J.A., [Coleman *et al.*] 1979,, 3rd Int. Conf. Mech. Behaviour of Matls, (*Conf. Proc.*), **2**, 193
- Collins, M.J., 1978, *Metals Technology*, **5**, 325
- Crevecoeur, G., 1985, *Remanent Life: Assessment & Extension*, (*Conf. Proc.*), Brussels, Sec. III, Paper 1,
- Darbyshire, J.M. and Knight, S.D., 1977 CEGB Report No RD/L/N 29/77
- Darken, L.S. and Gurry, R.W., 1953, “Physical Chemistry of Metals”, McGraw-Hill, New York, p.146
- Davenport, A.T., Berry, F.G. and Honeycombe, R.W.K., 1968, *Met. Sci.*, **2**, 104

- Day, R.V., Rowley, T. and Williams, J.A., 1979, CEGB Internal Report No. RD/M/R.227
- Dyson, B.F. and McLean, M., 1983, *Acta Metall.*, **31**, 17
- Dyson, B.F., 1976, *Metal Science*, **10**, 349
- Edmonds, D.V. and Honeycombe, R.W.K., 1978, *Met. Sci.*, **12**, 399
- Evans, W.J., 1976, *Met. Sci.*, **10**, 170
- Felix, W. and Geiger, T., 1961, *Sulzer Tech.*, **3/1961**, p. 37
- Fridberg, J., Trëndahl, L-E. and Hillert, M., 1969, *Jerkont. Ann.*, **153**, 263
- Gladman, T. and Woodhead, J.H., 1960, *J. Iron and Steel Inst.*, **194**, 189
- Goldstein, J.A. and Yakowitz, H. (Eds.), 1975, "Practical Scanning Electron Microscopy, Electron and Ion Microprobe Analysis", Plenum Press
- Goldstein, J.A., Costley, J.L., Lorimer, G.W. and Reed, S.J.B., [Goldstein *et al.*] 1977 *S. E. M.*, **1**, 315
- Goldstein, J.A., Lorimer, G.W. and Cliff, G., 1976, 6th European Congress on Electron Microscopy, (*Conf. Proc.*), Jerusalem, p. 56
- Goldstein, J.A. and Williams, D.B., 1978, *Scanning Electron Microscopy*, **1**, 427
- Gooch, D.J. and Townsend, R.D., 1986,
- Hart, R.V., 1976, *Metals Technology*, **3**, 1
- Hart, R.V., 1977a, *Metals Technology*, **4**, 442
- Hart, R.V., 1977b, *Metals Technology*, **4**, 447
- Hart, R.V., 1980, Engineering Aspects of Creep, (*Conf. Proc.*), Sheffield, **2**, 207
- Hehemann, R.F., Kinsman, K.R. and Aaronson, H.I., 1972 *Metall. Trans.*, **3**, 1077
- Hehemann, R.F., 1970, "Phase Transformations", ASM, Metals Park, Ohio, pp. 397-432 J
- Hillert, M., 1952, *Jern. Ann.*, **136**, 25
- Hillert, M., 1962, "The Decomposition of Austenite by Diffusional Process", Interscience, New York, p. 197
- Honeycombe, R.W.K. and Pickering, F.B., 1972, *Metall. Trans.*, **3**, 1099
- Honeycombe, R.W.K., 1984, "Phase Transformations in Ferrous Alloys", Met. Soc. AIME, New York, pp. 259-280
- Hultgren, A., 1947, *Trans. ASM*, **39**, 415

- Jenkins, C.H.H. and Mellor, C.A., 1942, *J. Iron and Steel Inst.*, **143**, 31
- Kachanov, L.M., 1958, *Izv. Akad Nauk. USSR Otd. Tekd. Nank*, **8**, 26
- Kinsman, K.R. and Aaronson, H.I., 1967, "Transformation and Hardenability in Steels", Climax Mo Co., Ann Arbor, Mich., pp. 39–53
- Kinsman, K.R., Eichen, E. and Aaronson, H.I., 1975, *Metall. Trans.*, **6A**, 303
- Ko, T. and Cottrell, S.A., 1952, *J. Iron and Steel Inst.*, **174**, 307
- Laird, C. and Aaronson, H.I., 1970, *Acta Metall.*, **18**, 845
- Liu, Y.C. and Aaronson, H.I., 1969, *Acta Metall.*, **17**, 505
- Lorimer, G.W., Al-Salman, S.A. and Cliff, G., 1977, EMAG '77, (*Conf. Proc.*), Inst. of Phys. Conf. Series, p. 369
- Ludwigsen, P.B., 1985, Remanent Life: Assessment & Extension, (*Conf. Proc.*), Brussels, Sec III, Paper 3
- Manier, G.N. and Szirmae, A. (coordinators), 1973, ASTM STP 547, pp. 20–23
- Mehl, R.F., 1939, "Hardenability of Alloy Steels", ASM, pp. 1–54,
- Morris, P.L., Davies, N.C. and Treverton, J.A., 1977, EMAG '77, (*Conf. Proc.*), Inst. of Phys. Conf. Series, p. 377
- Murphy, M.C. and Branch, G.D., 1969, *J. Iron and Steel Inst.*, **207**, 1347
- Needham, N.G., and Gladman, T., 1980, *Met. Sci.*, **14**, 64
- Ohmori, Y., 1971, *Trans. I.S.I. Japan*, **11**, 95
- Parker, J.D. and Sidey, D., 1986, *Materials Forum*, **9**, 78
- Pickering, F.B., 1967, "Transformation and Hardenability in Steels", Climax Mo Co., Ann Arbor, Mich., pp. 102–129
- Prado, J.M., 1986, *J. Mat. Sci. Letters*, **5**, 1075
- Price, A.T. and Williams, J.A., 1982, "Recent advances in Creep & fracture of Engineering Materials", Pineridge Press, Swansea, U.K.
- Puls, M.P. and Kirkaldy, J.S., 1972, *Metall. Trans.*, **3**, 2777
- Purdey, G.R. and Hillert, M., 1984, *Acta Metall.*, **32**, 823
- Rabotnov, Y.M., 1969, XIIth Int. Union Theoretical and App. Mech. Cong., (*Conf. Proc.*), Berlin, p. 342,
- Ricks, R.A., Howell, P.R. and Honeycombe, R.W.K., 1980, *Met. Sci.*, **14**, 121
- Robinson, E.L., 1952, *Trans. ASME*, **74**, 777

- Rostoker, W. and Dvorak, J.R., 1977, "Interpretation of Metallographic Structures", 2nd Ed., Academic Press, New York
- Russ, J.C., 1984, "Fundamentals of Energy-Dispersive X-Ray analysis", Butterworths
- Russell, K.C., 1969, *Acta Metall.*, **17**, 1123
- Sargent, P.M., 1979a, "Factors Affecting the Microhardness of Solids", PhD Thesis, Cambridge Univ., pp. 88–98
- Sargent, P.M., 1979b, *ibid.*, pp. 66–87
- Senior, B., 1988, EUREM '88, (*Conf. Proc.*), York, *in press*
- Shahinian, P. and Achter, M.R., 1963, Joint Int. Conf. on Creep, (*Conf. Proc.*), Inst. Mech. Eng/ASME, paper 28
- Shahinian, P. and Achter, M.R., 1965, "High Temperature Materials", J. Willey, London
- Smith, C.S., 1953, *Trans. A. S. M.*, **45**, 433
- Smith, G.M. and Honeycombe, R.W.K., 1982, 6th Int. Conf. on Strength of Metals and Alloys, (*Conf. Proc.*), Melbourne, p. 407
- Stark, I., Smith, G.W.D. and Bhadeshia, H.K.D.H., 1987, Phase Transformations '87, (*Conf. Proc.*), Inst. of Metals, London,
- Steen, M., 1983, *Int. J. Pressure Vessels and Piping*, **14**, 201
- Steen, M., 1984, 2nd Int. Conf. on Creep & Frac. of Eng. Mats., (*Conf. Proc.*), Swansea, **2**, 1195
- Stevens, R. and Flewitt, P.E.J., 1984, *Metall. Trans.*, **15A**, 707
- Townsend, R.D., 1986, *Materials Forum*, **9**, 90
- Umetoto, M., Furuhashi, T. and Tamura, I., 1986, *Acta Metall.*, **34**, 2235
- Umetoto, M., Horiuchi, K. and Tamura, I., 1982, *Trans. I.S.I. Japan*, **22**, 854
- Vierros, P., 1985, Remanent Life: Assessment & Extension, (*Conf. Proc.*), Brussels, Sec. III, Paper 4
- Watson, J.D. and McDougall, P.G., 1973, *Acta Metall.*, **21**, 961
- Widgery, D.J. and Knott, J.F., 1978, *Met. Sci.*, **12**, 8
- Williams, K.R., 1976, *Met. Sci.*, **10**, 332
- Williams, K.R., 1981, Int. Conf. on Creep & Frac. of Eng. Mats., (*Conf. Proc.*), Swansea, 489

Wilson, M., 1986, *Materials Forum*, **9**, 53

Zener, C., 1946, *Trans. AIME*, **167**, 50

APPENDIX ONE

STEELS USED IN THE PROGRAMME

We are grateful to the CEGB for provision of materials for the experimental programme outlined in this dissertation. This material comprised a large segment of power station steam pipe in the as-fabricated condition and two plugs of service exposed material from superheater steam header. The former sample was used extensively as a base material for a large programme of experimental work; the latter used principally in theoretical studies as a typical composition source. Details of the compositions and thermal histories of these specimens are given below.

The Large Pipe Segment

The chemical composition (wt %) of this material was as follows:

C	Si	Mn	P	S	Al	Cr	Mo
0.12	0.23	0.51	0.011	0.009	0.009	0.87	0.50

It had been subjected to the following heat treatments:

30 minutes at 930°C; air cooled

60 minutes at 700°C; air cooled

The pipe was then given an additional stress relief at 650°C in 1.5 hours, and supplied for use in several CEGB remanent creep life programmes

The Service Exposed Material

The CEGB also supplied two plugs of material from superheater steam headers. These were taken from non-critical areas which had partially exhausted their anticipated service life. Both plugs were taken from headers made from material originating in the same cast, which was manufactured by an electric

arc steel making process. The steam headers were fabricated by the Chesterfield Tube Company.

The chemical analysis of the original cast (wt %) was:

C	Si	Mn	S	P	Ni	Cr	Mo
0.13	0.25	0.55	0.027	0.015	0.14	1.01	0.54

Design operating conditions for the header are given below.¹

Pressure:	2450 psi (16.9 MPa) [drum 2680 psi (18.5 MPa), final superheater outlet 2400 psi (16.5 MPa)]
Temperature:	548°C (final outlet 565°C)
Dimensions:	17 7/8 in. (454 mm) outer diameter, 11 1/8 in. (283 mm) inner diameter, 3/8 in. (86 mm) thick, 43 ft. 9 in. (13.34 m) in length.
Design stress:	36.3 N/mm ² plain cylinder stress, 44.8 N/mm ² inter-alignment stress.

Actual service conditions were such that an effective average pressure of 1900 psi (13.1 MPa) was experienced, corresponding to a 27.5 N/mm² plain cylinder stress and a 34.0 N/mm² interligament stress.

Two of the plugs trepanned from this service exposed steam header material were supplied, both from non-critical areas (*i.e.*, , predicted life fraction consumed significantly less than unity).

PLUG U3B1: Sampled after 73 000 hours in service with a measured local temperature of 519°C. Present theory leads to an estimate of life fraction consumed for this material of 0.017 – 0.040 (mean estimate 0.025).

¹ The figures given are quoted directly in the same units as CEGB information. Approximate S.I. equivalents to these parameters are given in parentheses.

PLUG U4A1: Sampled after 61 000 hours in service with a measured local temperature of 560°C. This corresponds to an estimated life fraction consumed in this material of 0.125 – 0.330 (mean estimate 0.19).

These plugs had measured chemical compositions (in wt %) of:

	C	Si	Mn	S	P	Ni	Cr	Mo
U3B1	0.11	0.19	0.43	0.031	0.018	0.12	0.89	0.54
U4A1	0.13	0.22	0.52	0.026	0.017	0.13	1.02	0.53

APPENDIX TWO

PROGRAM TO SIMULATE STOCHASTIC SCATTER IN EDX COMPOSITION ANALYSIS

```
C
C
C calculates c - cbar from x as time increases.
C for consistency with the way experimental data was recorded,
C X is in micrometres, c in at %, in the input dataset,
C and data is converted in the prog.
C typical dataset:
C   time (hours) ,temp (C), sample size
C   diff coefficient, c alphatheta, c bar      (for Cr)
C   diff coefficient, c alphatheta, c bar      (for Mn)
C   diff coefficient, c alphatheta, c bar      (for Mo)
C
      DOUBLE PRECISION X(500), C0(3,500), C1(3,500),
+RESULT(20), CC(3,500), CALTH(3), CBAR(3), DIFF(3),
+SCAT(3), X2(100), CC2(100)
      INTEGER I, II, J, IFAIL, RAN(100), SAMPLE
      CHARACTER*10 NAME
C reads in ageing time (hours), temp (C), and size of sample
      READ (5,*) TIME, TEMP, SAMPLE
      TIME=TIME*3600.0
      TEMPA=TEMP+273.15
C reads in diff coeff, c alphatheta, c bar, standard deviation
C of stochastic scatter in measured c; the last three are all
C in ** atomic fraction **
      READ (5,*) (DIFF(II),CALTH(II),CBAR(II),SCAT(II), II=1,3)
      CALL G05CCF (0)
      DO 20 II=1,3
        DO 10 I=1,500
          C0(II,I) = G05DDF (CBAR(II), SCAT(II))
          IF (II .EQ. 1) THEN
13           X(I) = G05DDF (0.16, 0.05)
              IF (X(I) .LT. 0.05) GOTO 13
              X(I) = X(I) * 1.0D-06
          ENDIF
10          CONTINUE
20          CONTINUE
C
      CALL CHANGE(X,C0,C1,CC,TIME,DIFF,CALTH,CBAR)
      CALL SCATTER(CC,SCAT)
      CALL RANDOM(RAN,SAMPLE)
C
C making random selection and converting to microns and atomic
C percent for compatibility with experimental data
```

```

DO 40 II=1,3
  DO 30 I=1,SAMPLE
    IF (II .EQ. 1) X2(I) = 1.0 / (X(RAN(I)) * 1.0D06)
    CC2(I) = CC (II,RAN(I))*100.0
30  CONTINUE
    IF (II .EQ. 1) NAME='CHROMIUM'
    IF (II .EQ. 2) NAME='MANGANESE'
    IF (II .EQ. 3) NAME='MOLYBDENUM'
    CALL REG(X2,CC2,SAMPLE,RESULT,NAME)
40  CONTINUE
C
  END
C
  SUBROUTINE CHANGE(X,C0,C1,CC,TIME,DIFF,CALTH,CBAR)
C calculates new mli and composition after given time
  DOUBLE PRECISION X(500), C0(3,500), C1(3,500), CC(3,500),
+CALTH(3), CBAR(3), DIFF(3), TIME
  INTEGER I, II
  DO 20 II=1,3
    DO 10 I=1,500
      C1(II,I) = C0(II,I) +
& ((CBAR(II)-CALTH(II))/X(I))*((TIME*DIFF(II))**0.5)*2.25676
      CC(II,I) = C1(II,I) - CBAR(II)
10  CONTINUE
20  CONTINUE
    RETURN
  END
C
  END
C
  SUBROUTINE SCATTER (CC,SCAT)
C introduces random, normally distributed scatter into each
C value of c calculated in CHANGES.
  DOUBLE PRECISION CC(3,500), XX, SCAT(3)
  INTEGER I,II
  CALL G05CCF (0)
  DO 20 II=1,3
    DO 10 I=1,500
      XX = G05DDF (0.0, SCAT(II))
      CC(II,I) = CC(II,I)+XX
10  CONTINUE
20  CONTINUE
    RETURN
  END
C
  SUBROUTINE RANDOM (RAN, SAMPLE)
C selects random readings from CHANGE output
  DOUBLE PRECISION X
  INTEGER SAMPLE
  INTEGER RAN(SAMPLE)
  CALL G05CCF (0)

```

```

DO 5, I=1, SAMPLE
X = G05CAF (X)
RAN(I) = (SAMPLE*X+1)
5 CONTINUE
RETURN
END

C
C
SUBROUTINE REG(X,Y,N,RESULT,NAME)
IMPLICIT REAL*8 (A-H,O-Z)
DOUBLE PRECISION X(200), Y(200), RESULT(20)
INTEGER I, IFAIL, N
CHARACTER*10 NAME
WRITE(6,99998) NAME
WRITE(6,99996) (I,X(I),Y(I),I=1,N)
IFAIL = 1
CALL G02CAF(N, X, Y, RESULT, IFAIL)

C
C TEST IFAIL
C
IF (IFAIL) 20, 40, 20
20 WRITE (6,99995) IFAIL
GO TO 60
40 WRITE (6,99994) (RESULT(I),I=1,5)
WRITE (6,99993) RESULT(6), RESULT(8), RESULT(10)
WRITE (6,99992) RESULT(7), RESULT(9), RESULT(11)
WRITE (6,99991) (RESULT(I),I=12,20)
60 CONTINUE
99998 FORMAT (/ ,14H0 ELEMENT : ,A10)
99997 FORMAT (2F10.5)
99996 FORMAT (/ ,36H0 CASE INDEPENDENT DEPENDENT/10H NUMBER ,
* 25H VARIABLE VARIABLE//(1H , I4, 2F15.4))
99995 FORMAT (22H0ROUTINE FAILS, IFAIL=, I2/)
99994 FORMAT (46H0MEAN OF INDEPENDENT VARIABLE = ,
* F8.4/46H MEAN OF DEPENDENT VARIABLE = ,
* F8.4/46H STANDARD DEVIATION OF INDEPENDENT VARIABLE = ,
* F8.4/46H STANDARD DEVIATION OF DEPENDENT VARIABLE = ,
* F8.4/46H CORRELATION COEFFICIENT = , F8.4)
99993 FORMAT (46H0REGRESSION COEFFICIENT = ,
* D12.4/46H STANDARD ERROR OF COEFFICIENT = ,
* F8.4/46H T-VALUE FOR COEFFICIENT = , F8.4)
99992 FORMAT (46H0REGRESSION CONSTANT = ,
* D12.4/46H STANDARD ERROR OF CONSTANT = ,
* F8.4/46H T-VALUE FOR CONSTANT = , F8.4)
99991 FORMAT (32H0ANALYSIS OF REGRESSION TABLE :-//13H SOURCE,
* 55H SUM OF SQUARES D.F. MEAN SQUARE F-VALUE//
* 18H DUE TO REGRESSION, F14.4, F8.0, 2F14.4/14H ABOUT REGRES,
* 4HSION, F14.4, F8.0, F14.4/18H TOTAL , F14.4,
* F8.0)
RETURN
END

```

APPENDIX THREE

FINITE DIFFERENCE PROGRAM TO ANALYSE AGEING OF BAINITIC CEMENTITE

Copyright Dr. H. K. D. H. Bhadeshia, Department of Materials Science
C and Metallurgy, University of Cambridge, Pembroke Street, Cambridge
C CB2 3QZ, U. K. Telephone Cambridge 334301

C

C Last update of this version: P. Wilson, 3rd November 1989

C

C Program using finite difference method for the solution of the
C problem of enrichment of cementite with substitutional alloying
C elements during the ageing of bainitic steels

C

C

C EQFER=Equilibrium wt.% of X in ferrite at ageing temperature

C EQCEM=Equilibrium wt.% of X in cementite at ageing temperature

C EBAR=Average X wt.% in alloy

C FERS normalised concentration of X at ferrite surface

C CEMS normalised concentration of X at cementite surface

C TIMH time in hours

C TIM = Time, in seconds

C KTEMP=Absolute temperature

C TCEM=Thickness of cementite in metres

C TFER= Half thickness of ferrite in metres

C DFER=Diffusivity of X in ferrite

C DCEM=Diffusivity of X in cementite

C Concentrations normalized relative to average alloy concentration

C Dimension normalize relative to carbide particle thickness

C ICEM, IFER, J1 are the number of finite slices

C for dimension and time respectively

C IFER and J1 are calculated by the program

C A3 controls the amount of information that is printed out

C SETIME controls the time in hours that the experiment runs.

C JTEST modifies the mass balance condition when the CEMS reaches
C the equilibrium concentration. Hence mass conserved.

C Value set to true when CEMS reaches equilibrium.

C SOFTFER tests for soft impingement in ferrite (value true

C after onset of soft impingement

C SOFTCEM likewise for cementite

C

C Typical data

C 838.15 0.5D-03 39.0D+00 2.5D+00 1.0D-07 2.0D-06 1000 5

C 0.0003D+00 2.0D+00 1.0 1.0

C 1.11D-19 (Interdiffusion)

C End of data

C

```

C
  IMPLICIT REAL*8 (A-H,K-Z), INTEGER(I,J)
  DOUBLE PRECISION CFER(1500,2),CCEM(20,2),INTER,DFER,DCEM
  LOGICAL SOFTFER, SOFTCEM, JTEST
  SOFTFER=.FALSE.
  SOFTCEM=.FALSE.
  JTEST=.FALSE.
  READ(5,*)KTEMP,EQFER,EQCEM,EBAR,TCEM,TFER,ICEM
  READ(5,*)CFER(1,1),CCEM(1,1),A3,SETIME
  READ(5,*)INTER
  RFER=0.40D+00
  RCEM=RFER
  DFER=INTER
  DCEM=INTER
  STCEM=0.5D+00*TCEM/ICEM
  IFER=DINT(TFER/STCEM)
  STFER=TFER/IFER
  TIME=RFER*STFER*STFER/DFER
  J1=DINT(3.6D3*SETIME/TIME)
  WRITE(6,28)DFER,DCEM,TFER,TCEM,EQFER,EQCEM,KTEMP,ICEM,IFER
&,STCEM,STFER
C
C all except the first slices set to a normalised C of 1.0
  DO 6 I=2,ICEM
    CCEM(I,1)=1.0D+00
6    CONTINUE
  DO 26 I=2,IFER
    CFER(I,1)=1.0D+00
26   CONTINUE
C
  FERS=EQFER/EBAR
  DR=DFER/DCEM
  WRITE(6,12)CCEM(1,1),CFER(1,1)
C
C Finite difference analysis
C
  TIM=0.0D+00
  WRITE(6,34)
  DO 1 J=2,J1
    TIM=TIM+TIME
    TIMH=TIM/3600.0D+00
    IF(TIMH.GT.SETIME)GOTO 101
    CEMM=0.0D+00
C
C          **** Ferrite *****
C
C First slice
C
  IF(JTEST) FERS=((CCEM(1,1)-CEMS)/DR) + CFER(1,1)
C Note: surface concentration in ferrite is at equilibrium
C until CEMS reaches the equilibrium concentration

```

```

C
  CFER(1,2)=CFER(1,1) + RFER*(FERS - 2.0D+00*CFER(1,1)
&+ CFER(2,1))
  FER=CFER(1,2)*EBAR
  XTFER=STFER
  FERR=FER
  CFER(1,1)=CFER(1,2)
C
C
  DO 20 II=2,IFER-1
  CFER(II,2)=CFER(II,1)+RFER*(CFER(II-1,1)
&-2.0D+00*CFER(II,1)+CFER(II+1,1))
  FER=CFER(II,2)*EBAR
  XTFER=STFER*II
  FERR=FER+FERR
  CFER(II,1)=CFER(II,2)
20  CONTINUE
C
C Ensure reflection at last slice
  CFER(IFER,2)=CFER(IFER,1)+RFER*(CFER(IFER-1,1)
&-2.0D+00*CFER(IFER,1)+CFER(IFER-1,1))
  IF (.NOT.SOFTFER) CALL SOFT(CFER(IFER,2),1,SOFTFER,TIMH)
  FER=CFER(IFER,2)*EBAR
  XTFER=STFER*IFER
  FERR=FER+FERR
  CFER(IFER,1)=CFER(IFER,2)
C
C
C          ***** Cementite *****
DO 2 I=1,ICEM
C
  IF(I .EQ. 1) THEN
    CEMS=DR*(CFER(1,1)-FERS)+CCEM(1,1)
    IF(CEMS .GT. (EQCEM/EBAR)) THEN
      CEMS=EQCEM/EBAR
      IF(.NOT.JTEST) THEN
        WRITE(6,35)TIMH
        JTEST=.TRUE.
      ENDIF
    ENDIF
    CCEM(1,2)=CCEM(1,1) + RCEM*(CEMS-2.0D+00*CCEM(1,1)
& + CCEM(2,1))
C
C Reflect at position of symmetry
  ELSEIF(I .EQ. ICEM) THEN
    CCEM(ICEM,2)=CCEM(ICEM,1)+RCEM*(CCEM(ICEM-1,1)
& -2.0D+00*CCEM(ICEM,1)+CCEM(ICEM-1,1))
    IF (.NOT.SOFTCEM) CALL SOFT(CCEM(ICEM,2),2,SOFTCEM,TIMH)
  ELSE
    CCEM(I,2)=CCEM(I,1)+RCEM*(CCEM(I-1,1)
& -2.0D+00*CCEM(I,1)+CCEM(I+1,1))

```

```

        ENDIF
C Calculate surface concentration in cementite appropriate for mass
C balance
        CEM=CCEM(I,2)*EBAR
        XTCEM=I*STCEM
        CEMM=CEM+CEMM
        CCEM(I,1)=CCEM(I,2)
2      CONTINUE
C
C
C
        CEMM=CEMM/ICEM
        FERR=FERR/IFER
        DUMMY=J/A3
        DUMMY=DINT(DUMMY)-DUMMY
        IF(DUMMY.NE.0.0)GOTO 1
        AVER=(FERR*TFER + CEMM*0.5D+00*TCEM)/(TFER+0.5D+00*TCEM)
        WRITE(6,27)TIMH,CEMM,FERR,AVER,FERS*EBAR,CEMS*EBAR
1      CONTINUE
101     WRITE(6,25)
        DO 44 I=1,ICEM
        IF(CCEM(I,2).LT.1.0001)GOTO 46
        WRITE(6,7) I,CCEM(I,2),CCEM(I,2)*EBAR
44      CONTINUE
46      WRITE(6,24)
        DO 45 J=1,IFER
        IF(CFER(J,2).GT.0.999)GOTO 47
        WRITE(6,7) J,CFER(J,2),CFER(J,2)*EBAR
45      CONTINUE
47      CONTINUE
29      FORMAT(' TIME, s =',D12.4,' TIME, hrs. =',F12.3)
28      FORMAT(' Diffusion coefficient in ferrite, m**2/s = ',
&D12.4/' Diffusion coefficient in cementite, m**2/s, = ',D12.4/
&' Half thickness of ferrite, m =',D12.4/
&' Thickness of cementite, m =',D12.4/
&' Eq. conc. of X at interface, in ferrite, wt.% = ',D12.4/
&' Eq. conc. of X at interface, in cementite, wt.% = ',D12.4/
&' Absolute Temperature = ',F8.2,' ICEM, IFER = ',2I9/
&' STCEM (m) = ',D12.4,' STFER (m) = ',D12.4//)
34      FORMAT(' HOURS CEM FERRITE AVERAGE X FERS CEMS')
27      FORMAT(D12.4,F9.4,F9.4,F9.4,F9.4,2F9.4)
24      FORMAT(' No Norm. Conc. wt.%X in Ferrite')
25      FORMAT(' No Norm. Conc. wt.%X in Cementite')
7       FORMAT(I8,D12.4,2F10.4)
11      FORMAT('-----')
12      FORMAT(' Time 0, slice 1, cementite and ferrite norm conc ',
&2F12.4/)
35      FORMAT(' CEMENTITE SURFACE COMPOSITION AT EQUILIBRIUM'
&,F10.2,' hours')
        STOP
        END

```

C
C

```
      SUBROUTINE SOFT(A,I,TEST,TIMH)
      DOUBLE PRECISION A,TIMH
      LOGICAL TEST
      GOTO (1,2) I
1     IF(A .LT. 0.99) THEN
          WRITE(6,10)TIMH
          TEST=.TRUE.
      ENDIF
      GOTO 3
2     IF(A .GT. 1.01D+00) THEN
          WRITE(6,11)TIMH
          TEST=.TRUE.
      ENDIF
3     RETURN
10    FORMAT(' SOFT IMPINGEMENT IN FERRITE',F10.2,' hours')
11    FORMAT(' SOFT IMPINGEMENT IN CEMENTITE',F10.2,' hours')
      END
```